1-1-2012

Synthesis of Metal, Oxide, Alloy, and intermetallic Nanocrystals for Catalysis

Yijin Kang
University of Pennsylvania, kangyijin@gmail.com

Recommended Citation

Kang, Yijin, "Synthesis of Metal, Oxide, Alloy, and intermetallic Nanocrystals for Catalysis" (2012). *Publicly Accessible Penn Dissertations*. 525.
http://repository.upenn.edu/edissertations/525

Synthesis of Metal, Oxide, Alloy, and intermetallic Nanocrystals for Catalysis

Abstract

The synthesis of nanocrystals is the core of the nanoscience. The highly controlled nanomaterials are desirable for the studies of catalysis, in order to unambiguously correlate the catalytic properties with the structure and composition of catalysts. In this thesis, highly controlled nanocrystals are synthesized through solution phase synthesis. Shape controlled nanocrystals can be synthesized as cubes, octahedra, icosahedra, truncated cubes, cuboctahedra tetrapods, octapods and spheres. The nanocrystals with these morphologies selectively expose {100} and/or {111} facets as well as high-index facets, thus enabling various investigations of structure sensitive catalysis at the nanoscale. In addition to the shape control, the composition of metal catalysts is also tunable

by making alloy or intermetallic nanocrystals. The nanocrystals of Pt-Mn, Pt-Fe, Pt-Co, Pt-Ni, Pt-Cu, Pt-Zn, Pt-Pb, Pt3Mn, Pt3Fe, Pt3Co, Pt3Ni, Pt3Zn, Pt3Pb, FePt, and etc. allow the fundamental exploration of catalysis. Oxides, heterostructures, as well as artificial crystals which have a long range ordered crystalline structure, are also prepared. These highly controlled nanomaterials have been demonstrated as ideal model materials for studies of catalysis. In this thesis, formic acid and methanol electrooxidation, oxygen

reduction reaction, oxygen storage, CO oxidation, and enhanced stability are discussed.

Degree Type
Dissertation

Degree Name
Doctor of Philosophy (PhD)

Graduate Group
Chemistry

First Advisor
Christopher B. Murray

Second Advisor
Donald H. Berry

Keywords
alloy, catalysis, electrocatalysis, intermetallic, nanocrystal, nanomaterials

Subject Categories
Chemistry | Mechanics of Materials

SYNTHESIS OF METAL, OXIDE, ALLOY, AND INTERMETALLIC NANOCRYSTALS FOR CATALYSIS

Kang Yijin

A DISSERTATION

in

Chemistry

Presented to the Faculties of the University of Pennsylvania in Partial Fulfillment

of the Requirements for the Degree of Doctor of Philosophy

2012

Supervisor of Dissertation:

Christopher B. Murray
Richard Perry University Professor of Chemistry and Materials Science and Engineering

Graduate Group Chairperson:

Gary A. Molander
Hirschmann-Makineni Professor of Chemistry

Dissertation Committee:

Donald H. Berry, Professor of Chemistry

Larry G. Sneddon, Blanchard Professor of Chemistry

Patrick J. Walsh, Professor of Chemistry

SYNTHESIS OF METAL, OXIDE, ALLOY, AND INTERMETALLIC NANOCRYSTALS FOR CATALYSIS

Acknowledgement

First of all, I would like to express my sincere gratitude to my PhD adviser, Dr. Christopher B. Murray. Without his generous support, I will never have the exciting results in this thesis. In these years, he tough me so much, more than science, even English. His lab is fantastic, the best I have ever seen in all universities so far. It is my luck to work with him.

I want like to thank my committee, Dr. Donald H. Berry, Dr. Larry G. Sneddon, and Dr. Patrick J. Walsh, who provided many valuable comments and ideas to my research.

I wish to thank Dr. Radoslav R. Adzic and his group. They show me the right way to do electrocatalysis. Without their help, I might have made many mistakes in electrochemistry. That is my fortune to have the experience working with them. Dr. Adzic is also very supportive for my academic career development.

I am greatly grateful to Dr. So-Jung Park, Dr. Marisa Kozlowski, and Ms. Jessica Tolan Holfler. They brought me to University of Pennsylvania, the place that has great facilities and resources. They made the best opportunity for my first step of graduate study.

Here I wish to specially thank my high school chemistry teacher, Mr. ShangGuanYingQiang, who gave his life to chemistry and teaching. His spirit keeps me exploring the area of chemistry.

I am grateful to all my senior lab-mates in Fudan University and colleagues in GE, who helped me to refine my skills at early stage as a researcher. Especially Prof. Yahong Zhang helped me published the first one of my own scientific publications.

I want to thank all my lab-mates in Murray group and all my classmates in UPenn Chemistry. I have spent memorable years with them.

I wish to thank my entire family especially my parents and my wife, who greatly supports my study and work.

In the research part, I am grateful to all my collaborators: Mr. Xingchen Ye collaborated in the projects of “CO-assist synthesis”, “Pt shape control” and “artificial crystal”, prepared Pd nanocrystals in Chapter 2.3.2, Au nanocrystals in Chapter 2.6.2 and 4.2, Pt-Pd artificial crystals in Chapter 2.6.2 and 3.2; Ms. Jun Chen provided the FeOx nanocrystals shown in Chapter 2.5 and used in Chapter 2.6.2 and 4.2; Dr. Liang Qi conducted all the computational calculation mentioned in this thesis; Dr. Meng Li carried out the IRRAS (Figure 3.20), and provided valuable assistance in electrochemical measurements together with Dr. Yun Cai; Dr. Dianyuan Wang collaborated in the project of “2D-ceria for oxygen storage”, synthesized the ceria nanoplates presented in Chapter 2.5; Dr. Rosa Diaz and Dr. Dong Su provided assistance for the electron microscopic studies presented in Chapter 2.4.5; Mr. Naoki Kikuchi (JEOL) took the amazing high resolution SEM images, as Figure 3.5, 3.7 and 3.8; Mr. Jun-Beom Pyo reproduced many nanocrystals described in Chapter 2.3.3., 2.4.3, and 2.4.4. I am also grateful to these people who provided assistance and support in this research: Dr. Jin-Yi Wang (Fudan University) provided valuable discussion for formic acid oxidation. Dr. Gorte and Dr. Fan Yang (Brookhaven National Lab) provided helpful discussion and information for CO oxidation. Dr. Charles Black and Dr. Eric Stach provided support in user facilities at Brookhaven National Laboratory. Dr. Douglas Yates assisted and supported in the Penn Regional Nanotechnology Facility. Dr. David Vann provided assistance for the ICP-OES. Ms. Danielle Reifsnyder, Ms. Vicky Nguyen, and Mr. Tom Gordon edited most of my papers.

At the end, I wish to express my gratitude to Dr. Shouheng Sun, Dr. Raymond Gorte, and Dr. Vojislav Stamenkovic, in addition to Dr. Murray and Dr. Adzic, for their great support in my academic career.

ABSTRACT

SYNTHESIS OF METAL, OXIDE, ALLOY, AND INTERMETALLIC NANOCRYSTALS FOR CATALYSIS

Kang, Yijin

Christopher B. Murray

The synthesis of nanocrystals is the core of the nanoscience. The highly controlled nanomaterials are desirable for the studies of catalysis, in order to unambiguously correlate the catalytic properties with the structure and composition of catalysts. In this thesis, highly controlled nanocrystals are synthesized through solution phase synthesis. Shape controlled nanocrystals can be synthesized as cubes, octahedra, icosahedra, truncated cubes, cuboctahedra tetrapods, octapods and spheres. The nanocrystals with these morphologies selectively expose {100} and/or {111} facets as well as high-index facets, thus enabling various investigations of structure sensitive catalysis at the nano-scale. In addition to the shape control, the composition of metal catalysts is also tunable by making alloy or intermetallic nanocrystals. The nanocrystals of Pt-Mn, Pt-Fe, Pt-Co, Pt-Ni, Pt-Cu, Pt-Zn, Pt-Pb, Pt_3Mn, Pt_3Fe, Pt_3Co, Pt_3Ni, Pt_3Zn, Pt_3Pb, FePt, and etc. allow the fundamental exploration of catalysis. Oxides, heterostructures, as well as artificial crystals which have a long range ordered crystalline structure, are also prepared. These highly controlled nanomaterials have been demonstrated as ideal model materials for studies of catalysis. In this thesis, formic acid and methanol electrooxidation, oxygen reduction reaction, oxygen storage, CO oxidation, and enhanced stability are discussed.

Synthesis of Metal, Oxide, alloy, and Intermetallic Nanocrystals for Catalysis

Chapter 1. Introduction

One nanometer (nm) is 10^{-9} meter. A nanocrystal (NC) is a crystalline material that has at least one dimension smaller than 100 nm, although sometimes the term NC is also used for crystalline materials smaller than one micrometer (μm). A number of physical properties are significantly changed with the great reduction of particle size to the nano-scale[1-3]. Nanocrystals are currently of great scientific interest for their potential applications in mechanics, magnetics, optics, electronics, and catalysis, due to their distinctive properties that differ from those of bulk materials. My doctoral dissertation work deals with the catalytic properties of nanocrystals.

Due to their greatly increased surface area to volume ratio, nanocrystals are attractive for applications in catalysis. It has been demonstrated that the catalytic performance of a material can be improved by tuning the morphology or composition of the catalyst.

1.1 Morphology control of catalysts

Morphology control of catalysts is of great interest, simply because many catalytic processes are sensitive to the structure of catalysts, as demonstrated in surface science (e.g., ammonium synthesis over Fe surface[4] and ethane hydrogenolysis over Ni and Pt[5]). Numerous reports show that nanocrystals can be synthesized in different shapes, and that nanocrystals with different shapes can catalyze different reactions. Shape-dependent properties are added to the advantage of using nanocrystal catalysts instead of their bulk countparts. Many scientists ascribe the shape-dependent properties (i.e., activities or selectivities) to the geometric arrangement of surface atoms on nanocrystals. For example, Feliu et al. have reported shape-dependent methanol and formic acid (FA) electrooxidation on preferentially oriented Pt nanoparticles[6], Zaera et al. have described that tuning the selectivity of isomerization reactions can be achieved by controlling the particle shape of Pt[7,8], and Yang and Somorjai et al. have demonstrated the shape effects of Pt nanocrystals on benzene hydrogenation selectivity[8]. However, some researchers ascribe the difference in catalytic properties to the different surface properties of nanocrystals, which are not strongly tied to the shape and geometry. Fundamentally, this controversy stems from "shape-controlled" nanocrystals, since nanocrystal samples do not always reach the level of uniformity desired to make solid conclusions about shape-dependent properties. Therefore, reliable shape-controlled synthesis of nanocrystals is highly desired. In my work, I focus on the shape-controlled synthesis of metal, alloy, and intermetallic nanocrystals so that uniform samples can support the research of structure sensitive catalysis. In my thesis, I describe syntheses of shape-controlled nanocrystals as good as, or better than, the state of the art. I have also demonstrated the control of reactivity by tuning the nanostructure of nanocrystals. Examples are given in chapter 2.6.

1.2 Composition control of catalyst

Composition control is another important direction to modify the properties of catalysts. For example, Stamenkovic et al. show a "volcano type" relationship in electrocatalytic trends on Pt_3M (M=Ni, Co, Fe, Ti, V) surfaces between the experimentally determined surface electronic structure (the *d*-band centre) and activity for the oxygen-reduction reaction[9]. In addition, Adzic et al. have demonstrated several compositionally-controlled results: 1) monolayers of a foreign metal (i.e. Cd, Tl, Pb, Bi) underpotential deposited on Pt exhibit enhanced activity and pronounced catalytic effects on the electrocatalysis of FA oxidation[10,11]; 2) the kinetic activity of oxygen reduction reaction (ORR) can be tuned by manipulating a layered structure of Pt and other metals[12,13]; 3) the stability of oxygen electrode catalyst can be significantly enhanced by adding Au onto Pt[14]. The combination of Au and iron oxides is an exceptionally active catalyst toward CO oxidation, while neither Au nor iron oxide is particularly active for such a reaction[15]. In this thesis, I describe the synthesis of Pt-based alloys and demonstrate the effect of the alloy elements for various catalytic reactions. I have also carried out studies on heterostructures and self-assemblies.

This chapter briefly introduces the motivation of the research described in this thesis. More detailed introduction for the context of the work is spread in each chapter.

Chapter 2. Synthesis

Materials synthesis and preparation are the fundament and the core of the nanoscience research[16]. Many synthesis methods have been developed to produce nanomaterials[17], that include sol-gel method[18], hydrothermal/solvothermal treatment[17,19-21], sputtering[22], ball-milling[23], vapor-phase deposition[24-26], and solution-phase synthesis[27-29]. A key requirement for a synthetic method is the uniformity (or monodispersity) of the product in size, shape and composition, because only the well-controlled materials enable us to unambiguously correlate the structure of materials with the physical properties[16]. My thesis focuses on the solution-phase synthesis, as it renders a high degree of control for the production of nanomaterials, especially nanocrystals[2]. The syntheses of metals, oxides, alloys, and intermetallic nanocrystals, nanowires (NWs), and heterostructures are described in this chapter. The fabrication of complex nanostructures by self-assembly of nanocrystals is also demonstrated.

2.1 Methods

The synthesis of nanocrystals through solution-phase synthesis usually involves either co-reduction or pyrolysis (thermal decomposition) of precursors[2].

The key to achieve a high uniformity of nanocrystals is to separate the nucleation step and the following growth step described in the framework of the La Mer model[30], as shown in Figure 2.1A[2,30]. Rapid addition of precursor to the reaction raises the precursor concentration above the nucleation threshold. A burst of nucleation rapidly consumes the precursor and relieves the super-saturation. No new nuclei form if the consumption of precursor by the growth of nanocrystals has a higher rate than that of the addition of precursor into the reaction. If the percentage of nanocrystal growth during the nucleation period is relatively small compared with subsequent growth, the nanocrystals can become more uniform over time, referred to as focusing of the size distribution. Many systems such as some metal nanocrystal growth exhibit a second growth phase called Ostwald ripening, in which the large nanocrystals grow by consuming the small nanocrystals.

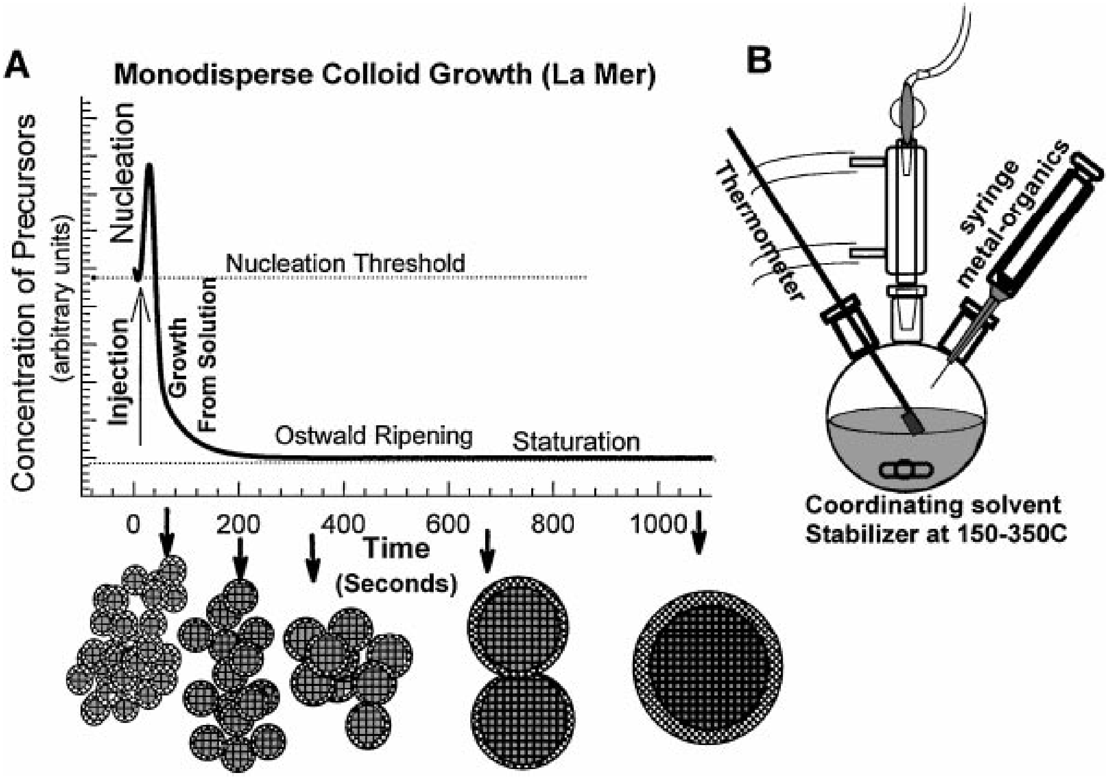

Figure 2.1 (*A*) the stages of nucleation and growth for the synthesis of nanocrystals in the framework of the La Mer model. (*B*) Typical set-up for the synthesis of nanocrystals[2].

A typical reaction set-up is shown in Figure 2.1B. A typical reaction mixture includes metal source (precursor), stabilizer (capping agent, or ligand), solvent, and sometimes a reducing agent. The acetylacetonates and carbonyls of metal are the most common precursor compounds. Oleic acid and oleylamine are the mostly used stabilizers. Benzyl ether, phenyl ether, dichlorobenzene, toluene, and octadecene (ODE) are best choices for solvent, depending on the desired reaction temperature. Based on their reducing ability, the reducing agents can be classified into: 1) weak reducing agent, including various diols, alcohols, or even precursor itself and its byproduct; 2) mild reducing agent, including H_2, CO, Zn, and etc.; 3) strong reducing agent, such as $NaBH_4$ and various borane complexes; 4) super reducing agent, such as superhydride, $LiAlH_4$, Li, Na, K and complex of Li, Na, K. When the reactant or product is sensitive to air or moisture, a technique called Schlenk technique which employs an inert gas protection, is used. The detailed syntheses for each type of nanocrystals are described in this chapter.

2.2 Characterization

This part covers major characterization techniques used in my PhD work.

2.2.1 Electron microscopes

An electron microscope is a type of microscope that uses a beam of electrons to illuminate the specimen and generate a magnified image. Electron microscopes have a greater resolution than the regular optical microscopes, because electrons have much smaller wavelengths than visible light (photons). Electron microscopes are used for observation and analysis of nanocrystal morphologies, as well as for elemental analysis. Electron microscopes are powerful tools for nanoscience research, thus they are the routine characterization used in this thesis.

2.2.1.1 TEM

Transmission electron microscope (TEM) uses a high voltage electron beam transmitted through the specimen to create an image. The high voltage electrons also carry information for other analysis, such as structure analysis and elemental analysis.

TEM is a powerful analytic tool as it can integrate many functions or techniques in one system. High resolution TEM (HRTEM), energy-dispersive X-ray spectroscopy (EDX, or EDS), electron energy loss spectroscopy (EELS) and the energy filtered imaging based on EELS, are added to the basic imaging function of TEM. The sample holder designed to tilt and rotate sample enables a topology reconstruction. An in-situ TEM allows researcher to directly watch the growth of nanocrystals or to observe the morphology change of catalyst in a catalytic process. The detailed introduction of mechanism, instrument, and operation can be found in **Transmission Electron Microscopy**, edited by David B. Williams and C. Barry Carter.

TEM images in this thesis are taken on JEOL1400 TEM at 120 kV and JEOL2010F TEM at 200kV. HRTEM images and EDX data are taken on JEOL2010F TEM at 200kV. Partial HRTEM images are taken using a Cs-corrected FEI Titan 80-300 at 300kV, with the aberration corrector tuned to a flat phase region of >20 mrad (<0.1 nm information transfer), leaving a residual spherical aberration <1.5 microns. Partial STEM images are taken on FEI Titan 80-300. The samples are prepared by drop-casting of nanocrystal solution, nanomaterial suspension, or catalyst ink onto TEM grids. For the membrane samples self-assembled at a liquid-air interface, a TEM grid is placed under the floating membrane using tweezers and then gently lifted upwards to collect the membrane. The subsequent drying in a vacuum chamber removes residual solvents.

2.2.1.2 SEM

A scanning electron microscope (SEM) is a type of electron microscope that scans the sample with electron beam then provides the image or other information of the sample by the electrons interacted with the sample. EDX is also available on SEM. The details of SEM can be found in **Scanning microscopy for nanotechnology: techniques and applications**, edited by Weilie Zhou and Zhong Lin Wang.

JEOL JSM7600F and JEOL JSM7500 are used to collect SEM images for this thesis. The samples are powders, crystals, or self-assembly of nanocrystals, which are directly put on a metal sample holder. An adhesive carbon tape can be used to firmly hold sample. Samples loaded on TEM grids can also be directly used as SEM samples.

2.2.1.3 STEM

A scanning transmission electron microscope (STEM) employs scanning of focused electron beam to provide sample information. It can be integrated with either a TEM or a SEM.

The HR-STEM images, HAADF images, EDX line scans and EDX mappings are taken using a Hitachi HD2700C dedicated 200kV cold emission STEM. Samples loaded on TEM grids are directly used as STEM samples.

2.2.2 X-ray techniques

X-ray techniques such as X-ray diffraction (XRD) provide information regarding crystal structure, grain size, shape, and local orientation of the sample. The theoretical foundation of X-ray techniques is the Bragg's law and the Scherrer Equation. More details about X-ray techniques can be found in **Introduction to X-ray powder diffractometry**, edited by Ron Jenkins and Robert L. Snyder.

XRD patterns presented in this thesis are obtained on Rigaku smartlab diffractometer with Cu Kα radiation (λ = 1.5418 Å). The samples are prepared by drop-casting of nanocrystal solution onto a frosted glass slide to form an opaque thin film of nanocrystals.

2.2.3 Others

2.2.3.1 TGA

Thermal gravimetric analysis (TGA) is a test monitoring the mass change of sample, with the change in temperature. TGA is usually used to investigate the composition of a material or the components in a mixture when part of the material or mixture can transform into gas phase up to a certain temperature. In chapter 4.1, the TGA is also employed to determine the oxygen storage capacity (OSC) of ceria nanomaterials.

The TGA measurements for this thesis are carried out on TA Instruments, SDT Q600 TGA/DSC.

2.2.3.2 ICP-OES

Inductively coupled plasma optical emission spectroscopy (ICP-OES) is an analytical technique that uses the emission spectra of excited atoms or ions produced by the inductively coupled plasma. It is a particularly effective and sensitive way to measure the concentrations of elements in the sample. More details about ICP-OES are available in **Inductively Coupled Plasmas in Analytical Atomic Spectrometry**, edited by Akbar Montaser and D. W. Golightly (Chapter 10.An overview of analysis by inductively coupled plasma-atomic emission spectrometry).

Quantitative elemental analyses for the composition of NCs, the concentration of the NC solutions, and the loading of catalysts are carried out on SPECTRO GENESIS ICP spectrometer. The standard solutions (1000ppm) are purchased from Aldrich, and then diluted to desired concentrations. The samples are prepared by digesting nanocrystals in aqua regia (solution of HCl/HNO_3 at a ratio of 3:1).

2.2.3.3 FT-IR and IRRAS

Fourier transform infrared spectroscopy (FT-IR) is used to qualitatively identify infrared active species within sample, as well as to quantitatively analyze the infrared active species. It is particularly helpful to monitor or to identify products or reaction intermediates. The *in-situ* infrared reflection absorption spectra (IRRAS) allow monitoring the catalytic reaction in real time.

In-situ IRRAS has been used to study formic acid electrooxidation in this thesis. It is carried out with a Nicolet Nexus 670 Fourier-transform infrared spectrometer equipped with a mercury cadmium telluride (MCT) detector cooled with liquid nitrogen. An unpolarized light beam is used. The spectral resolution is set to 8 cm^{-1} and 128 interferograms are together added to each spectrum. Spectra are given in absorbance units defined as $A = -\log(R/R_0)$, where R and R_0 represent the reflected infrared intensities corresponding to the sample and reference single-beam spectrum, respectively. The reference spectrum is collected at 0.005 V. All spectra are collected in the solution of 0.1 M formic acid and 0.1 M sulfuric acid. The nanocrystals are placed on Au(111) surfaces to ensure a good current collection and reflectivity. A ZnSe hemisphere is used as the infrared window.

2.3 Single component metal

2.3.1 Fe, Co, Ni, Cu

Fe, Co, Ni, and Cu nanocrystals can be synthesized by thermal decomposition of acetylacetonate of Fe, Co, Ni, and Cu. Fe and Co NCs can also be made by decomposition of their carbonyls[31]. Though the synthesis of Fe NCs with a bcc structure has been reported by Sun et al.[32], the decomposition of $Fe(CO)_5$ usually produces iron oxides (the phase of Fe_3O_4 in most cases). The syntheses of iron oxides are described in chapter 2.5.

Co NCs can be synthesized through thermal decomposition of $Co_2(CO)_8$ in the presence of trioctylphosphine oxide (TOPO)[31], or through reduction of Co^{2+} with superhydride in the presence of oleic acid and trioctylphosphine (TOP)[33]. The oleic acid and oleylamine can also be used as stabilizer to synthesize Co NCs via the decomposition of $Co_2(CO)_8$, but the size and shape control is not as good as the synthesis using TOPO. The size of Co NCs can be controlled from 6nm to 16nm. The TEM images and the detailed synthesis of typical Co NCs are shown below.

By superhydride reduction: 0.16 g $CoCl_2$ and 0.315 ml oleic acid are dissolved in 20 mL octylether under N_2 atmosphere. Then 3 mmol TOP is added in to the formed light blue solution, and the solution is heat to 200°C to form a dark blue solution. At 200°C, 2 mmol superhydride is injected into the solution. The solution immediately turns to black upon the injection. After 20 min, the reaction mixture is cooled down and the products are isolated by adding ethanol and centrifugation. The NCs are redispersed in hexane.

By thermal decomposition of $Co_2(CO)_8$: A solution of 0.4 g Co2(CO)8 dissolved in 3 ml of *o*-dichlorobenzene is injected into a solution of 12 ml of *o*-dichlorobenzene, 0.2 ml oleic acid, and 0.2 g TOPO preheated to 180°C. The reaction mixture is allowed to reflux at 180°C for 30min. After 30 min, the reaction mixture is cooled down and the products are isolated by adding ethanol and centrifugation. The NCs are redispersed in hexane.

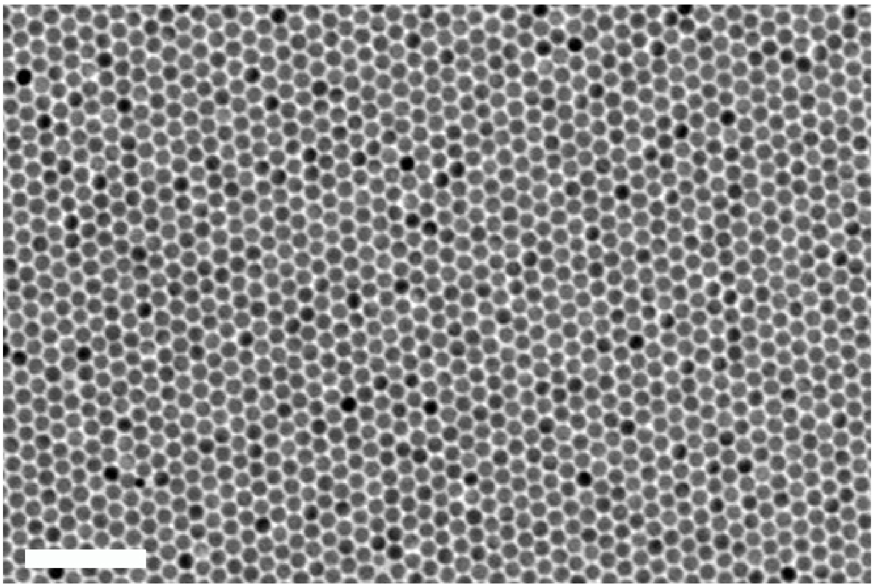

Figure 2.2. 6 nm Co nanocrystals synthesized by using superhydride. Scale bar: 50nm

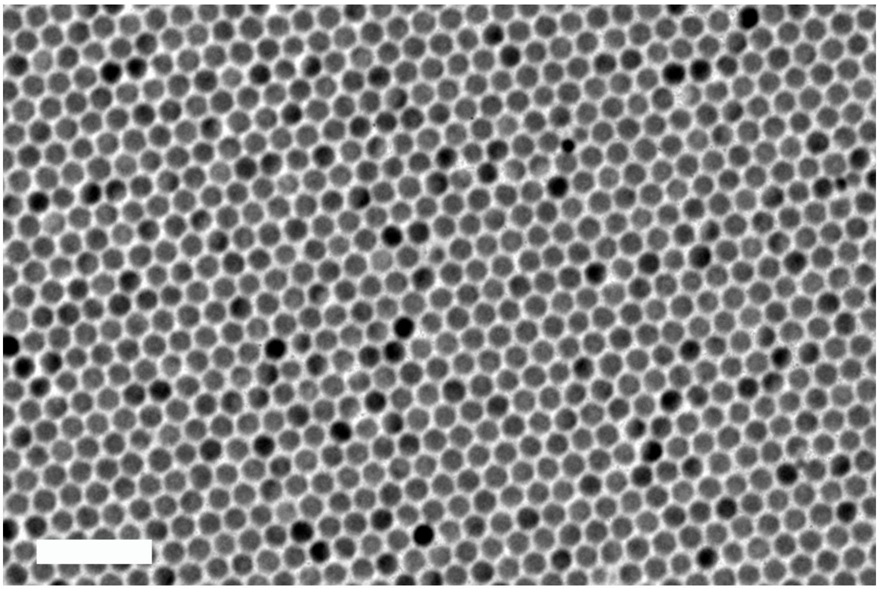

Figure 2.3. 10 nm Co nanocrystals synthesized by decomposition of $Co_2(CO)_8$ in the presence of TOPO. Scale bar: 50nm

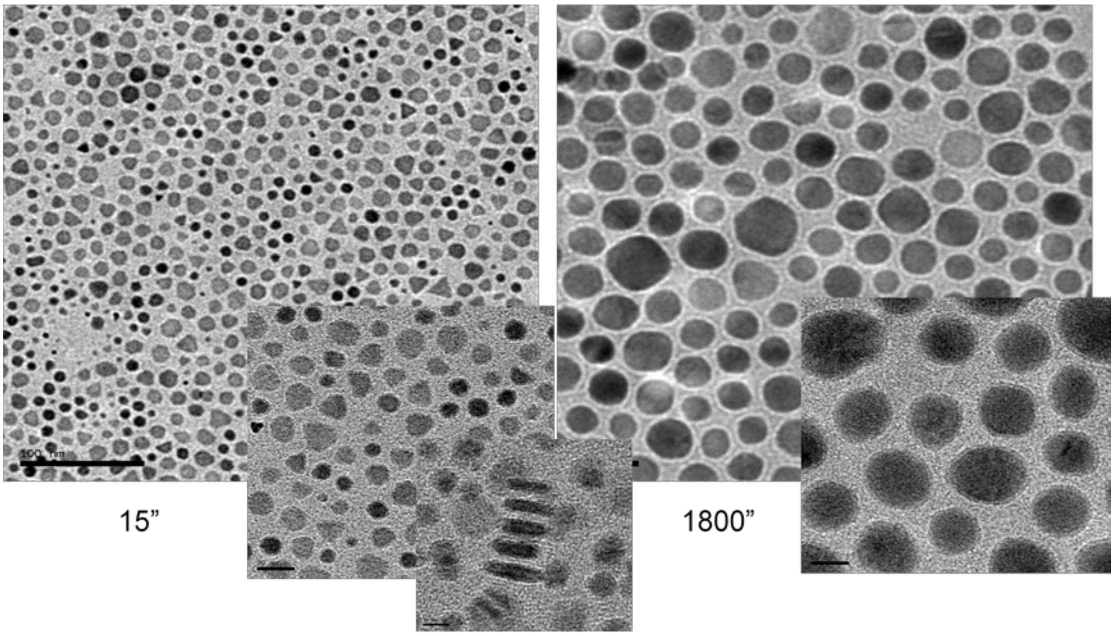

Figure 2.4. Co nanocrystals synthesized by decomposition of $Co_2(CO)_8$ in the presence of oleic acid and oleylamine.

Ni NCs are prepared in similar synthetic routes of Co NCs[34]. The size is tunable in the range of 4-16 nm. The TEM images of typical Ni NCs are shown in Figure 2.5.

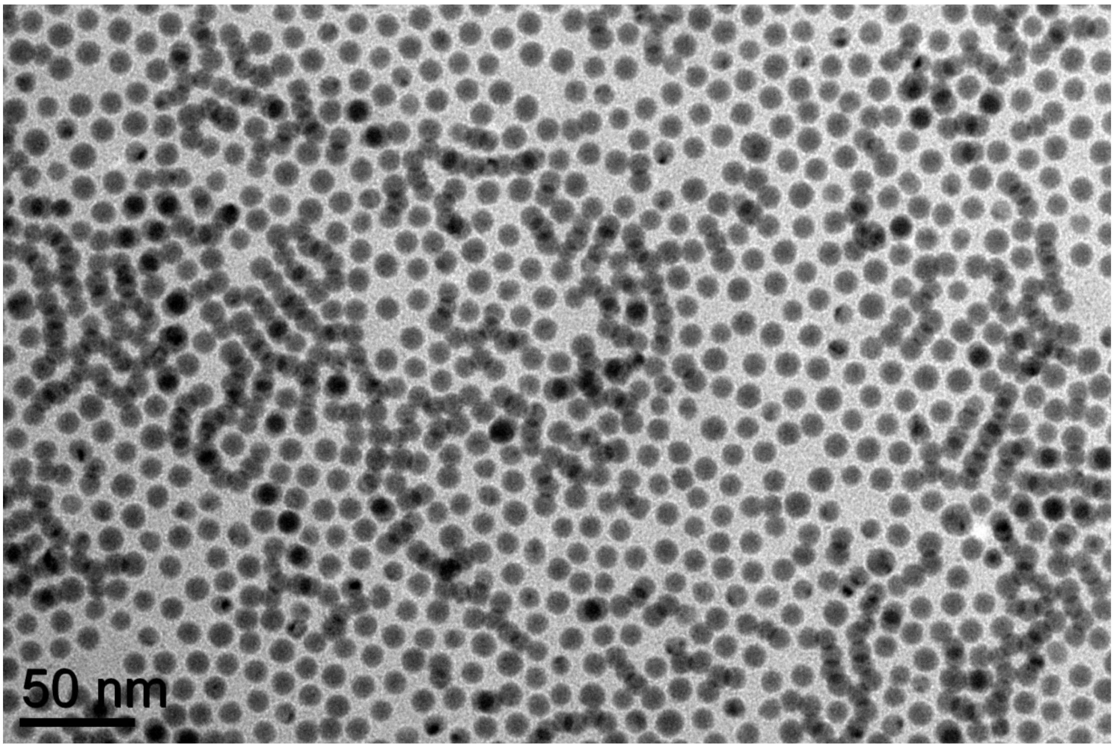

Figure 2.5. TEM image of typical Ni nanocrystals

The typical synthesis for Cu NCs is modified from literature[35]: 0.26 g $Cu(acac)_2$ and 0.278 g tridecylphosphoric acid (TDPA) are dissolved in 10 ml trioctylamine (TOA). The mixture is heated at 100°C to form a milk-like Cu-TDPA complex. Then the reaction temperature is raised to 270°C and is kept at 270°C for 15 min. A product in shining red color is isolated by adding ethanol and centrifugation. The NCs are redispersed in hexane.

The typical Cu NCs are shown in Figure 2.6. The size of Cu NCs as synthesized from the procedure described above is 12 nm. By changing the decomposition temperature and the reaction time, the size is tunable in the range of 6-16 nm. The as-synthesized Cu NCs are readily oxidized, as indicated by a color change from red to blue. With careful control of the oxidation process, the Cu oxides NCs in solid, hollow or core-shell morphologies can be made, as reported by Yang et al[35].

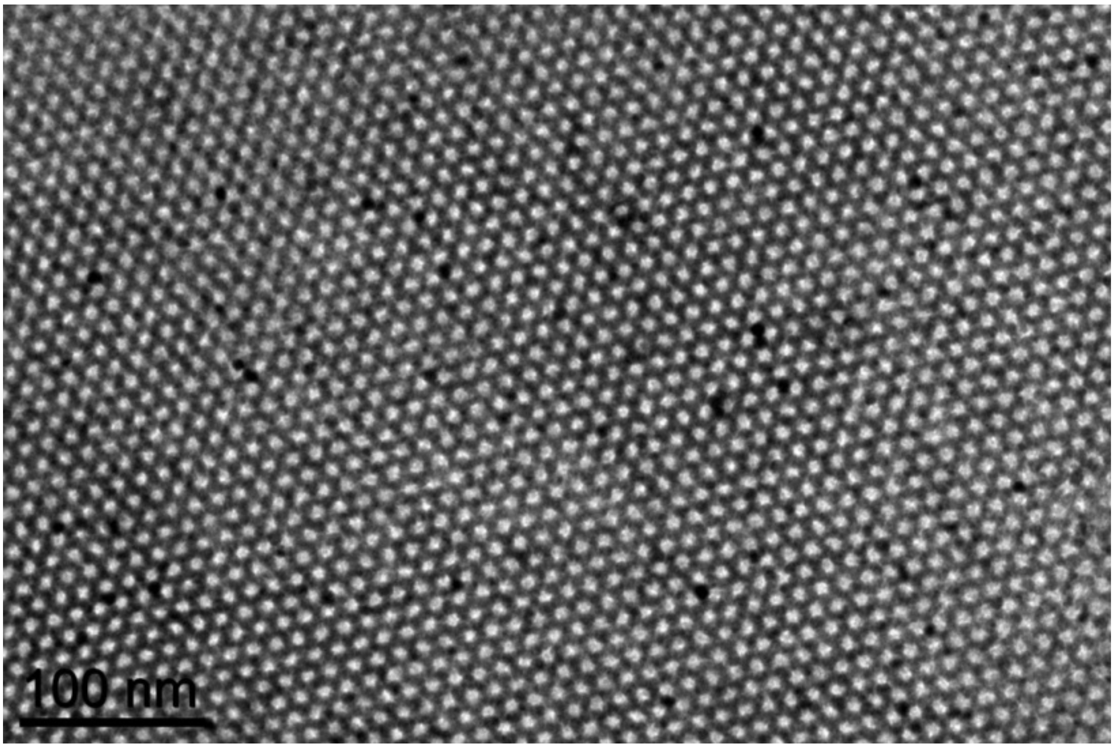

Figure 2.6. TEM image of typical 12 nm Cu nanocrystals self-assembled into superlattice.

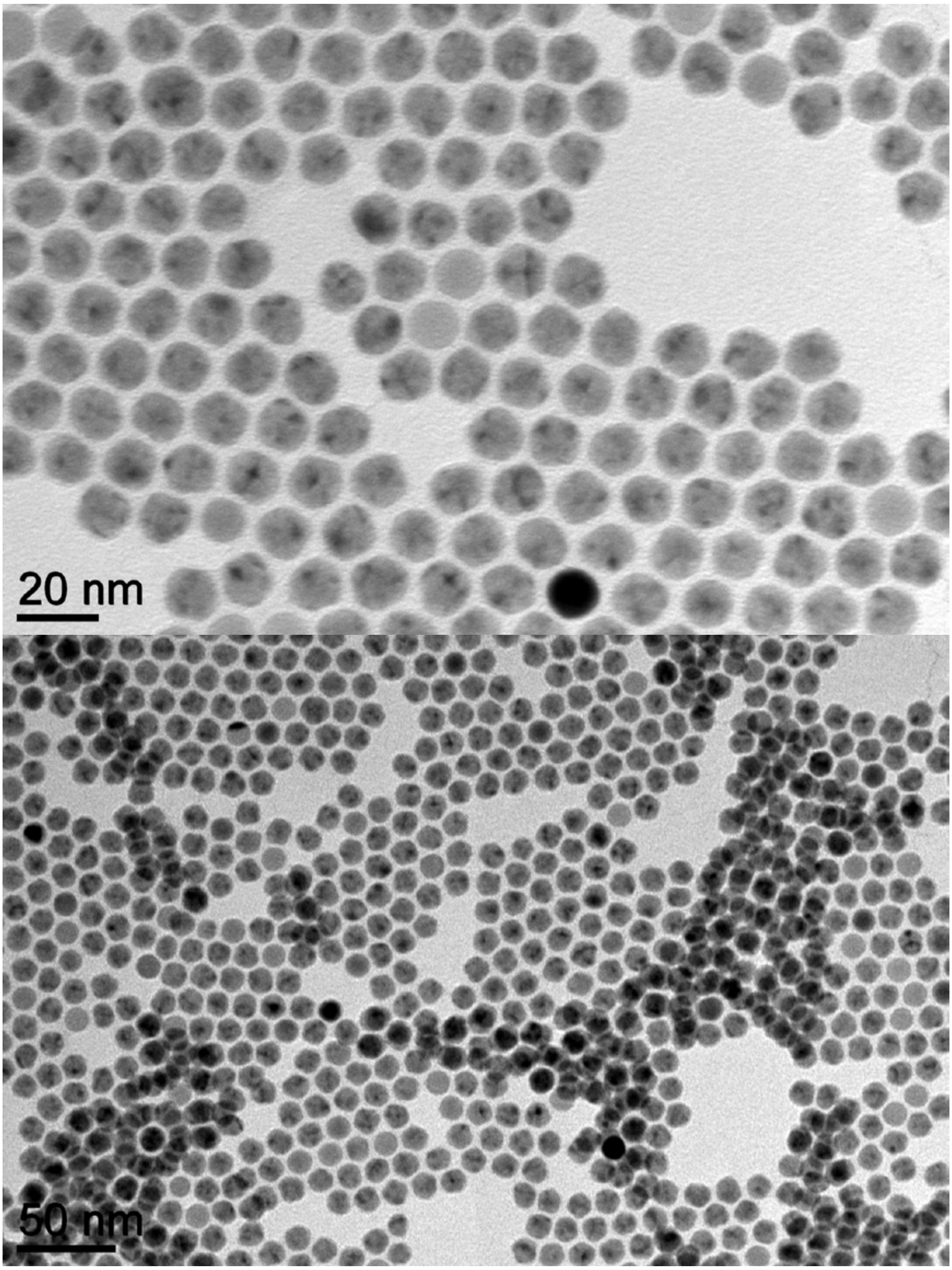

Figure 2.7. TEM image of Cu nanocrystals.

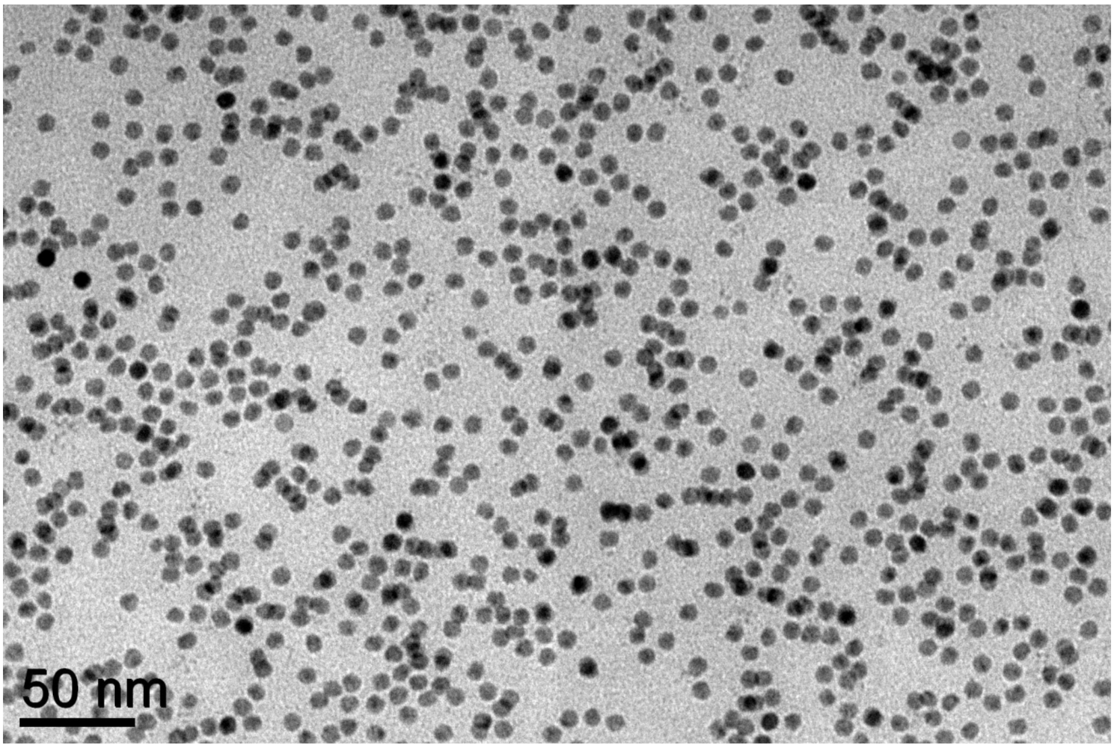

Figure 2.8. TEM image of Cu nanocrystals synthesized at reduced reaction temperature.

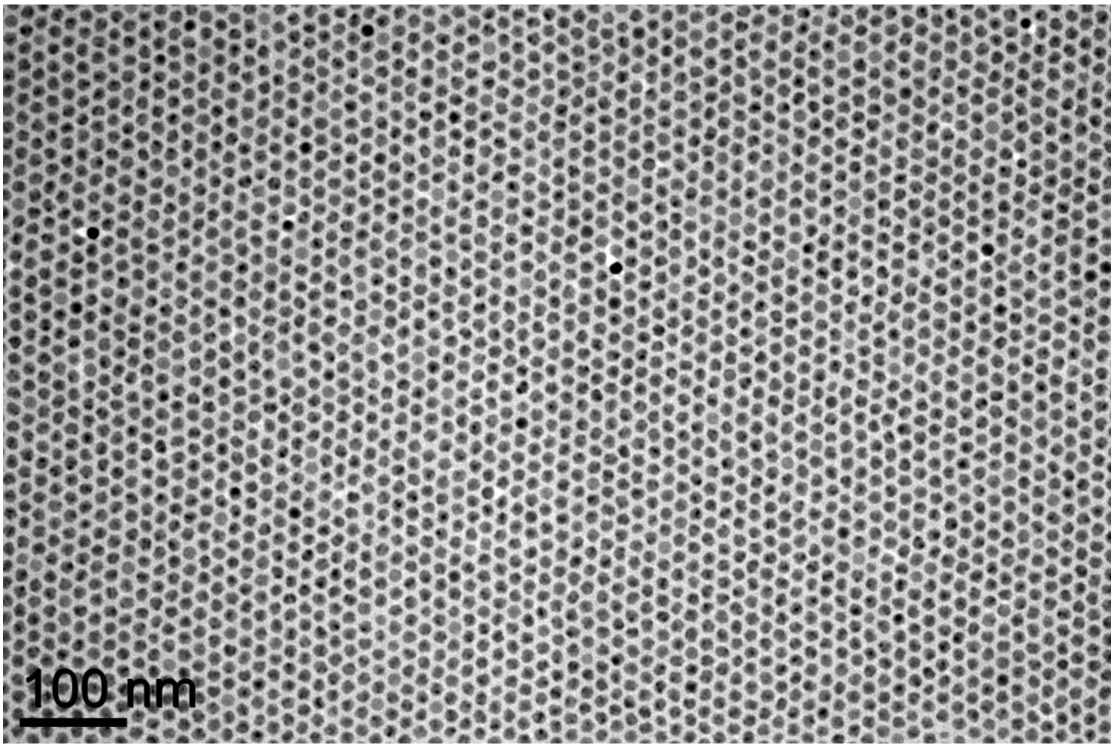

Figure 2.9. TEM image of slightly oxidized Cu nanocrystals.

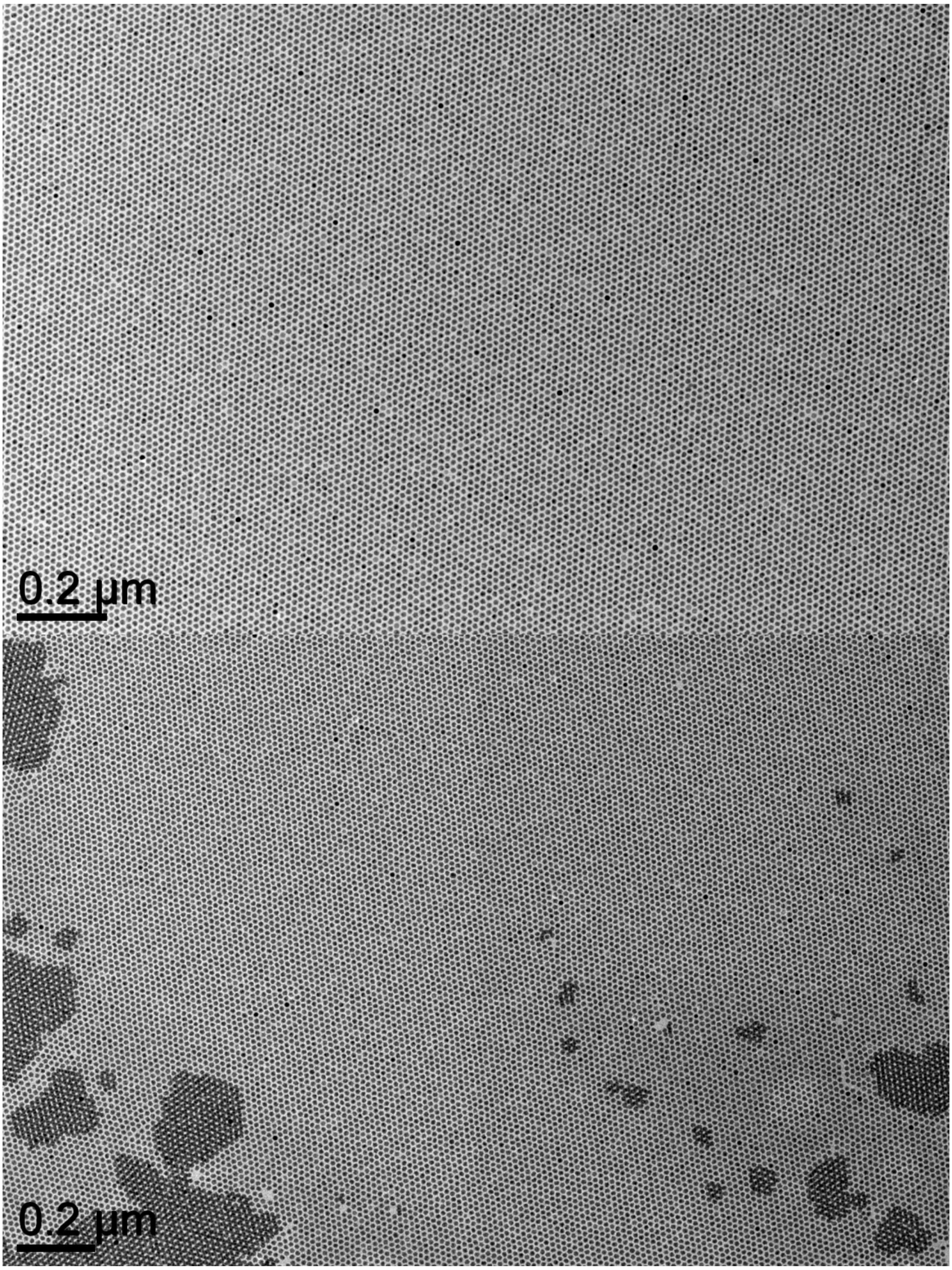

Figure 2.10. TEM image of 12 nm Cu nanocrystals for a large area.

2.3.2 Pt, Pd, Au

Recently I published the synthesis of Mn-Pt nanocubes (see Chapter 2.4.1.2) with a composition of Mn:Pt ≈ 1:3[27]. However, by reducing the amount of $Mn_2(CO)_{10}$, uniform Pt nanocubes can be produced rather than the Mn-Pt nanocubes[29]. Sun et al. have reported the synthesis of Pt nanocubes by using $Fe(CO)_5$, demonstrating that the presence of $Fe(CO)_5$ facilitates the nucleation and controls the growth of Pt nanocubes[36]. Several subsequent reports also focus on the synthesis of Pt nanocubes employing metal carbonyls[37,38]. Some researchers claim that the metal (W, Co) decomposed from carbonyl compounds plays the key role (serving as the nucleation center or as the in-situ generated reducing agent) during the synthesis of Pt nanocubes[37,38]. However, based on our observations, the presence of neither foreign metals (W, Co) nor metal carbonyls are necessary for the growth of uniform Pt nanocubes. Furthermore, metal carbonyls can introduce impurities either as alloy incorporated into Pt or as adatoms on Pt surfaces. This could result in surface properties distinct from those of “clean” Pt NCs[39]. In contrast, here I describe a CO-assisted synthesis which produces Pt nanocubes with high chemical purity, crystallinity and shape uniformity. The synthesis of Pt nanocubes employs CO (generated by dehydrating of formic acid, Figure 2.11) as a mild reducing agent. The procedure is described below.

The gaseous CO is generated at point-of-use by dehydrating formic acid. Briefly, formic acid is delivered into warm concentrated sulphuric acid (60°C) at a constant rate using syringe pump (Caution: CO is toxic and all operation should be done inside a well-ventilated hood!).

Synthesis of Pt nanocubes: 0.04g Pt(acac)$_2$ are dissolved in 5mL benzyl ether, 3.68mL oleylamine, and 0.63mL oleic acid under N_2 atmosphere. Gaseous CO is then introduced to the solution (~10cm^3/min) at room temperature. The reaction flask is then placed into a preheated oil bath. After 15min of reaction at 200°C, the solution is cooled down and the products are isolated by adding ethanol and centrifugation. The NCs are redispersed in hexane.

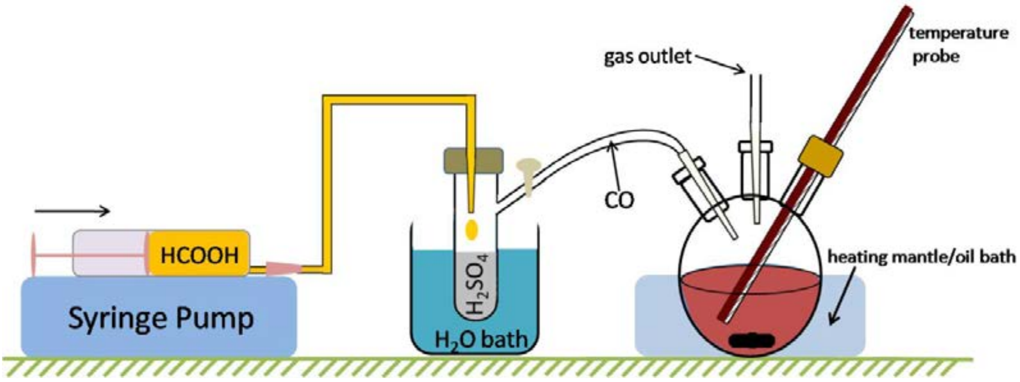

Figure 2.11. Schematic illustration of the reaction setup.

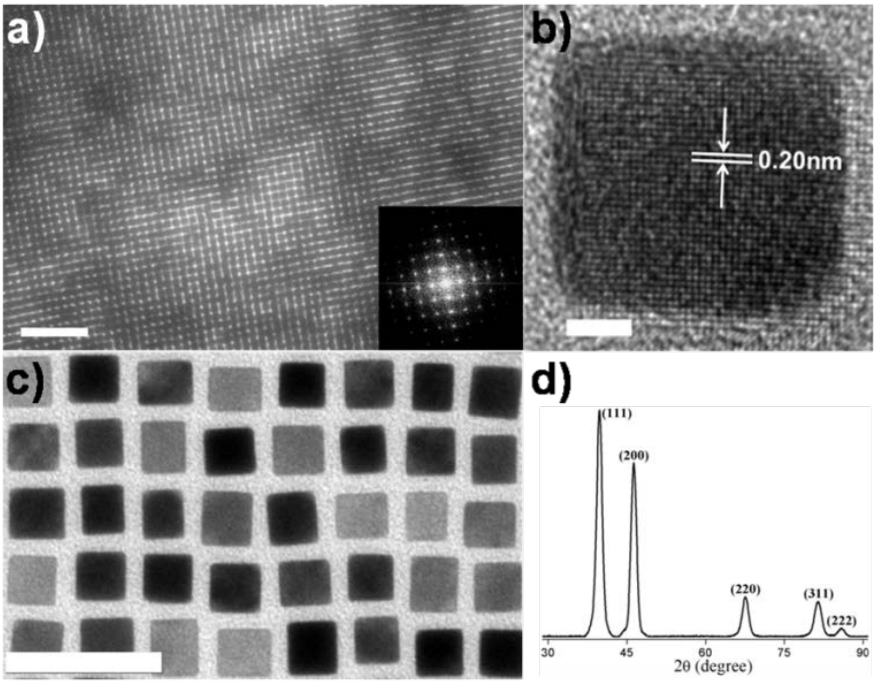

Figure 2.12. TEM images(a, c), HRTEM image (b) and XRD pattern (d) of Pt nanocubes synthesized using gaseous CO. Inset of (a), fast-Fourier-transform pattern of the self-assembled Pt nanocube superlattices with simple cubic symmetry. The scale bars represent (a) 100 nm, (b) 2 nm and (c) 30 nm.

Pt nanocubes with straight edges (edge length=8.9 nm, σ=6%) and sharp corners are produced after 15min of reaction at 200°C (Figure 2.12). The XRD pattern (Figure 2.12d) of the as-synthesized Pt nanocubes confirms the face-centered cubic (fcc) crystal structure. HRTEM image of a single Pt nanocube reveals an interplanar distance of ~0.20nm, consistent with the lattice spacing of the {100} planes of the fcc platinum structure (Figure 2.12b). Furthermore, study of the shape evolution (Figure 2.13) reveals that NCs formed at the early stage (2-4min) of the reaction typically adopt a polyhedral shape. As the reaction proceeds, the particles transform to cubes. The reaction exhibits a minimum size-and shape-dispersity at ~15min, after which the size distribution broadens and other shapes (rods, truncated cubes and polyhedron) start to appear. To confirm the role of CO as a reducing agent, the following control experiments are performed: the reaction mixture is bubbled with CO for 10min at room temperature and then purged with N_2 for 20min. After that, the solution is brought to 200°C and is kept at this temperature for 15 min. This only produces large aggregates of irregular shaped NCs (Figure 2.14c), similar to the products synthesized in the absence CO (Figure 2.14a, b). This observation implies that in the present case CO neither serves as ligand nor forms complex with platinum, which is different in mechanism from previous studies using $Pt(dba)_2$ (dba=dibenzylideneacetone) precursors[40,41]. In addition, the FT-IR spectra (Figure 2.15) of the Pt nanocubes show no peaks in the region of 1800-2300cm^{-1}, suggesting that there is no Pt-CO species in the products.

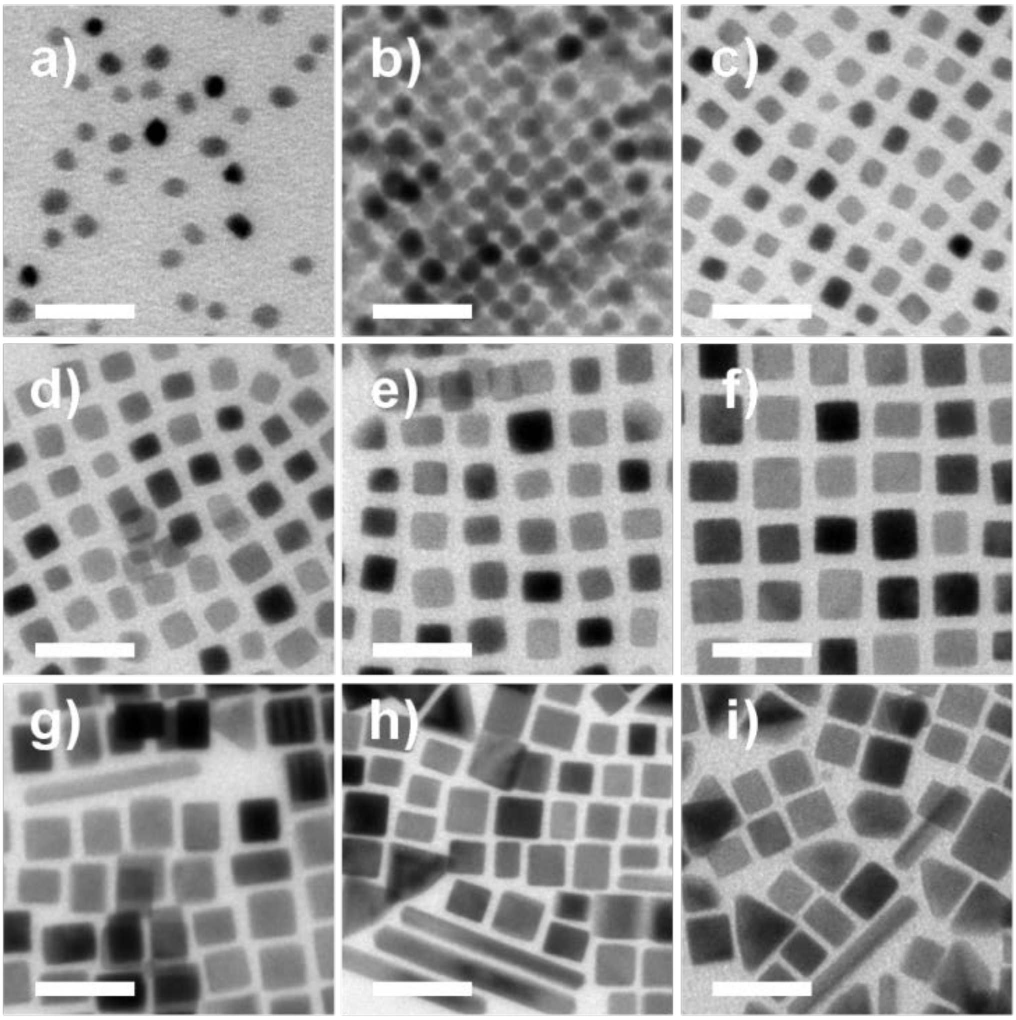

Figure 2.13. TEM images taken at different stages of Pt nanocube syntheses using CO. (a) 2min, (b) 4min, (c) 6min, (d) 8min, (e) 10min, (f) 15min, (g) 20min, (h) 30min, (i) 90min. The scale bars represent 20nm.

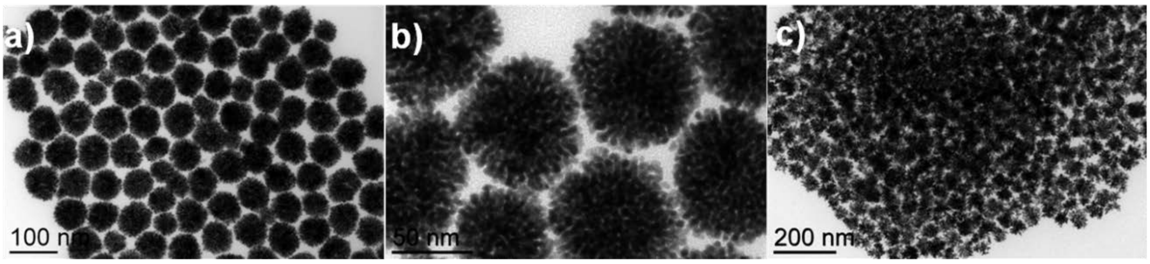

Figure 2.14. TEM images of Pt nanocrystals synthesized (a,b) in the absence of CO, and (c) with the reaction mixture bubbled with CO for 10min followed by purging with N_2 for another 20min before being dipped into the oil bath

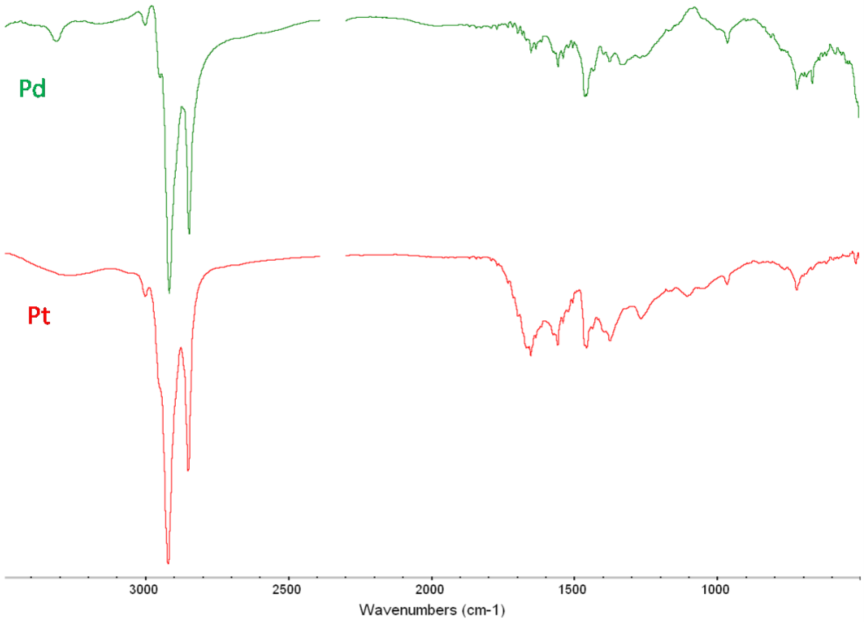

Figure 2.15. FTIR spectra of the Pd nanoparticles and Pt nanocubes synthesized by CO

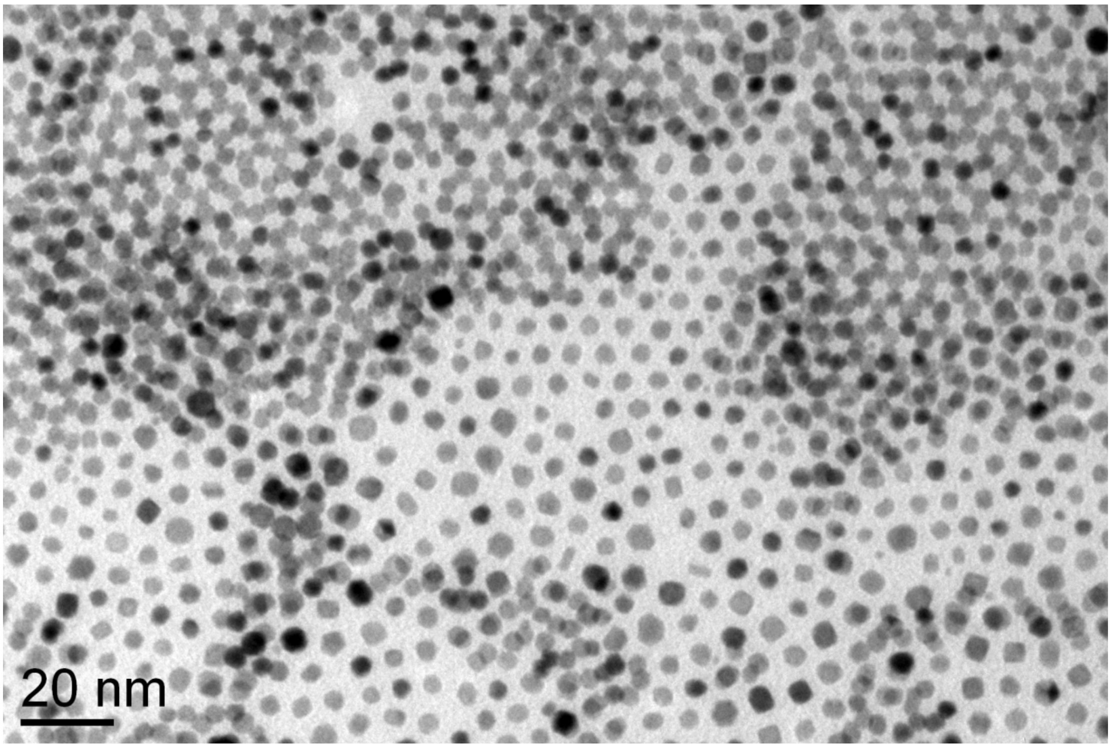

Figure 2.16. TEM image of the Pt nanocrystals synthesized using CO in the absence of oleic acid

In recognition of the fact that foreign metals (Fe, W, Co, etc.) are not essential for the formation of well-faceted metal NCs, we extended the synthetic use of CO as a reducing agent to other metal NCs. Palladium is widely used as catalysts in catalytic converters[42] and in a range of organic reactions including cross coupling reactions[43] and hydrogenation[44]. Several groups have also demonstrated the use of Pd NCs as primary catalysts or co-catalyst for fuel cell applications with enhanced performance and greater stability compared to pure Pt catalysts[45,46]. Despite the recent advances in the shape-controlled synthesis of Pd nanostructures[47], one-pot synthesis of monodisperse spherical Pd NCs has been limited. Importantly, previous studies showed that TOP can serve as an effective ligand in the synthesis of monodisperse Pd NCs[48]. Here we demonstrate that by using the Pd-TOP precursor, monodisperse Pd NCs can be produced under CO blanket within 10 minutes at 195°C.

Synthesis of Pd spherical NCs: The Pd-TOP complex is prepared by dissolving 0.05g of $Pd(acac)_2$ in 0.6mL of TOP. The resulting precursor is mixed with 0.15mL TOP, 2mL oleic acid and 13mL oleylamine at room temperature. Under a constant heating rate of 15°C/min, the solution is brought to 195°C when CO is introduced to the reaction flask (~15cm^3/min). The reaction is conducted for 10min and the products are purified as described above.

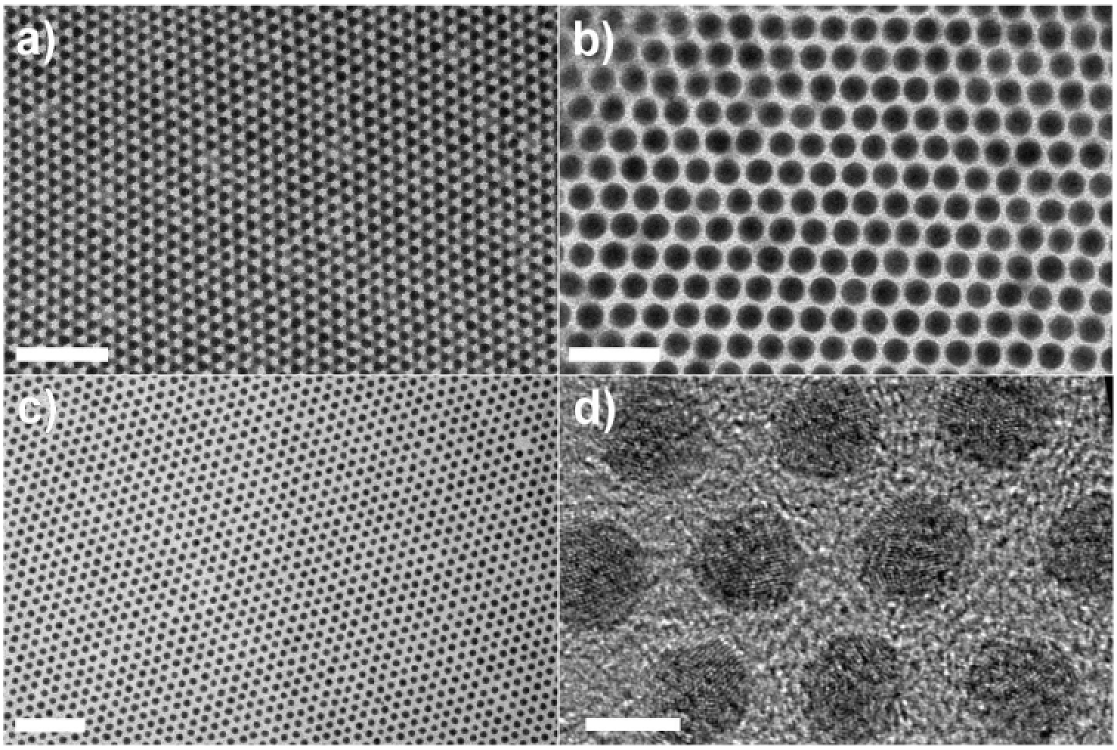

Figure 2.17. TEM images of (a,b) 5.8 nm and (c) 5.0 nm Pd NCs. (d) HRTEM image of the 5.8nm Pd NCs. The scale bars represent (a,c) 50 nm, (b) 20 nm and (d) 5 nm.

TEM images (Figure 2.17a, b) show that 5.8 nm Pd NCs self-assemble into close-packed superlattices. HRTEM image of the 5.8nm Pd NCs reveals that most NCs are twinned, which is commonly seen in small metal NCs (Figure 2.17d). Transmission small-angle X-ray scattering (TSAXS) pattern (Figure 2.23) of the 5.8nm Pd NCs is fitted to the spherical model with a diameter of 6.05nm and a size distribution of ~9%, consistent with the TEM and HRTEM observations. The powder XRD pattern confirms the fcc crystal structure (Figure 2.18). By changing the reaction medium from a mixture of oleic acid and oleylamine to trioctylamine, 5.0 nm Pd NCs are produced as well (Figure 2.17c).

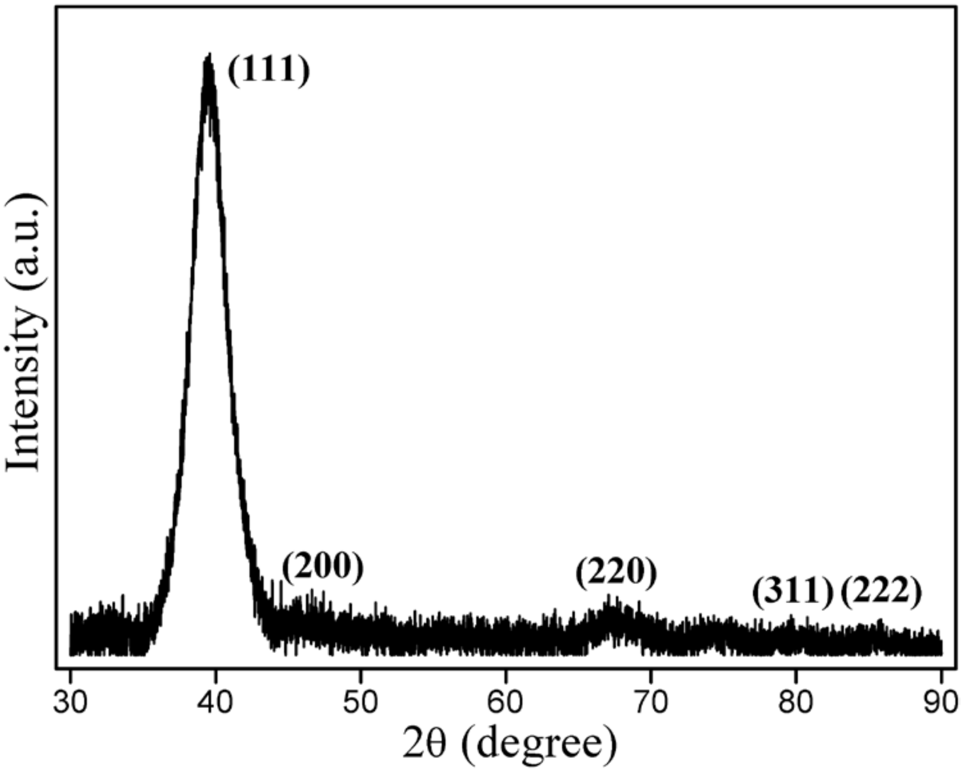

Figure 2.18. XRD pattern of the 5.8nm Pd nanocrystals.

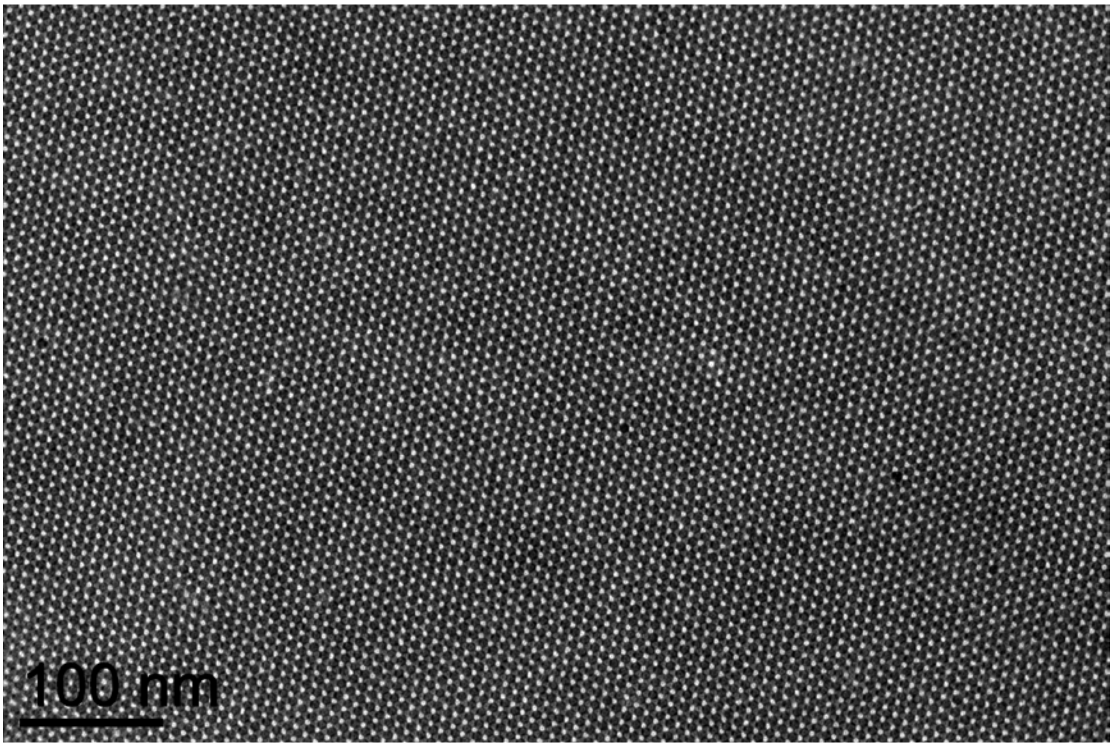

Figure 2.19. TEM image of a hexagonal close-packed array of 5.8nm Pd nanoparticles

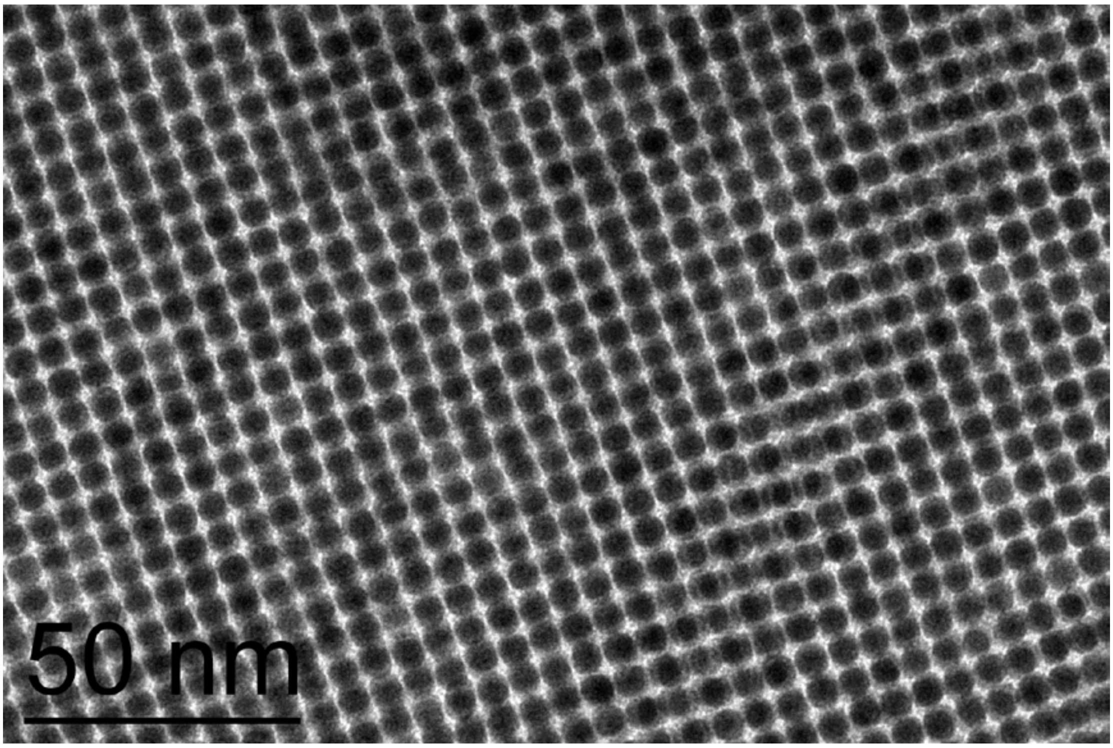

Figure 2.20. TEM image of an array of 5.8nm Pd nanoparticles with simple cubic packing symmetry

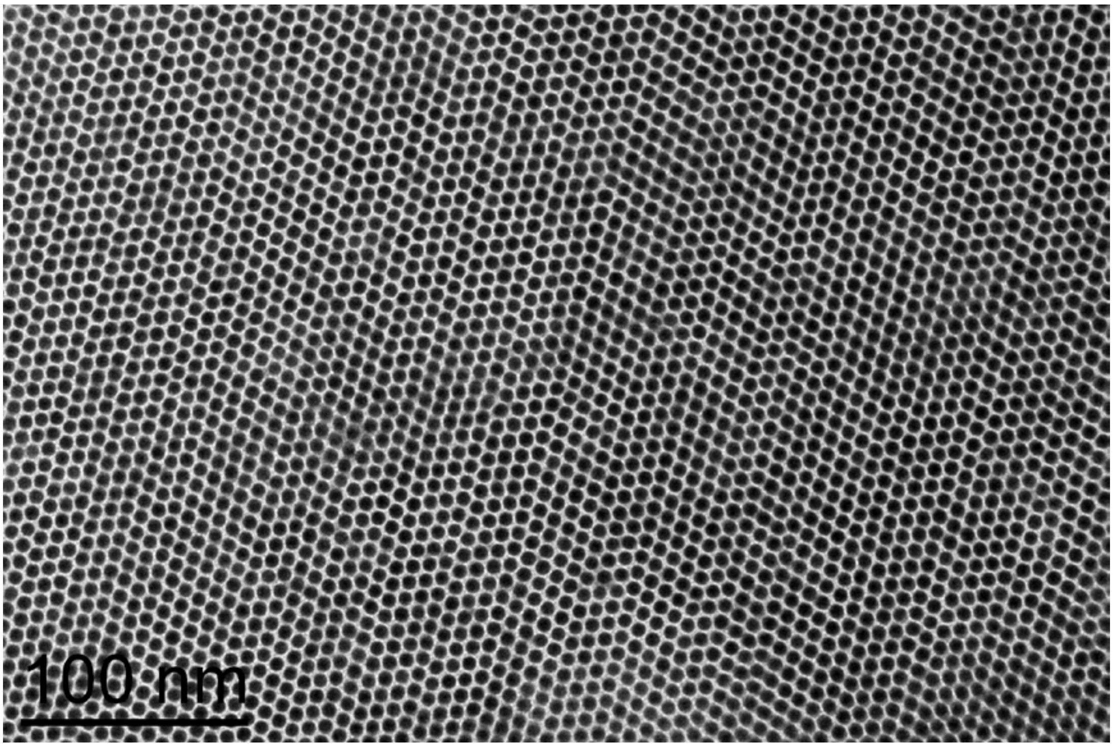

Figure 2.21. TEM image of the close-packed superlattices self-assembled from 5.8nm Pd nanoparticles

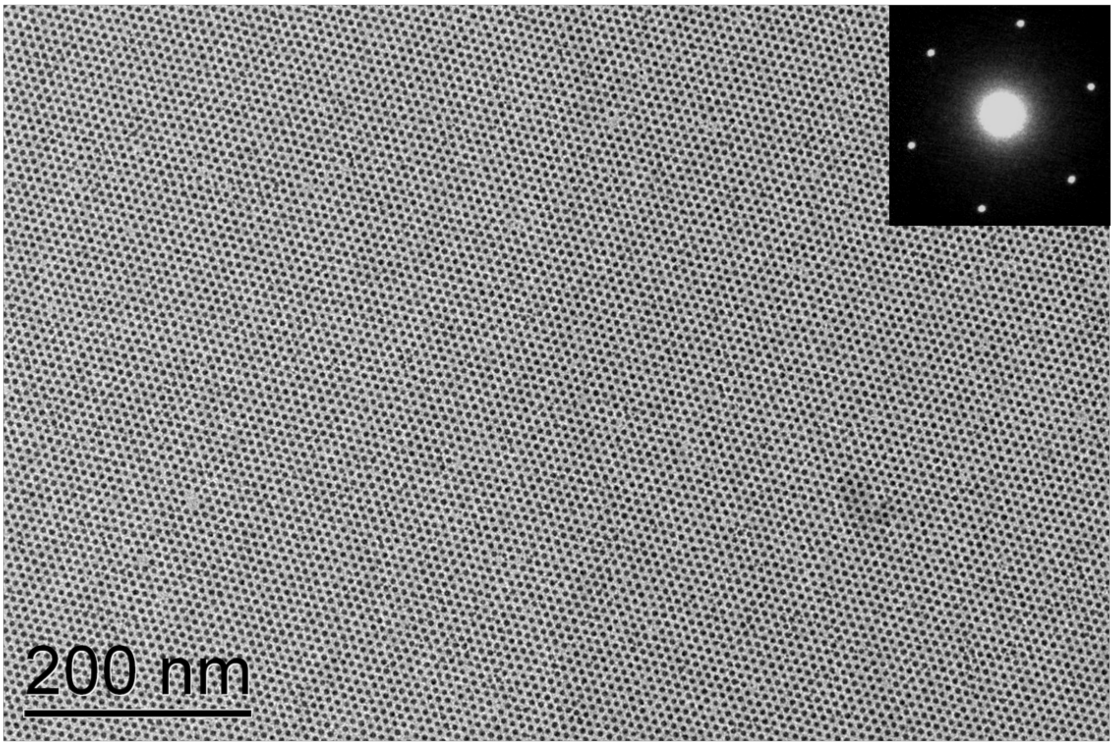

Figure 2.22. TEM image of large area monolayer composed of 5.0nm Pd nanoparticles
Inset: Small-angle electron diffraction pattern recorded from this region

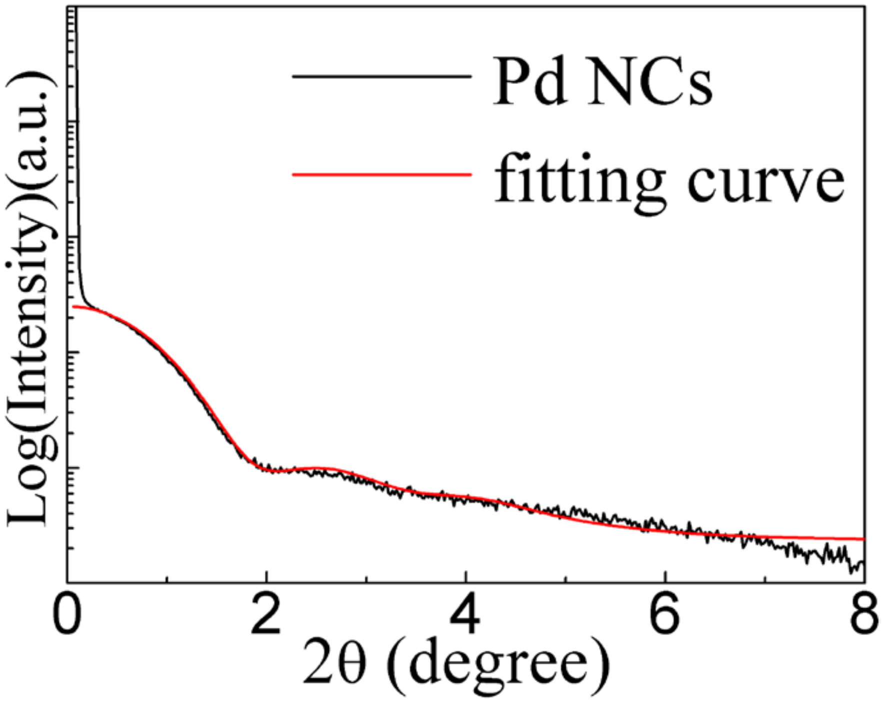

Figure 2.23. Transmission small-angle X-ray scattering (TSAXS). The data was fitted to a spherical model with a 6.1 nm diameter and a size distribution of ~9%.

Recognizing the potential of CO to accelerate reaction rates, we target the use of CO to the synthesis of ultrathin Au NWs. Several groups have developed colloidal methods to synthesize uniform Au NWs. However, these recipes usually require hours or even days[49-52]. As a final example, we demonstrate that the ultrathin Au NWs can be synthesized within 10 minutes by reducing AuCl-oleylamine complexes with CO.

Synthesis of Au NWs using AuCl: 0.046g AuCl is dissolved in 20mL chloroform and 1.84mL oleylamine. The mixture is then heated to 60°C and CO is introduced to the reaction flask (~15cm^3/min). After 10min, the solution is cooled to room temperature and is diluted with hexane. The NWs are precipitated by centrifugation at 6000rpm.

Synthesis of Au NWs using $AuCl_3$: 0.050g $AuCl_3$ is dissolved in 3mL o-dichlorobenzene and 12mL oleylamine. The mixture is then heated to 80°C at a rate of 15°C/min and CO is then introduced to the reaction flask (~15cm^3/min). After 5min of reaction, the solution is cooled to room temperature and the Au NWs are isolated by adding ethanol and centrifugation. The products are redispersed in hexane.

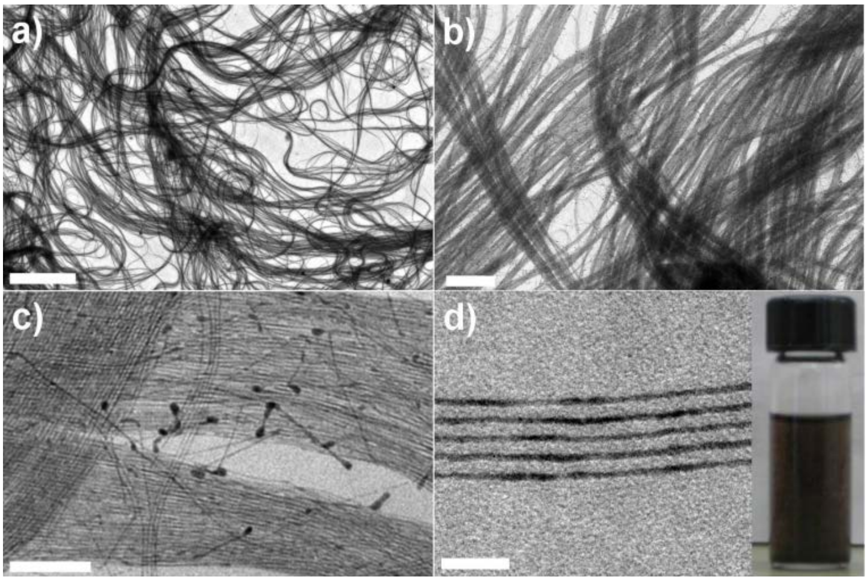

Figure 2.24. TEM images of ultrathin Au nanowires. Inset of d) shows the photograph of Au nanowires dispersed in hexane. The scale bars represent a) 5 µm, b)0.5 µm, c)100 nm, and d) 20 nm.

The Au NWs forms within 2 min after introducing CO, growing longer as the reaction proceeds (Figure 2.26). TEM images of different magnifications show that the Au NWs obtained tend to assemble into bundles (Figure 2.24, 2.25, 2.26). Individual Au NW typically terminates with enlarged spherical ends (Figure 2.24c). Similar wires have been observed and proposed to result from oriented-attachment during the growth[53]. The Au NWs are of ~2.5 nm in width and of several microns in lengths (Figure 2.24d). In addition, ultrathin Au NWs can also be produced with $AuCl_3$, albeit in lower yield (Figure 2.30). These one-dimensional metal nanostructures are promising building blocks for plasmonic waveguides[54] and nano-electronic devices[55].

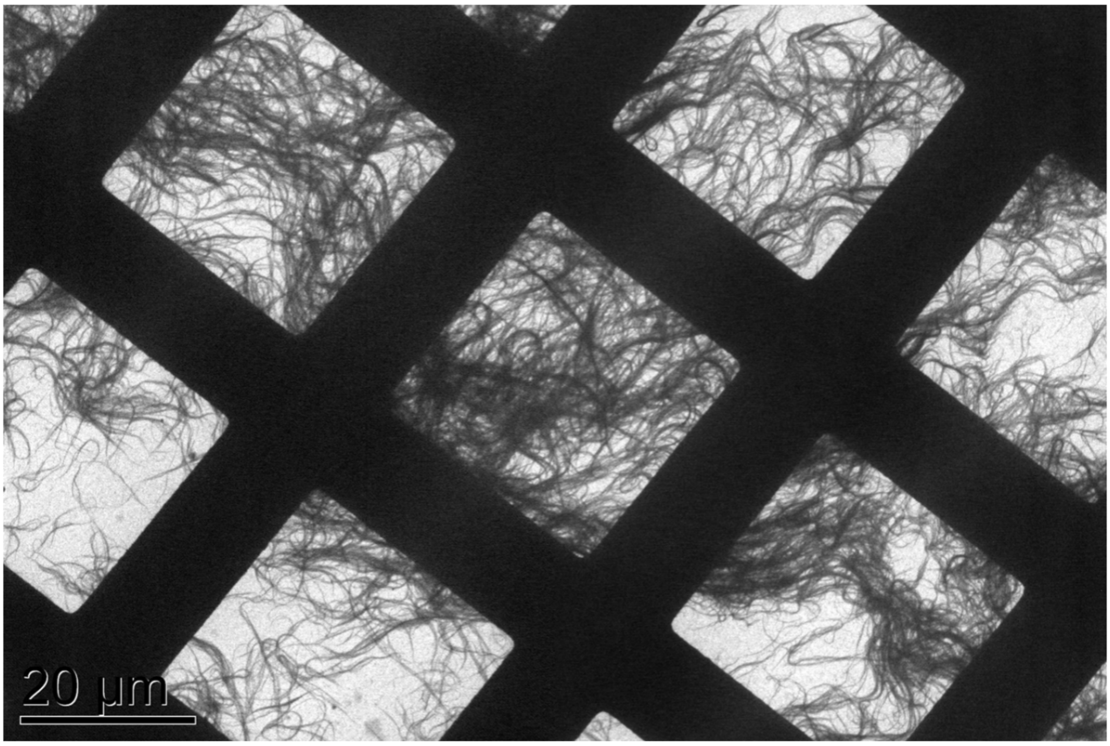

Figure 2.25. Low magnification TEM image of typical Au nanowires synthesized using gold (I) chloride (AuCl)

Figure 2.26. Large area TEM image of typical Au nanowires synthesized using gold (I) chloride (AuCl)

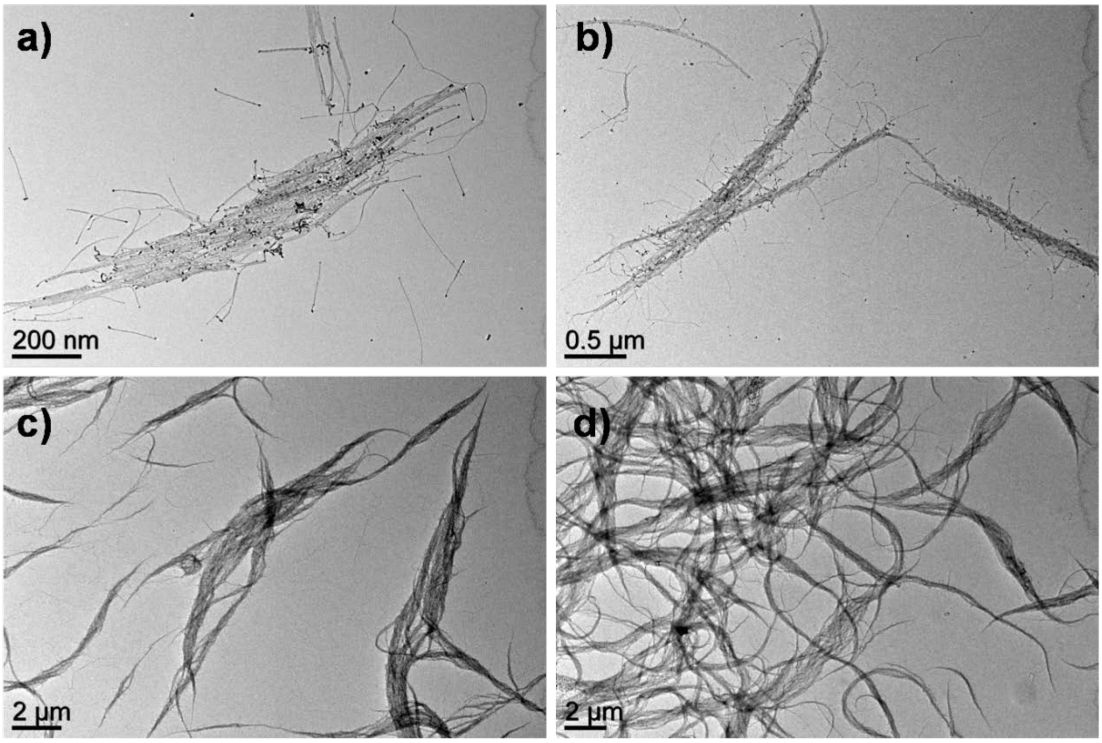

Figure 2.27. TEM images taken at different stages of Au nanowires syntheses using CO. (a) 2min, (b) 4min, (c) 6min, (d) 8min.

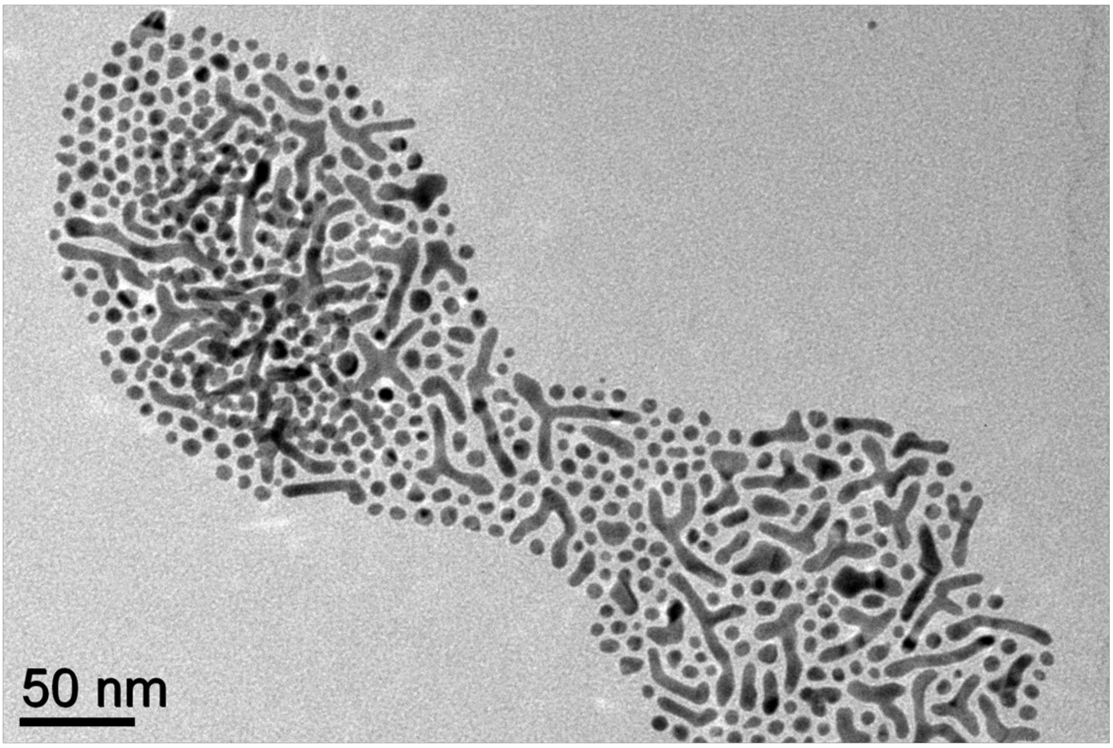

Figure 2.28. TEM image taken after 24 hours of Au nanowires synthesis in the absence of CO

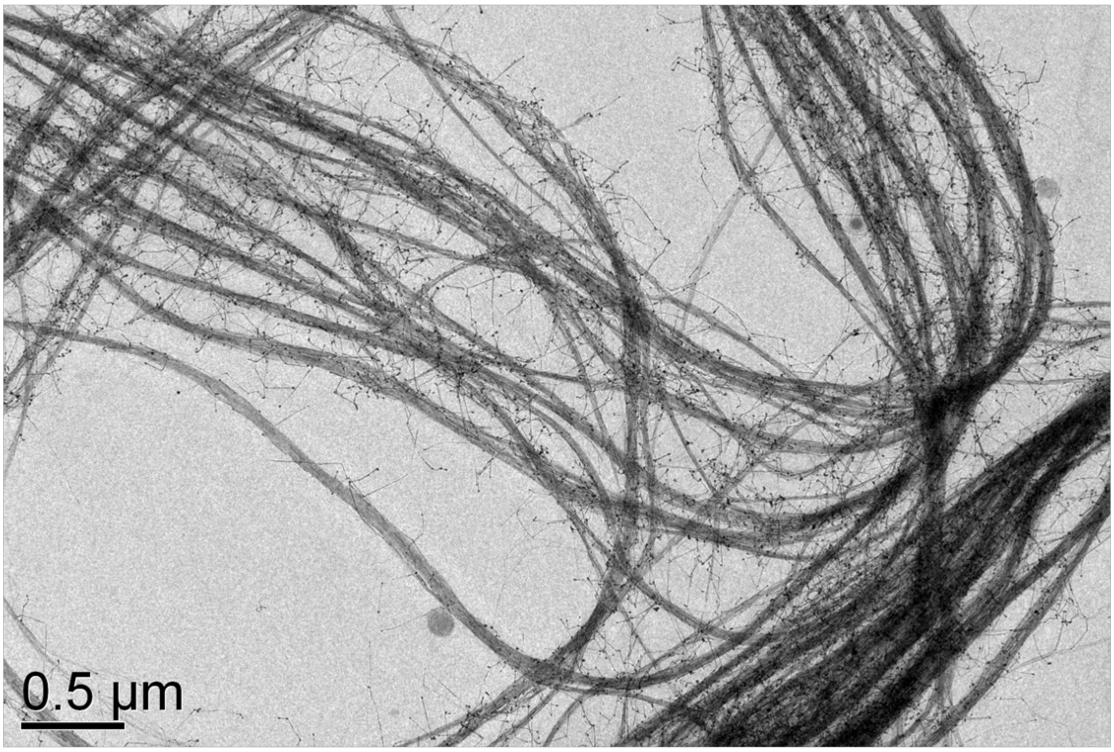

Figure 2.29. TEM image of Au nanowires synthesized with AuCl in the presence of both oleic acid and oleylamine

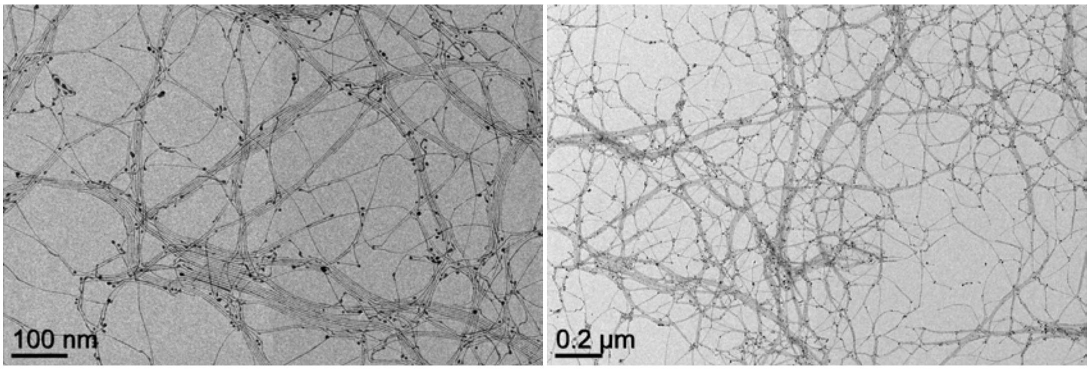

Figure 2.30. TEM image of Au nanowires synthesized using gold (III) chloride ($AuCl_3$)

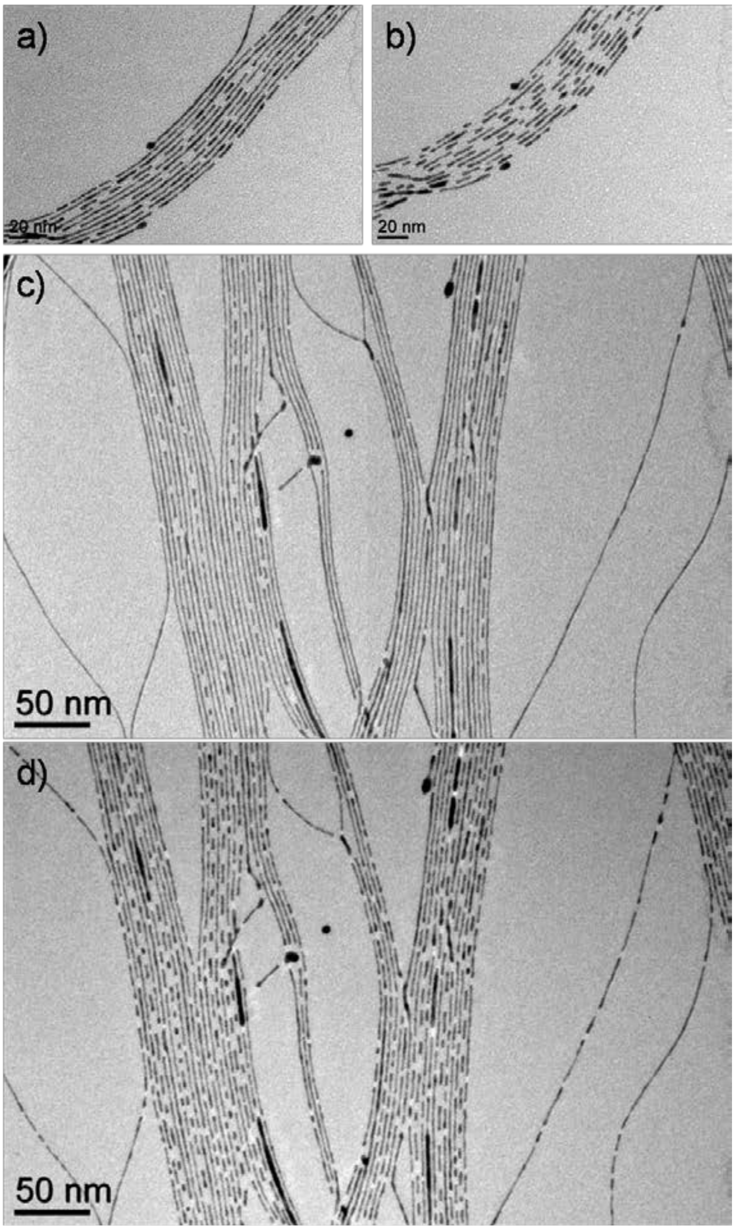

Figure 2.31. TEM images showing the electron beam damage of Au nanowires. Images (b) and (d) were taken after 1 min electron beam exposure of the same region as in (a) and (c), respectively.

2.3.3 Shape control of Pt nanocrystals

In recent decades, researchers have made great progress towards applying the knowledge gained from surface studies to the real catalysts[7,16]. Shape control of nanocrystals is an important aspect of this approach. Pt nanocrystals receive particularly intensive attention because Pt is active in many catalytic processes. These have been numerous reports (since as early as 1996)[56] of the shape-controlled syntheses of Pt nanocrystals in which the exposed facets are controlled; and a number of structure sensitive reactions have also been described. For example, Feliu, et al. have reported shape-dependent methanol and formic acid electrooxidation on preferentially oriented Pt nanoparticles[6], Zaera, et al. have described tuning the selectivity of isomerization reactions by controlling the particle shape of Pt[7], and Yang and Somorjai, et al. demonstrated the shape effects of Pt nanocrystals on benzene hydrogenation selectivity[8].

Well-controlled synthesis of nanocrystals enables unambiguous correlation between the structural properties and the catalytic properties. Therefore, high quality nanocrystals not only provide insight into the reactivity of catalysis, but could also provide meaningful improvements towards the development of highly efficient catalysts. While shape control at the scale of hundreds nanometer has been achieved[57-59], the preparation of well-controlled Pt nanocrystal at sub-10 nm is still highly challenging[16]. In this report, we describe the preparation of current “best Pt nanocrystals” with a variety of morphologies through solution-phase-synthesis and a unique purification method.

The synthesis of Pt nanocrystals involves using Pt acetylacetonate as source of Pt, oleic acid and oleylamine as capping agents, and CO gas and/or metal carbonyls as additives. In previous research, we have found that by reducing the amount of metal carbonyls, we can produce pure Pt nanocubes rather than Pt-based alloy nanocubes, and that Pt nanocubes can be even synthesized using only CO as reducing agent, in the absence of metal carbonyls[29]. I have also experimented with solvents in which the metal carbonyls are dissolved prior to injection. Interestingly, we notice that by using chloroform, pure Pt nanocrystals (close to 100%) are produced, while other solvents (benzyl ether, hexane, dichlorobenzene, toluene, and etc.) produce Pt-based alloys. Surprisingly, ammonium chloride is produced as a major byproduct. Recognizing that chloroform can prevent the formation of alloys with Pt, we use a chloroform solution of dimanganese decacarbonyl as additive agent to control the shape of Pt nanocrystals.

Pt nanocrystals enclosed by {111} facets

Numerous surface science studies have focused on (111) and (100) surfaces, because they are the most common low-index surfaces. Therefore, to design the new generation catalysts with high performance, it is crucial to understand the catalytic properties of {111} and {100} in real catalysts for various structure sensitive reactions. While highly monodisperse Pt nanocubes exposing {100} facets can be synthesized by several methods[29,36-38]; highly controlled synthesis of Pt nanocrystals with {111} facets have not been reported yet, although preferentially {111}-oriented Pt nanoparticles have been produced by several pioneering groups[6,7,56,60,61]. The lack of high-quality Pt (111) models has limited scientists either to statistically attribute the shape dependent properties to each of the shapes present within a sample[6,7], or to indirectly compare the structure-sensitivity of a reaction on {100} facets of a cube to the mixed {111} and {100} of a cuboctahedron or a sphere[8,27]. Here, we first present two morphologies of highly controlled Pt nanocrystals with primarily (111) surface --- Pt octahedra and Pt icosahedra.

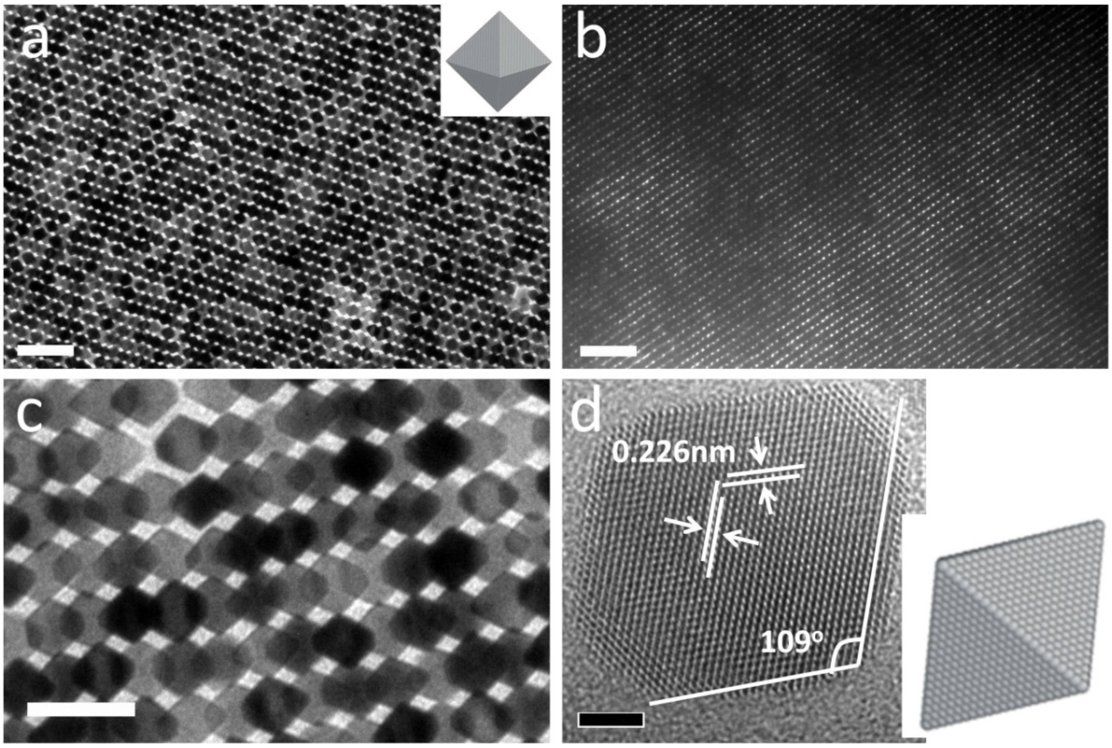

Figure 2.32. a-c) TEM images and d) HRTEM images of Pt octahedra and a) a superlattice and b) a 3D-superlattice formed from the Pt octahedra. Scale bars: a, b) 50nm, c) 20nm, d) 2nm.

Pt octahedra are synthesized via the reduction of Pt(acac)$_2$ by a chloroform solution of $Mn_2(CO)_{10}$, in the presence of oleic acid and oleylamine. The atomic ratio of Mn/Pt in the precursor is 1/5. However, the atomic % of Mn is less than 1% in the final product (by ICP-OES), thus the final product of octahedra can be considered as pure Pt octahedra. The Pt octahedra have a size of 12.56 ± 0.36 nm (vertex to vertex), and readily assemble to form a superlattice with a structure known as Minkowski lattice, as shown in Figure 2.32. Aberration-corrected HRTEM image of single Pt octahedra reveals an interplanar distance in the range from 0.222 nm to 0.226 nm, which is consistent with the lattice spacing of 0.227 nm for the {111} planes of the fcc platinum structure (Figure 2.32d). The measured angle between two faces is about 109^o, which is close to the dihedral angle of octahedra which is 109.5^o. The {111} planes are parallel to the surface of octahedra as shown in the HRTEM image. All of these together confirm the octahedral shape of the Pt nanocrystals, as the HRTEM image is the projection of the octahedral model (Figure 2.32d). An attempt to tune the size of the Pt octahedra has been made through changing the Pt/Mn ratio, Pt/ligands ratio, reaction time, or reaction temperature. However, these reactions produced Pt nanocrystals at other morphologies which are described in following paragraphs, thus the size of the Pt octahedra is not tunable in this system.

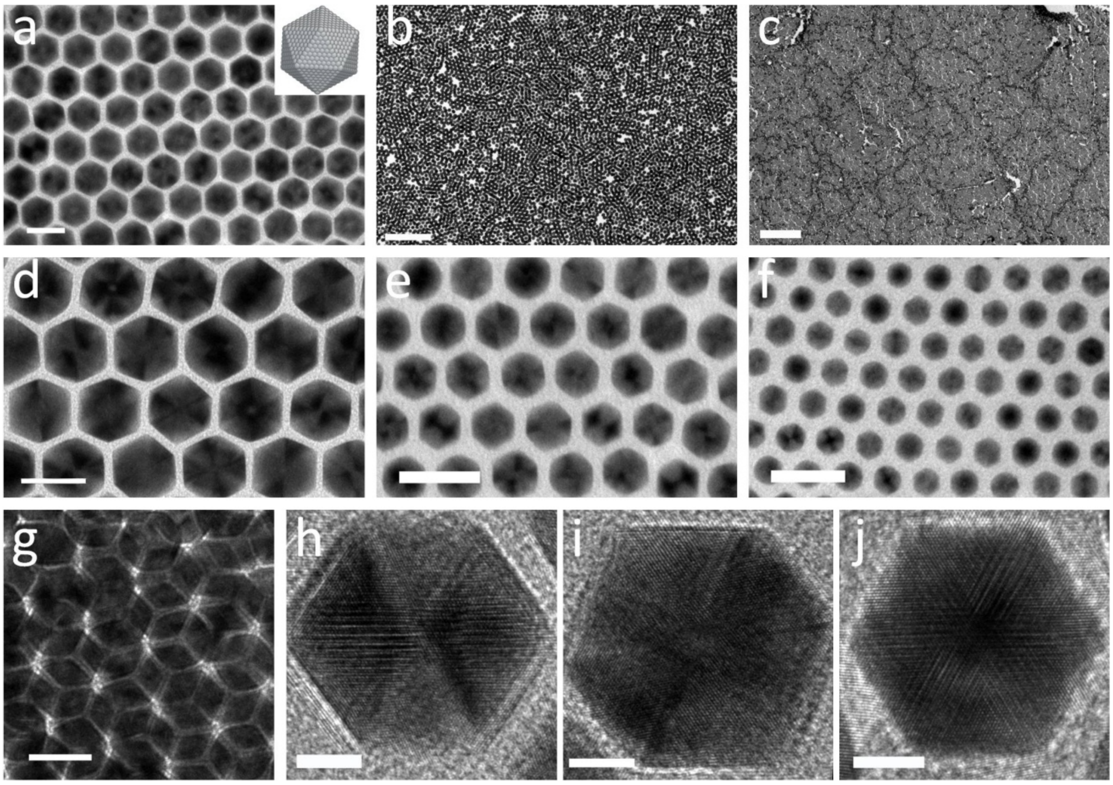

Figure 2.33. a-g) TEM and h-j) HRTEM images of Pt icosahedra. a) shows the typical Pt icosahedra; b, c) show the Pt icosahedra over a large area; d-f) show the size of Pt icosahedra is tunable: d) 20.43 nm, e) 11.92 nm, f) 8.07 nm; g) shows the Pt icosahedra in a self-assembly behave as semi-hard spheres; h-j) the HRTEM images show the distinctive pattern for the morphology of icosahedra. Scale bars: a, d, e, f, g) 20 nm, b) 200 nm, c) 1µm, h, i, j) 5 nm.

During the investigation of Pt octahedra, we notice that Pt icosahedra are also produced as byproduct in various quantities, depending on the synthetic conditions. An icosahedron is another shape in which only {111} facets are exposed. Icosahedron has a multi-twinned structure, in which 20 fcc-structured single crystalline tetrahedra share one apex. Such multi-twinned structure may render nanocrystals other interesting properties besides the reactivity of the {111} facets. Icosahedra of Fe, Pd, Au, and Ag have been prepared previously[62-67]. However, to the best of our knowledge, Pt icosahedra have not been reported to date. Here, we modify and optimize the synthesis to produce high quality icosahedra.

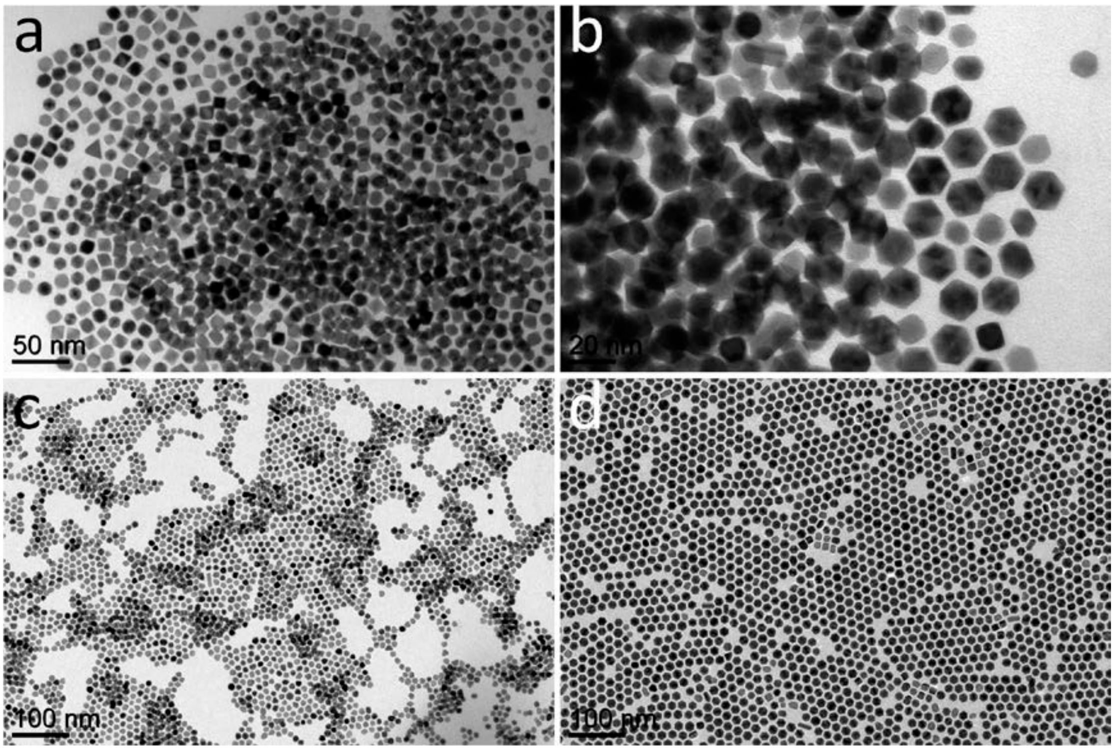

Figure 2.34. a) shows the icosahedra are major byproduct in the synthesis of Pt octahedra; b) shows the coexistence of icosahedra and cuboctahedra in a product mixture from the optimized synthesis; c) shows the cuboctahedra and d) shows the icosahedra separated from the product mixture.

Although the Pt icosahedra are observed in the synthesis of Pt octahedra and they can be collected through the size selective precipitation, the yield is too low to be a routine synthetic method to prepare Pt icosahedra. The literature suggests that the growth of multi-twinned nanocrystals is a kinetically-controlled reaction at slow reaction conditions[63,66]. Therefore, reducing the overall reaction rate may favor the growth of icosahedra, which may be achieved through simply lowering the reaction temperature. Because the minimum temperature to efficiently decompose and reduce Pt precursor is about 180°C, we adjust the temperature to around 190°C while retaining the other synthetic parameters used in the synthesis of Pt octahedra. The yield of Pt icosahedra is ~50%, while the remaining product consists of truncated cubes or cuboctahedra, depending on the actual reaction. The as-synthesized Pt icosahedra are less soluble than the other Pt nanocrystals, and are barely soluble in hexane. Simply washing the product mixture with hexane (containing 1% oleylamine) can effectively purify the Pt icosahedra (Figure 2.34). After the purification process, the purity (in terms of shape) of Pt icosahedra can reach as high as 98% (~500 nanocrystal counts), as shown in Figure 2.33. TEM images (Figure 2.33a-d) present the highly monodisperse ($\sigma < 1\%$) Pt icosahedra with the size of 20.43 ± 0.13 nm (shortest vertex to vertex distance). The special interference patterns shown in HRTEM images (Figure 2.33h-j) are the distinctive characteristic of icosahedra, as described in literature[66,67]. The size of Pt icosahedra is tunable through use of other metal carbonyls, which affects the reaction rate, although the yield is impacted. For example, the Pt icosahedra synthesized by using $Re_2(CO)_{10}$ instead of $Mn_2(CO)_{10}$ are much smaller, having a size of 11.92 ± 0.36 nm (Figure 2.33e), and the Pt icosahedra as a byproduct separated from Pt octahedra synthesis have a size of 8.07 ± 0.23 nm (Figure 2.33f).

Pt nanocrystals enclosed by {100} facets

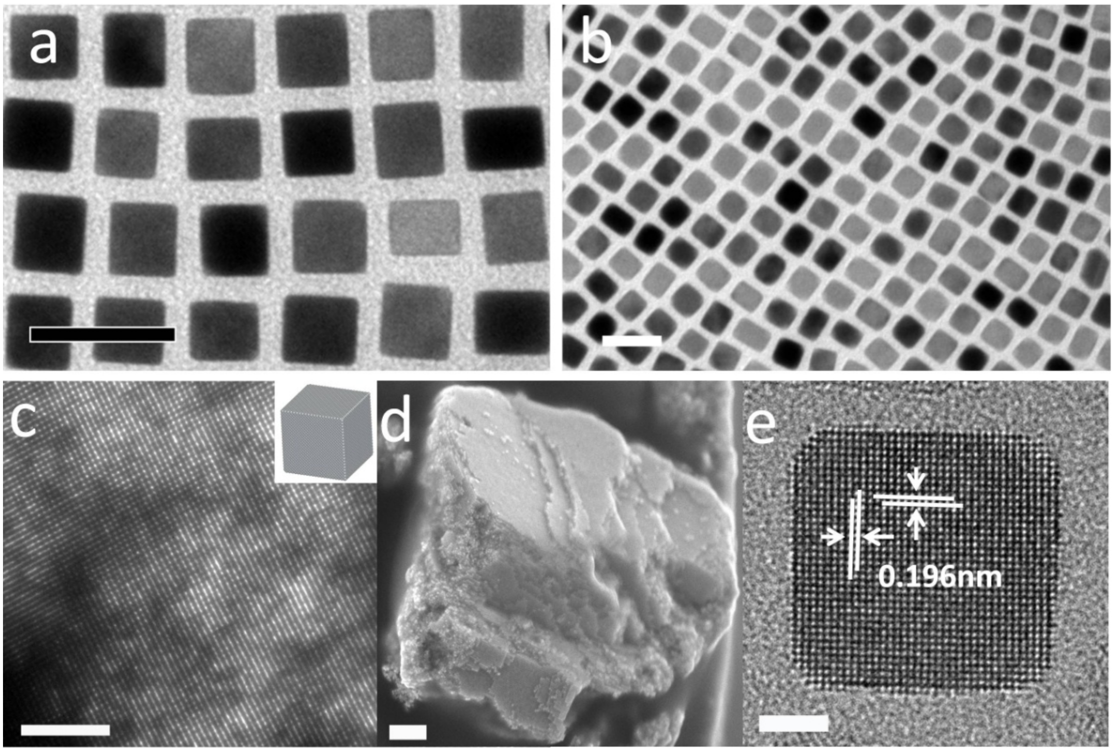

Figure 2.35. a-c) TEM, d) SEM, and e) HRTEM images of Pt nanocubes. a) Pt nanocubes synthesized using CO as reducing agent; b) Pt nanocubes obtained using $Mn_2(CO)_{10}$ at 240oC; c) large area superlattice and d) super-crystal can be made by self-assembly of high quality Pt nanocubes; e) a HRTEM image confirms that the facets of Pt nanocubes are Pt(100). Scale bars: a, b) 20 nm, c, d) 200 nm, e) 2 nm.

Pt nanocubes exposing {100} facets can be synthesized using CO as reducing agent, or using a reduced amount of Mn carbonyl. Using CO as reducing agent produces Pt cubes which are very uniform in shape but possess a larger size distribution when compared to using Mn carbonyl. In order to assemble nanocubes produced using CO into the superlattices or super-crystals as shown in Figure 2.35c and 2.35d, further purification steps are necessary. On the other hand, although the size is more uniform, a Mn-Pt alloy phase may be involved in the initial nucleation stage during the synthesis of Pt nanocubes involving Mn carbonyl, thus the final product is inevitably contaminated by Mn, that may an issue for some applications. Nevertheless, the Pt nanocubes prepared through these two methods are as good as, or better than those reported in literature.

As shown in aberration corrected HRTEM images (Figure 2.35e), the interplanar distances measured are in the range of 0.196-0.198 nm, which correlate with the lattice spacing for the {200} planes of Pt (0.196 nm). In addition, that the facets of Pt nanocubes are parallel to {200} planes confirms that Pt nanocubes are terminated by Pt (100). It is worth noting that the same recipe used to synthesize Pt octahedra also produce cubes at temperatures above 240°C (Figure 2.35b), instead of Pt octahedra.

Other morphologies of Pt nanocrystals

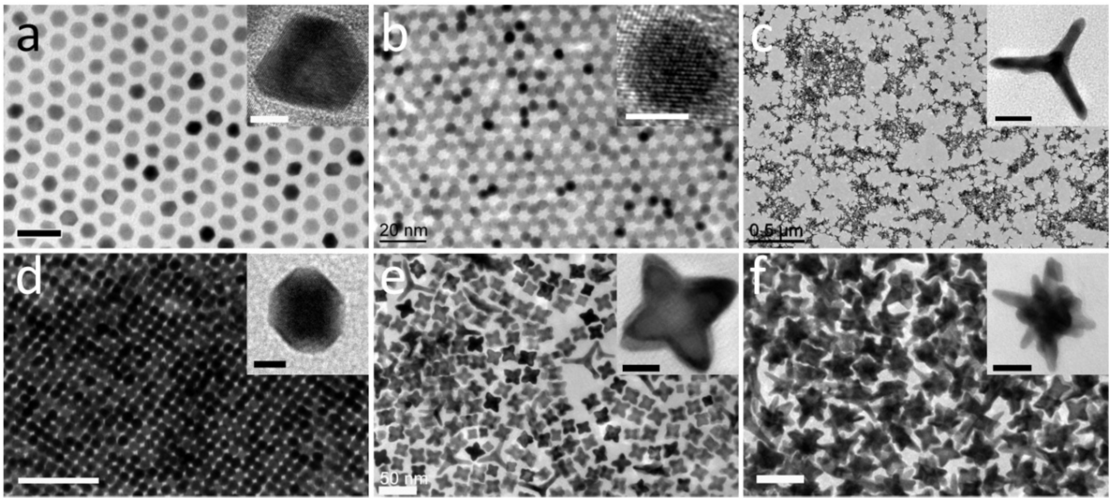

Figure 2.36. TEM images of a) Pt cuboctahedra, b) Pt spheres, c) Pt tetrapods, d) Pt truncated cubes, e) Pt star (octapods), f) Pt multi-pods. Scale bars: a, b) 20 nm, c) 0.5 µm, d, e, f) 50 nm, insets of a, b, d) 5 nm, insets of c, f) 20 nm, inset of e) 10 nm.

Pt nanocrystals in various morphologies can be obtained through the use of Mn carbonyl, as shown in Figure 2.36. By increasing Mn/Pt ratio to 1:1, Pt cuboctahedra with a size of 7.03 ± 0.35 nm (shortest vertex to vertex distance) can be synthesized (Figure 2.36a). By further increasing the Mn/Pt ratio to 2:1, near spherical Pt nanocrystal with a size of 4.68 ± 0.20 nm (diameter) are produced (Figure 2.36b).

As mentioned previously, using same amount of Mn carbonyl but reducing the reaction temperature can produce mixtures of truncated cubes (or cuboctahedra) and icosahedra. The lower temperature (i.e. 180-190^{o}C) favors the formation of truncated cubes while the cuboctahedra are preferentially produced at higher temperature (i.e. 190-200^{o}C). In reality, both of these two shapes are "truncated" cubes. When the edge length of {100} facets are equal (or close, if not strictly) to that of {111} facets, the shape is usually referred to as cuboctahedron; when the degree of truncation (in the <111> direction) is less than a cuboctahedron has, the shape is defined as truncated cube. After separating icosahedra from the mixture, the Pt cuboctahedra have similar quality to the sample shown in Figure 2.36a; while Figure 2.36d presents the typical Pt truncated cubes.

In the synthesis of Mn-Pt nanocubes, tetrapods are observed. Elemental analysis by ICP-OES indicates that such tetrapods are pure Pt (>98%). By monitoring the shape evolution, we observe concave Mn-Pt nanocubes form before the formation of Mn-Pt nanocubes, similar as observed in Pt-Cu nanocubes[68]. During this stage, a few of pyramids have formed, most likely as the defect of cubes. While the Mn-Pt concaved cubes grow to nanocubes, those pyramids grow into tetrapods gradually out from four apexes (Figure 2.37). The yield of tetrapods is usually so low that they are overlooked under most circumstances. The origin of such growth of tetrapods has not been identified, thus the optimized synthesis for the tetrapods is not been developed. Nonetheless, as shown in Figure 2.36c, the tetrapods can be separated from major product through the size selective precipitation (tetrapods remain in the precipitation).

For some applications in which the quantity of materials is not important, this preparation of Pt tetrapods that relies on separation could feasibly be used.

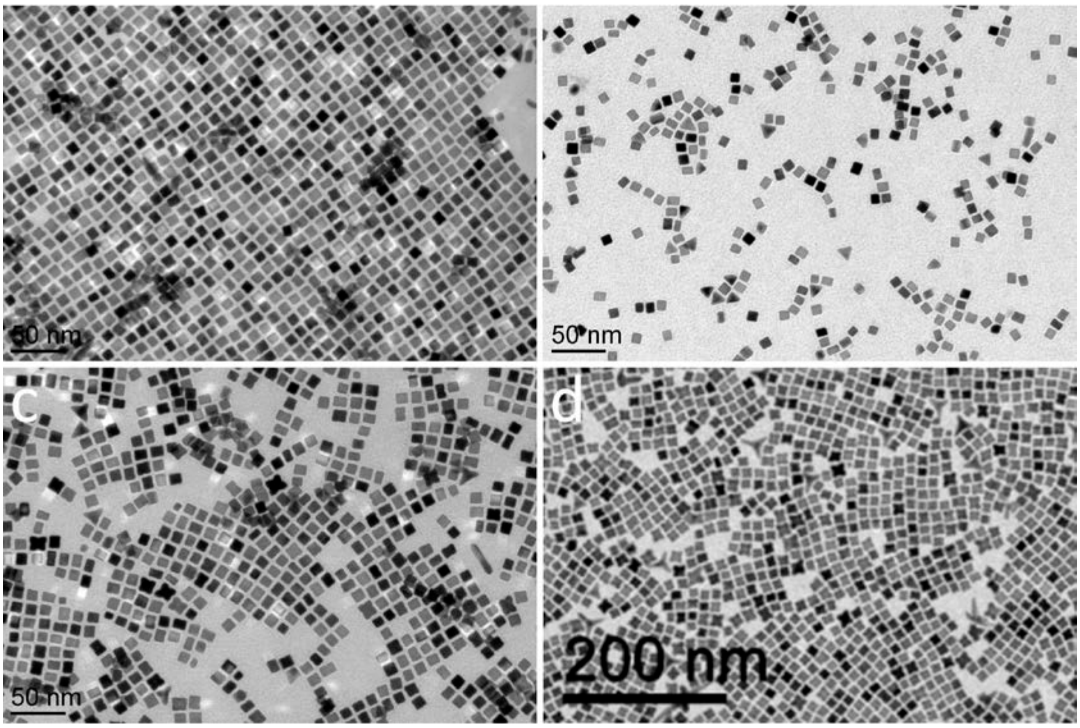

Figure 2.37. a) the concaved Mn-Pt nanocubes; b) the tetrahedra exist as defects of cubes; c) the Pt grows out of the 4 apexes of tetrahedra; d) Pt keeps growing on tetrahedra to form tetrapods.

By reducing the amount of Mn carbonyl to Mn/Pt = 1:5, relative pure Pt nanocubes (>99%) are produced rather than Mn-Pt alloy nanocubes. By further decreasing the Mn/Pt ratio to below 1:10 and increasing the reaction time, the Pt stars (octapods) and multi-pods are produced (Figure 2.36e, f). The octapods and multi-pods usually coexist; lower reaction temperature favors the formation of more multi-pods over the star-shape octapods. For example, a reaction at 220^{o}C preferentially produces octapods; the multi-pods become major product at 200^{o}C. If the reaction time is increased from 30min to 90min, the branches of Pt nanocrystals can further grow to produce a spike-like hyper-branched structure (Figure 2.38).

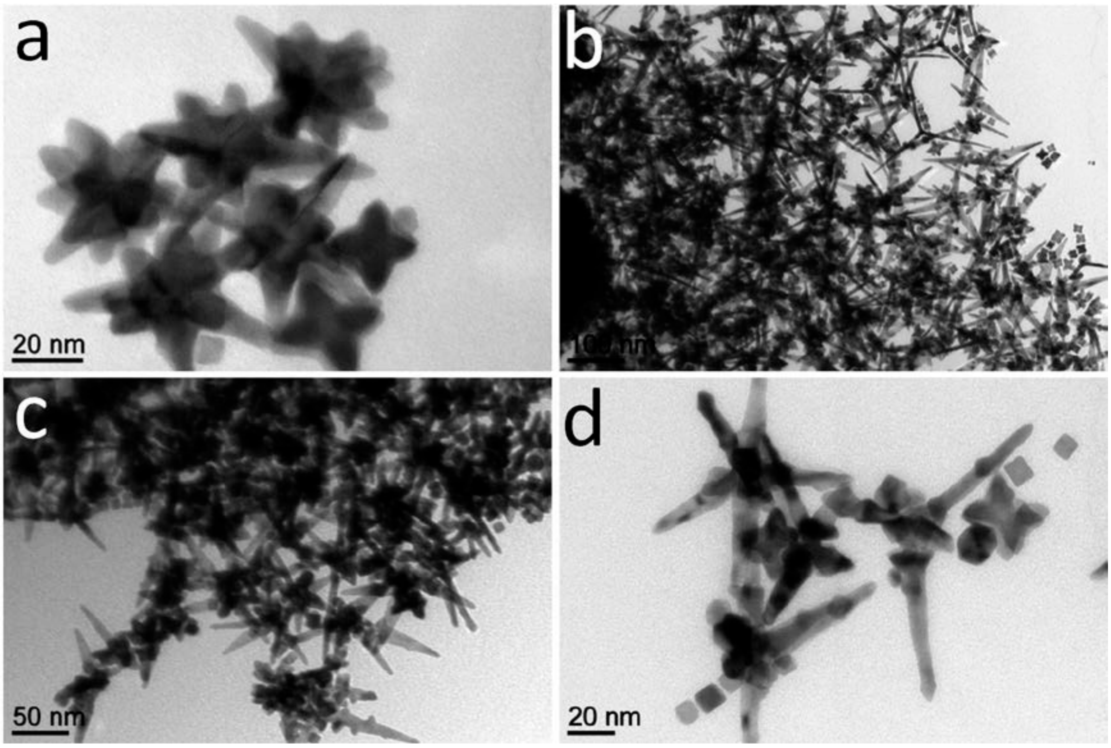

Figure 2.38. The hyper-branched Pt nanocrystals.

Discussion for Plausible Mechanisms

Putting all of the syntheses together, we find some general trends, and plausible mechanisms are discussed here. The use of chloroform is the key to avoid the formation of a Mn-Pt alloy phase even at a Mn/Pt ratio as high as 2:1, and NH_4Cl forms as one major byproduct in these reactions. Oleylamine is the only source of N and the chloroform is the only source of Cl. However, to the best of our knowledge, no literature explains the reaction of amine and chloroform to produce NH_4Cl. Thus, this process is not clear yet.

In this reported synthetic system, the role of $Mn_2(CO)_{10}$ has been investigated, as it is used in most of the syntheses. We have found the relationship between $Mn_2(CO)_{10}$ and CO, as reported previously. While using CO as reducing agent, high quality Pt nanocubes can be synthesized, the Pt octahedra of any size have never been observed no matter how other reaction parameters are tuned (Figure 2.40), indicating that the Mn must be involved in the formation of octahedra. A shape evolution of octahedra has been investigated by taking aliquots out of reaction after the injection of $Mn_2(CO)_{10}$ (Figure 2.39b). The cubes are observed within as early as one minute. After that, the cubes gradually become truncated, while icosahedra also start to form. After around 15 min, most cubes have transformed into cuboctahedra, which is terminated between a cube and an octahedron. After 20 minutes, the majority of the nanocrystals have finished the transformation from cubes to octahedra.

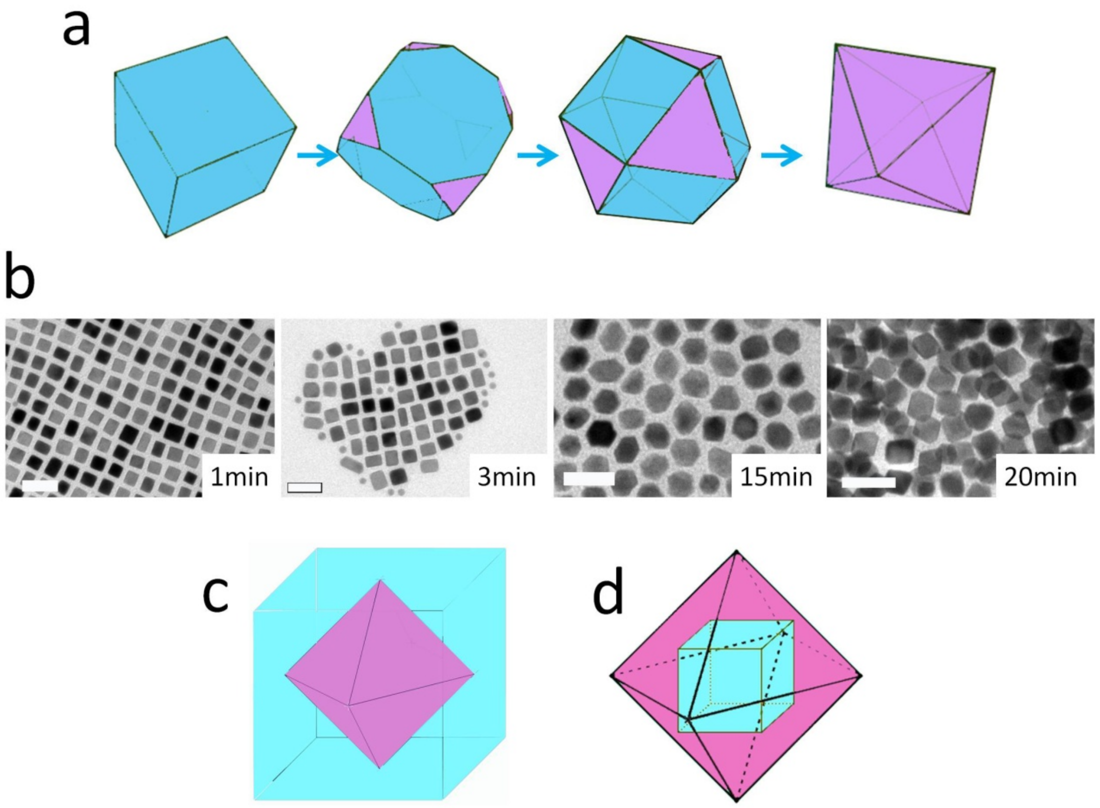

Figure 2.39. a) the relation in the morphologies of cube, truncated cube, cuboctahedron, and octahedron (blue: {100}, purple: {100}); b) TEM images of aliquots taken after the injection of Mn carbonyl solution; c) octahedra is dual to a cube, representing the etching mechanism; d) cube is the dual polyhedron to a octahedron, showing the way that a cube grows into an octahedron. Scale bars: 20 nm.

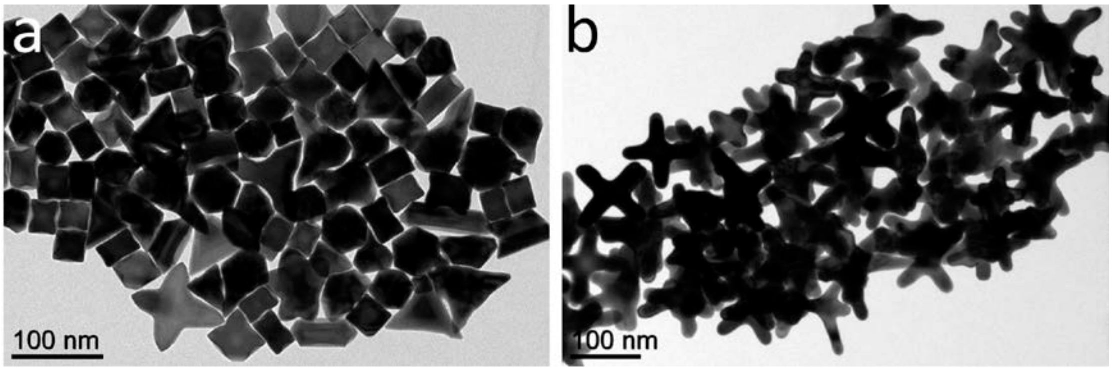

Figure 2.40. TEM images of a) product from the synthesis of octahedra using CO to substitute Mn carbonyl, and b) product from the synthesis using CO at the temperature above 220^{o}C.

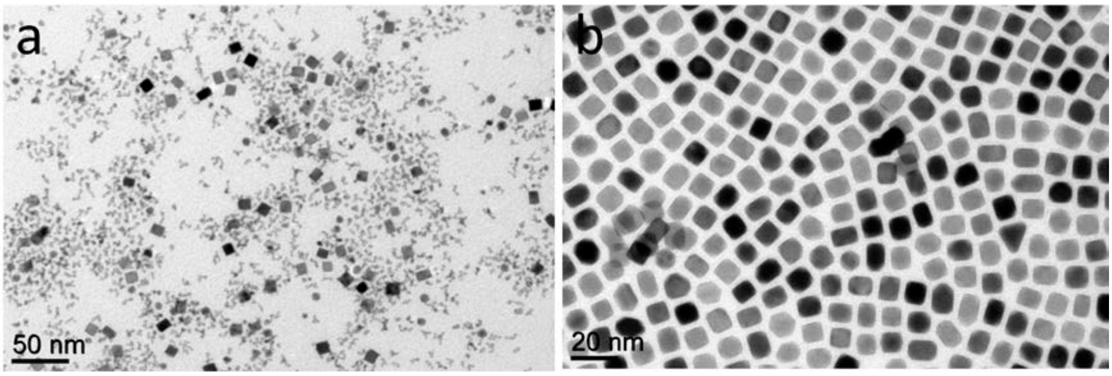

Figure 2.41. TEM images of products from a) the synthesis of octahedra using a vigorous stirring, and b) the synthesis of octahedra using Pt nanocubes to replace Pt(acac)$_2$, as a “post-treatment” test.

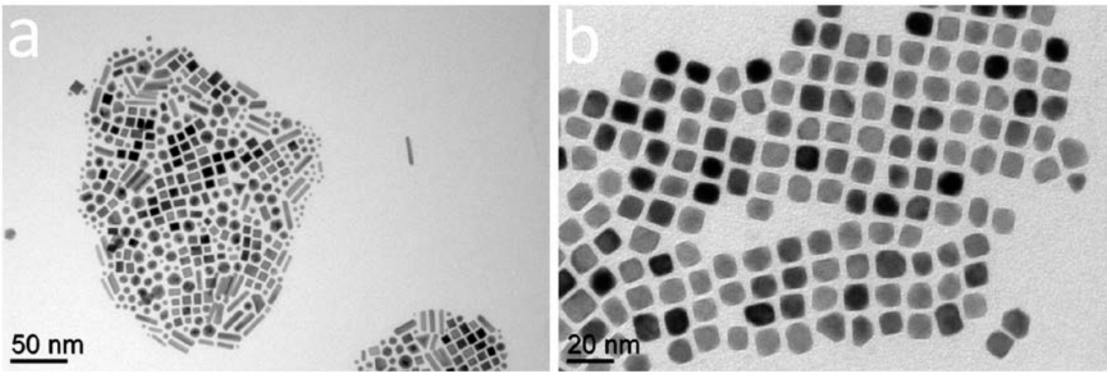

Figure 2.42. TEM images of products from the synthesis using of Mn$_2$(CO)$_{10}$ at reaction temperature of a) 160^{o}C and b) 180^{o}C.

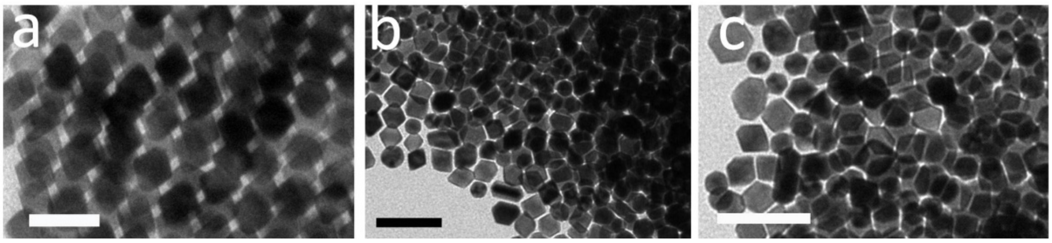

Figure 2.43. TEM images of products from the synthesis of octahedra using a) $Co_2(CO)_8$, b) $Re_2(CO)_8$, and c) $Cr(CO)_6$ as the replacement of $Mn_2(CO)_{10}$. Scale bars: 20 nm.

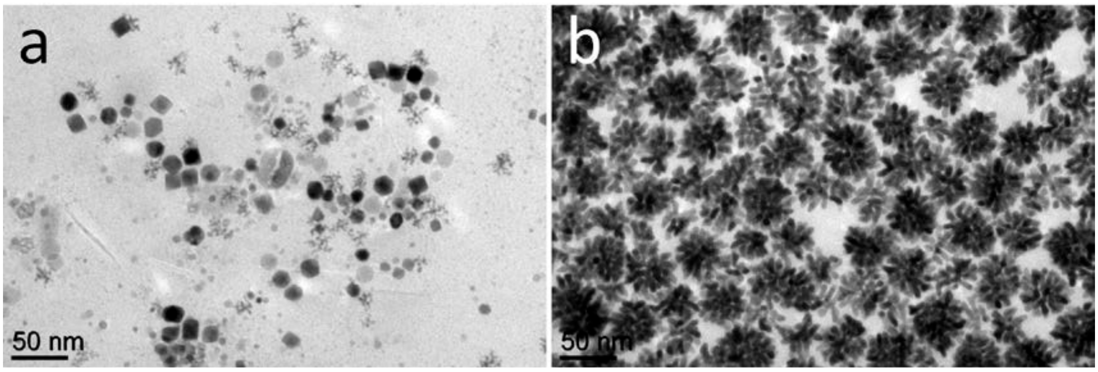

Figure 2.44. TEM images of products from the synthesis of octahedra using a) Fe powder b) Mn powder to substitute Mn carbonyl.

The process of such transformation could possibly be an etching process starting from a cube followed by dissolution in the <111> directions (Figure 2.39c), or a growth process started from a cube (Figure 2.39d). In geometry, the octahedron is the dual polyhedron to the cube, where the vertexes of an octahedron correspond to the faces of a cube. It can be used to describe an octahedron formed by etching a cube (Figure 2.39c). If this is the case, the vertex to vertex distance of octahedron should be equal to the edge length, which is not true here. Therefore, the etching mechanism can be ruled out. In addition, it is further confirmed by a "post-treatment" test, in which Pt cubes (those shown in Figure 2.35b) are used as the replacement of $Pt(acac)_2$ in the synthesis of Pt octahedra, and after 30min reaction no morphology change of Pt cubes is observed (Figure 2.41b). The cube is also the dual polyhedron of an octahedron, visualizing the octahedra grown from cubes (Figure 2.39d). In this case, the length of octahedron must be two times the cube edge length, which is consistent with the experimental results if the rounded vertex of the octahedra is considered, which reduces the vertex-to-vertex distance slightly. The Mn from the decomposition of $Mn_2(CO)_{10}$ may selectively deposit on Pt (100), and then reduce Pt^{2+} to Pt^0 which takes the position Mn atom occupied. Another possibility is that Mn species (Mn atoms or ions) selectively stabilize Pt(111). A more sensitive tool such as surface probe is necessary to unambiguously identify the growth mechanism. Due to the lack of access to such tool, or experimental data, such as adsorption energy of Mn species on Pt (111) and Pt (100), which would confirm the selective deposition of Mn on Pt (100), we use an indirect method to determine the mechanism. We have tested many other metal carbonyls for the reduction of Pt to form Pt nanocrystals (Figure 2.43). Similar results are obtained from using $Fe(CO)_5$ or $Co2(CO)_8$ in place of $Mn_2(CO)_{10}$. $Cr(CO)_6$ or $Re2(CO)_8$ also produces Pt octahedra, but not as well-controlled. $W(CO)_6$ and $Mo(CO)_6$ exhibit similar results to CO gas, which only produces Pt nanocubes. The powders of Mn and Fe are also tested as a substitute for carbonyls (Figure 2.44). The reaction with Fe powder generates some Pt octahedra though both of the quality and quantity is low, which reinforces the fact that adding a transition metal is important for the formation of octahedra. Mn powder does not produce Pt octahedra, most likely because it fails to provide Mn^0 due to the oxidation, despite the attempt to remove the surface oxides through acid wash has been made. The ability of zero valent metals which result from the decomposition of carbonyls to survive in the presented reaction system follows the order: Co, Fe > Mn > Re > Cr > W, Mo. This order is generalized based on how easily the zero valent metal can be made through the decomposition of metal carbonyls. The ability of metal carbonyls to produce Pt octahedra also follows this trend, implying the existence of zero valent metal is important in the synthesis of Pt octahedra rather than that of metal ions. Moreover, the desired process is mass-transfer-limited. The high quality Pt octahedra are obtained under a mild stirring which is enough for the heat transfer; when the vigorous stirring is employed, only cubes and worm-like product are generated (Figure 2.41a). This observation indicates that the growth process is suppressed and that after formation of cubes the remaining Pt precursor forms the product which is usually seen in the decomposition of $Pt(acac)_2$ in benzyl ether, implying that the selective deposition of Mn is interrupted. Herein, we can conclude that the $Mn_2(CO)_{10}$ has a bi-functional role in the synthesis of Pt octahedra, in which CO provides the reducing power and Mn acts as a shape directing agent.

In the synthesis of Pt cuboctahedra (Figure 2.36a), the amount of $Mn_2(CO)_{10}$ used is 5 times of that used in the synthesis of octahedra. When the proposed growth proceeds, the Pt precursor depletes before the complete formation to octahedra, thus, the final product is in between of cubes and octahedra. Moreover, the size of cuboctahedra is smaller than that of octahedra, because the high concentration of CO and Mn produces more Pt nuclei so that each nanocrystal has less mass of Pt. Due to this reason, when the Mn/Pt ratio is further increased to 10 times of that in synthesis of octahedra, the size of produced Pt nanocrystals is so small that the faceted crystal looks like a sphere (Figure 2.36b).

In summary, we have developed a synthetic system using $Mn_2(CO)_{10}$ to control the shape of Pt nanocrystals very precisely. In this system, high quality Pt nanocrystals are synthesized in various morphologies, including octahedra, icosahedra, cubes, truncated cubes, cuboctahedra, spheres, tetrapods, star-shape octapods, multi-pods, and hyper-branched structure. Among these morphologies, we demonstrate the first synthesis of Pt icosahedra. In addition, we first demonstrate the range of morphologies of high quality Pt nanocrystal, which can be made at the level of material supply. The Pt nanocrystals selectively exposing {111} or {100} facets enable many interesting experiments for catalysis, such as the investigation of structure sensitive reactions. The branched nanostructures could also be useful for applications, such as surface enhanced Raman spectroscopy (SERS). These highly controlled Pt nanocrystals are also perfect building blocks to study the self-assembly process at nano-scale. This research will greatly contribute to the nano-science and engineering, as the synthesis of high quality materials is always the core of the nano-science.

A special purification method --- self-cleaning of superlattice

In order to isolate high quality nanocrystal samples, especially when mixtures of morphologies are present, a purification process is necessary. The most popular method of purification is size selective precipitation (SSP). In SSP, adding non-solvent to a mixture of nanocrystals selectively fractionates the products in terms of size and shape. SSP is particularly effective when the size or shape of different components in the mixture is distinctively different. For example, as described above, it is very easy to separate icosahedra from cubes or truncated cubes, or to remove very small particles (less than 2 nm) from a sample of spherical Pt nanocrystals. However, SSP is not as useful if the components are too similar to each other, both in size and shape (e.g. separate 8nm truncated cubes from 9nm cubes). Moreover, it is difficult to substantially improve the size/shape distribution by SSP, if the distribution is already narrow (i.e. σ = 5%). We have noticed that the nanocrystals, which self-assemble into a single crystal domain of superlattice, are highly uniform both in size and shape. The nanocrystals which are not the same in size and shape as those in superlattice are excluded from the self-assembly of superlattice (Figure 2.46-2.48).

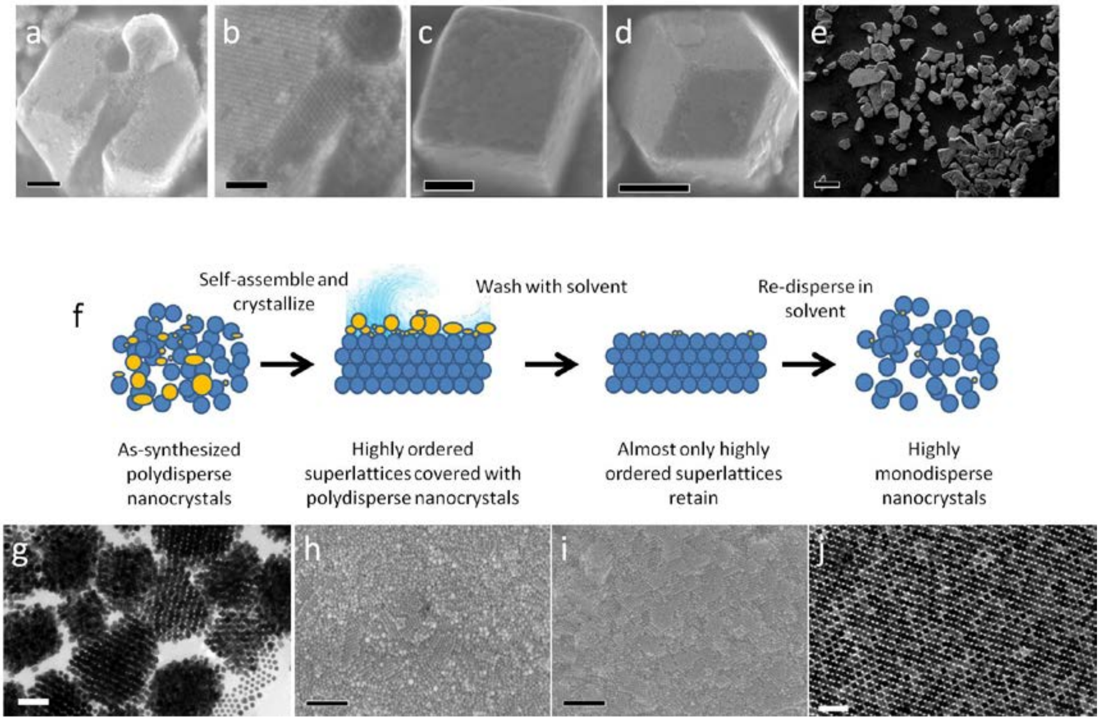

Figure 2.45. a-e) SEM images of super-crystals consisted of Pt nanocrystals. a, b) In side of a super-crystal, the building blocks (Pt octahedra) are highly uniform both in size and shape. c) Pt nanocubes grow into a cubic super-cystal. d) Pt octahedra grow into a rhombic dodecahedral super-crystal. e) Poly-oriented super-crystals crystallized from Pt octahedra. f) the illustration of the purification method using the self-cleaning process during the formation of superlattices (super-crystals). g, j) TEM and h, i) SEM images corresponding to each step shown in f): g) as-synthesized Pt octahedra; h) the surface of the super-crystal covered with poly-disperse Pt nanocrystals; i) the ordered surface of the super-crystal consisted of monodisperse Pt octahedra, after washing with hexane; j) the highly monodisperse Pt octahedra are obtained by dissolving and re-dispersing the super-crystals in hexane, after the purification. Scale bars: a, d, h, i) 200 nm, b) 100 nm, c) 500 nm, e) 200 µm, g, j) 50 nm.

Recognition of this phenomenon has allowed us to utilize this “self-cleaning” property of nanocrystals and the process of self-assembly to purify samples of nanocrystals (Figure 2.45). In brief, the solution of nanocrystals is allowed to dry out in very slow rate (in weeks). Then, the solid formed in this drying process is transferred onto a piece of filter paper, and is washed using a solvent such as hexane. Because the defected nanocrystals are excluded from the formation of super-crystals, they dissolve first and are absorbed by the filter paper. The remaining solid is then collected and re-dissolved in hexane to form a solution with higher purity, in terms of shape and size.

For instance, the as-synthesized product of Pt octahedra usually contains roughly 70-80% nanocrystals which are octahedral; after the unique purification process, the percentage of octahedra is close to 100%. Thus, this method maximizes maximizes the proportion of (111) surface on the nanocrystals, which are intended to be used as (111) model in the study of catalysis. Here, we have demonstrated the synthesis of Pt nanocrystals with various morphologies which have the highest quality up-to-date, and are very suitable for study of structure sensitive catalytic reactions.

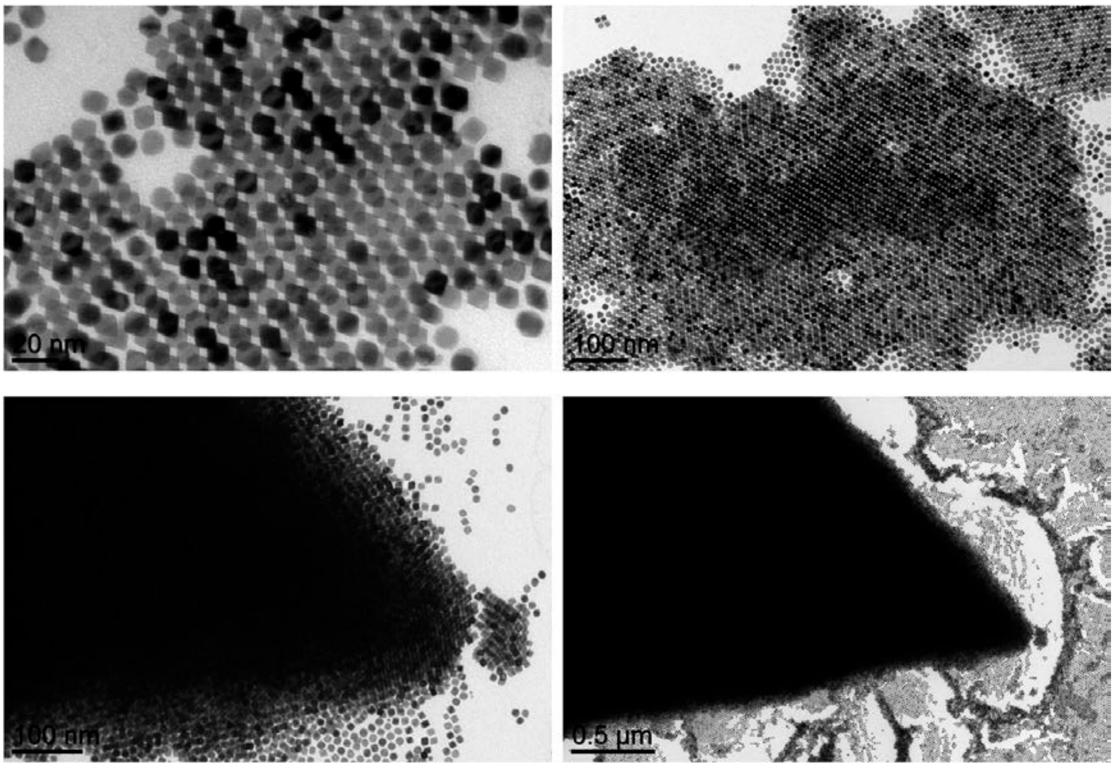

Figure 2.46. TEM images of Pt octahedra show that the self-assembly has an ability of self-cleaning that can exclude the poly-disperse portion of Pt nanocrystals from the formation of superlattice.

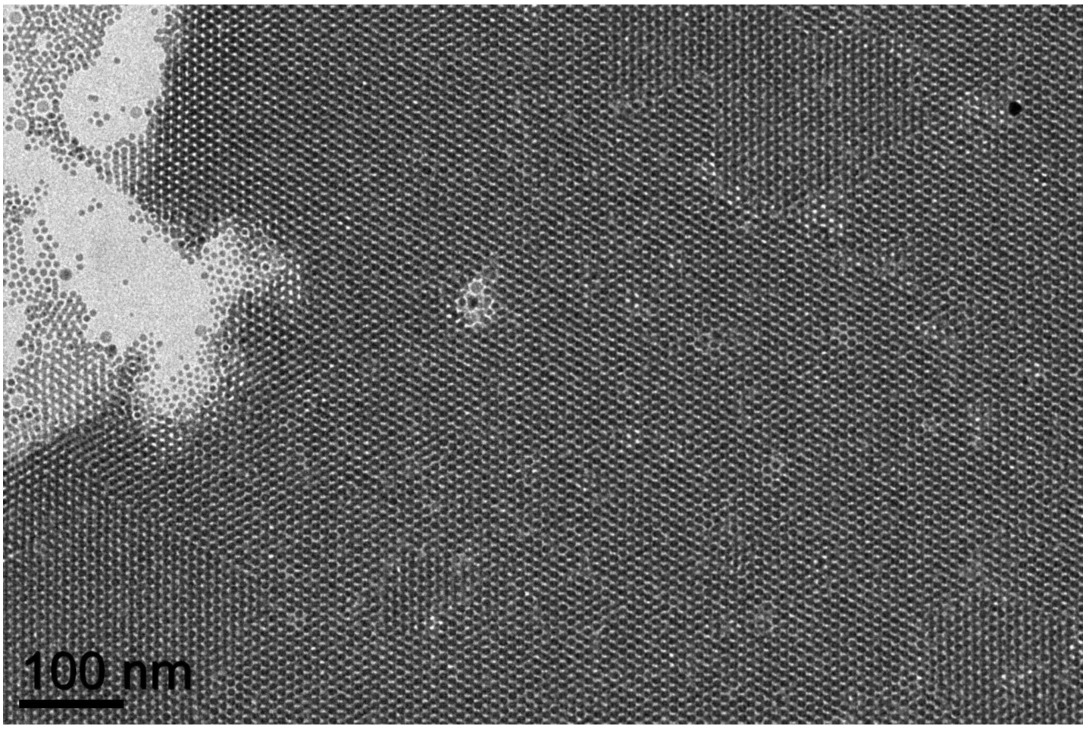

Figure 2.47. TEM image of Pd nanocrystal show that the self-assembly has an ability of self-cleaning that can exclude the poly-disperse portion of Pd nanocrystals from the formation of superlattice.

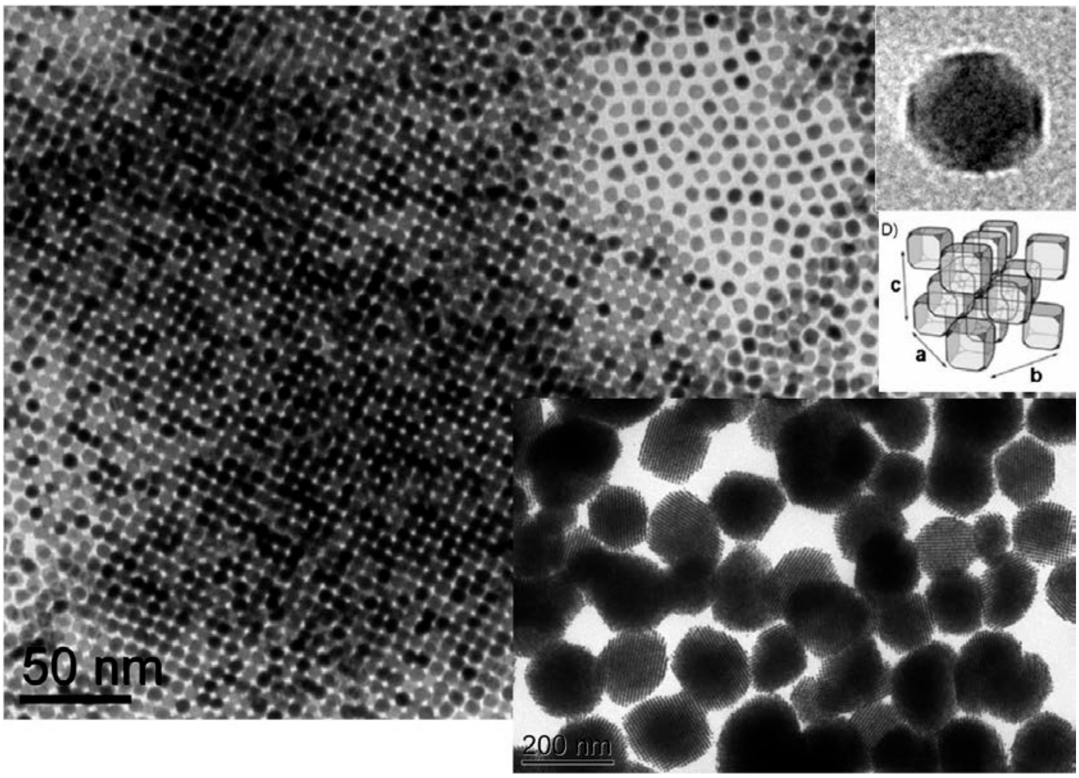

Figure 2.48. TEM images of Pt truncated cubes show that the self-assembly has an ability of self-cleaning that can exclude the poly-disperse portion of Pt nanocrystals from the formation of superlattice.

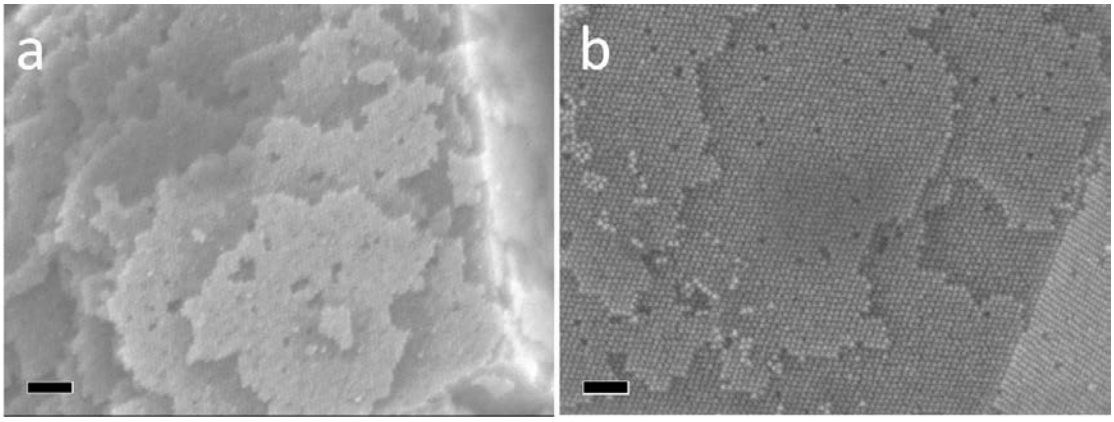

Figure 2.49. SEM images of super-crystals formed by self-assembly of a) Pt nanocubes and b) Pt octaherda. Scale bars: 100 nm.

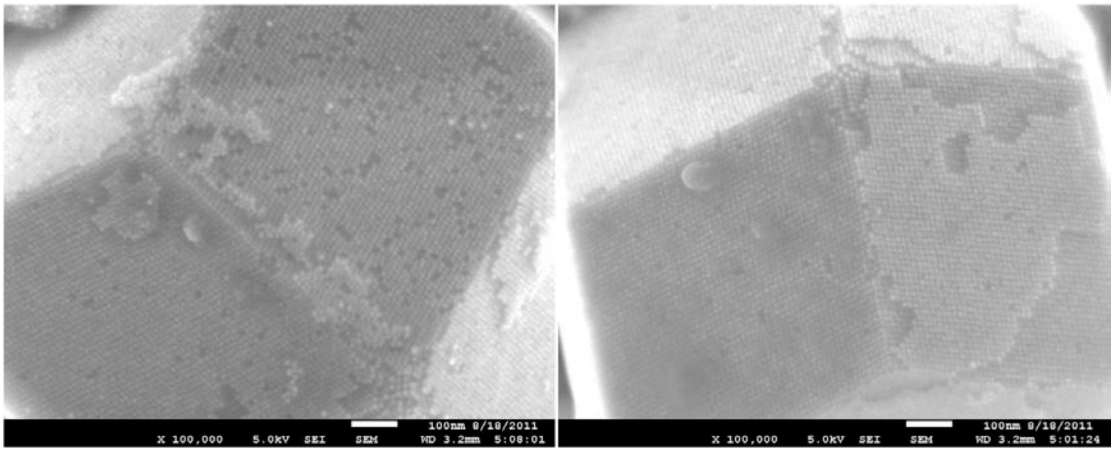

Figure 2.50. SEM images of super-crystals formed by self-assembly of Pt octaherda.

2.4 Binary alloy

2.4.1 Pt-Mn

Manganese oxides are widely used as ORR catalysts in alkaline environments, but the acidic environment in PEM fuel cells limits the application of manganese oxides[69]. Alloying Mn and Pt may provide a less expensive, more active catalyst in acidic media. For instance, it has been reported that PtMn/C had better ORR activity than Pt/C[70]. Recent reports have also suggested that the NC shape has a dramatic catalytic effect[6,8,60,71]. Markovic et al. have reported that the ORR activity of Pt is higher on the (100) faces than on the (111) faces in H_2SO_4[72]. Moreover, a cubic shape exposing (100) surfaces has been found to benefit a number of catalytic systems[60,73]. Through the low-temperature solution-phase synthesis, I have prepared Mn-Pt NCs and have studied their ORR and small organic-molecule oxidation activities (see Chapter 3.2 and 3.3). The synthesis of Mn-Pt NCs using Pt(acac)2 and either manganese acetylacetonate [$Mn(acac)_2$] or dimanganese decacarbonyl [$Mn_2(CO)_{10}$] as precursor has been reported previously[74,75]. My syntheses are described below.

Preparation of $Mn_2(CO)_{10}$ Stock solution

The 0.01M $Mn_2(CO)_{10}$ stock solution is prepared by dissolving 0.078 g $Mn_2(CO)_{10}$ solid in 20 mL benzyl ether (or phenyl ether), and then keeping the solution out of light. (The stock solution is light sensitive. The color of stock solution changes from bright yellow to dark yellow if it has been exposed to light for long time.)

Synthesis of cubic Mn-Pt nanocrystals (nanocubes)

Under a nitrogen flow, 0.04 g $Pt(acac)_2$ is dissolved in 5ml benzyl ether, 3.68 mL oleylamine and 0.63 mL oleic acid. The formed solution is dipped into oil bath which is preheated to 200-210°C. Once the temperature of solution in the reaction flask reaches 160°C, 3.5 mL of $Mn_2(CO)_{10}$ stock solution is injected into reaction flask.

The temperature is kept at 200-205°C for 30 minutes after the injection of $Mn_2(CO)_{10}$ stock solution. The solution is cooled down (quenched) by adding cold solvent. The product is precipitated by ethanol, and then re-dispersed in hexane.

Synthesis of spherical Mn-Pt nanocrystals

Under a nitrogen flow, 0.04 g $Pt(acac)_2$ is dissolved in 5ml benzyl ether, 3.68 mL oleylamine and 0.63 mL oleic acid. Before the formed solution is dipped into oil bath which is preheated to 200-210°C, 3.5 mL of $Mn_2(CO)_{10}$ stock solution is injected into reaction flask. The solution turns to bright orange color upon the injection of $Mn_2(CO)_{10}$ stock solution. The temperature is kept at 200-205°C for 30 minutes after dipping into oil bath. The solution is cooled down to room temperature. The product is precipitated by ethanol, and then re-dispersed in hexane.

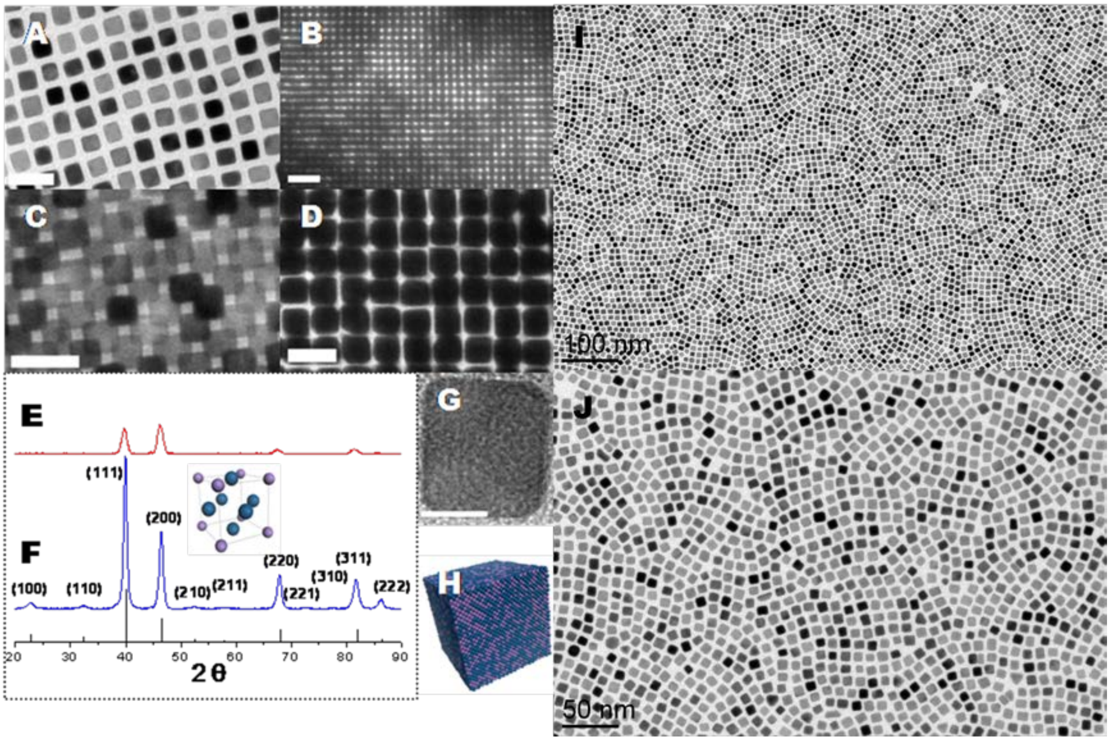

Figure 2.51. (A-D) TEM images of (A) as-synthesized Mn-Pt nanocubes, (B) a large area of self-assembly, and (C, D) self-assembled Mn-Pt nanocubes. (E, F) XRD patterns of UV-ozone-treated Mn-Pt nanocubes (E) before and (F) after annealing at 600°C. The inset shows the $MnPt_3$ unit cell. (G) High-resolution TEM image of Mn-Pt nanocubes. (H) Model representing as-synthesized Mn-Pt nanocubes with a disordered structure. (I, J) TEM images of Mn-Pt nanocubes for large area. Scale bars: 20 nm for (A, C, D); 100 nm for (I); 50 nm for (B, J); 5 nm for (G). Purple and blue balls represent Mn

and Pt atoms, respectively. The annealed sample in (F) confirmed the general stoichiometry of Mn/Pt = 1:3.

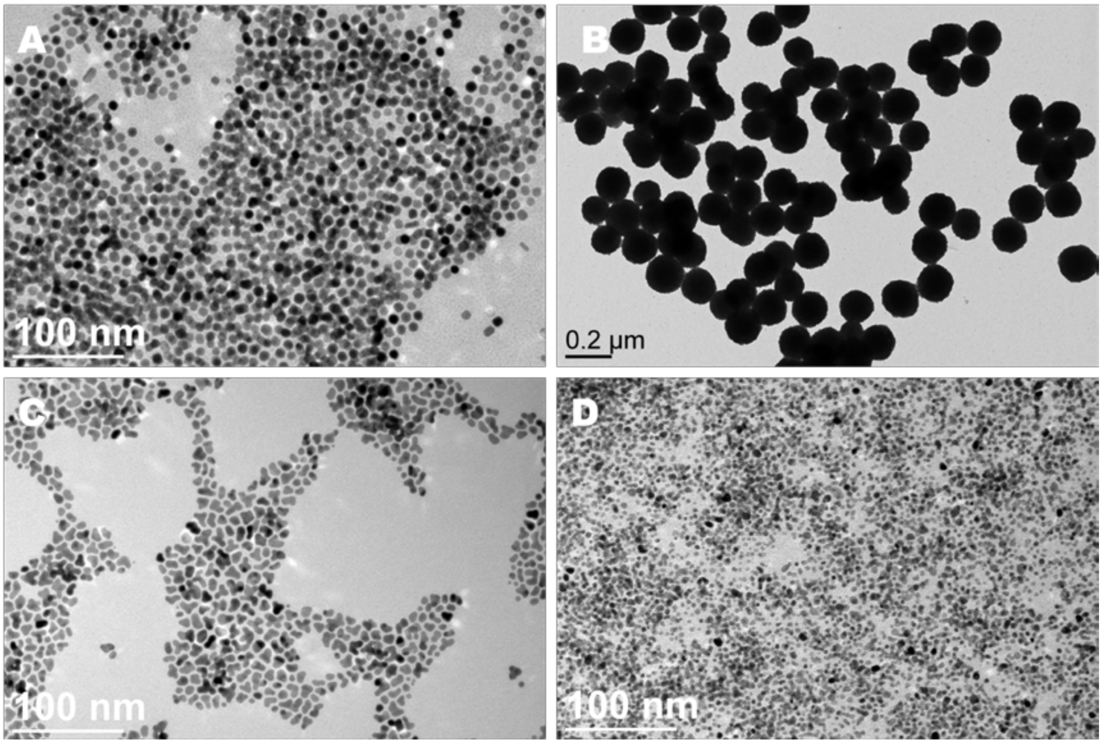

Figure 2.52. TEM images of (A) of spherical Mn-Pt nanocrystals, (B) Mn-Pt nanoparticle synthesized in absence of both oleic acid and oleylamine, Mn-Pt nanocrystals synthesized in absence of (C) oleylamine, or (D) oleic acid

TEM images of the as-synthesized nanocubes are shown in Figure 2.51A, I, and J; images of self-assembled nanocubes are shown in Figure 2.51B-D. The average edge length of the Mn-Pt nanocubes was 7.7 nm (σ = 6.0%). The combination of oleic acid and oleylamine is essential to obtain particles of uniform size and shape (Figures 2.52). The as-synthesized nanocubes are chemically disordered, with Mn and Pt in an fcc unit cell of the *A*1 phase. After the nanocubes are annealed at 600°C for 30 min, the nanocube structure is converted from the A_1 phase to the ordered L_{12} phase ($AuCu_3$ structure; Figure 2.51F). The annealed nanocubes are identified as $MnPt_3$ (JCPDS 65-3260) by XRD. Manganese carbide is identified as an impurity in the annealed sample; it is presumably formed from carbonized ligands and traces of excess manganese. The impurity peaks can be removed by UV-ozone treatment (Figure 2.56). In the XRD patterns, the enhanced (200) peak intensities come from the (100) textured assembly as a result of the preferred orientation of the cubic NCs. The Mn/Pt ratio, which is close to 1:3, is confirmed by both EDX spectroscopy (Mn/Pt = 22:78; Figure 2.53) and ICP-OES (Mn/Pt = 27:73). Interestingly, the Mn:Pt ratio remains at 1:3 or less, regardless of whether excess Mn precursor is added. This 1:3 Mn/Pt ratio is consistent with the published result of Lee et al. Spherical Mn-Pt NCs (Figure 2.52A), which are actually polyhedral NCs enclosed by (100) and (111) facets, are synthesized by including $Mn_2(CO)_{10}$ as a starting material instead of utilizing hot injection at 160°C. This synthesis of spherical Mn-Pt NCs is similar to those reported by Lee[75] and Ono[74].

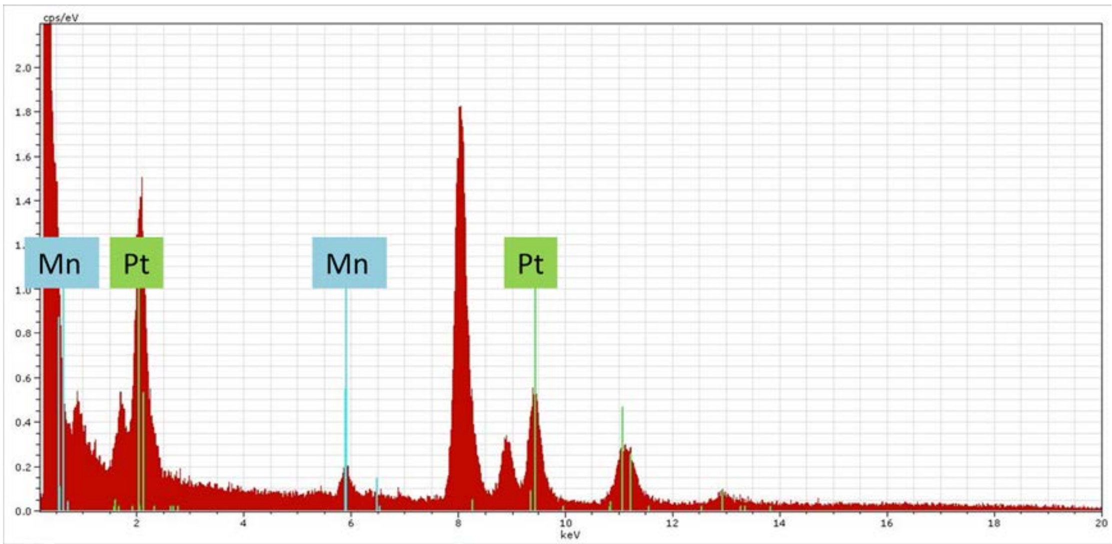

Figure 2.53. EDX spectrum of Mn-Pt nanocubes

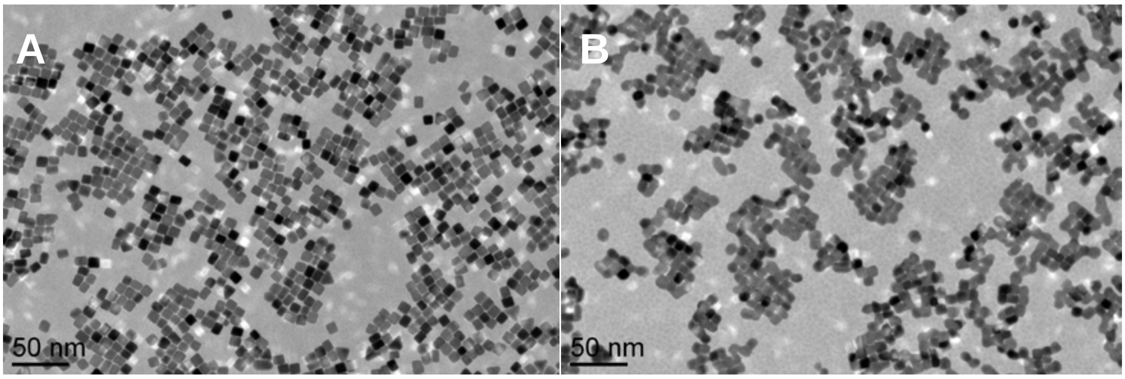

Figure 2.54. TEM images of UV/ozone treated Mn-Pt nanocubes (A) before and (B) after exposure under TEM electron beam for 3 minutes

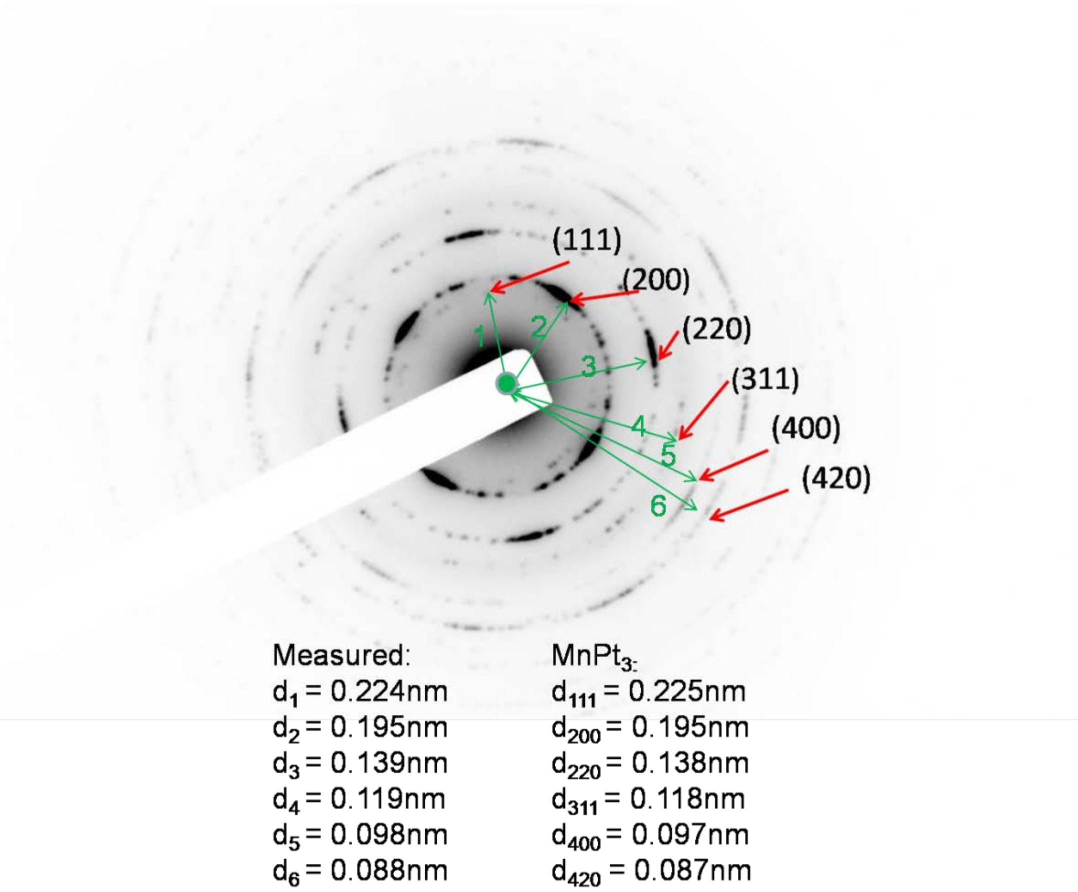

Measured:	$MnPt_3$:
d_1 = 0.224nm	d_{111} = 0.225nm
d_2 = 0.195nm	d_{200} = 0.195nm
d_3 = 0.139nm	d_{220} = 0.138nm
d_4 = 0.119nm	d_{311} = 0.118nm
d_5 = 0.098nm	d_{400} = 0.097nm
d_6 = 0.088nm	d_{420} = 0.087nm

Figure 2.55. SAED pattern (negative) of Mn-Pt nanocubes

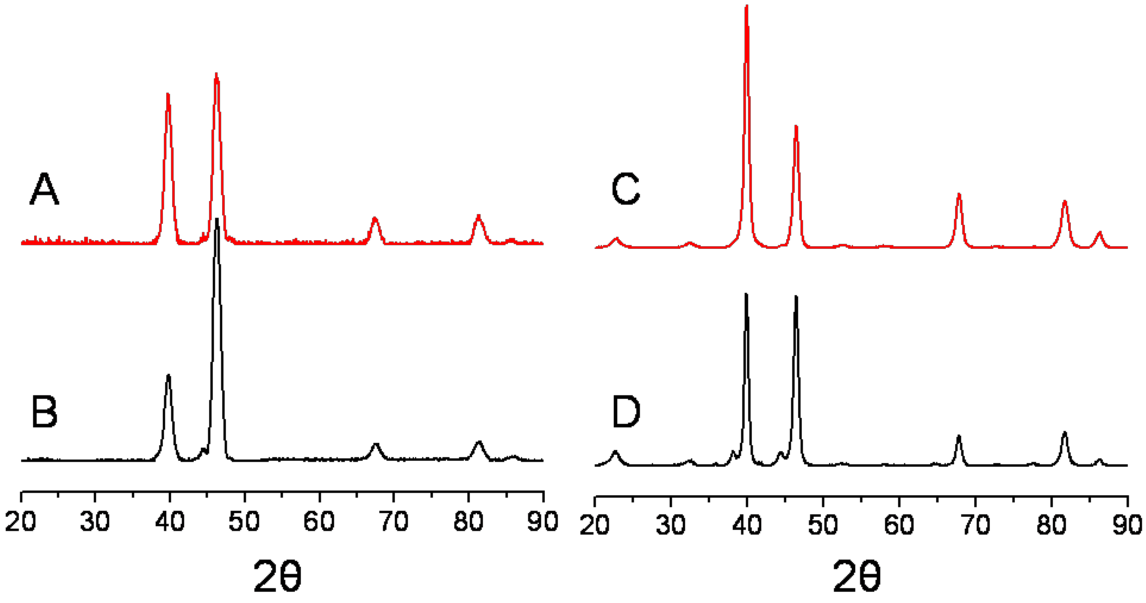

Figure 2.56. XRD patterns of as-synthesized Mn-Pt nanocubes (A) after and (B) before UV-ozone treatment, and XRD patterns of annealed Mn-Pt nanocubes (C) after and (D) before UV-ozone treatment.

2.4.3 Pt-M (M=Fe, Co, Ni)

The synthesis of Pt-M (M = Fe, Co, Ni) usually employs the co-reduction or simultaneous decomposition of two metal precursors in the presence of capping agents (ligands, or stabilizers), where oleic acid and oleylamine are most frequently used. By manipulating the reaction parameters, different size or composition may be obtained.

Pt-Fe

Pt-Fe can be prepared in a FePt or a Pt_3Fe stoichiometry. After annealing, the Pt-Fe alloy nanocrystals in these two stoichiometries can be transformed into an fct FePt or an fcc Pt_3Fe intermetallic phase, respectively. Intermetallic FePt has distinctive magnetic properties, so it is attractive for many related applications such as data recording and storage[3]. FePt nanocrystals are produced according to the recipe reported by Sun et al.[3], and Pt_3Fe nanocrystals are synthesized through the decomposition of $Pt(acac)_2$ and $Fe(acac)_3$ simultaneously, as described below:

Synthesis of FePt NCs: 0.197 g $Pt(acac)_2$ and 0.39 g 1,2-hexadecanediol are dissolved in 20 ml dioctylether under N_2 atmosphere, and heated to 100°C. A solution of 157 µl oleic acid, 230 µl oleylamine, and 135 µl $Fe(CO)_5$ is injected into the reaction mixtures at 100°C. The reaction mixture is brought to 295°C and is kept at this temperature to reflux for 30-60 min. The reaction mixture is cooled and purified by hexane/ethanol. The final products are redispersed in hexane.

Synthesis of Pt_3Fe NCs: 0.0985 g $Pt(acac)_2$ and 0.1765 g $Fe(acac)_3$ are dissolved in 157 µl oleic acid, 230 µl oleylamine, and 10ml benzyl ether under N_2 atmosphere. The reaction mixture is brought to 295°C and is kept at this temperature to reflux for 30-60 min. The reaction mixture is cooled and purified by hexane/ethanol. The final products are redispersed in hexane. The reaction works in the way if it is scaled up by 5 times that produces Pt-Fe nanocrystals at a gram-scale.

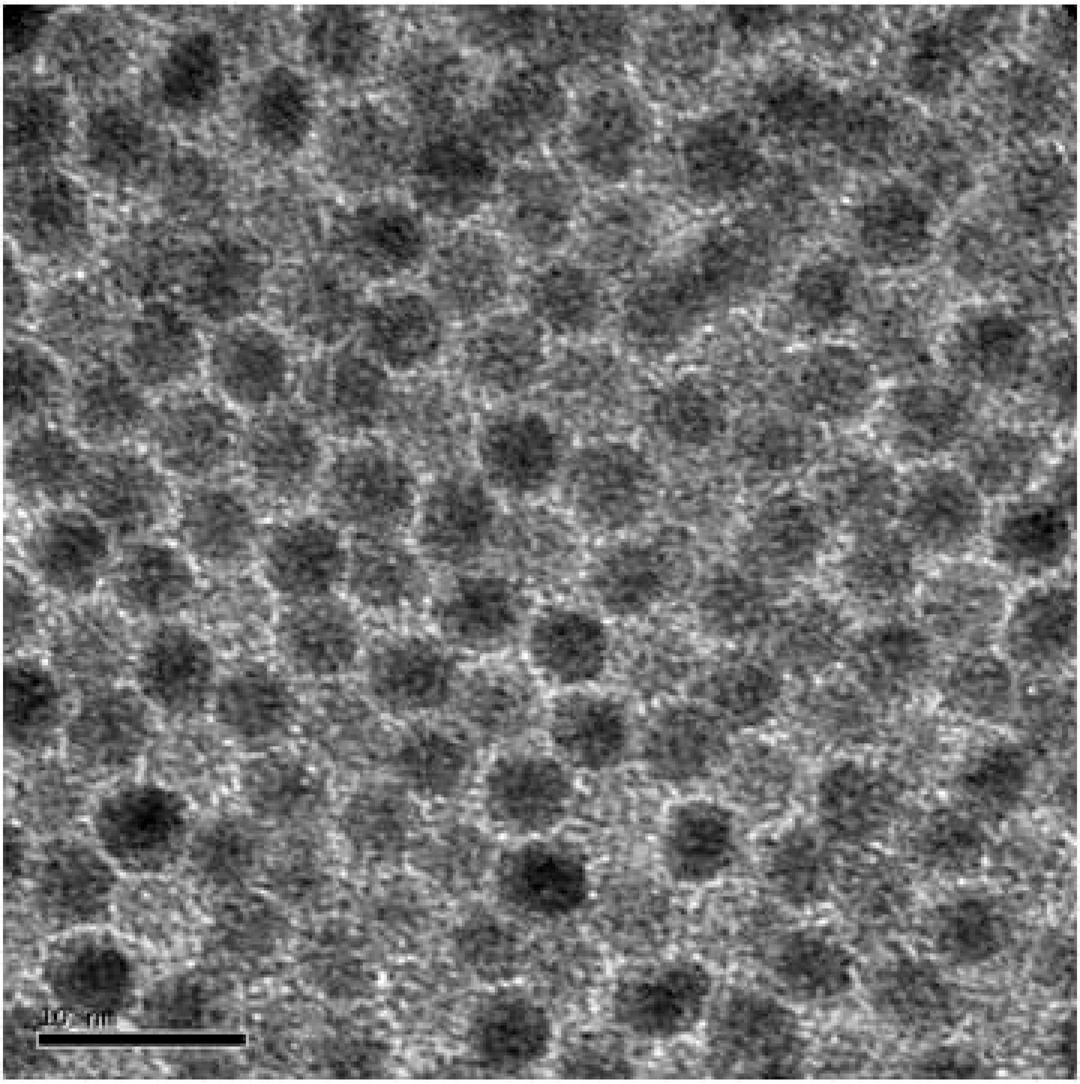

Figure 2.57. TEM image of typical FePt nanocrystals with a size of 4 nm.

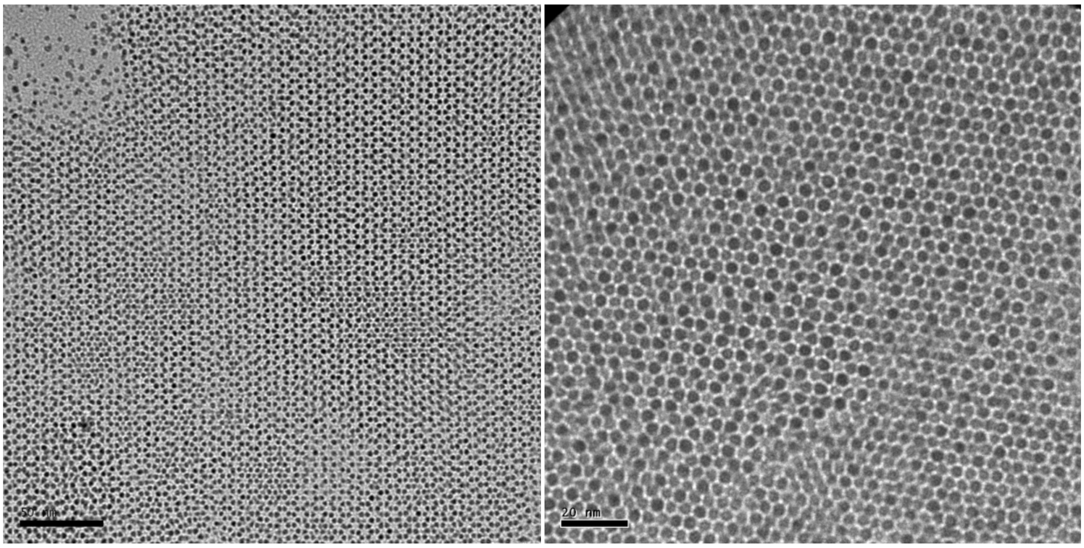

Figure 2.58. TEM images of typical Pt-Fe (Pt$_3$Fe) nanocrystals.
Scale bars: left) 50 nm, right) 20nm

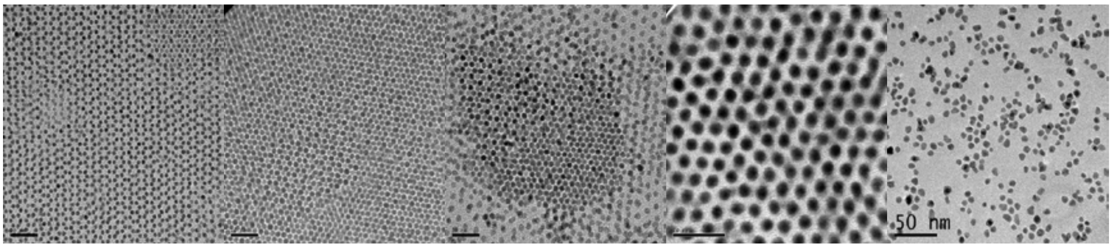

Figure 2.59. Size of Pt-Fe nanocrystals is tunable in the range of 3-8 nm.

The typical FePt nanocrystals have a size of 4 nm (Figure 2.47); the size of typical Pt$_3$Fe nanocrystals is 3.5-4 nm (Figure 2.48). The size is tunable in the range of 3-8 nm, by changing the metal to ligand ratio (Figure 2.49). The higher concentration of ligands (oleic acid and oleylamine in these syntheses) yields larger Fe-Pt nanocrystals. For instance, by increasing the amount of oleic acid and oleylamine by 10 times, the 8 nm Fe-Pt nanocrystals can be synthesized.

By using dodecane to substitute benzyl ether as the solvent, the ultra-small Fe-Pt nanocrystals with a size of 1-1.5 nm are synthesized, as shown in Figure 2.60. The magnetic properties of ultra-small Fe-Pt nanocrystals are measured to have an H$_c$ of

360 O_e and a T_b of 44 K (Figure 2.61). The magnetic properties are not particularly interesting for applications such as data storage. However, due to the ultra-small size which is close to 1 nm, these small Fe-Pt nanocrystals may find application in catalysis.

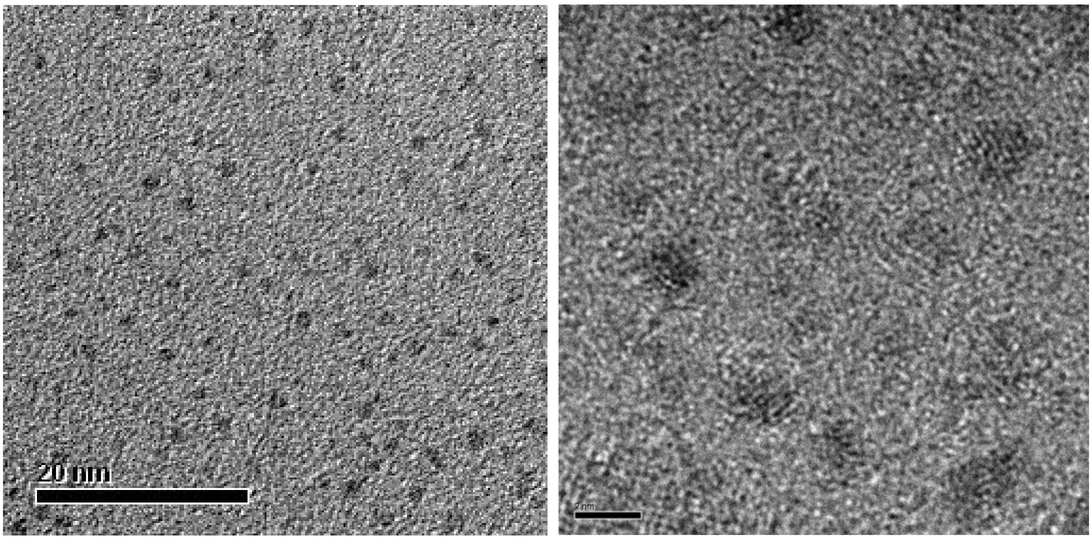

Figure 2.60. TEM and HRTEM images of ultra-small Fe-Pt nanocrystals synthesized by using dodecane as solvent. Scale bars: left) 20 nm, right) 2 nm.

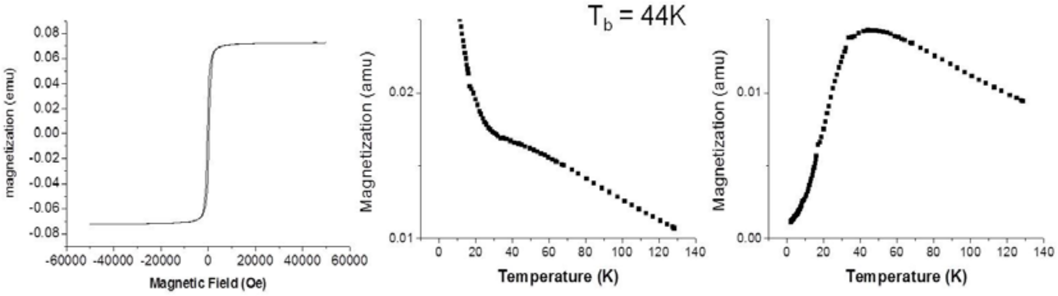

Figure 2.61. Magnetic properties of ultra-small Fe-Pt nanocrystals.

Pt-Co

Pt-Co nanocrystals synthesized in this thesis usually have a stoichiometry of Pt_3Co. The Pt-Co nanocrystals can be synthesized by simultaneous decomposition of $Pt(acac)_2$ and $Co2(CO)_8$, as reported in literature[76]. One alternative using $Co(acac)_2$ is also used to produce Pt-Co nanocrystals shown in Figure 2.62.

Synthesis of Pt_3Co NCs: 0.0985 g $Pt(acac)_2$ and 0.1286 g $Co(acac)_2$ are dissolved in 157 µl oleic acid, 230 µl oleylamine, and 10ml benzyl ether under N_2 atmosphere. The reaction mixture is brought to 295°C and is kept at this temperature to reflux for 30-60 min. The reaction mixture is cooled and purified by hexane/ethanol. The final products are redispersed in hexane. The reaction works in the way if it is scaled up by 5 times that produces Pt-Fe nanocrystals at a gram-scale.

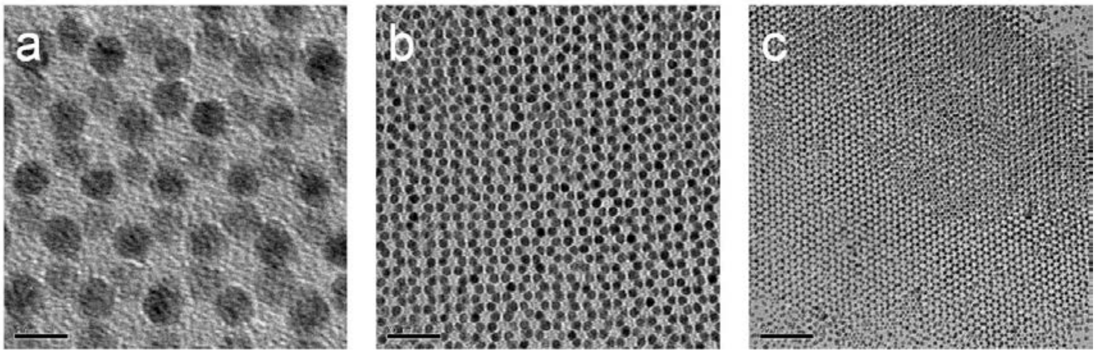

Figure 2.62. TEM images of typical Pt_3Co nanocrystals. Scale bars: a) 5 nm, b) 20 nm, c) 50nm.

Pt-Ni

Pt-Ni nanocrystals are synthesized as reported in literature[77].

2.4.4 Pt-Cu

In previous reports, Pt-Cu alloy nanocrystals have been synthesized in various morphologies, including nanocubes[68,78] and nanorods[79], and they exhibit excellent catalytic properties toward CO oxidation, methanol and formic acid electrooxidation. With modified recipes, we have synthesized spherical Pt-Cu nanocrystals and nanowires. As shown in Figure 2.63, Pt-Cu nanocrystals are synthesized by decomposition or reduction of $Pt(acac)_2$ and $Cu(acac)_2$, as described below.

Synthesis of Pt-Cu NCs by thermal decomposition: 0.08 g $Pt(acac)_2$ and 0.052 g $Cu(acac)_2$ are dissolved in 1.25 ml oleic acid, 7.36 ml oleylamine, and 10ml benzyl ether under N_2 atmosphere. The reaction mixture is brought to 295°C and is kept at this temperature to reflux for 30 min. The reaction mixture is cooled and purified by hexane/ethanol. The final products are redispersed in hexane.

Synthesis of Pt-Cu NCs using TBAB as reducing agent: 0.08 g $Pt(acac)_2$ and 0.052 g $Cu(acac)_2$ are dissolved in 1.25 ml oleic acid, 7.36 ml oleylamine, and 10ml benzyl ether under N_2 atmosphere. The reaction mixture is brought to 220°C and 2 mmol TBAB (*tert*-butylamine-borane) is injected into reaction mixture at this temperature. Then the reaction is brought to 300°C to reflux for 30 min. The reaction mixture is cooled and purified by hexane/ethanol. The final products are redispersed in hexane.

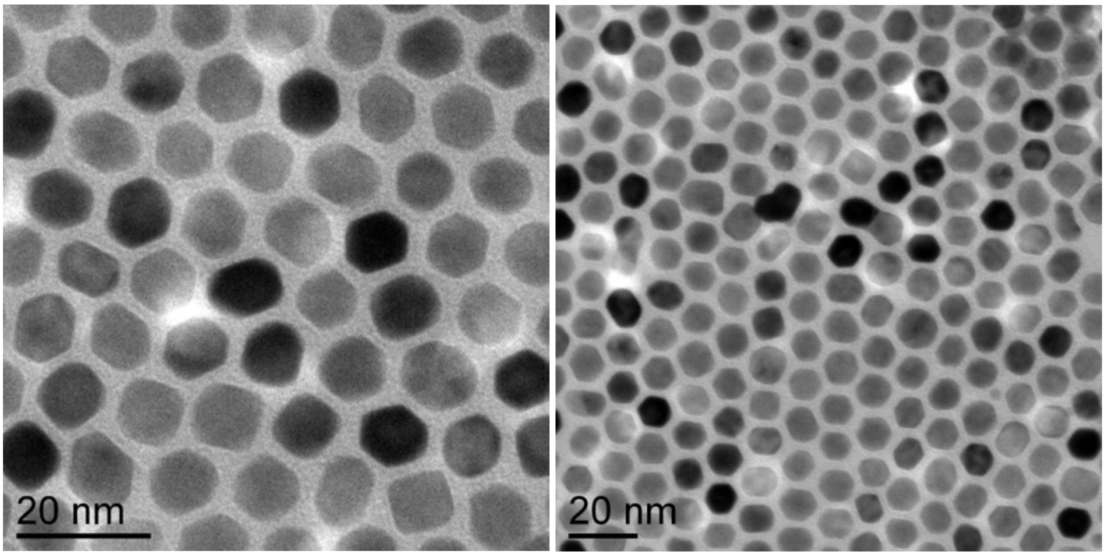

Figure 2.63. TEM images of 9 nm Pt-Cu nanocrystals synthesized by thermal decomposition.

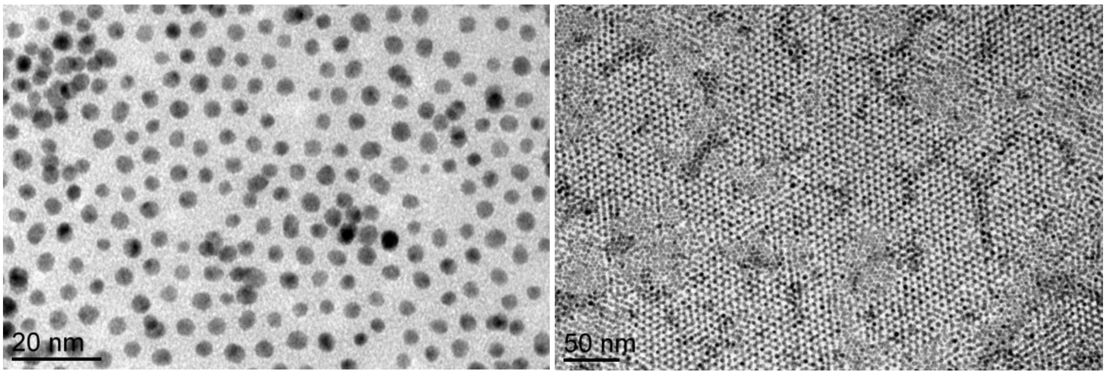

Figure 2.64. TEM images of 4 nm Pt-Cu nanocrystals synthesized using TBAB as reducing agent.

As shown in Figure 2.63, the Cu-Pt nanocrystals synthesized by the thermal decomposition have a size of 9 nm; while the Cu-Pt nanocrystals produced through TBAB reduction show a size of about 4 nm, as shown in Figure 2.64. Some nanowires have been observed in the synthesis of Cu-Pt nanocrystals by thermal decomposition. Based on this finding, we have optimized the reaction to produce Cu-Pt nanowires. It is found that at a reduced temperature, the ratio of nanowires to particles can be increased, and a maximized yield of nanowires can be achieved at the temperature of 200-210 °C that is just enough for the decomposition reaction (Figure 2.66). The Cu-

Pt nanowires can be separated from the reaction mixture by centrifuge as the particles remain in the solution after centrifuge. Figure 2.67 shows the purified Cu-Pt nanowires, which have a diameter about 2 nm and a length of several hundred nanometers. As reported previously, we have developed a synthetic method using CO as reducing agent that can accelerate the formation of Au nanowires. We try to use the same way to promote the formation of Cu-Pt nanowires. However, instead of nanowires, the worm-like product which has short length and a branched structure has been made, as shown in Figure 2.65. The yield of such worm-like Cu-Pt nanocrystals is high, suggesting the growth process is so fast that depletes the precursor quickly.

The elemental analysis by ICP-OES reveals that the high temperature thermal decomposition and the TBAB-reduction produce Cu-Pt nanocrystals at a stoichiometry of about 1:1; while the Cu-Pt nanocrystals and nanowires generated at a reduced temperature show a Pt_3Cu stoichiometry. This suggests that the decomposition/reduction of Cu precursor is a slower reaction than that of Pt. At high temperature or under a strong reducing environment, the competition of reduction/decomposition between Cu and Pt is eliminated, so the balanced 1:1 ratio is obtained in the final product. At the boundary condition of the decomposition, the Cu decomposition is the limiting step and a phase of Pt_3Cu is obtained. The Pt-Cu nanocrystals at different stoichiometry are perfect candidate of model materials for some studies of catalysis, and the Cu-Pt nanowires may find their application in electronics.

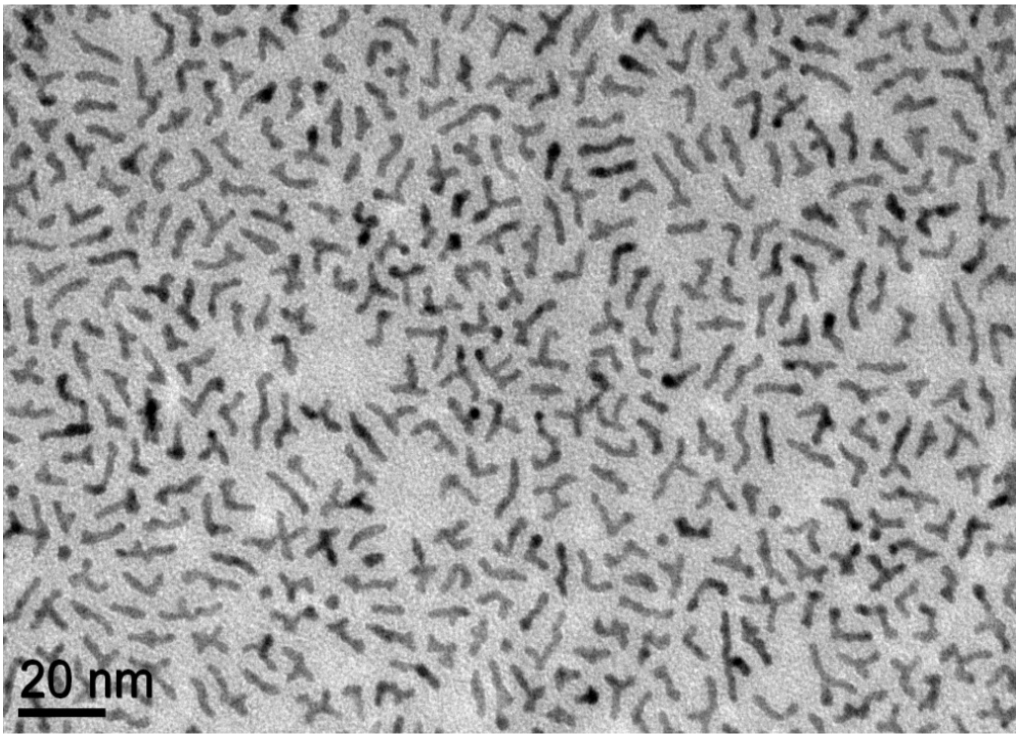

Figure 2.65. TEM images of worm-like Pt-Cu nanocrystals synthesized using CO.

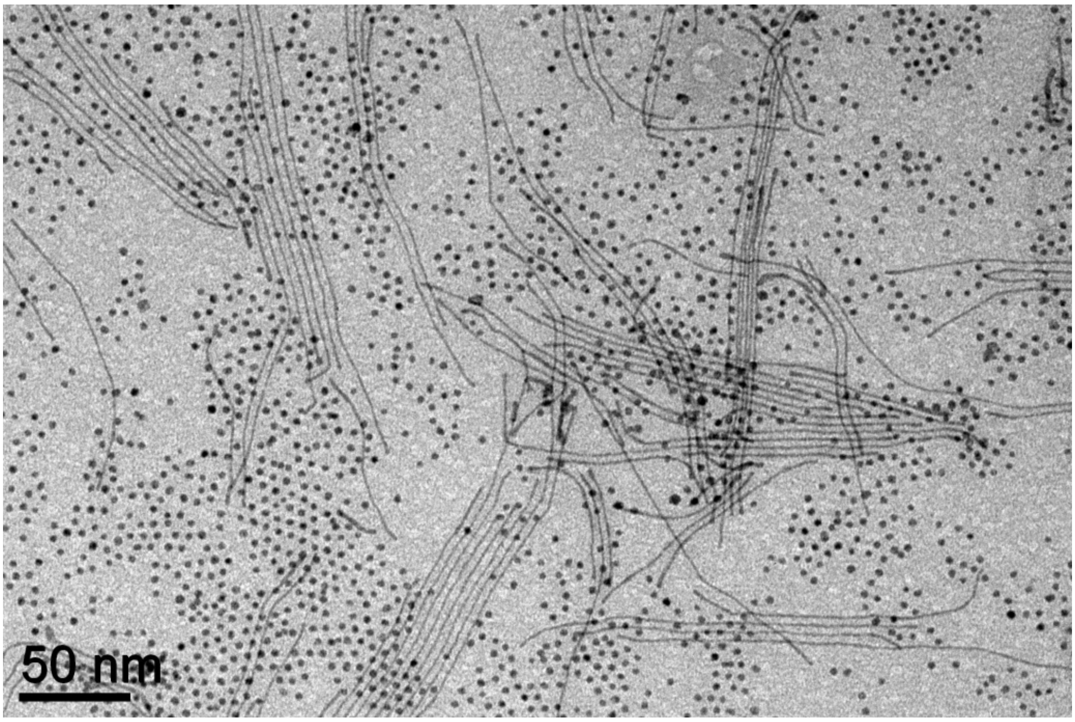

Figure 2.66. Thermal decomposition at 200-210°C produces Cu-Pt nanocrystals and nanowires in a Pt3Cu stoichiometry.

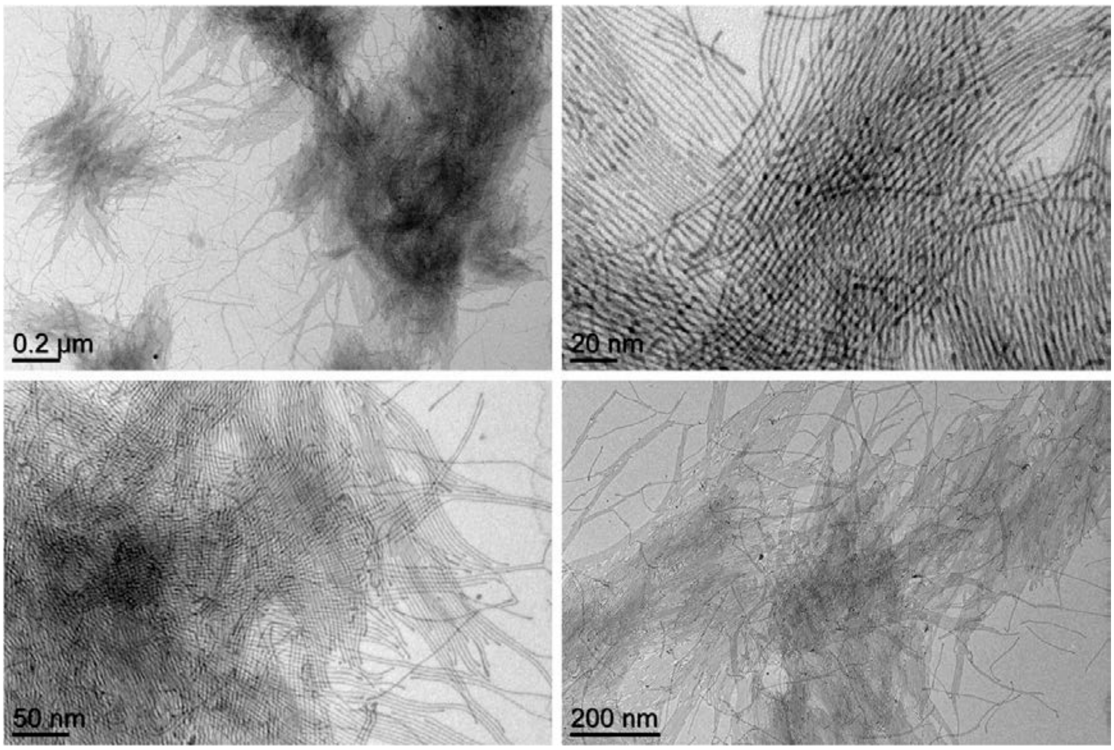

Figure 2.67. Cu-Pt nanowires separated from the mixture shown in Figure 2.66.

2.4.5 Pt-Zn

Recently, intermetallic PtZn particles with high activities toward formic acid and methanol oxidation have been prepared by reaction of Pt in Zn vapor[80]. However, to my knowledge, the direct synthesis of Pt-Zn NCs has not been achieved. I report the first synthesis and shape control of Pt_3Zn NCs. Compared to commercial Pt catalyst, Pt_3Zn NCs show superior poisoning tolerance for methanol oxidation while maintaining comparable activities (see Chapter 3.3).

Synthesis of spherical Pt_3Zn NCs: 0.08g $Pt(acac)_2$ and 0.05g (anhydrous basis) $Zn(acac)_2$ are dissolved in 15ml oleylamine, and 2.5ml oleic acid under N_2 atmosphere. The solution is brought to 350°C and is kept at this temperature for 30-60min. The reaction mixture is cooled and purified by hexane/ethanol. The final products are redispersed in hexane.

Synthesis of cubic Pt_3Zn NCs: 0.08g $Pt(acac)_2$ and 0.05g (anhydrous basis) $Zn(acac)_2$ are dissolved in 7.5ml oleylamine, 1.25ml oleic acid and 5ml benzyl ether under N_2 atmosphere. The solution is brought to 330°C and was kept at this temperature for 30-60min (Caution: strong heating power may cause danger.). The reaction mixture is cooled and purified by hexane/ethanol. The final products are redispersed in hexane.

For the synthesis of spherical Pt_3Zn NCs, $Pt(acac)_2$ and zinc acetylacetonate [$Zn(acac)_2$] are dissolved in oleylamine and oleic acid, which are used as both stabilizer and solvent. Cubic Pt_3Zn NCs (Figure 2.68a-b, 2.69) are made by adding benzyl ether while spherical Pt_3Zn NCs (Figure 2.68c-d) are produced in the absence of benzyl ether. From TEM images shown in Figure 2.68, the size of Pt_3Zn NCs is measured to be 4.5 nm (diameter, σ < 5%) for spherical NCs and 6.9 nm (edge length, σ = 8%) for cubic NCs. The HRTEM images (Figure 2.68a, f, 2.73) indicate both spherical and cubic Pt_3Zn NCs are single crystals with high crystallinity. The HRTEM images also reveal an interplanar distance of about 0.19 nm for a cubic Pt_3Zn NC (corresponding to the lattice spacing of the Pt_3Zn {200} planes), and interplanar distances of about 0.27nm and 0.22 nm for a spherical Pt_3Zn NC (corresponding to the lattice spacing of the Pt_3Zn {110} and {111} planes, respectively). The SAED pattern (Figure 2.69) of the cubic Pt_3Zn NCs confirms the high crystallinity, and indicates the (100) texture of the cubic Pt_3Zn NCs by an enhanced {200} diffraction. The as-synthesized NCs are actually Pt- Zn alloys at a stoichiometry of Pt:Zn = 3:1, which is determined by both EDX and ICP-OES. After annealing at 600°C for 30 min, the alloy phase is converted to the ordered intermetallic phase ($AuCu_3$ structure, JCPDS 65-3257; Figure 2.68e).

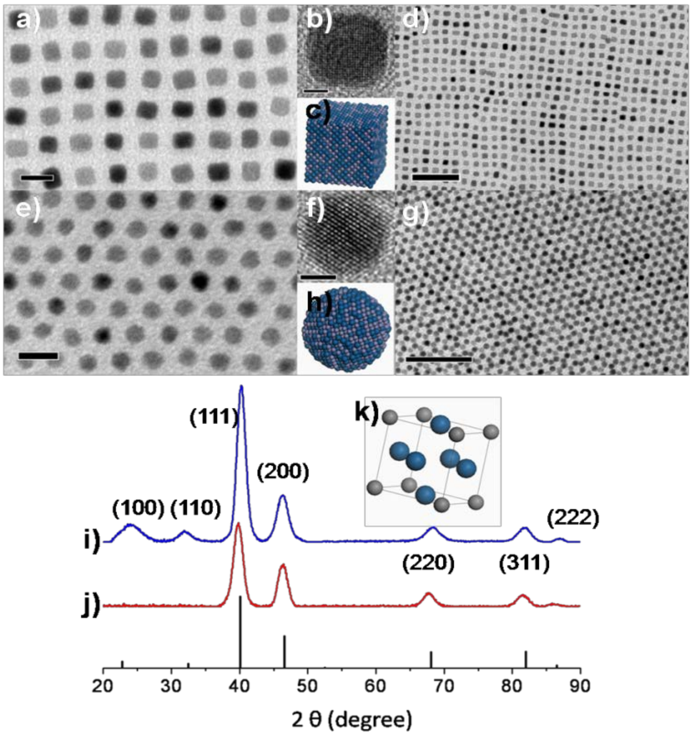

Figure 2.68. a,d) TEM images, b) HRTEM image, and c) model of cubic Pt_3Zn NCs; e,g) TEM images, f) HRTEM image, and h) model spherical Pt_3Zn NCs; XRD patterns of cubic Pt_3Zn NCs j) before and i) after annealing at 600°C; k) unit cell of Pt_3Zn. Scale bars: a,e) 10 nm, d,g) 50 nm, b,f) 2nm. The grey and blue balls represent Zn and Pt atoms, respectively.

Among many reaction parameters, the temperature of synthesis is the most important in dictating the Pt:Zn ratio. As shown in Figure 2.70, syntheses carried out in the range of 300-330°C produce Pt-Zn alloys with less than 25% (mol) Zn and below 270°C, pure Pt NCs are produced. The composition of final alloy products is independent of the Pt:Zn ratio in the reaction precursors, as examples (syntheses carried out at 300°C) shown in Figure 2.70b. The combination of oleic acid and oleylamine is essential to the synthesis of monodisperse Pt-Zn NCs. The ultra-small NCs with an irregular shape are produced in the absence of oleylamine (Figure 2.71A) and NCs with broad size distribution are produced in the absence of oleic acid (Figure 2.72B). The presence of oleylamine and benzyl ether appears to be the key to obtain cubic Pt-Zn NCs. No cubic NCs are found using oleic acid and benzyl ether as ligand and solvent (Figure 2.72C), while a mixture of both spherical and cubic NCs is observed when oleylamine and benzyl ether are used (Figure 2.72D). Notably, using other high boiling point solvents, such as diphenyl ether or 1-octadecene, also produces spherical NCs (Figure 2.71).

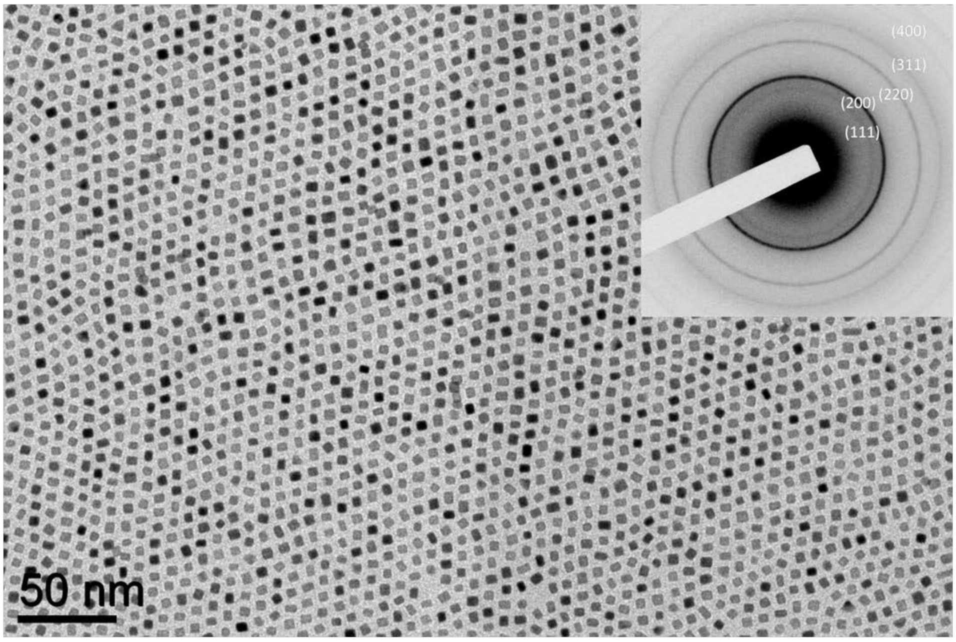

Figure 2.69. TEM image and SAED pattern (inset, negative) of the cubic Pt_3Zn NCs.

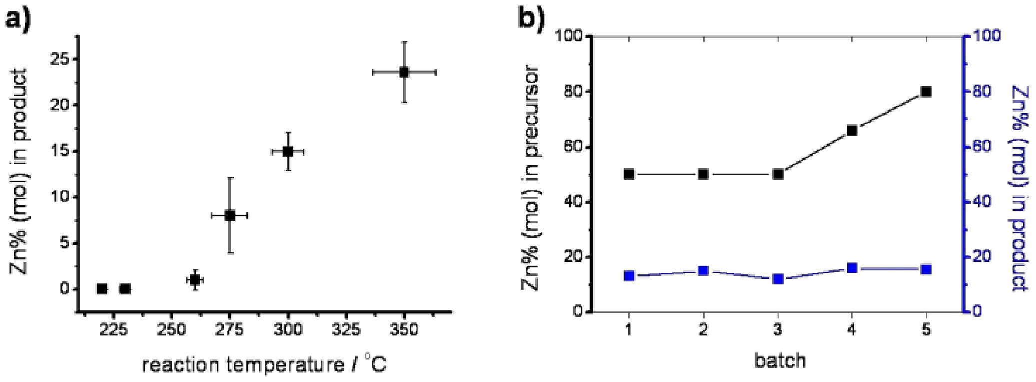

Figure 2.70. The Zn ratio in the product of Pt-Zn NCs is a) dependent on reaction temperature of syntheses, b) independent of the Zn ratio in the precursor.

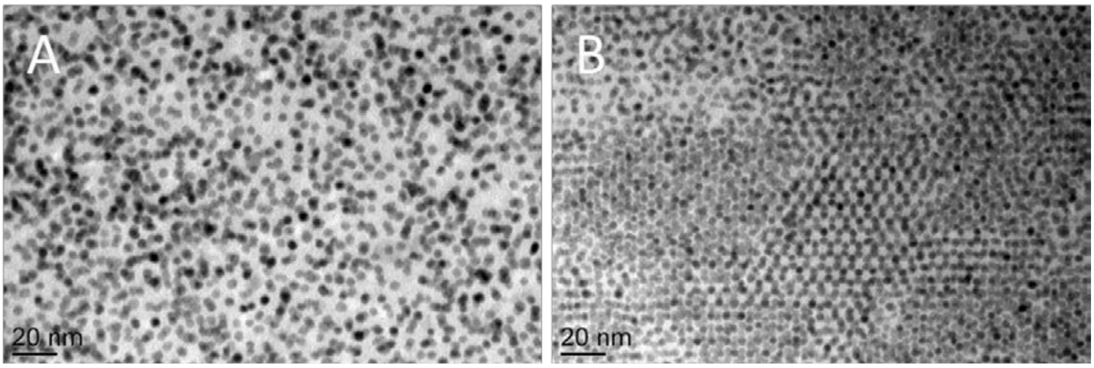

Figure 2.71. Pt-Zn NCs synthesized by using ODE (A) and DPE (B) as co-solvent.

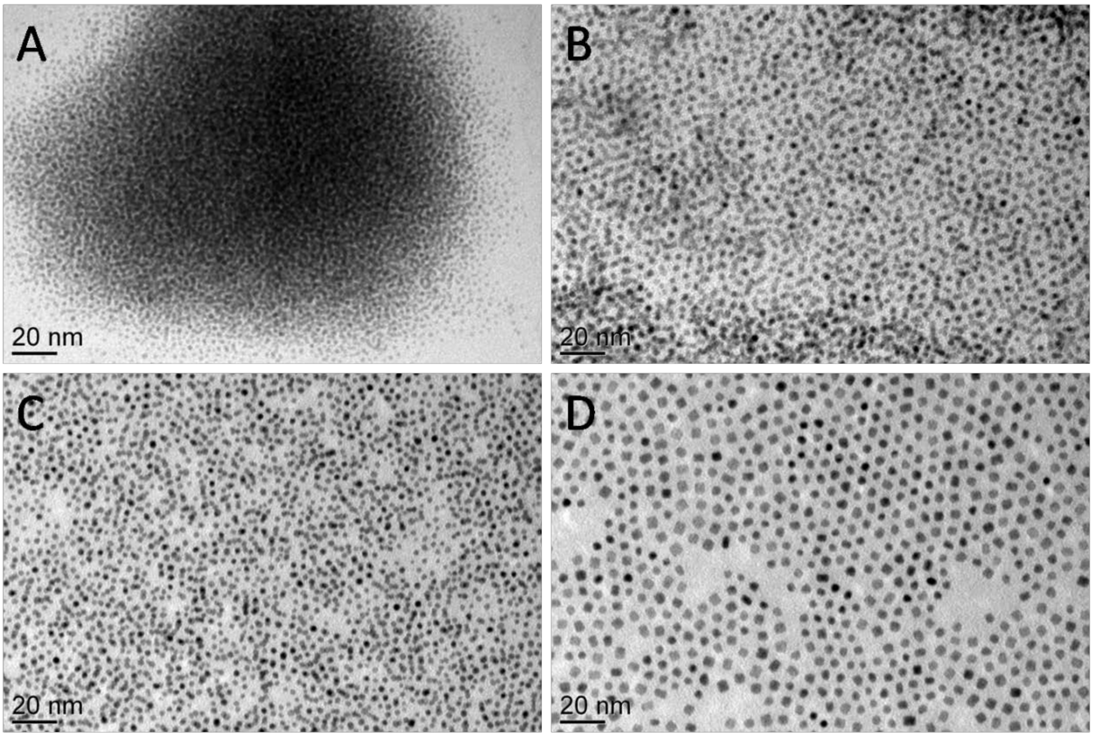

Figure 2.72. NCs synthesized in (A) oleic acid only, (B) oleylamine only, (C) oleic acid and benzyl ether, (D) oleylamine and benzyl ether.

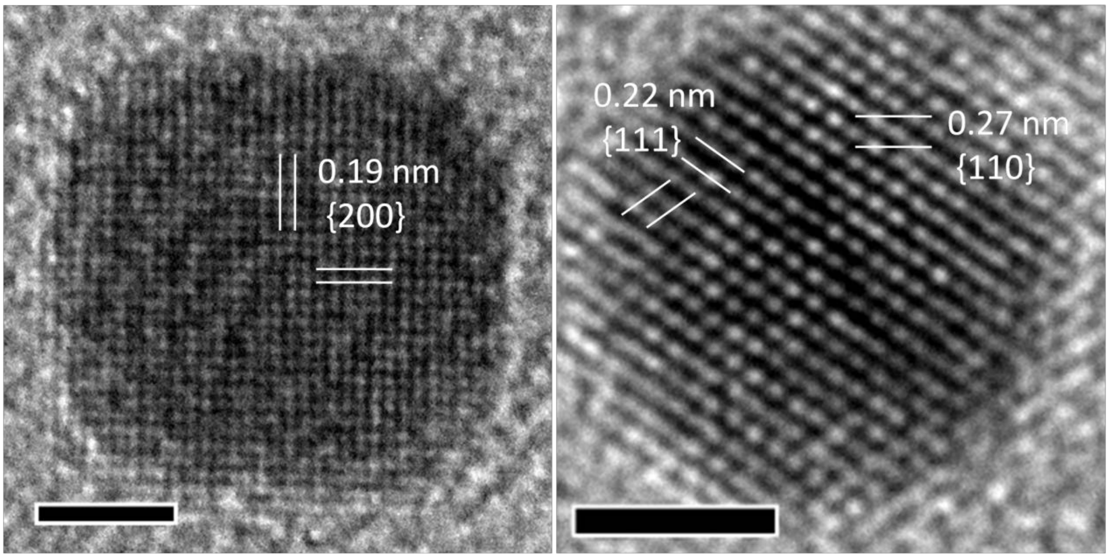

Figure 2.73. HRTEM images of cubic and spherical Pt_3Zn NCs. Scale bars: 2nm

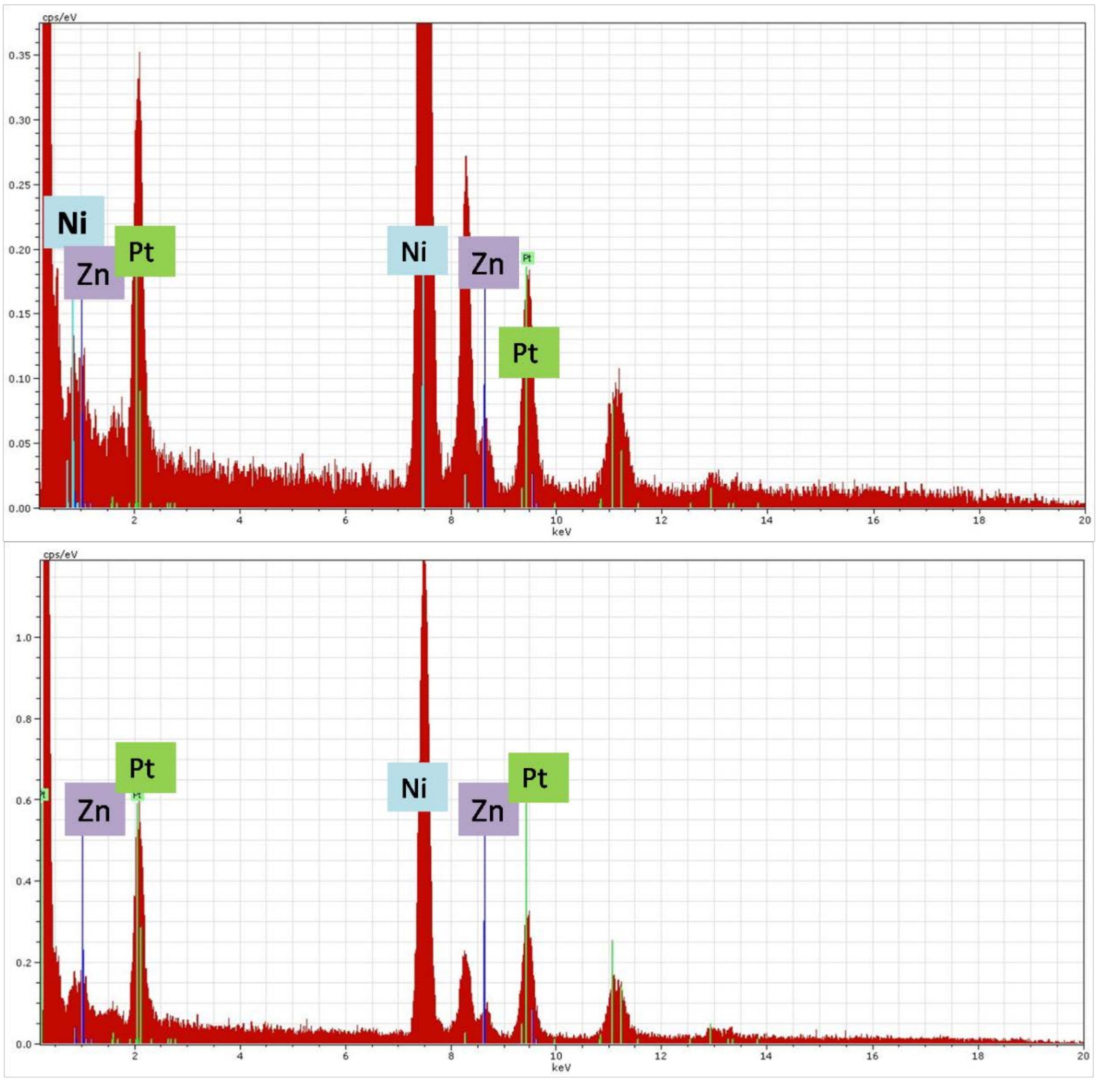

Figure 2.74. EDX spectra of Pt_3Zn NCs (loaded on Ni grid).

2.4.6 Pt-Pb

Adding Pb into Pt electrocatalysts to enhance their activity has been demonstrated by both underpotential deposited Pb and PtPb alloys made by high temperature annealing[10,11,81]. Here, I describe the first synthesis of Pt_3Pb NCs.

Under a nitrogen flow, 0.2 g $Pt(acac)_2$ and 0.2 g $Pb(acac)_2$ are dissolved in 5 ml benzyl ether, 18.4 mL oleylamine, 3.2 mL oleic acid and 11.1 mL 1-hexadecanethiol. The formed solution is dipped into oil bath which is preheated to 180°C. Once the temperature of solution in the reaction flask reaches 180°C, 0.46 mL of borane-triethylamine complex is injected into reaction flask. The temperature is kept at 180°C for 30 minutes after the injection. After reaction, the solution is allowed to cool down. The product is precipitated by ethanol, and then is re-dispersed in hexane. The hexane solution is further purified by centrifuge at 50,000 rpm (Thermo, WX Ultra 100). The high speed centrifuge is necessary to obtain pure Pt_3Pb NCs, as shown in Figure 2.75.

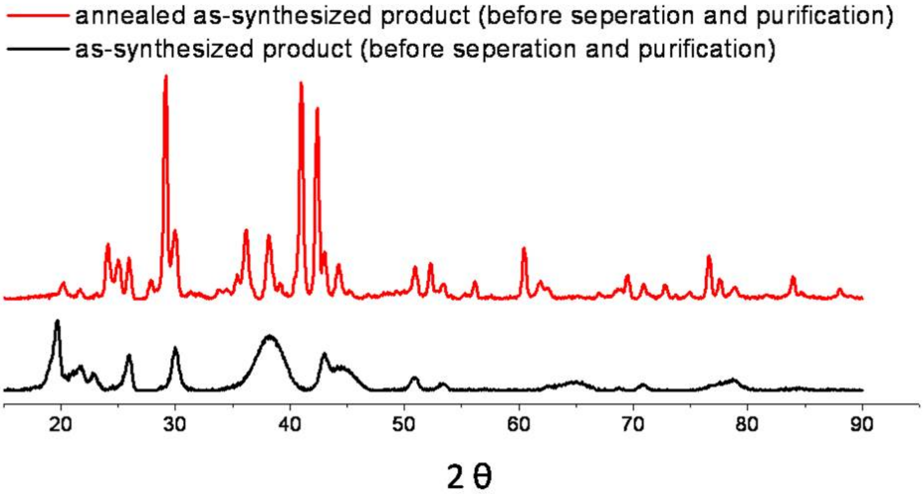

Figure 2.75. XRD patterns of as-synthesized product from Pt_3Pb synthesis, before any further separation and purification. The annealing was carried out at 600°C, under N_2.

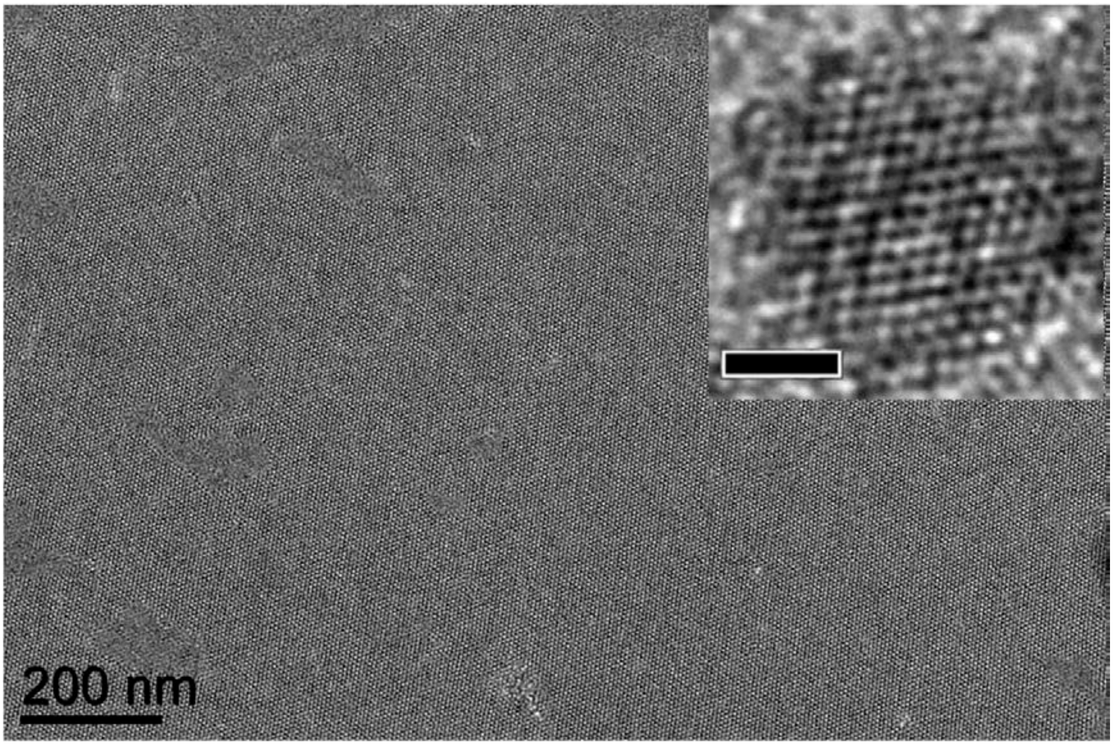

Figure 2.76. TEM image of the large-area superlattice self-assembled from Pt_3Pb nanocrystals. Inset: HRTEM image of one Pt_3Pb nanocrystal, scale bar is 2nm.

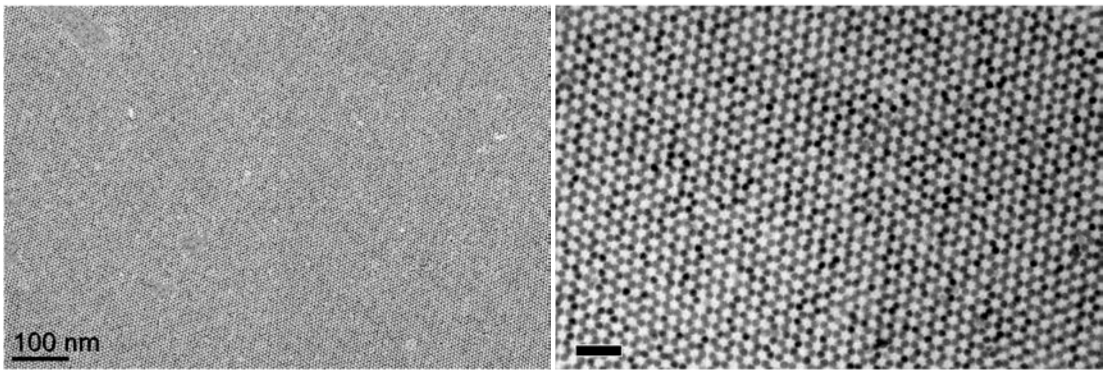

Figure 2.77. TEM image of the Pt_3Pb nanocrystals. Scale bar: left) 100nm, right) 20nm.

To synthesize Pt_3Pb NCs, $Pt(acac)_2$ and $Pb(acac)_2$ are dissolved in benzyl ether, oleic acid, oleylamine and hexadecanethiol and the reaction mixture is brought to 180°C. The reducing agent, borane-triethylamine complex (BTEA) is injected into reaction at 180°C. After 30 minutes, Pt_3Pb NCs of 3.7 nm diameter ($\sigma < 5\%$) are purified and collected. Figure 2.76 and 2.77 shows the TEM images of the monodisperse Pt_3Pb NCs with a size of 3.7 nm ($\sigma < 5\%$). The interplanar distance measured from

HRTEM is 2.34 Å (Figure 2.76 inset), corresponding to the lattice spacing of the Pt_3Pb planes. The TEM-deduced lattice constant is 4.05 Å, which is consistent to the values calculated from X-ray diffraction (XRD) data (4.08 Å) and DFT calculation (4.13 Å). The stoichiometry of Pt:Pb = 3:1 is confirmed by both EDX ($Pt_{76}Pb_{24}$, $\sigma < 5\%$) and ICP-OES ($Pt_{74.8}Pb_{25.2}$, $\sigma < 1\%$). Due to their extremely narrow size distribution, the Pt_3Pb NCs readily form large area superlattices (Figure 2.76 and 2.77). The combination of long chain carboxylic acid, amine, and thiol are essential to the synthesis of Pt_3Pb NCs, though they can be substituted by similar ligands (Table 2.79). The combination of hexadecylamine, adamantanecarboxylic acid and hexadecanethiol produces nanorods in PtPb phase as reported by Yang *et al*[82].

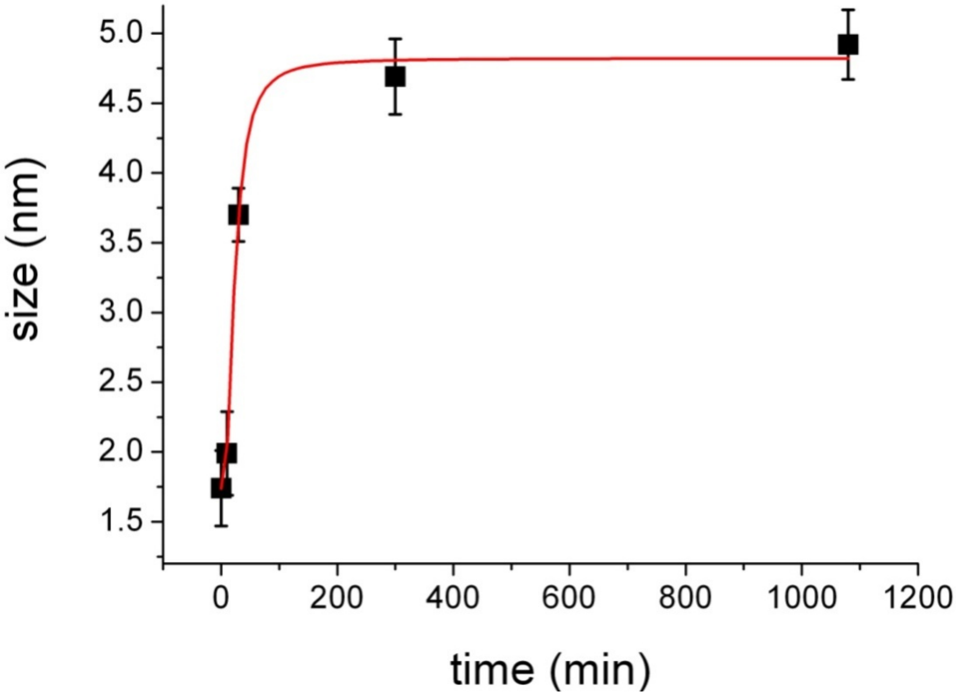

Figure 2.78. Size of Pt_3Pb nanocrystals vs. reaction time (red curve is a fitting curve).

Table 2.79. Synthesis of Pt-Pb nanocrystals with different combination of ligands

amine	acid	thiol	co-solvent	Time	Size
OLAM	OLAC	HDT	BE	30min	3.7nm (σ< 5%)
OLAM	ACA	HDT	BE	30min	4.5nm (σ= 5%)
OLAM	OLAC+ACA	HDT	BE	30min	3.4nm (σ= 7%)
trioctylamine	ACA	HDT	BE	30min	3.7nm (σ= 8%)
dioctylamine	ACA	HDT	BE	30min	4.2nm, 1.8nm (bimodal)
octylamine	ACA	HDT	BE	30min	4.0nm (σ= 7%)
octylamine	ACA	octanethiol	BE	30min	3.9nm (σ= 7%)
octylamine	octanoic acid	octanethiol	BE	30min	4.0nm, 2.0nm (bimodal)
dodecylamine	lauric acid	dodecanethiol	BE	30min	4.0nm (σ> 10%) PtPb rods exist
butylamine	butyric acid	butanethiol	BE	30min	bulk
OLAM	none	HDT	BE	30min	4.5nm (σ> 10%)
OLAM	OLAC	none	BE	30min	bulk
OLAM	OLAC	octanethiol	BE	30min	5.0nm (σ= 5%)
none	none	HDT	BE	30min	2.5nm (σ> 30%)

Table 2.80. Synthesis of Pt-Pb nanocrystals with various reducing agents

Reducing agent (re)	[re]/[Pt]	Time	size
BTEA	6	30min	3.7 nm (σ< 5%)
BTEA	1	30min	3.7 nm (σ= 16%)
BTEA	3	30min	3.7 nm (σ= 8%)
BTEA	10	30min	3.7 nm (σ= 6%)
BTEA	30	30min	1.8 nm (σ= 19%)
superhydride	6	30min	4.0 nm (σ= 7%)
TBAB (1M solution in BE)	6	30min	4.0nm (σ= 5%)

OLAC: oleic acid
OLAM: oleylamine
HDT: hexadecanethiol
BE: benzyl ether
ACA: adamantanecarboxylic acid
TBAB: *tert*-butylamine-borane
BTEA: borane-triethylamine complex

2.5 Oxides

2.5.1 Iron oxides

The nanocrystals of iron oxides are synthesized as reported in literature[83]. The size of iron oxides nanocrystals is tunable in a large range. The representative TEM images are given below.

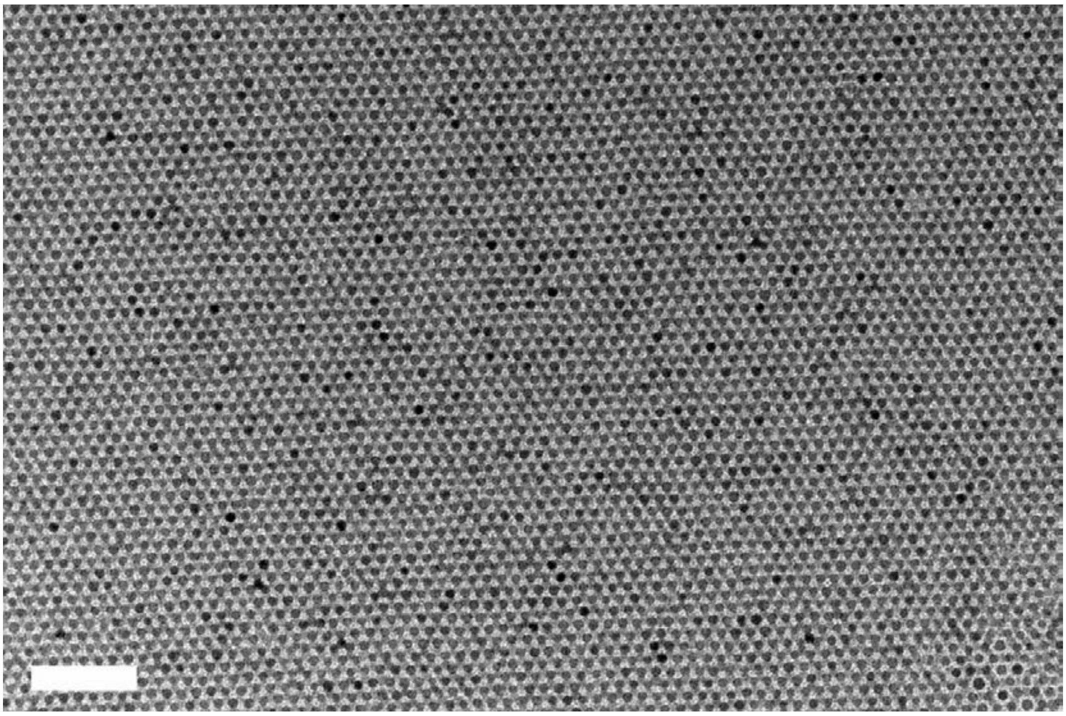

Figure 2.81. 5 nm Fe_2O_3 nanocrystals. Scale bar is 50 nm.

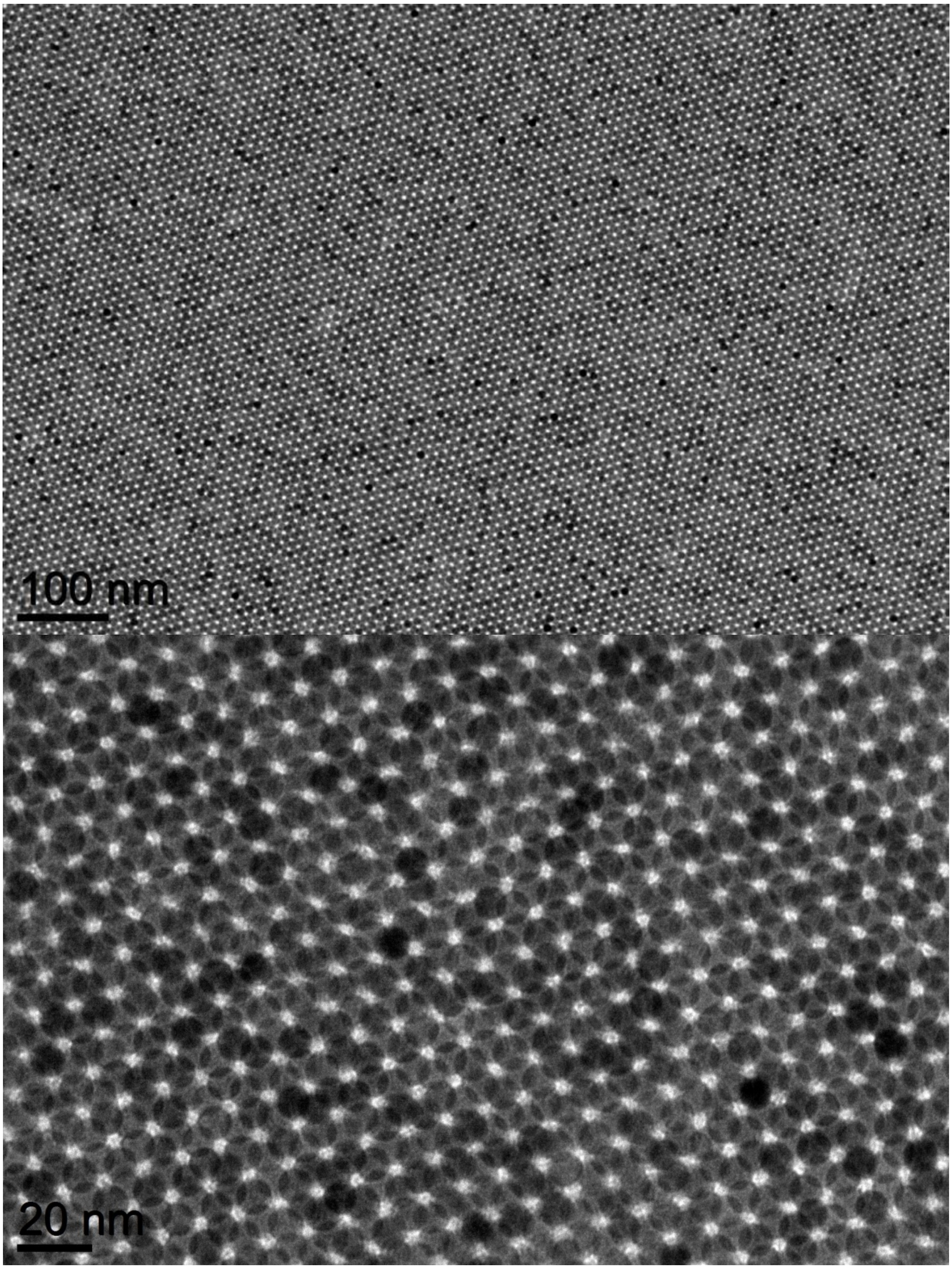

Figure 2.82. TEM images of 12 nm Fe_3O_4 nanocrystals

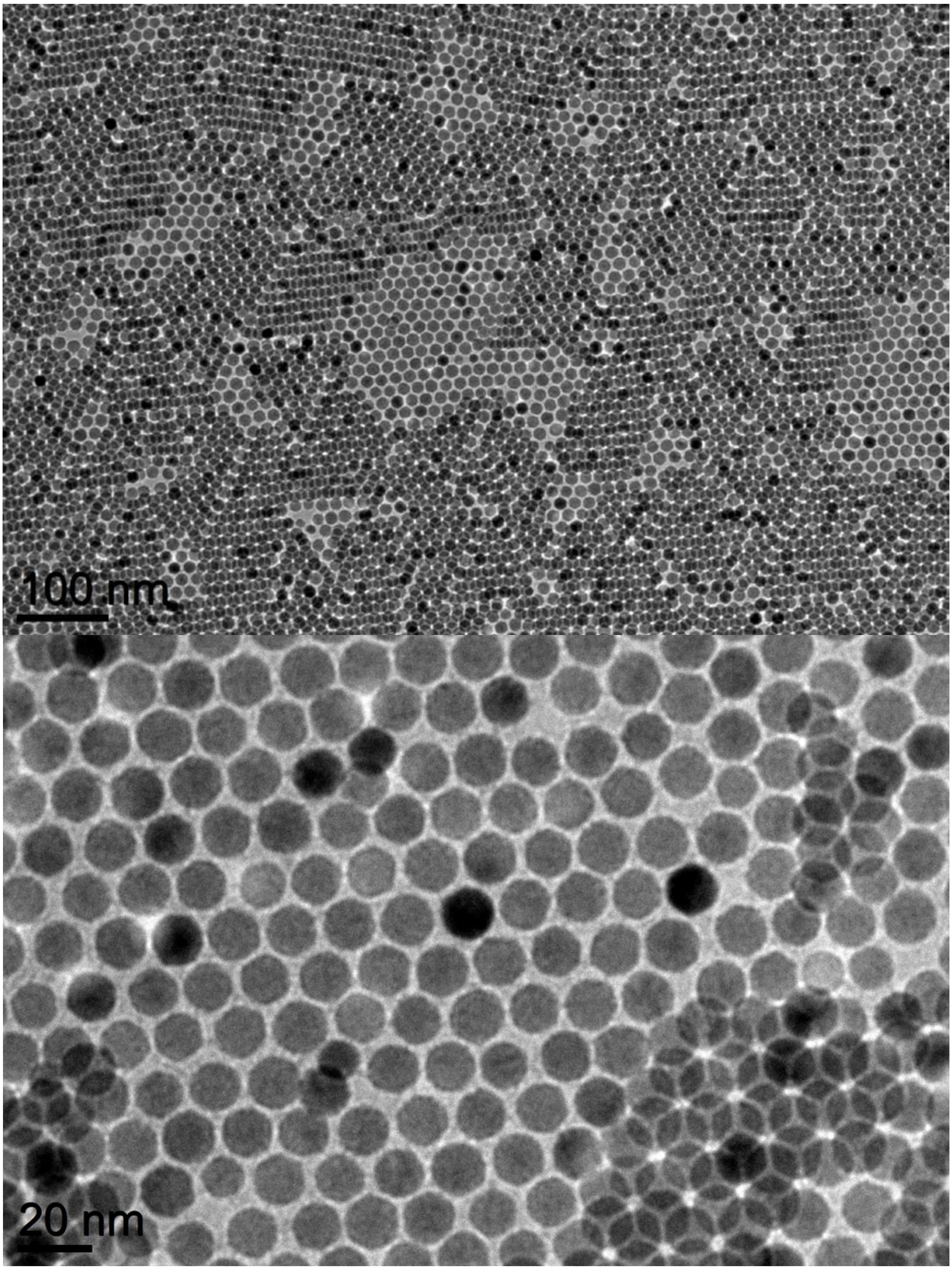

Figure 2.83. TEM images of 16 nm Fe_3O_4 nanocrystals

2.5.2 Ceria[28]

Ceria has been widely used in catalysis[84], optics[85], sensors[86], and solid oxide fuel cells[87]. Due to its high OSC (see chapter 4.1)[19,88], which originates from easy conversion between CeO_2 and CeO_{2-x}, ceria has found its primary utilization in catalysis as an oxygen carrier[20,84,88-100]. Ceria nanomaterials with various morphologies, mainly polyhedra, have been reported[19,20,101-104]. Recently, 1-D ceria nanostructures, such as nanowires[102], have also been reported. However, with the exception of one report on the preparation of nanosheets[104], well-controlled 2-D ceria nanomaterials have not been explored and the comparison of the OSC properties between 3-D and 2-D structures has not been possible. On the other hand, the different properties of the (100), (110), and (111) ceria facets has been debated[19,98,105]. There is no consensus on whether crystallographic orientation or particle size affects reactivities. Therefore, high quality ceria nanocrystals selectively exposing different low Miller-index surfaces, are crucial to enabling experiments that resolve the controversy.

Here we report a simple, robust solution-phase synthesis of ultrathin ceria nanoplates in the presence of mineralizers. The morphology of nanoplates can be easily controlled by changing reaction parameters, such as precursor ratio, reaction time, etc. In addition, we also prepare ceria nanomaterials in various 3-D morphologies by hydrothermal and combustion methods. The OSC of our 2-D ceria materials have been tested and compared to the OSC of their 3-D counterparts (see chapter 4.1).

Synthesis of ceria nanoplates: for square nanoplates, 0.1g cerium acetate hydrate, 0.53g sodium diphosphate, 1mL oleic acid, 2.5mL oleylamine, and 4.5mL 1-

octadecene are used as starting materials, and **for elongated nanoplates,** the starting materials are 0.1g cerium acetate hydrate, 0.61g sodium oleate, 0.5mL oleic acid, 2mL oleylamine, and 5.5mL 1-octadecene. The above starting materials are mixed well in a three-necked flask at room temperature. The resulting mixture is heated to 120ºC whilst stirring and aged at this temperature for 20min under N_2 atmosphere. The mixture is then heated to 320-330ºC with vigorous magnetic stirring and maintained at this temperature for 30min under N_2 atmosphere. After 30min, the solution is cooled down and the ceria nanoplates are flocculated by adding ethanol and centrifugation. The nanoplates are redispersed in hexane.

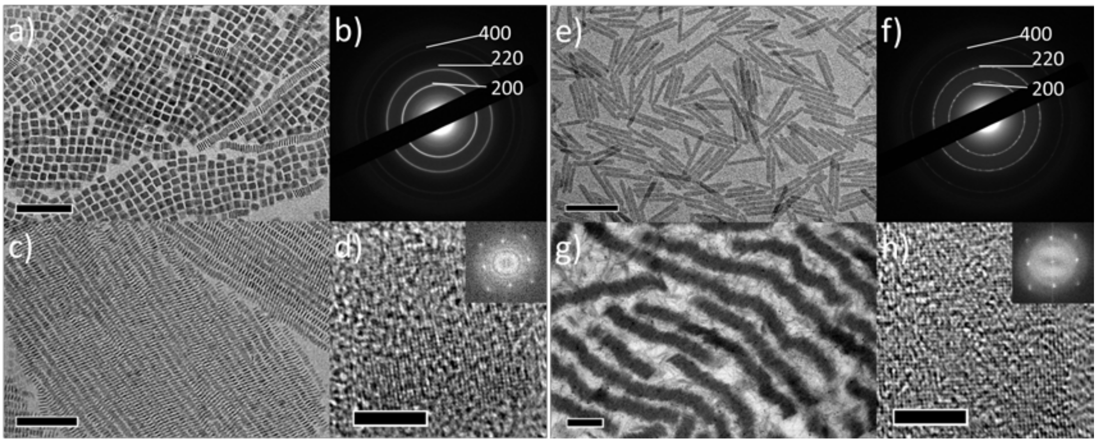

Figure 2.84. TEM images of a) square ceria nanoplates, c) stacking square ceria nanoplates, e) elongated ceria nanoplates, and d) stacking elongated ceria nanoplates; SAED patterns of b) square ceria nanoplates and f) elongated ceria nanoplates; HRTEM images of d) square ceria nanoplates and h) elongated ceria nanoplates. (Insets of d, h: FFT patterns of HRTEM images.) Scale bars: a, c) 100nm, e, g) 200nm, d, h) 5nm.

The synthesis of ceria nanoplates involves the thermal decomposition of cerium acetate at 320-330ºC in the presence of oleic acid and oleylamine as stabilizers and employs sodium diphosphate or sodium oleate as mineralizers. TEM images of ceria nanoplates are shown in Figure 2.84. Square ceria nanoplates (S-nanoplates, Figure 2.84a) with an edge length of 11.9nm ($\sigma = 7\%$), are synthesized with sodium diphosphate as the mineralizer while elongated ceria nanoplates (L-nanoplates, Figure 2.84e) with a length of 151.6nm (σ = 9%) and a width of 14.3nm (σ = 12%), are produced with sodium oleate as the mineralizer. The nanoplates in both samples have a thickness of about 2nm. As shown in Figure 2.84c and g, the stacks of nanoplates comfirm that the sample consists of 2-D plates rather than 3-D cubes or rods. S-nanoplates readily form the demonstrated stacking arrays as seen in drop-cast TEM samples. L-nanoplates only form stacks by a self-assembly at a liquid-liquid (e.g. hexane-ethylene glycol) interface. The S-nanoplates also self-assemble to a ceria nanosheet at a hexane-acetonitrile interface, as shown in Figure 2.89a. HRTEM images of both nanoplates (Figure 2.84d, h, and 2.85c) reveal an interplanar distance of 0.27nm, consistent with the (200) lattice spacing of the ceria crystal. The Fast Fourier Transform (FFT) patterns confirm the {100} textures of ceria nanoplates. Plates (e.g. square plates) could be enclosed by either six (100) facets or a combination of two (100) facets and four (110) facets. As illustrated in Figure 2.89, our HRTEM images and simulations of HRTEM images suggest that our ceria nanoplates are enclosed by six (100) facets, similar to reported gadolinium-oxide nanoplates[106]. SAED patterns of ceria nanoplates (Figure 2.84b, f) show the enhanced (200), (220) and (400) diffraction rings, consistent to the proposed plate structures.

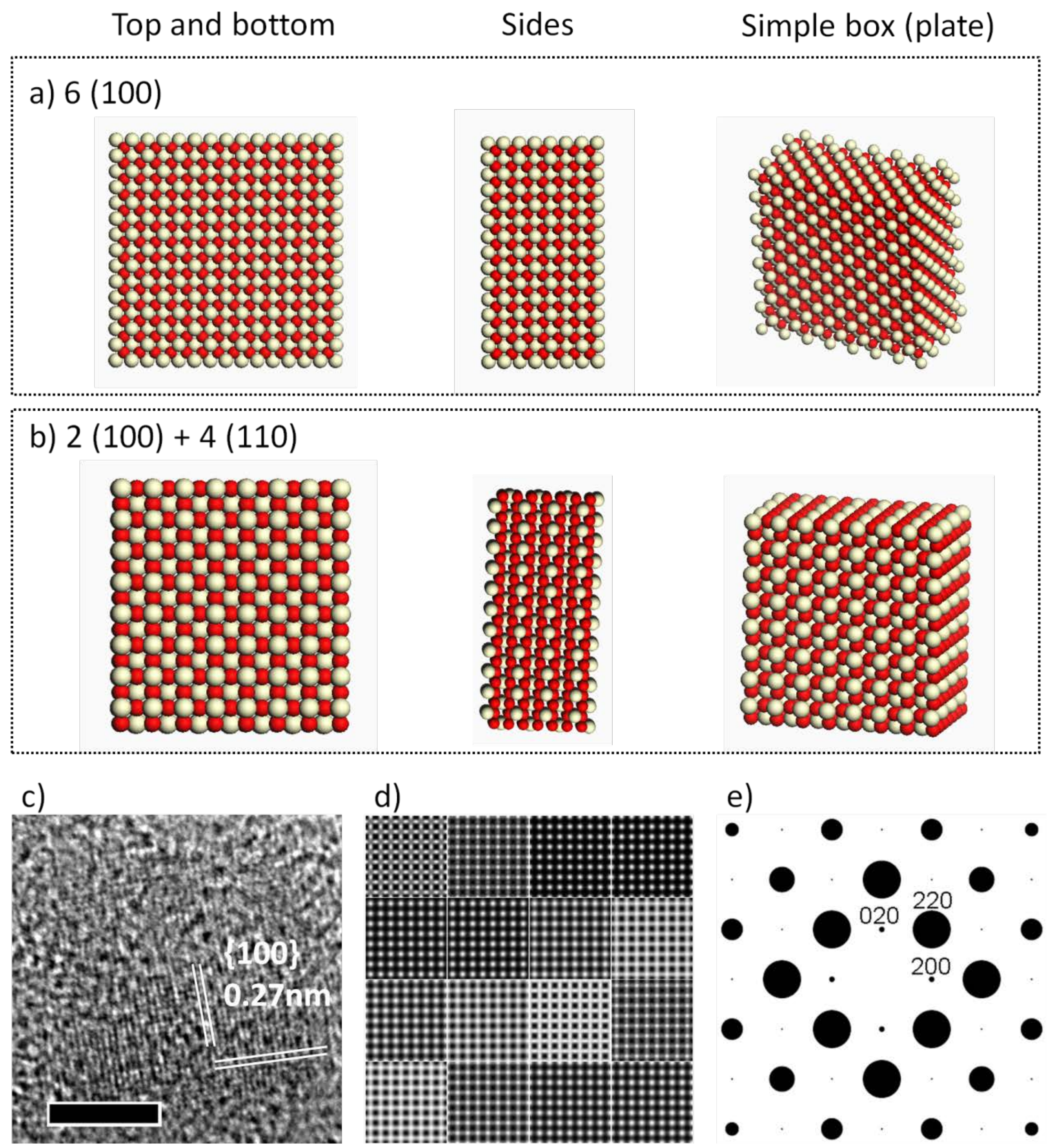

Figure 2.85. A ceria plate (simple box) having a fluorite unit cell could be enclosed by a) six (100) facets, or b) two (100) facets and four (110) facets. c) HRTEM image (scale bar: 5nm) of ceria nanoplate shows lattice fringes parallel or perpendicular to the edges of plate, implying the agreement with patterns shown in Figure S1a rather than S1b. d) Simulated HRTEM images of [001] zone axis of CeO_2. From left to right and from top to bottom, the defocuses are from 0 nm to -75 nm, with a defocus step of 5 nm. e) Simulated electron diffraction pattern of [001] zone axis of CeO_2. Electron diffraction simulation and HRTEM image simulation were performed with EMS Software (Pierre Stadelmann). Here, the HRTEM image and simulation suggest that the ceria nanoplates should be enclosed by six (100) facets.

The XRD patterns (Figure 2.86) of the ceria nanoplates confirm the fluorite crystal structure (JCPDS No. 34-0394). The XRD pattern of S-nanoplates shows diminished

(200) and (400) peaks, due to the preferred orientation (stacking) as shown in Figure 2.84c. For the L-nanoplates, the sharp (200), (400) and broadened other peaks indicate that the dimension is relatively large on {100} facets but very small on any other facets.

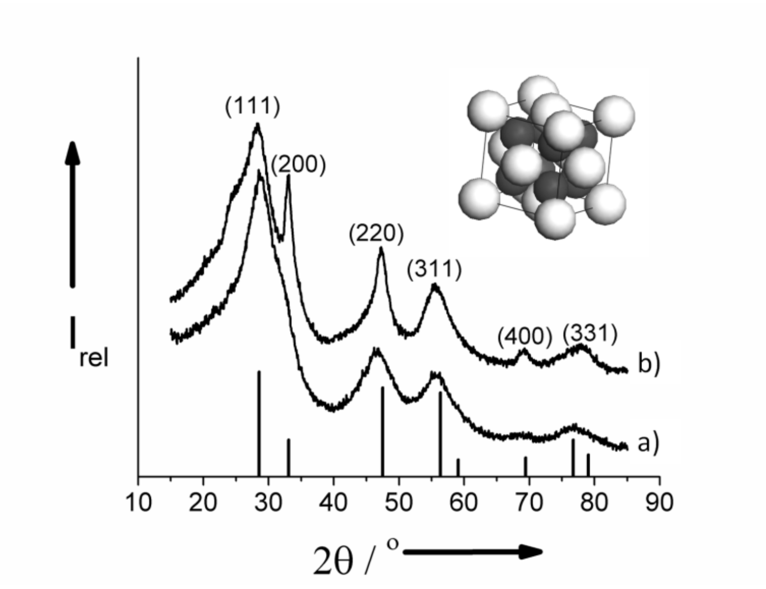

Figure 2.86. XRD patterns of a) square ceria nanoplates and b) elongated ceria nanoplates. Inset is the unit cell of CeO_2.

The key to this nanoplate synthesis is the incorporation of mineralizers that accelerate the crystallization process and control the morphology of ceria nanocrystals. In the absence of mineralizers, product yield of ceria nanocrystals is very low, and the morphologies are not controlled, as shown in Figure 2.87. In the presence of mineralizers, the syntheses are very easy to control (i.e. reaction parameters are acceptable in a large range). The nanoplate synthesis can be done even under the ambient environment (i.e. without inert gas protection) in the presence of mineralizers. The stabilizer/solvent combination allows a high reaction temperature (above 320ºC) which is required to form nanoplates. The shape and size of ceria nanoplates can be also controlled by adjusting the synthesis parameters such as the ratio of the stabilizers and the reaction time. For example, increasing the amount of stabilizers (i.e. oleic acid and oleylamine) but keeping other conditions identical to the synthesis of S-nanoplates, cirlular ceria nanoplates with a diameter of 12nm (σ = 6%) are produced (Figure 2.89b); the L-nanoplates with a reduced length (80-120nm) are made by decreasing the reaction time (Figure 2.89c).

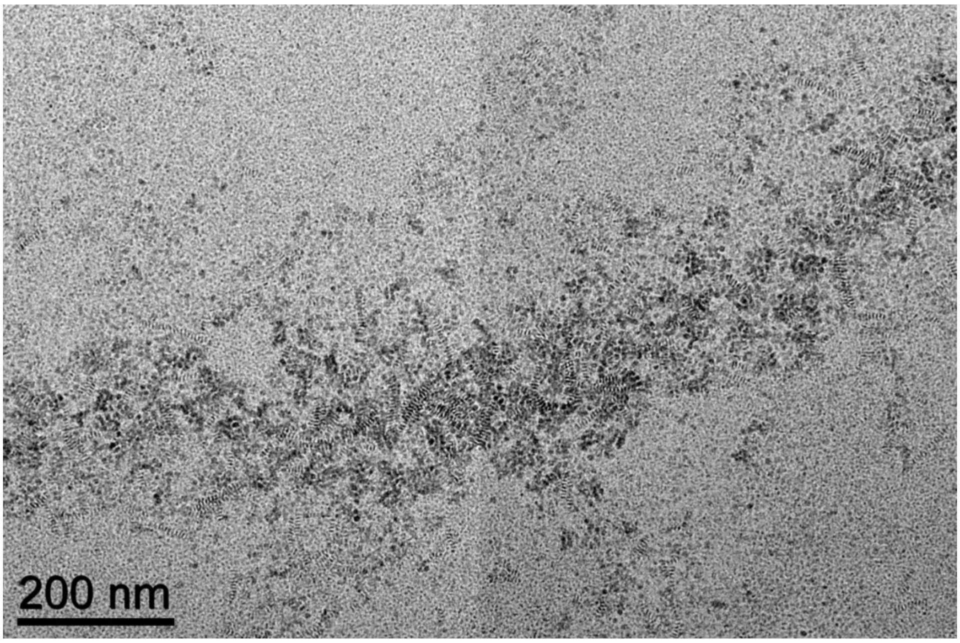

Figure 2.87. TEM image of the product synthesized in the absence of mineralizers.

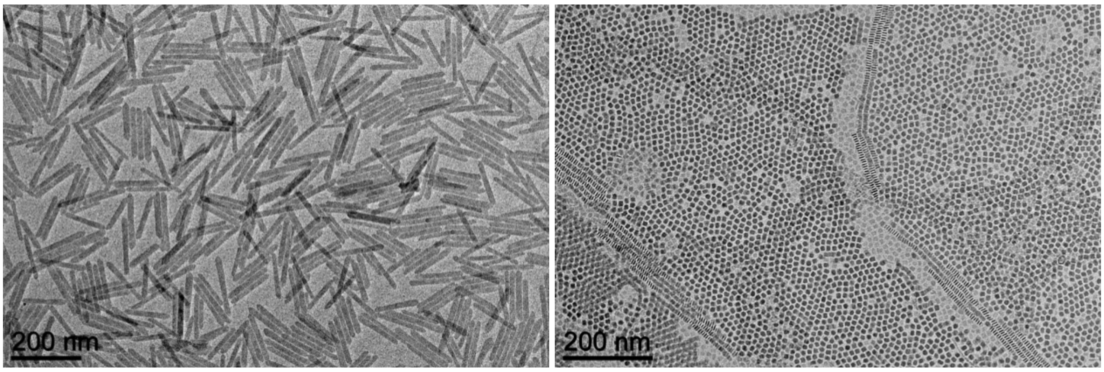

Figure 2.88. TEM images of ceria nanoplates synthesized under ambient environment (without inert gas protection).

Ceria NC powder and ceria nanospheres are also prepared by combustion method[107] (Figure 2.89d) and hydrothermal method[108] (Figure 2.89e), following the precedures described below.

Combustion synthesis of CeO_2 nanocrystals: 0.22g cerium (III) nitrate hexahydrate and 0.9g urea are dissolved in 10ml de-ionized water. The resulting solution is concentrated by heating it in a porcelain crucible until excess free water evaporated. When the water is almost gone, the temperature rises quickly and ignites. The combustion process lasts only a few seconds and light-yellow foam is obtained. And then the foamy product is calcined at 1000ºC for 1 hour in air.

Hydrothermal synthesis of CeO_2 nanospheres: 0.5ml 0.5M $Ce(NO_3)_3$ aqueous solution is mixed with 15ml ethylene glycol. The formed solution is transferred into a tightly sealed steel autoclave. The autoclave is heated in an oven at 180 ºC for 24 hours. After hydrothermal treatment, the product is washed and collected by ethanol and centrifuge.

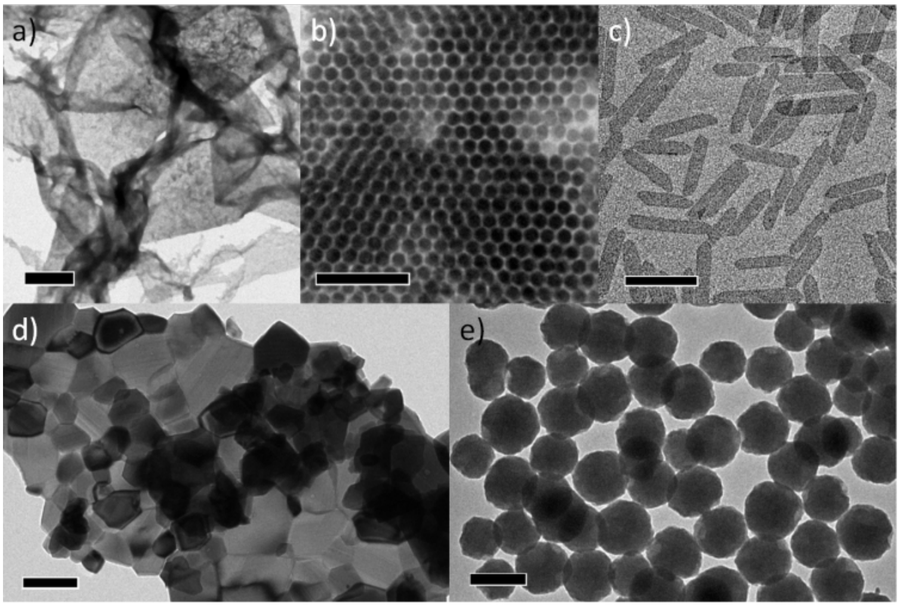

Figure 2.89. TEM images of a) nanosheets self-assembled from square ceria nanoplates, b) round ceria nanoplates, c) less elongated ceria nanoplates, d) ceria nanomaterials prepared via combustion, and e) hydrothermally synthesized ceria nanospheres. Scale bars: a) 1μm, b, c, d, e) 100nm.

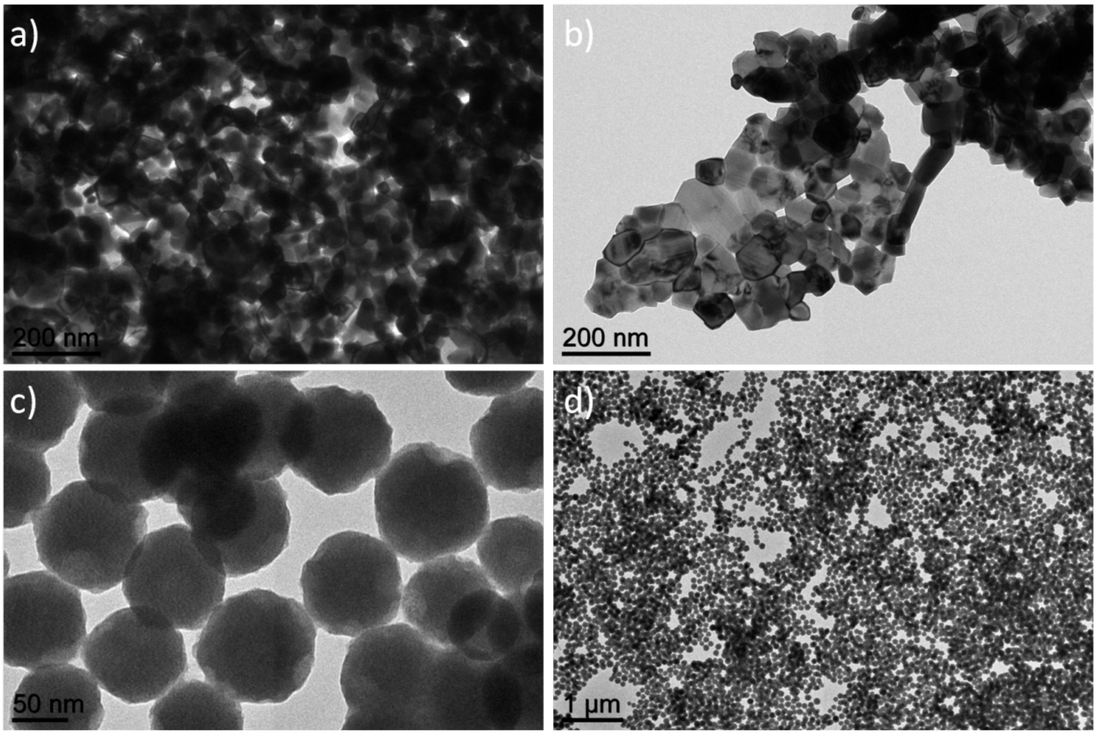

Figure 2.90. TEM images of a, b) combustion prepared ceria nanomaterials and c, d) hydrothermal treatment prepared ceria nanomaterials (spheres).

2.6 Nanostructures

Building complicated nanostructures is one effective way to study the interaction, interface, and any possible synergistic effect of nanocrystals in catalytic processes. It can be achieved by synthesis, subsequent growth, or self-assembly.

2.6.1 Heterostructure

The heterostructure is a structure constructed with 2 or more building blocks in different composition or morphology. A heterostructure may combine the physical and chemical properties of different materials in one single nanostructure. A heterostructure may offer new opportunities to study the synergistic effect raised from the interaction of nanocrystals[109,110]. It can also be used as a model to study the interface of materials. The heterostructures and all the advantages they bring can be employed to better understand the catalytic processes or to provide valuable knowledge and information toward design of novel catalyst. For instance, Sun et al. has reported a Au-Fe_3O_4 dumbbell heterostructure, that successfully be used as improved ORR electrocatalysts and effective CO oxidation catalysts[111,112].

A FePt-Fe_3O_4 dumbbell heterostructure has been made by simply increasing the amount of Fe precursor in the synthesis of FePt. In brief, a reaction mixture of 0.13 g $Pt(acac)_2$, 0.18 ml $Fe(CO)_5$, 2.1 ml oleic acid, 3 ml oleylamine, and 13 ml benzyl ether is heated at 295°C for 30 min to produce the FePt-Fe_3O_4 dumbbell heterostructure, as shown in Figure 2.91. Another synthetic route and a mechanism to describe the formation of such heterostructure are reported by Figuerola et al[113]. The FePt-Fe_3O_4 dumbbell heterostructure is potentially useful to study catalytic and magnetic properties.

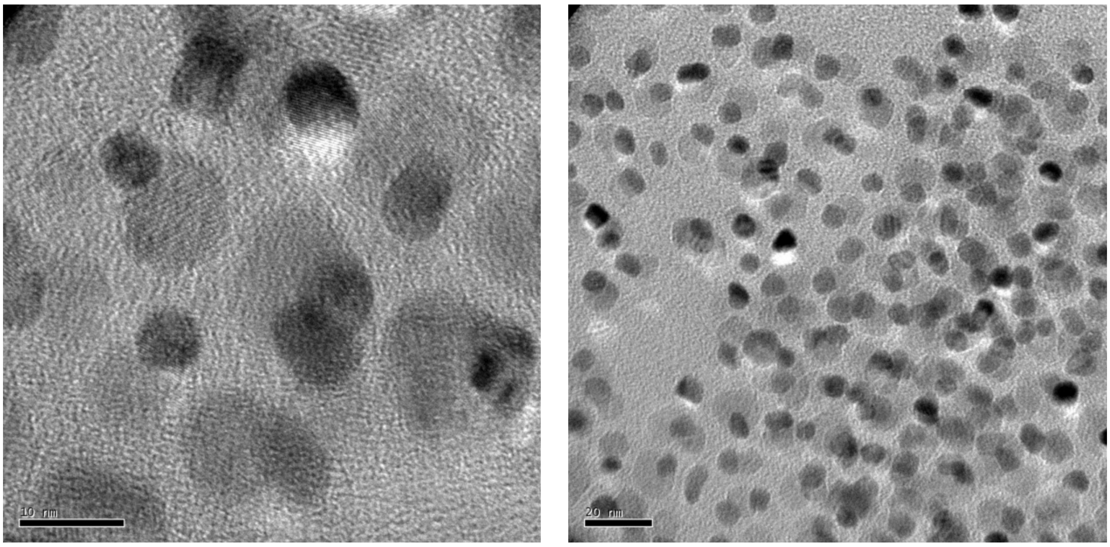

Figure 2.91. TEM images of FePt-Fe_3O_4 dumbbell heterostructures.
Scale bar: (left) 10nm, (right) 20nm.

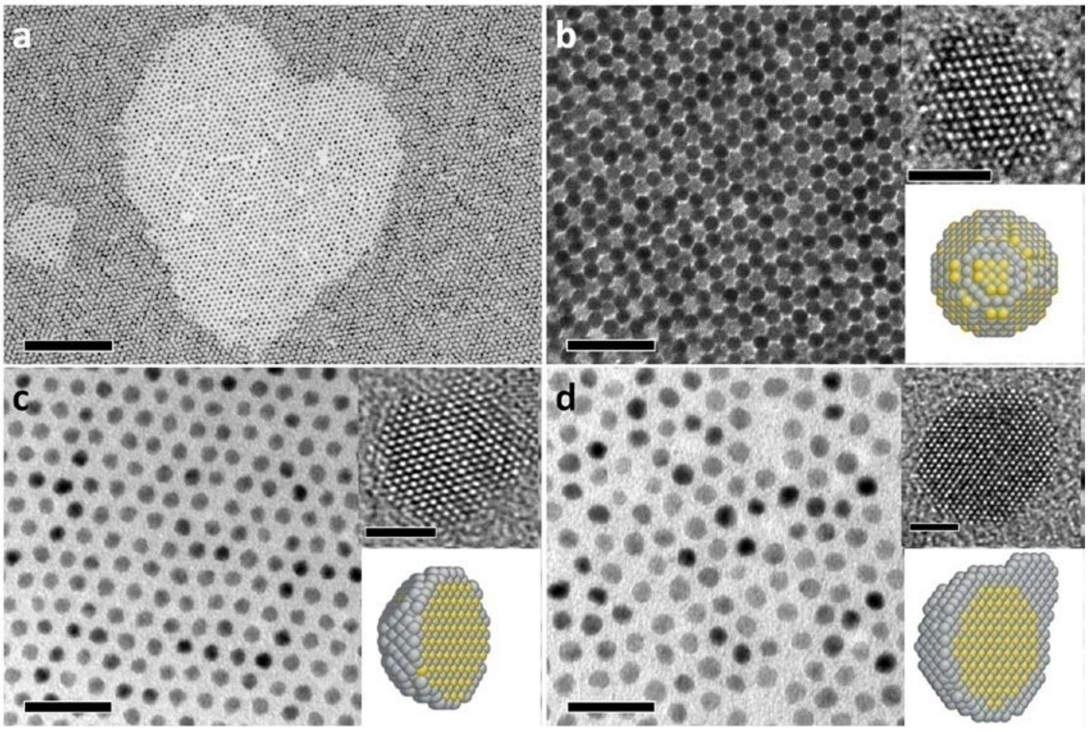

Figure 2.92. TEM images and (insets) HRTEM image of a, b)Pt_3Pb NCs; TEM and HRTEM images of c) Pt_3Pb-Pt(type A) NCs and d) Pt_3Pb-Pt(type B) NCs. Scale bars: a)100nm, b, c, d) 20nm, insets) 2nm

As described in Chapter 2.4.3, I synthesize Pt_3Pb as FA oxidation electrocatalysts. To better study the catalytic properties of Pt_3Pb, I prepare two more Pt-Pb core-shell nanostructures as control systems for comparison. I use the as-synthesized Pt_3Pb as seeds upon which to grow a second Pt layer. High temperature growth facilitates the Pt precursor decomposition inducing growth on any possible seed sites, usually forming islands as well as layers; while at lower temperature slower growth allows Pt to grow uniformly onto Pt_3Pb seeds at a low yield, forming epitaxial layers. Figure 2.92c and 2.92d presents the TEM images of these as-synthesized Pt_3Pb-Pt NCs. The size of Pt_3Pb-Pt NCs (here, we name them as "Pt_3Pb-Pt(type **A**)") by slow-growth is 4.0 nm ($\sigma = 6\%$), slightly larger than the original Pt_3Pb NCs while the size of Pt_3Pb-Pt NCs (here, we name them as "Pt_3Pb-Pt(type **B**)") by rapid-growth is 4.9 nm ($\sigma >$ 10%) at broadened size distribution. Many Pt_3Pb-Pt(type **B**) NCs adopt an elongated morphology rather than a uniform spherical morphology, indicating an island structure (Figure 2.92e-h, 2.95, 2.96). The monodisperse Pt_3Pb-Pt(type **A**) NCs form large area superlattice as readily as the original Pt_3Pb NCs. Due to their broad size and shape distribution, Pt_3Pb-Pt(type **B**) NC only form small area superlattices (Figure 2.94). The composition of Pt:Pb = 83:17 ($\sigma < 5\%$) for Pt_3Pb –Pt(type **A**) and Pt:Pb = 92:8 ($\sigma < 5\%$) for Pt_3Pb-Pt(type **B**) is determined by both EDX and ICP-OES. The Pt:Pb ratio of a Pt_3Pb NC covered with a monolayer of Pt is calculated to be 82:18 (at size of 4.0 nm), which is in good agreement with the Pt_3Pb-Pt(type **A**) composition. The XRD pattern of Pt_3Pb-Pt(type **A**) is similar to Pt_3Pb with an fcc structure. Compared to Pt_3Pb and Pt_3Pb-Pt(type **A**), the XRD pattern of Pt_3Pb-Pt(type **B**) is shifted to greater 2-theta angle (i.e. smaller lattice constant), indicating a Pt-rich composition. Noting that the alloy phase could transform into an intermetallic phase upon annealing, we exploit this phenomena to investigate the composition and structure of these Pt-Pb NCs. After annealing at 600°C for 30 minutes, the NC structures are converted from the $A1$ phase to the ordered $L1_2$ phase ($AuCu_3$ structure), and phase segregation is observed (Figure 2.97). The major peaks of Pt_3Pb NCs fit the Pt_3Pb intermetallic phase. The trace impurity peaks are ascribed to the slight excess of Pt in the NCs. The Pt_3Pb-Pt(type **A**) NCs show increased amount of Pt and the Pt_3Pb-Pt(type **B**) exhibit even stronger signals for pure Pt phase. These XRD data, with EDX, ICP-OES data and TEM images, support the proposed mechanism of the Pt layer growth.

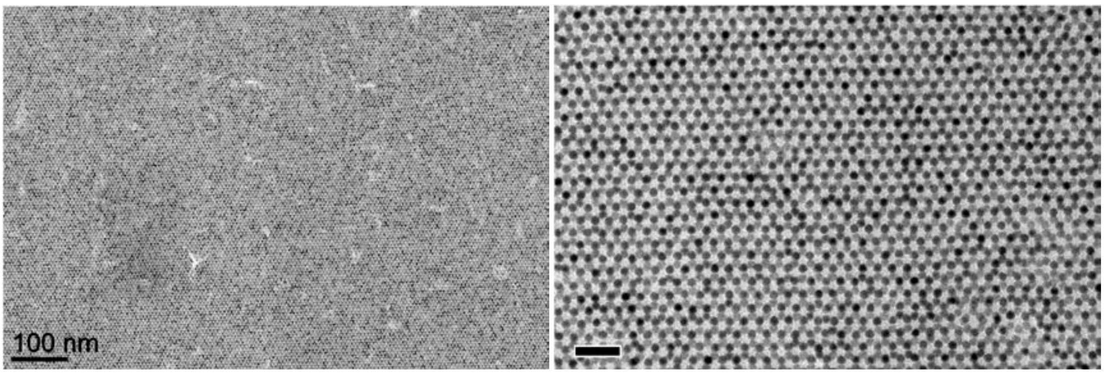

Figure 2.93. TEM image of the large-area superlattices self-assembled from Pt_3Pb-Pt(type **A**) nanocrystals. Scale bars: left)100nm, right) 20nm.

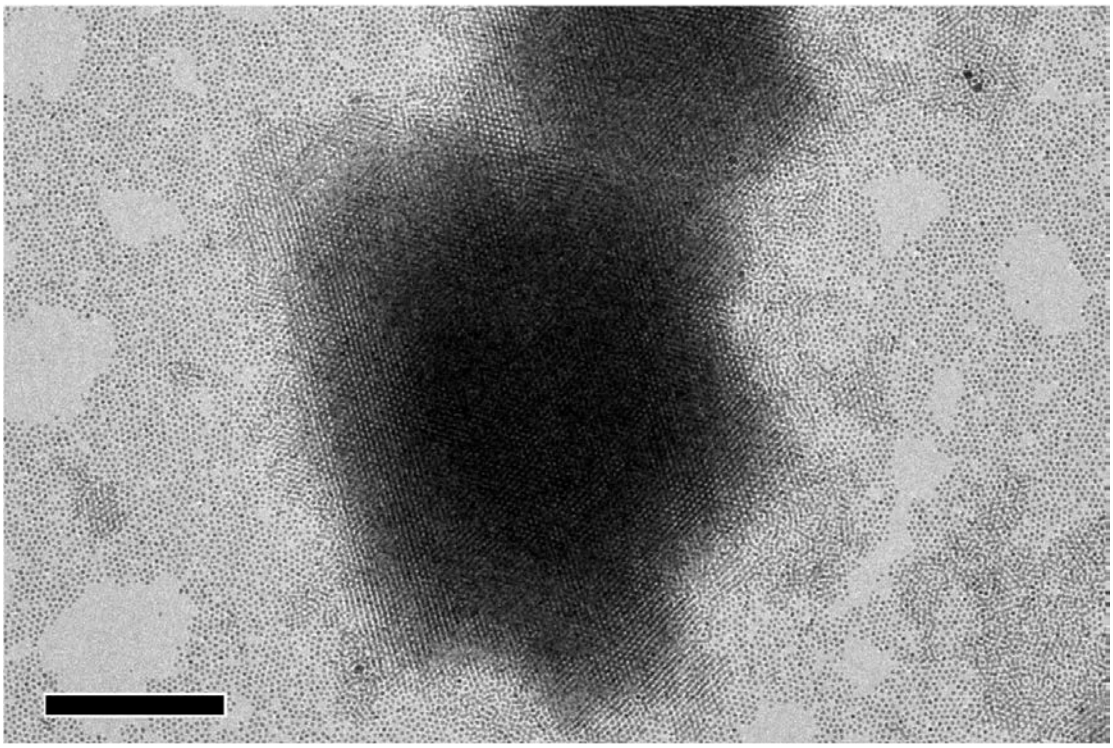

Figure 2.94. TEM image of the Pt_3Pb-Pt(thick) nanocrystals show that the Pt_3Pb-Pt(thick) nanocrystals can only form small area superlattice. Scale bar: 200nm

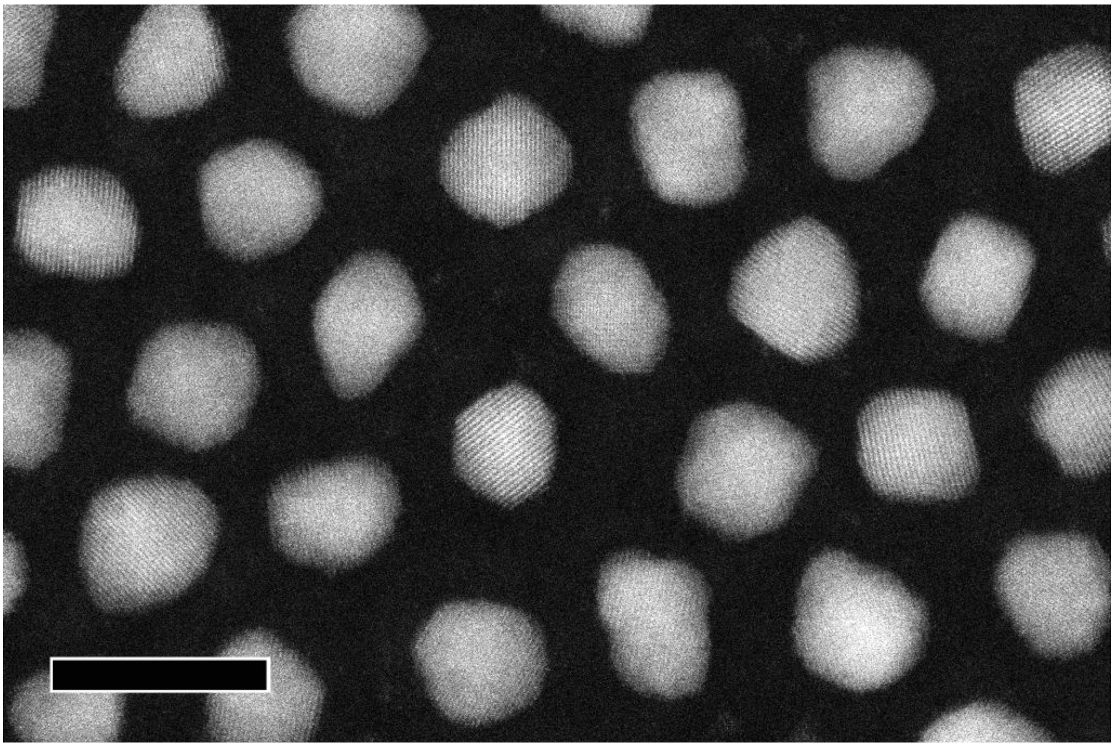

Figure 2.95. High angle annular dark field (HAADF) scanning transmission electron microscopy (STEM) image of the Pt_3Pb-Pt(thick) nanocrystals. Scale bar: 10nm

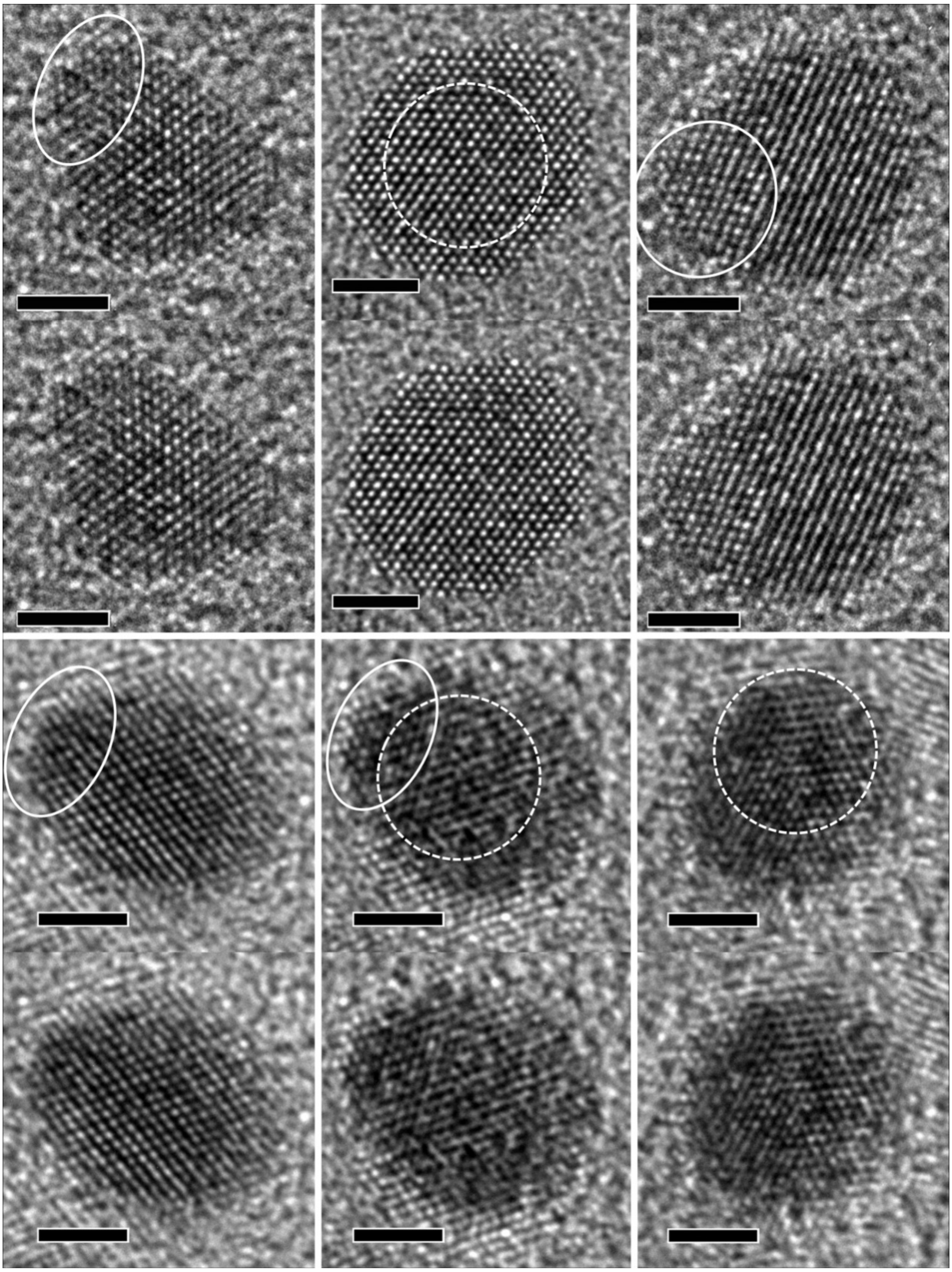

Figure 2.96. HRTEM images of Pt_3Pb-Pt(thick) nanocrystals. The circles represent the Pt_3Pb cores (dashed) and Pt islands (solid). For comparison purpose, exactly same images but without circles are given below each circled image. Scale bars: 2nm.

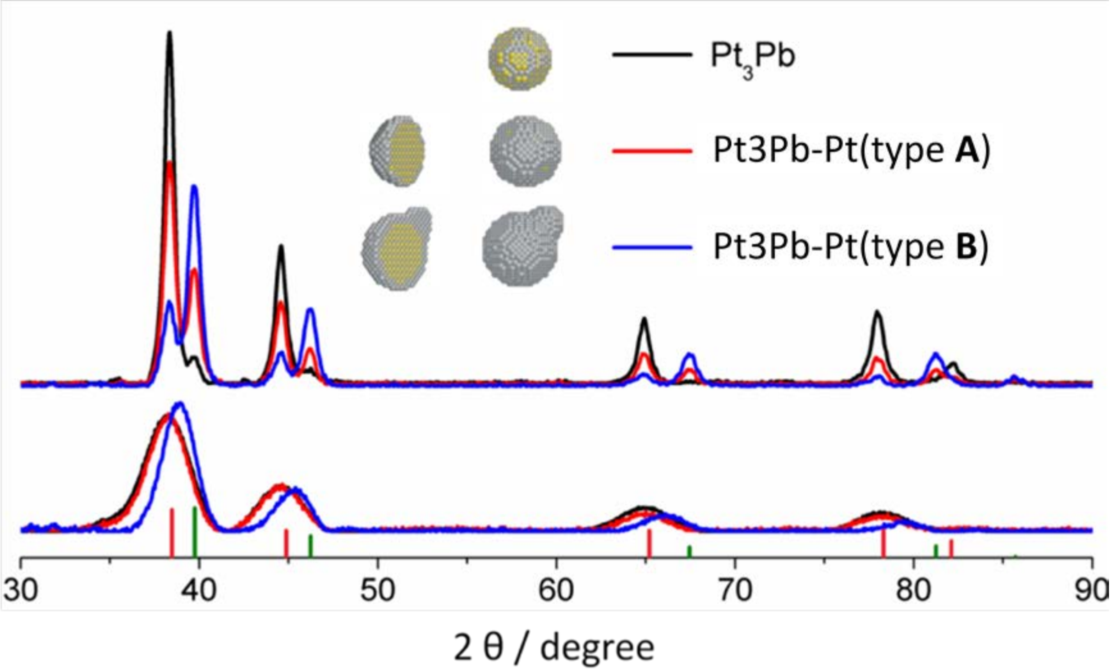

Figure 2.97. XRD patterns of (upper) annealed NCs and (lower) as-synthesized NCs. Index: (pink) Pt_3Pb, (green) Pt. Insets: models to represent Pt-Pb nanostructures (yellow: Pb, grey: Pt)

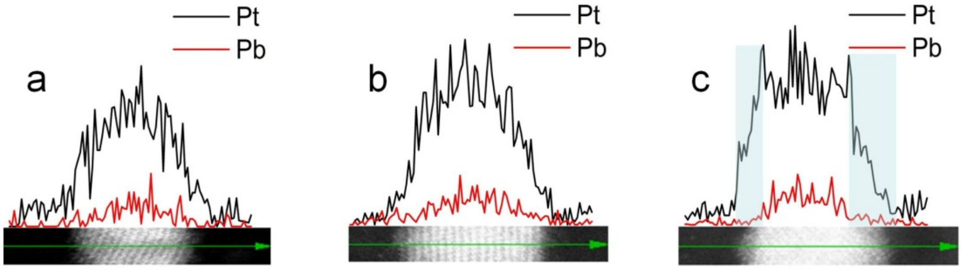

Figure 2.98. EDX line scans of a) Pt_3Pb, b) Pt_3Pb-Pt(type **A**), and c) Pt_3Pb-Pt(type **B**) NCs.

2.6.2 Artificial crystal

Recent development in self-assembly allows large scale fabrication of multi-component nanocrystal superlattices, that offers new opportunities to combine the chemical and physical properties of different materials within a single nano-structured, crystalline architecture, and to exploit new synergistic behaviors that arise as nanocrystals interact in these more complex systems[114]. In particular, the self-assembly of two types of nanocrystal into binary superlattices (BNSLs, or artificial crystal) architecture, has been of great interest to design functional metamaterials[115]. Here, we report the first attempt to build artificial crystals to study nanocatalysis. The artificial crystals not only offer new insight to understand catalytic processes, but also provide valuable knowledge for design of highly efficient catalyst. In this report, by using Au-FeOx BNSLs, we have identified the active sites for CO oxidation on Au-FeOx catalysts; we have combined shape effect and synergistic effect of Pt-Pd to demonstrate the design of high-performance electrocatalysts; we have employed artificial crystals to demonstrate that the stability of catalysts can be optimized by manipulating the local structure of catalysts. Moreover, a variety of currently available artificial crystals provides an extensive tool box for diversified purposes.

Complimentary to conventional model materials such as single crystals, various “small model materials” in nano-scale have been proposed, intending to provide a better equivalent to the real catalysts, of which the dimensions are usually also in nano-scale. Because the experiments are usually performed in a clean environment such as ultra-high vacuum, the conventional models provide more convincing interpretation of catalysis than those “small models”. However, the knowledge gained on conventional models is not always applicable on real catalysts, due to the significant discrepancies between conventional models and real catalysts, such as size, morphology, or surface state. On the other hand, the factors been studied on the nano-materials are difficult to be isolated from each other, because of the lack of precise control. Therefore, a gap exists between the classical surface science which use the conventional models and the industrial level testing on real catalysts. Although challenging, it is critical to prepare well-controlled nano-materials to bridge the conventional models and real catalysts. Moreover, Yang et al. have demonstrated that nano-structured multi-component nanocrystal architecture may archive the tandem catalysis which cannot be obtained by simply mixing the components[116]. With the highly ordered structures and precise-controlled stoichiometry, the artificial crystal is an ideal model for investigation of catalytic processes; however, they are not accessible until we have been able to fabricate in a large scale (millimeter to centimeter) by the recently developed liquid-air interface self-assembly.

Fabrication of artificial crystals: We fabricate artificial crystals by the liquid-air interface self-assembly method as described in previous report[114]. In brief, the hexane solutions of building block nanocrystals are mixed. The mixed solution is dropped on to a surface liquid (usually, EG or DEG is used for this purpose). The mixed hexane solution is allowed to evaporate at a very slow rate. A solid film forms at the liquid-air interface upon the complete evaporation of hexane solvent. The formed film of artificial crystals is transferred to a Si wafer for catalysis, to a glassy carbon disc for electrocatalysis, or to a TEM grid for characterization.

As shown in Figure 2.99, the typical artificial crystals possess many characters seen in conventional models, such as well-defined terraces, steps, kinks and vacancies, as well as grain boundaries and faceted crystal planes. The diversity of precisely controlled structures renders the excellent control for modeling. In this thesis, I employ the artificial crystals to study CO oxidation and ORR, as well as thermal stabilities of catalysts. Details are described in Chapter 4.

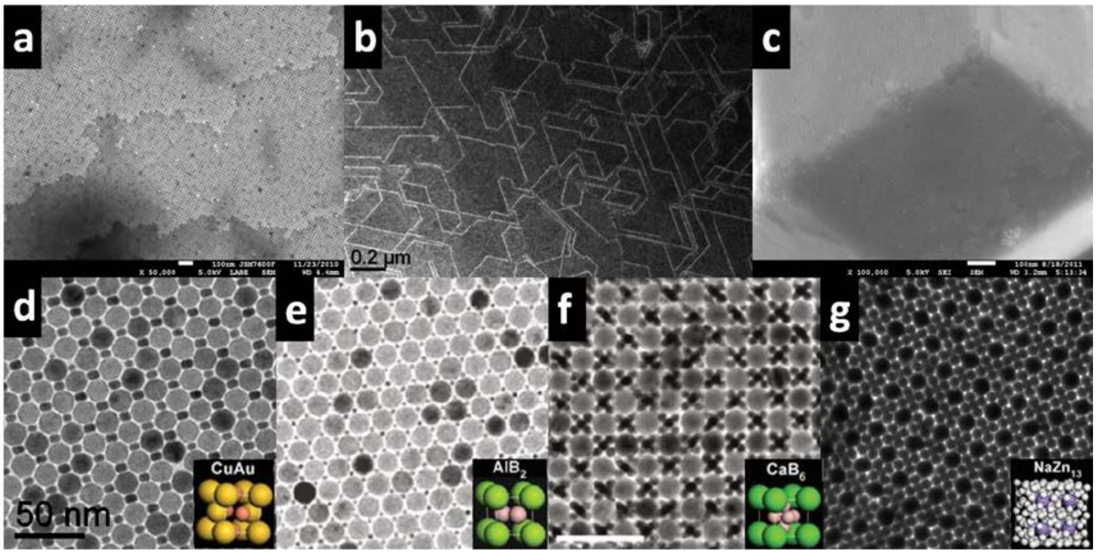

Figure 2.99. Artificial crystals showing characters analogue to single crystals, and the diversified structures. a) Pt-Pd artificial crystal that has terraces, steps, kinks, and vacancies, similar to those in single crystals. b) Au-FeOx artificial crystal that shows grain boundaries. c) A super-crystal of Pt that has faceted surface. Au-FeOx Artificial crystals having structures analogue to d) CuAu, e) AlB2, f) CaB6, g) NaZn13.

Moreover, we have a great variety of available compositions and structures of artificial crystals. Excluding the catalytically inactive combinations, we have Pt-Pd, Pt-Au, Pt-Ni, Pt-MnO, Pt-FeO_x, FePt-FeO_x, CoPt3-FeO_x, FePt-MnO, Au-Cu, Ni-Cu, Au-Ni, Au-FeO_x, Cu-FeO_x, Pd-FeO_x, MnO-FeO_x in various structures. These artificial crystals can be useful as models to study catalysis, as demonstrated in the case of Au-FeOx. For instances, Pt-Ni and Au-Ni can be used to study methanol reforming reaction; the Pd-FeOx could be helpful to understand the catalytic process of water gas shift reaction.

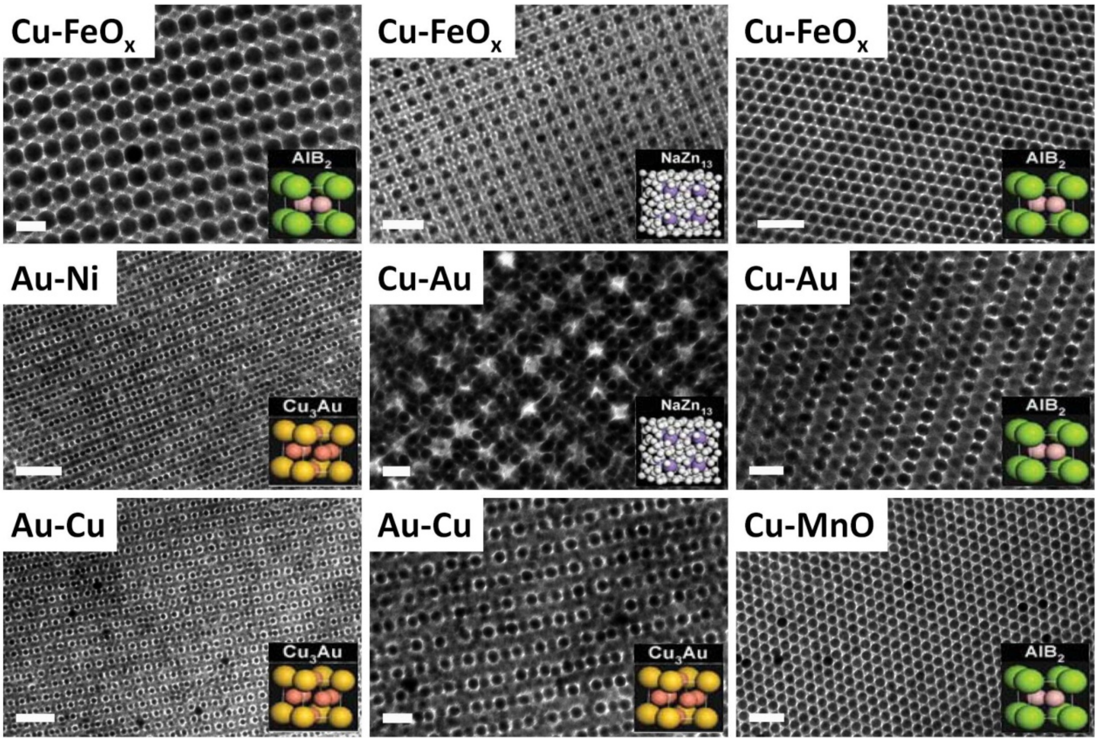

Figure 2.100. Selected artificial crystals in various compositions (upper left) and structures (lower right).

3. Electro-catalysis

Electrocatalysis is fundamental to the technologies that involve an electrocatalytic process. The most related application is fuel cell --- a device converts chemical energy to electric energy. This thesis deals with two types of most common electrocatalytic processes --- ORR and small organic molecule oxidation, which are directly related to the cathode and anode in the fuel cells, respectively.

3.1 Methods

The most applied methods to study electrocatalysis at a laboratory-scale are potential sweep methods based on a potentiostatic circuit.

3.1.1 Cyclic voltammetry

In cyclic voltammetry (CV), the potential is linear swept at a certain sweep rate, and then inverted at a selected reversing point. The sweep range is usually selected between the oxygen evolution (positive) and hydrogen evolution (negative). The sweep rate is usually between 50-500 mV/s for a reproducible surface. A typical CV curve of polycrystalline Pt is shown in Figure 3.1.

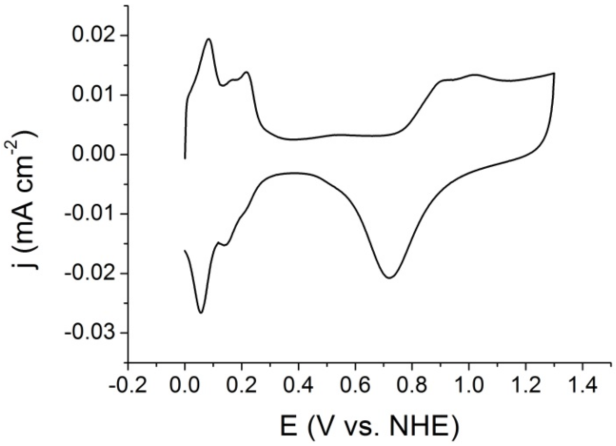

Figure 3.1 Typical CV profile for poly-crystalline Pt (here, Pt black)

3.1.2 Normalization of active surface

Surface area determination is a basic requirement for surface reaction studies. A classical method to determine the surface area has been well established by Brunaer, Emmet, and Teller, and this method is thus called BET method. However, BET measurement does not work well to determine the surface area of an electrocatalyst, because the amount of catalyst loaded on electrode is usually very small. Based on this consideration, a hydrogen adsorption method is more commonly used to determine the surface area of a metal electrode, especially Pt electrode.

As well-studied on Pt single crystal surfaces, the voltammetric profile for the adsorption-desportion of hydrogen on Pt is characteristic. To estimate the surface area of electrocatalyst by such hydrogen adsorption-desorption, two assumptions have to be made: 1) one exposed Pt atom only adsorb one H atom; 2) the potential at which a monolayer of H forms on Pt is the onset potential of hydrogen evolution.

One electron corresponds to one adsorbed H atom, according to the reaction

$$H_{ads} \rightarrow H^{+} + e^{-}$$

The total charge involved in this reaction can be calculated from the CV curves (Figure 3.1) by the equation

$$-$$

Where v is the sweep rate, j is the measured current, and j_{dl} is the current for a double layer charging. The region from 0.05 V-0.5 V in CV curves is usually taken for such surface area estimation.

The experimental measured charge per unit area for adsorbed hydrogen on Pt surface is 209 µCcm^{-2} for non-reconstructed Pt(100), and 200 µCcm^{-2} for Pt(110). Because the CV profile for Pt(111) is very special, it is difficult to select the potential range for the surface area calculation. A value of 241 µCcm^{-2} is obtained by integrating the current up to 0.6 V. The integration of CV curve up to 1.0 V gives the number of 295 µCcm^{-2} in H_2SO_4 and 320 µCcm^{-2} in $HClO_4$. With the uncertainty and many assumptions, 210 µCcm^{-2} has been widely accepted normalization factor in electrocatalysis, for a polycrystalline Pt catalyst.

3.1.3 Rotating disc method

Many electrocatalytic reactions are limited by the step of mass transfer, i.e. diffusion limited. The research on electrocatalysis is more interested on the kinetic behavior of electrocatalysts, thus, the mass transfer is usually enhanced by a rotating disc electrode (RDE). The high speed rotating disc can create a vortex that draws the liquid up along the rotating axis and flings it our radially. In such situation, an electrochemical process can be described by the Levich-Koutecky equation

– – —

$$j_{\mathrm{diff}} = 0.62\, n\, F\, D^{2/3}\, v^{-1/2}\, \omega^{1/2}\, C^{o}$$

Where j is the measured current, j_k is the kinetic current, j_{diff} is the diffusion limiting current, n is the number of electrons involved in the reaction, F is the Faraday constant, D is the diffusion coefficient, v is the kinematic viscosity, ω is the angular velocity (rotating speed), C^o is the bulk concentration.

In some circumstances, rotating disc is also employed to suppress gas formation, which interfere the electrochemical measurements.

3.2 Oxygen reduction reaction

ORR is the chemical process that occurs in the cathode of a PEM (polymer electrolyte membrane) fuel cell. It is also involved in the metal-air batteries[69,117]. The ORR has a much lower kinetics than many other electrocatalytic processes that are involved in the industry of fuel cells and batteries. Therefore, ORR is the limiting step for the cell reactions, thus, limiting the overall performance of electrochemical devices. Development of the electrocatalyst for ORR aims at lower cost and better performance than that the current Pt catalysts have. As introduced earlier, making Pt-base alloy may be a way to tune the electrocatalytic properties and reduce the cost of using precious metal at same time. I have tested the Mn-Pt nanocrystals for ORR, and the results are promising[27].

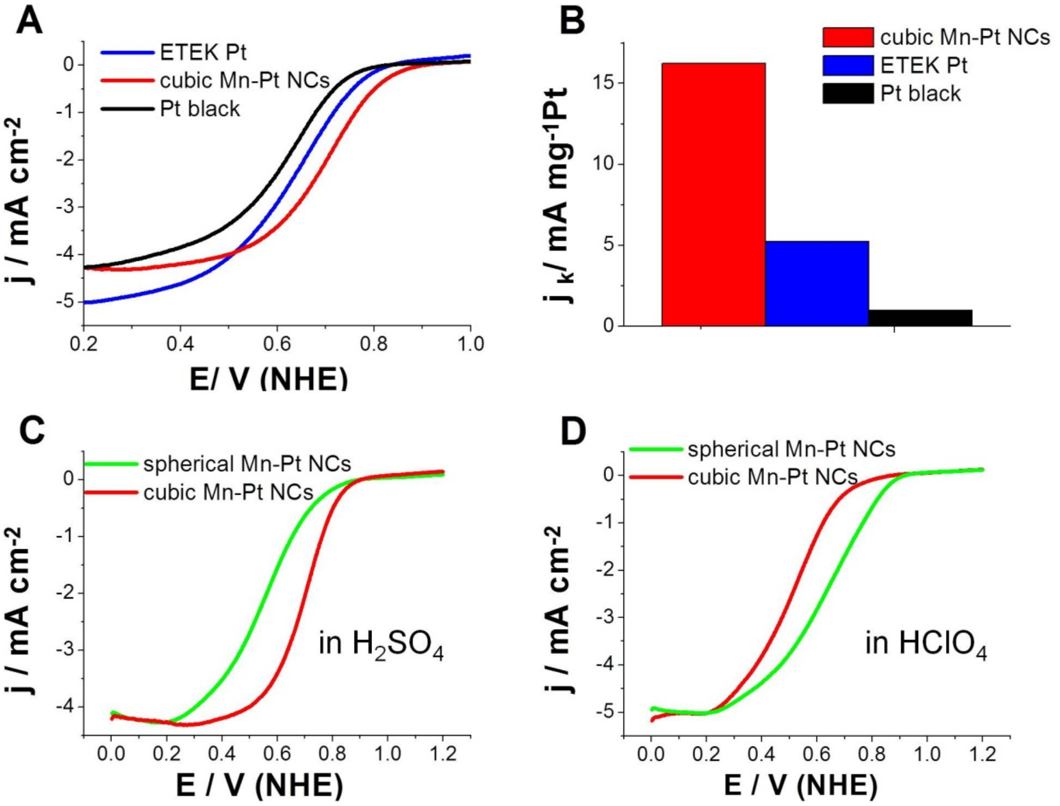

Figure 3.2. (A) ORR polarization curves for Mn-Pt nanocubes, ETEK Pt, and Pt black normalized to geometric area. (B) Mass activity (as kinetic current densities at 0.8 V) for the three catalysts. (C, D) ORR polarization curves for cubic and spherical Mn-Pt nanocrystals in (C) 0.1 M H_2SO_4 and (D) 0.1 M $HClO_4$.

Figure 3.2A shows the ORR polarization curves for as-synthesized cubic Mn-Pt NCs, commercial ETEK Pt catalysts, and Pt black. In the kinetically controlled region, the current density on cubic Mn-Pt NCs is higher than those on both the Pt black and ETEK Pt catalysts. Figure 3.2B shows the kinetic current densities (at 0.8 V) normalized to the effective mass of Pt, which indicate that cubic Mn-Pt NCs are much more active for ORR than the Pt black and ETEK Pt catalysts. The Pt-mass-normalized activity of cubic Mn-Pt NCs is over 3 times greater than that of the commercial catalyst. The ORR activity of Mn-Pt is also shape-dependent (structure-sensitive). The ORR activities of cubic and spherical Mn-Pt NCs in H_2SO_4 and $HClO_4$ are shown in Figure 3.2C, D, respectively. Interestingly, cubic Mn-Pt NCs show higher ORR activity than spherical Mn-Pt NCs in H_2SO_4, while the spherical NCs are more active in $HClO_4$. This implies that the ORR activity of Mn-Pt NCs is higher on (111) than on (100) in $HClO_4$, whereas the ORR activity is higher on (100) than on (111) in H_2SO_4 because of sulfate anion adsorption[72]. This shape-dependent property of Mn-Pt is very similar to that reported for Pt[72].

The artificial crystals offers the opportunity to combine physical and chemical properties of different building blocks in a single crystalline architecture, we take the advantage of artificial crystals to design high performance electrocatalyst. Previous research results indicate that Pd can promote the performance of Pt catalysts for various catalytic reactions, such as formic acid oxidation and ORR[12,13,45,118-120]. In the aspect of Pt, it is well know that Pt(111) possesses higher ORR activity than Pt(100)[121,122]. Therefore, the Pd-promoted Pt catalysts with Pt(111) facets are highly desirable. Unfortunately, the catalyst with such structure is highly challenging to prepare. The artificial crystals offer an alternative for the catalyst design: to physically attach Pd onto Pt(111) when the chemical method does not work well. Here, we try to put the shape effect of Pt and synergistic effect raised from the Pt-Pd interaction together into a single catalyst material.

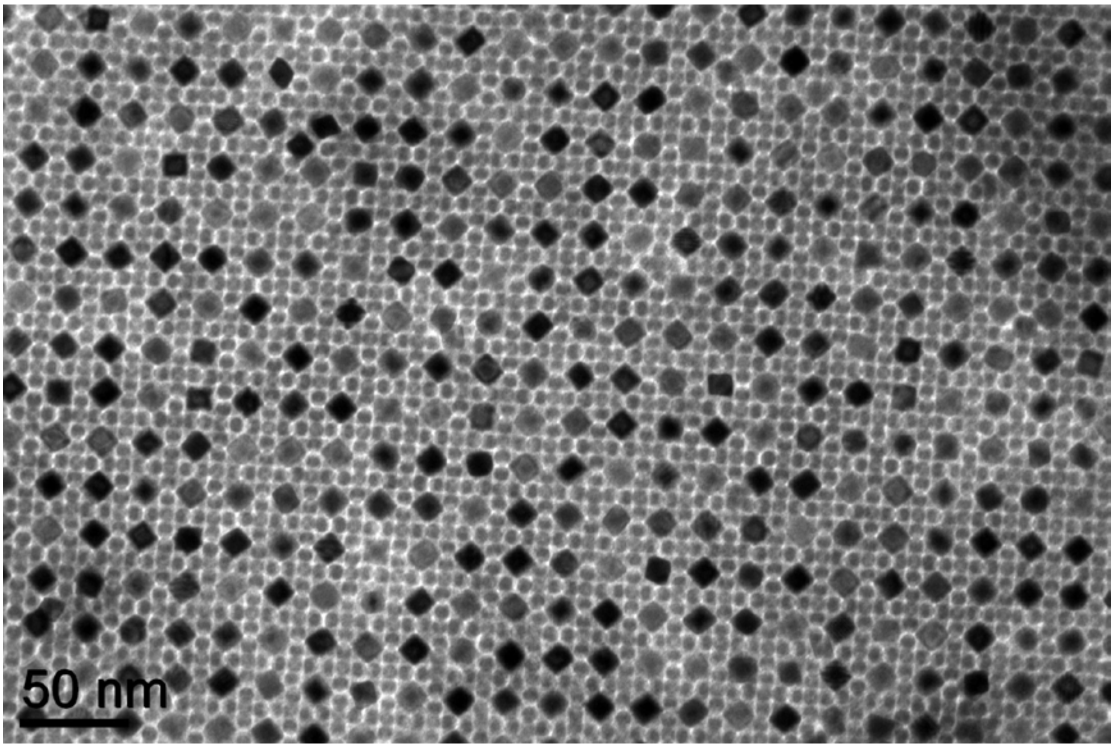

Figure 3.3 TEM image of Pt-Pd artificial crystal in the structure of $NaZn_{13}$

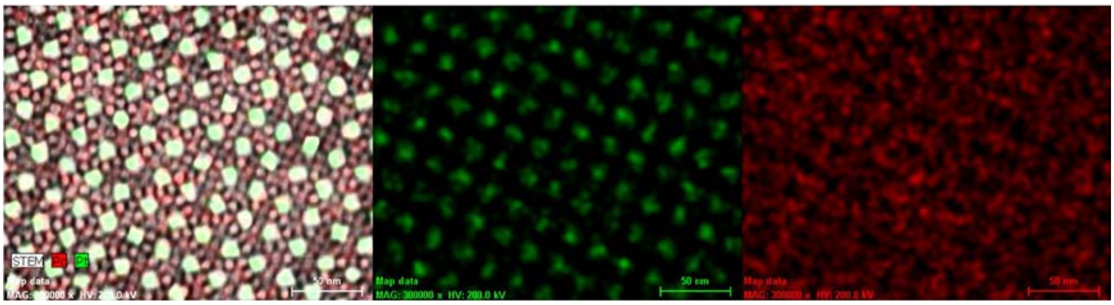

Figure 3.4 EDX mapping of Pt-Pd artificial crystal. Pt: green, Pd: red

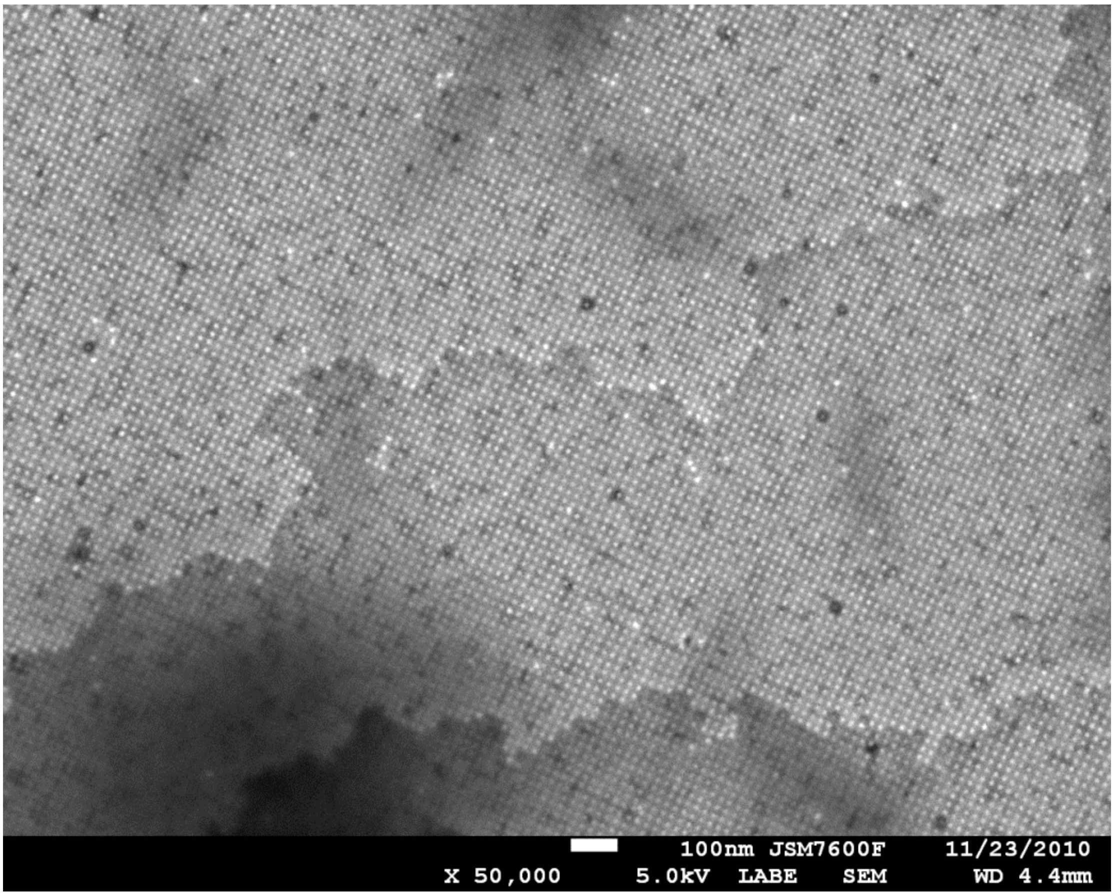

Figure 3.5 SEM image of the Pt-Pd artificial crystal for a large area

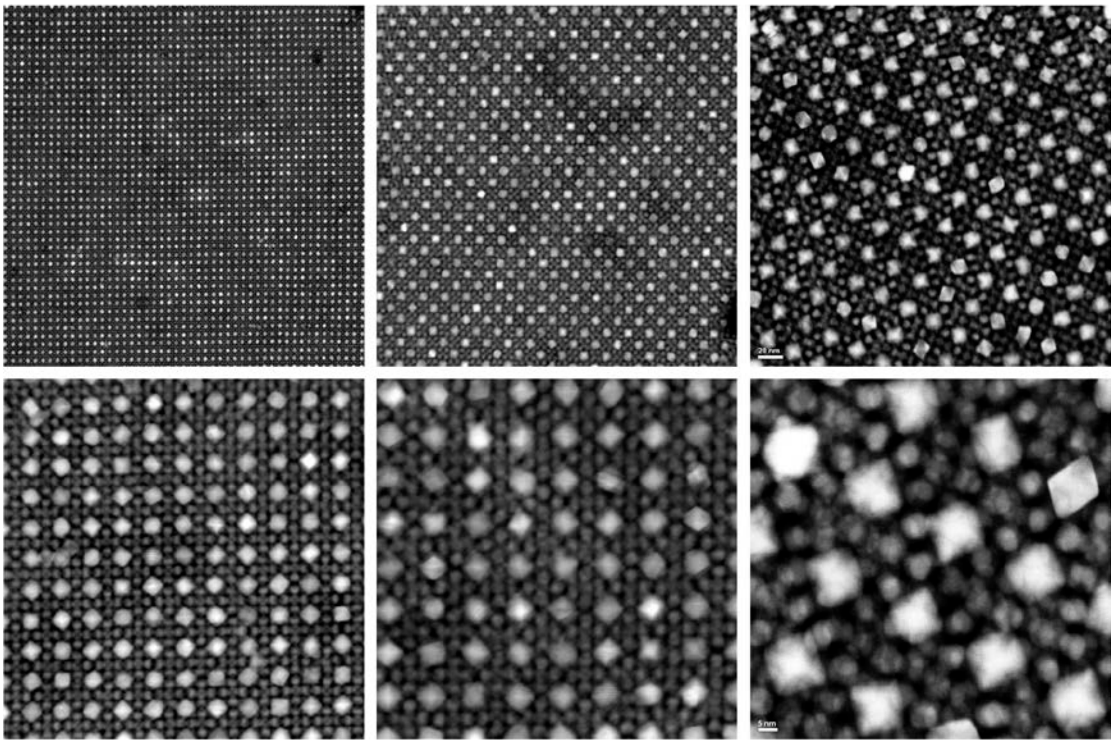

Figure 3.6 STEM-HAADF images of the Pt-Pd artificial crystals

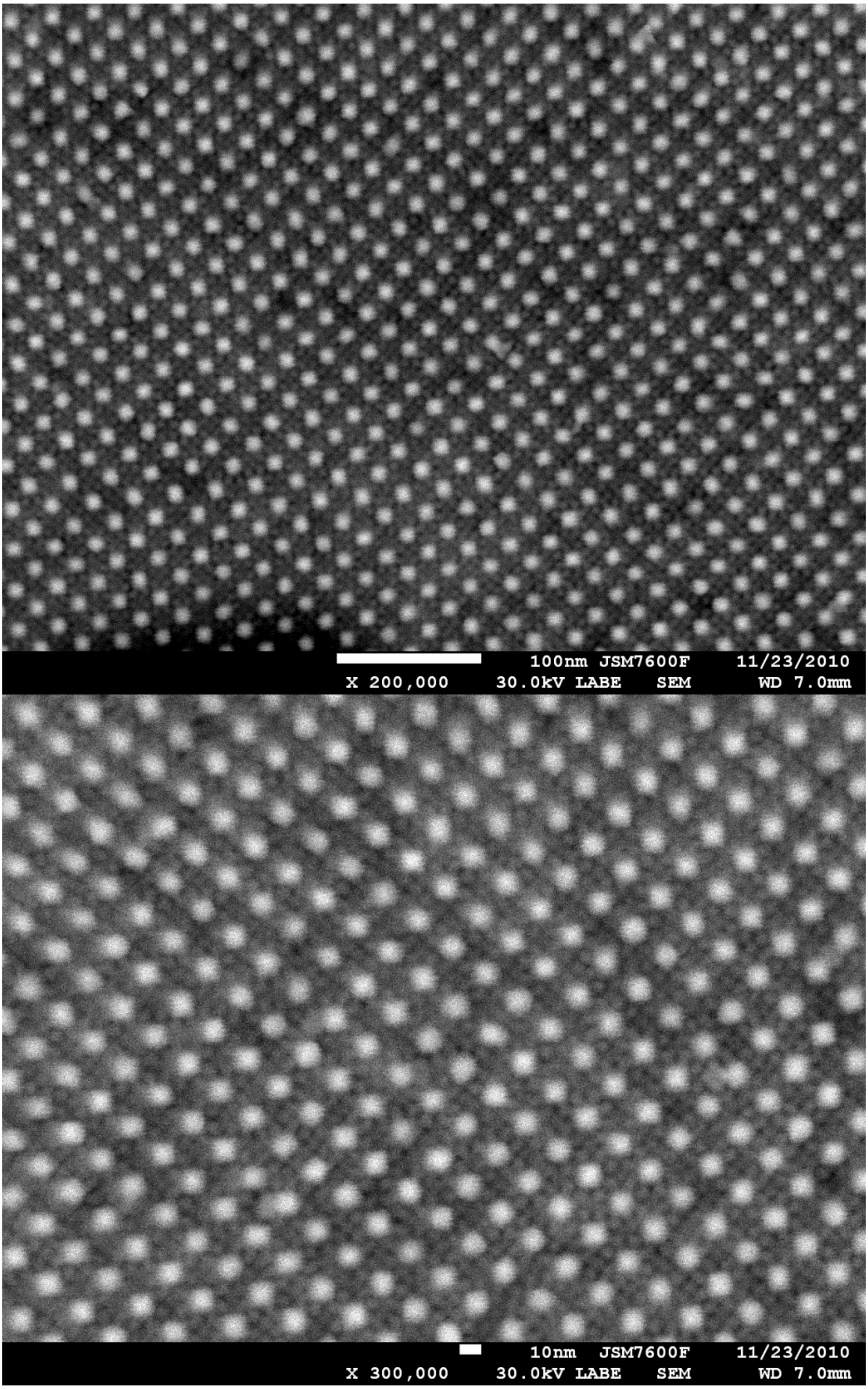

Figure 3.7 SEM images of the Pt-Pd artificial crystal showing the structure of $NaZn_{13}$

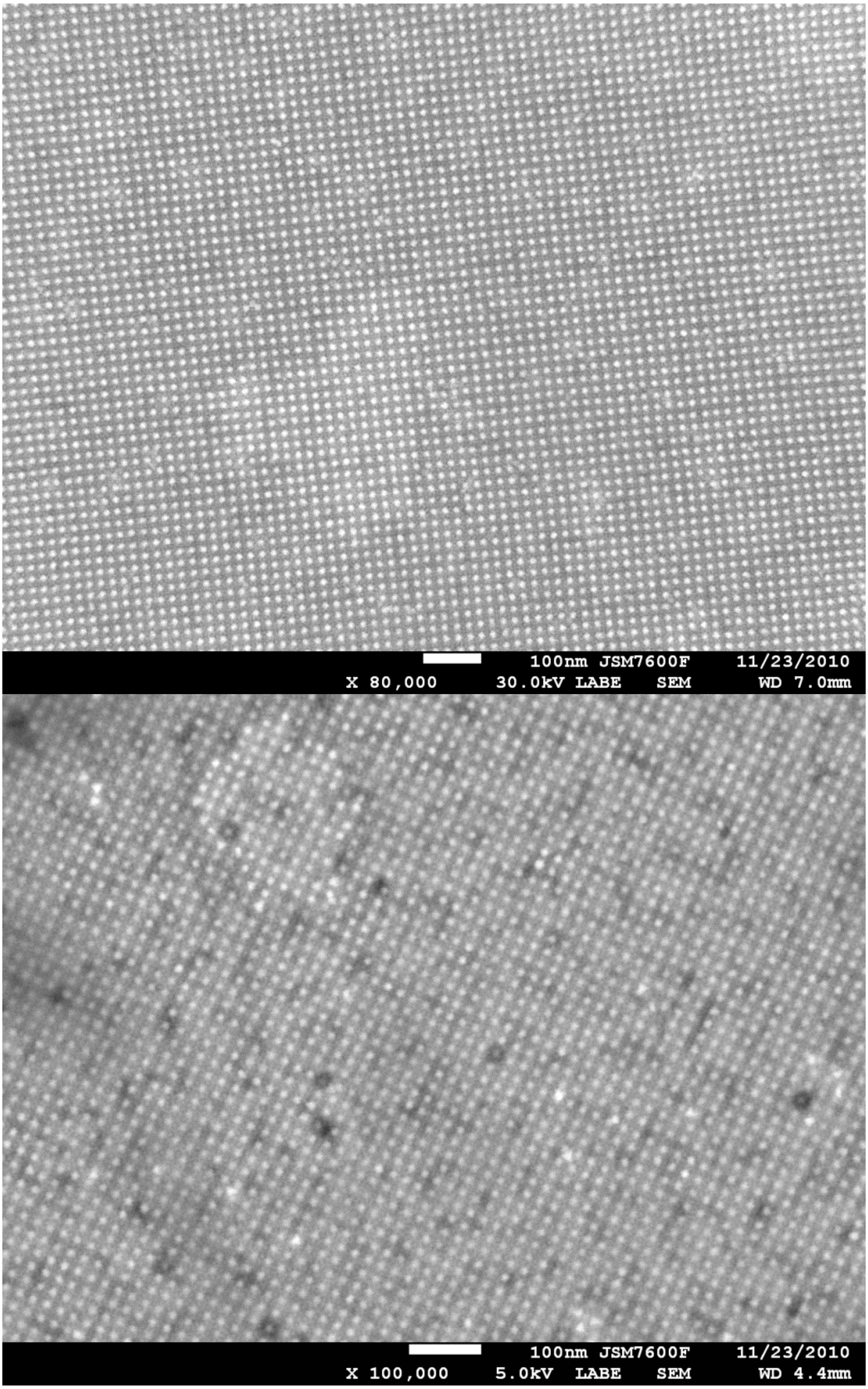

Figure 3.8 SEM images of the Pt-Pd artificial crystal showing the structure of $NaZn_{13}$

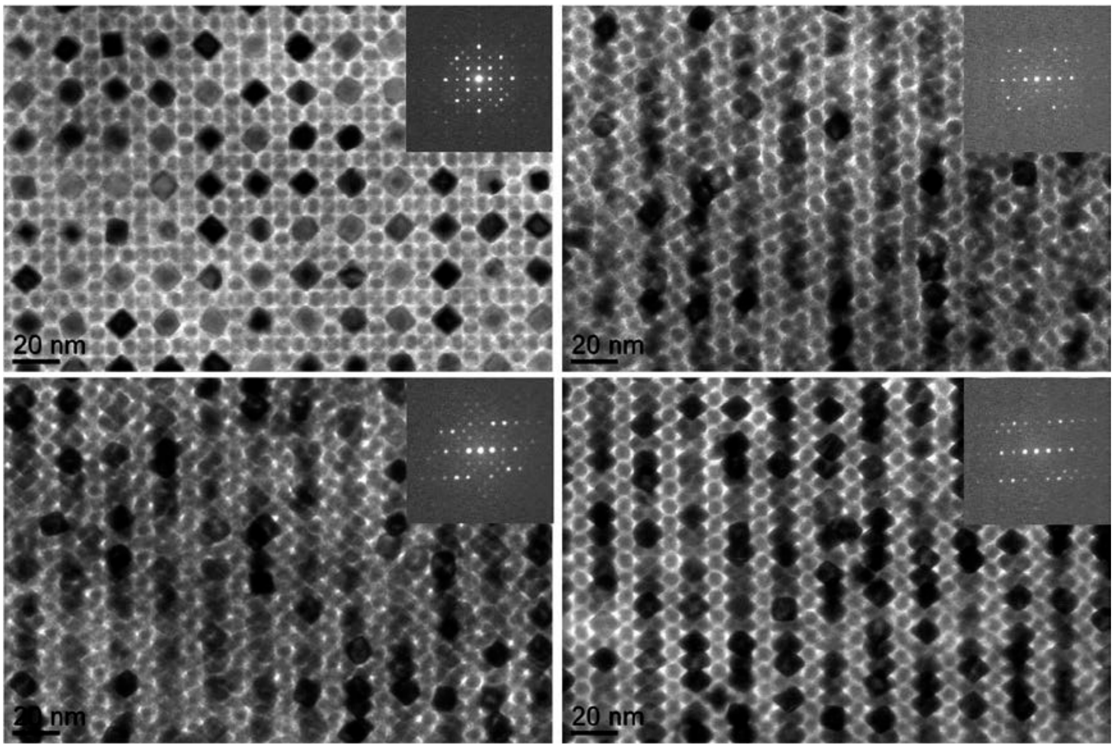

Figure 3.9 A topology analysis confirms the $NaZn_{13}$ structure for the Pt-Pd artificial crystals[123]

We assemble 5 nm Pd NCs and 13 nm (vertex to vertex) Pt octahedra which expose (111) facets, into a first 3D BNSL that consist of building blocks with shape other than sphere. The Pt-Pd artificial crystals shown in Figure 3 have an AB_{13}-structure analogue to $NaZn_{13}$. The Pt-Pd artificial crystals exhibit distinctive properties, compared to Pt or Pd alone. As Pd shows a poor ORR activity as compared to Pt, the mixture of Pt and Pd nanocrystals should be expected to have an activity in between that of Pd and Pt if there is no any synergistic effect. However, the ORR activity obtained with Pt-Pd artificial crystals is better than both of Pd and Pt, indicating the ordered structure successfully incorporated the desirable shape effect of Pt and the synergistic effect of Pt-Pd.

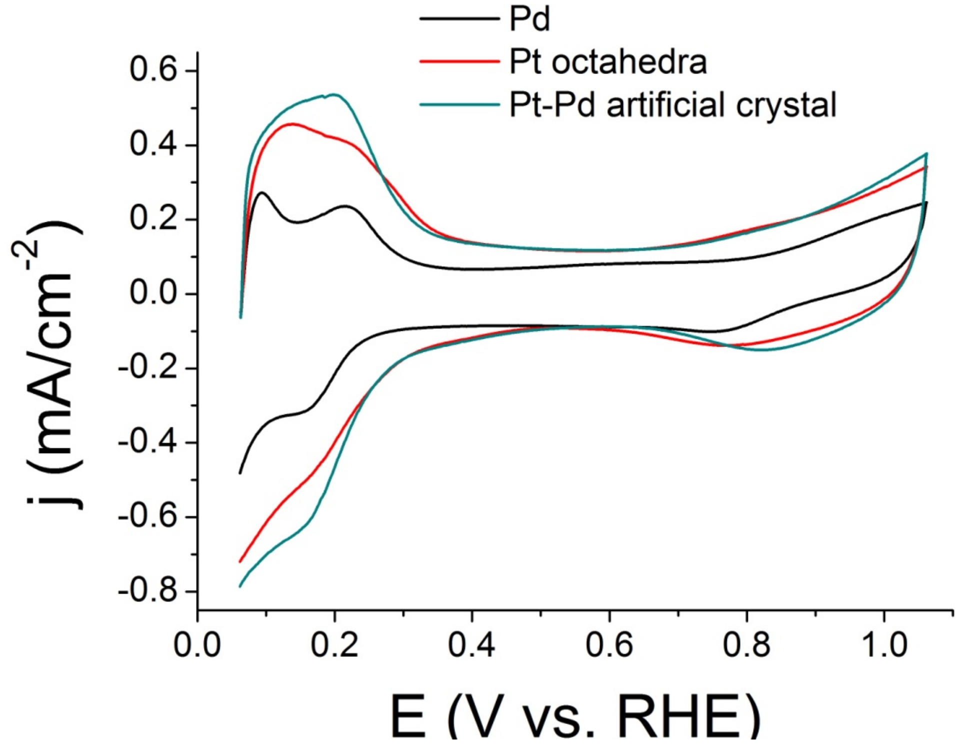

Figure 3.10 CV curves of Pt octahedra, Pd nanocrystals, and the Pt-Pd artificial crystals

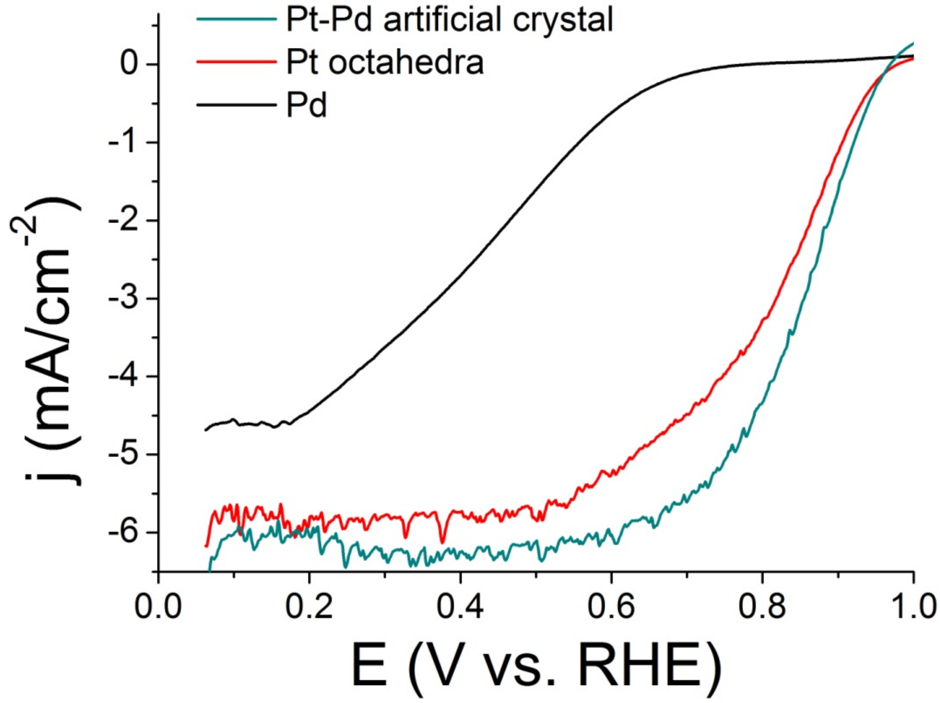

Figure 3.11 Polarization curves of ORR on Pt octahedra, Pd nanocrystals, and the Pt-Pd artificial crystals

The Pt-Pd artificial crystals in AB and AB_2-structure have also been made. However, the phase-purity and the grain size have not been optimized yet for the purpose of property measurements. It will be interesting to see the structure dependent properties on Pt-Pd after the large-scale fabrication of Pt-Pd artificial crystals in various structures become available in the near future. Based on the knowledge learned from Au-FeOx and Pt-Pd artificial crystals, we expect that a small size of Pd is desirable to maximize the utilization of Pd, thus, a catalyst of Pt octahedra decorated with ultra-small Pd particles can be highly efficient toward ORR. Such catalyst is being developed in an ongoing project. Moreover, as the artificial crystals can be controlled at a monolayer, they are promising to be a new class of high-performance catalysts, because the monolayer may help to substantially reduce the cost of materials and increase the efficiency.

3.3 Small organic molecule oxidation

Organic molecule can be directly used as fuels in fuel cells. The small organic molecules receive particular attention, because they are simplified as models to study electrooxidation reactions, and, they are easy to be produced, through either routine chemical process or low-cost biochemical production. The typical small organic molecules include methanol, formic acid, formaldehyde, ethanol, and etc. In this thesis, I focus on formic acid and methanol, two simplest organic molecules.

3.3.1 Formic acid oxidation

Electrocatalysis of FA oxidation reactions has been intensively studied for two main reasons: first, FA is an attractive chemical fuel for fuel cell applications due to its high energy density (1740 Wh/kg, 2086 Wh/L) and easy storage[124-126]; second, FA is the smallest molecule that has four most common chemical bonds in organic compounds (C-H, C=O, C-O, O-H), making FA a perfect model molecule for studying electrooxidation reactions.

Three possible reaction pathways of FA oxidation have been proposed[127-130]:

(i) $HCOOH^* \rightarrow COOH^* + H^+ + e^- \rightarrow CO_2 + 2H^+ + 2e^-$

(ii) $HCOOH^* \rightarrow HCOO^* + H^+ + e^- \rightarrow CO_2 + 2H^+ + 2e^-$

(iii) $HCOOH^* \rightarrow CO^* + H_2O \rightarrow CO_2 + 2H^+ + 2e^-$

Here, * represents an adsorbed state. (i) is referred to as the direct pathway, where the removal of the first hydrogen atom (dehydrogenation) from the C-H bond occurs to produce a hydroxy carbonyl, and then a second dehydrogenation step occurs at the O-H bond to produce CO_2. (ii) is called the formate pathway, in which the dehydrogenation first occurs at the O-H bond to produce formate, and then at the C-H bond to generate CO_2. (iii) is known as the indirect pathway, in which CO* is produced by non-Faradaic dehydration of FA, then is further oxidized to CO_2. Both (i) and (ii) are accomplished by dehydrogenation (via different intermediates) to form CO_2 directly, so (i) and (ii) are sometimes referred to "direct pathway" jointly.

The electrocatalysis of FA oxidation has been studied on various metal surfaces. Among all the pure metals, platinum (Pt) exhibits the highest activity. Figure 3.12b shows a typical voltammetry curve of FA oxidation on Pt catalyst. The first peak (peak **I**) in the anodic scan appears at ≈0.5 V, corresponding to the direct pathway (including the formate pathway here). The current of peak **I** is usually very low, because the inactive poisoning intermediates are accumulated long before the potential reaches 0.5 V. Taking the example of reactions at 0 V, as shown in Figure 3.12c, the first steps of the formate pathway (ii) and the indirect pathway (iii) are favorable due to their low reaction barriers while the generated CO* species are strongly adsorbed on the Pt surface. In addition, the large reaction barriers of the second steps of (ii) and (iii) make the poisoning intermediates particularly stable on the Pt surfaces. The second anodic peak (peak **II**) shows up at ≈0.9 V, with higher current than peak **I**, because at high potential (Figure 3.12d, e) the reaction barrier of the second step is significantly reduced. In the cathodic scan, the current (peak **III**) is much higher than that of peak **I** and **II** due to the removal of the poisoning intermediate at high potential.

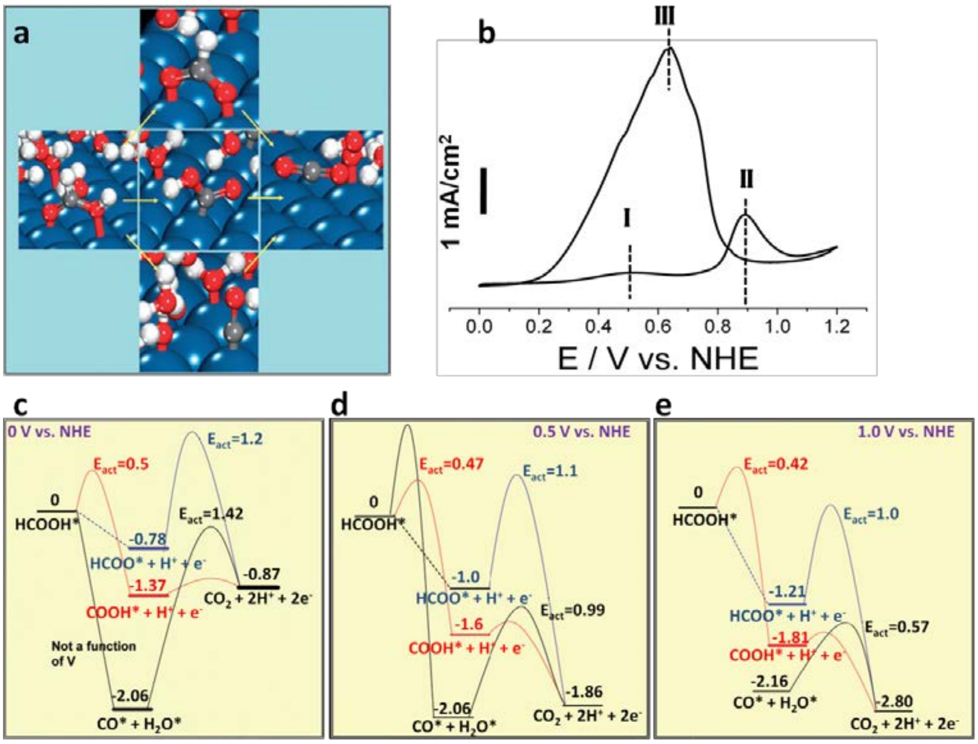

Figure 3.12. a) Models representing formate pathway (top), direct pathway (center), and indirect pathway (bottom); b) a typical cyclic voltammetry curve for formic acid electrooxidation on (poly-oriented) Pt catalyst; c-e) DFT-calculated potential energy surface for the direct, indirect, and formate pathways for the oxidation of formic acid over Pt(111), held at constant potentials. *[130] – Reproduced by permission of The Royal Society of Chemistry*

The FA oxidation is structure sensitive to the surface of Pt. Experiments done on the well-defined single crystals of Pt (Figure 3.13) have demonstrated that the poisoning effect is strongest on Pt(100) and weakest on Pt(111), and the total activity follows the trend of Pt(100) > Pt(110) > Pt(111)[131,132]. The studies on preferentially oriented Pt nanoparticles also suggest the same trends as observed on single crystals[6]. In the real catalysts, poly-oriented Pt crystal inevitably brings the poisoning problem. For this reason, existing Pt-based electrocatalysts can accomplish FA oxidation only at extremely positive potentials (i.e., at potentials without technological interest). Therefore, the development of direct formic acid fuel cells (DFAFCs) has been impeded by the low activity of existing electrocatalysts at desirable operating voltage (i.e. at low oxidation potential).

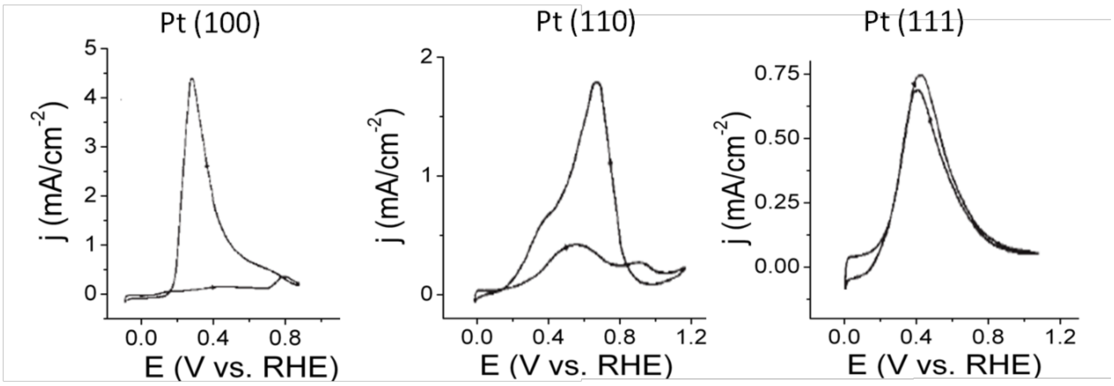

Figure 3.13. Electrooxidation of formic acid (0.26M) on single crystal Pt electrodes with (100), (110), and (111) orientations in 1M $HClO_4$, sweep rate: 50mV/s. *[132] – Reproduced by permission of Nature Publishing Group*

Various efforts have been made to improve the Pt-based electrocatalysts. One direction is the use of foreign metal adatoms. As early as in 1975, Adzic et al. demonstrated that monolayers of a foreign metal (i.e. Cd, Tl, Pb, Bi) underpotential deposited on Pt exhibit enhanced activity and pronounced catalytic effects on electrocatalysis of FA oxidation[10]. By recognizing that a foreign metal may promote the performance of Pt toward FA electrooxidation, scientists have attempted to employ Pt-based alloys for the new generation of electrocatalysts. For instance, cubic Mn-Pt alloy nanocrystals (Figure 3.14) and Pt-Ru alloy[133] surface can effectively reduce the poisoning effect on the electrocatalyst. However, the maximum current is still obtained at fairly high oxidation potential.

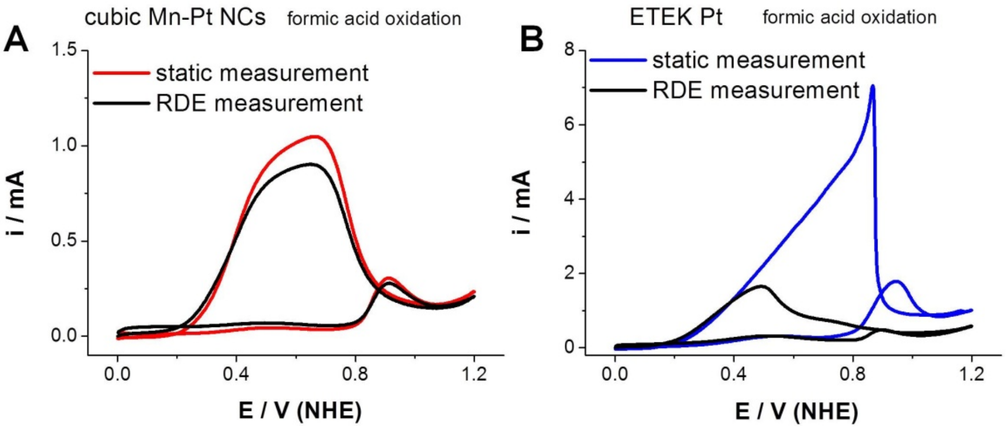

Figure 3.14. Formic acid oxidation measurements performed on static electrodes and RDE (2500rpm). Each RDE measurement is carried out immediately after the static measurement on the same electrode. On Pt catalysts, the poisoning CO species are usually formed during the anodic sweep, and are partially removed at high potentials. The rotating disc brings fuels to electrode much faster than diffusion, poisoning the electrode even faster. Therefore, the RDE measurements show lower current than the static measurements. However, on cubic Mn-Pt nanocrystals, this accelerated poisoning effect is not as significant as in the case of on ETEK Pt catalysts, indicating that Mn-Pt may have better tolerance to poisoning.

Ideally, an electrocatalyst should have both good poisoning tolerance and high activity at low oxidation potential. For this consideration, Pb has been targeted as promising adatom or alloying element to enhance FA oxidation activity and CO-poisoning tolerance. Adding Pb into Pt electrocatalysts to improve their performance has not only been demonstrated by underpotential deposited Pb[10,134], but has also been reinforced by PtPb alloys made under high temperature annealing[81]. Pt-Pb nanoparticle electrocatalysts in various compositions and phases have also been developed subsequently[135-138]. Taking Pt_3Pb NCs synthesized via solution-phase-synthesis as an example (see Chapter 2.4 and 2.6), Figure 3.15a shows the superior electrochemical performance of Pt_3Pb NCs, compared to pure Pt (Pt black, Aldrich). As described earlier, FA oxidation on electrocatalysts follows both direct (including the formate pathway) and indirect pathways, corresponding to peak **I** and peak **II** in Figure 3.15d, respectively. The indirect pathway dominates the reactions on Pt catalysts, making the Pt unsuitable for DFAFC. However, on Pt_3Pb the direct pathway is more favorable, with little reaction occurring via the indirect pathway. At 0.3V (typical anodic working voltage in DFAFC), the FA oxidation activity on Pt_3Pb is 33 times greater that on Pt.

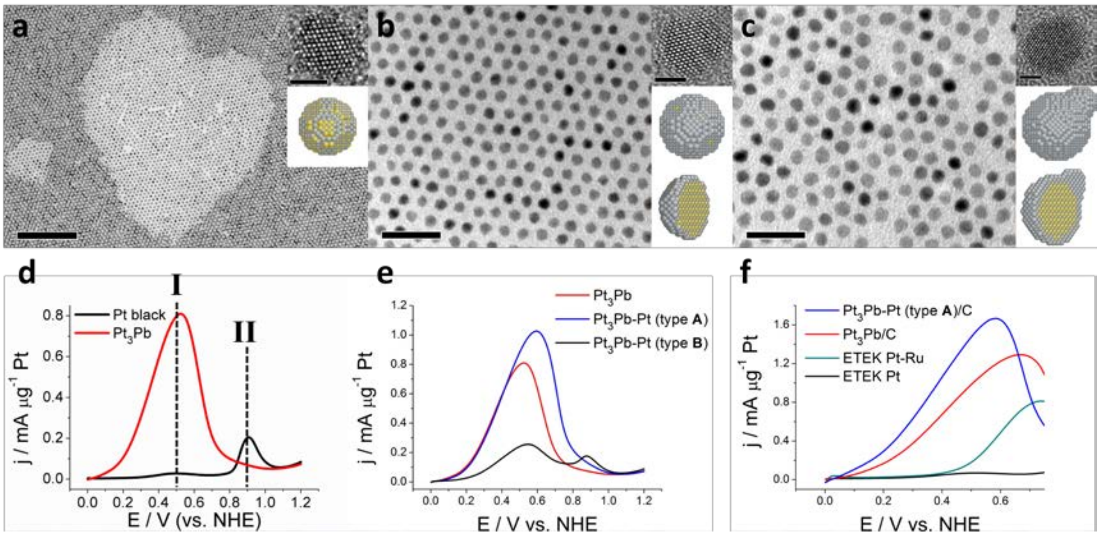

Figure 3.15. TEM and HRTEM (insets) images of a) Pt_3Pb NCs, b) type **A** and c) type **B** Pt-Pb core-shell NCs. Scale bars: (a)100nm, (b, c)20nm, (insets)2nm. Polarization curves of d) formic acid oxidation on Pt black and Pt_3Pb, e) formic acid oxidation on Pt_3Pb and Pt-Pb core-shell NCs, and (f) maximum activities of formic acid oxidation on carbon supported catalysts, in the solution of 0.5M formic acid and 0.1M H_2SO_4, sweep rate: 20mV/s.

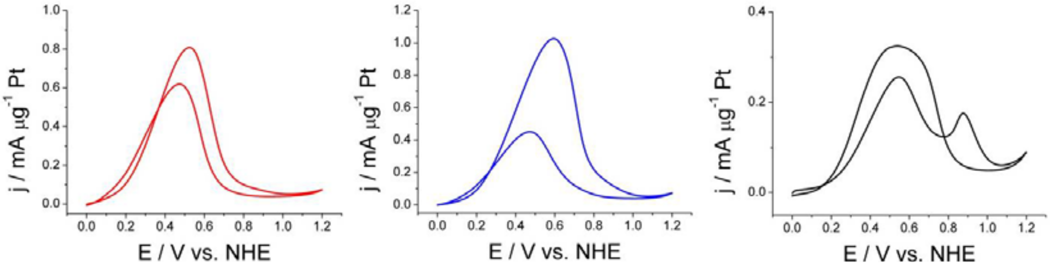

Figure 3.16. Full polarization curves of FA oxidation on (red) Pt_3Pb NCs, (blue) type **A** and (black) type **B** Pt-Pb core-shell NCs.

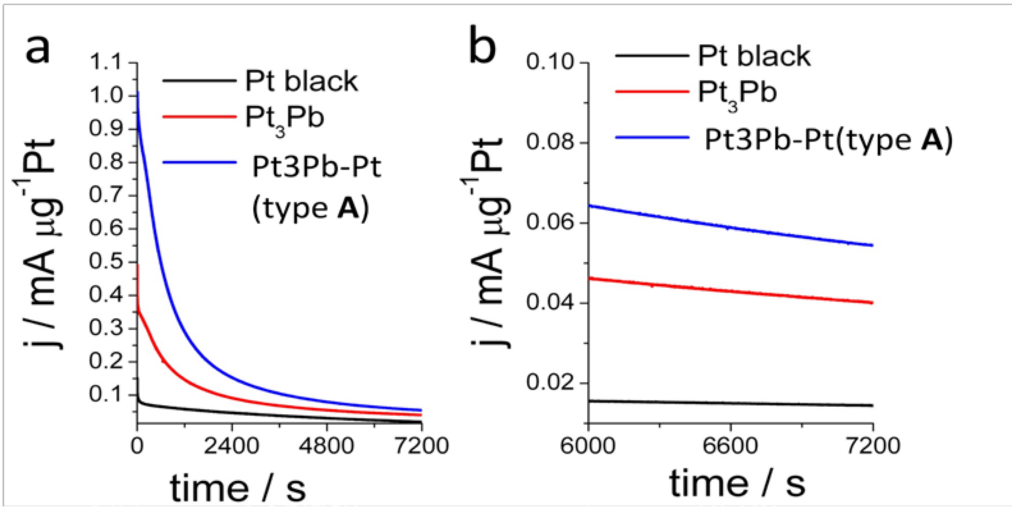

Figure 3.17. Chronoamperometric curves (at 0.4V) of formic acid oxidation on Pt_3Pb, Pt_3Pb-Pt(type **A**), and Pt black.

Not only the composition, but also the structure of electrocatalysts is important for desirable performance[119,120,139-142]. Figure 3.15b shows the Pt-Pb NCs with a monolayer of Pt on the Pt_3Pb NC seeds (we call this type **A** core-shell Pt-Pb NCs); Figure 3.15c shows the NCs with much thicker Pt shell, as well as some Pt islands (we call this type **B** core-shell Pt-Pb NCs). Figure 3.15e presents the comparison of activities for the different Pt-Pb nanostructures. The Pt_3Pb–Pt(type **A**) NCs show the highest activity toward FA oxidation. The activity on Pt_3Pb–Pt(type **B**) NCs is much lower than that on the other two Pt-Pb nanostructures, while a peak at higher potential is observed, indicating the FA oxidation on Pt_3Pb–Pt(type **B**) NCs does occurs via the indirect pathway. It is worth noting that the Pt-Pb electrocatalysts demonstrated in Figure 3.15d and 3.15e are dense film (Figure 3.18) rather that a supported catalyst. ETEK Pt, a commercial fuel cell catalyst, Pt is supported on high surface area carbon (Vulcan-72R), which enables much higher catalyst utilization of ETEK Pt. To make the Pt-Pb electrocatalysts comparable to the commercial electrocatalysts, the Pt-Pb NCs are loaded on to Vulcan-72R. The resulting Pt_3Pb/C and Pt_3Pb-Pt(type **A**)/C catalyst exhibit high activity, which is about 15 and 25 times (at 0.3V) higher respectively than the corresponding activity of the commercial Pt/C catalyst (Figure 3.15f). Figure 3.20 shows *in-situ* infrared reflection absorption spectra (IRRAS) of FA oxidation on different catalysts. The positive-going band at 2343cm^{-1} is attributed to the asymmetric stretch vibration of CO_2, the product of FA oxidation. The band at around 2030cm^{-1} is assigned to linear bound CO_L, the poison intermediate generated from FA indirect pathway. The CO_L bands on Pt_3Pb-Pt(type **B**) NCs show lower intensity compared to the ones generated from pure Pt, and no CO_L band is observed on both Pt_3Pb and Pt_3Pb-Pt(type **A**) NCs. The results suggest that FA oxidation occurs on Pt_3Pb or Pt_3Pb-Pt(type **A**) via the direct pathway, and on Pt_3Pb-Pt(type **B**) or Pt black via the indirect pathway.

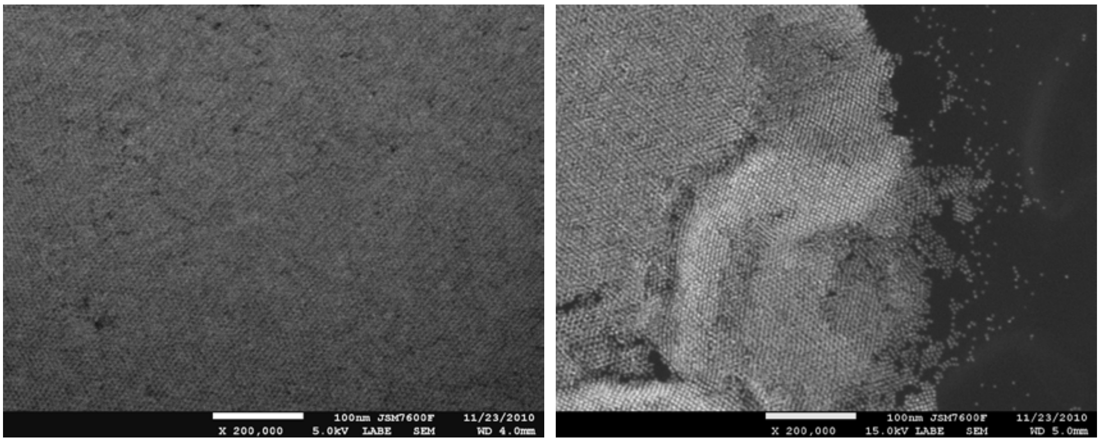

Figure 3.18. SEM images show a dense film (and the edge of the film) of the Pt_3Pb nanocrystals. Scale bars: 100nm

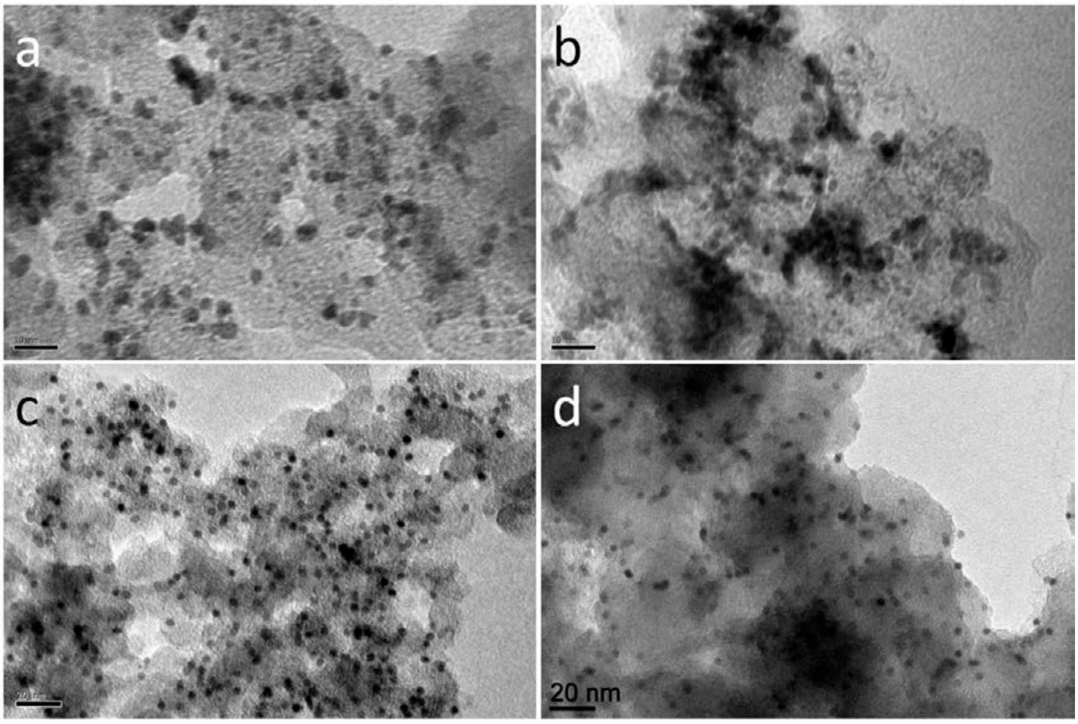

Figure 3.19. TEM images of a) ETEK Pt, b) ETEK PtRu, c) Pt_3Pb/C, and d) Pt_3Pb-Pt(type **A**)/C catalysts. Scale bars: a, b) 10nm, c, d) 20nm

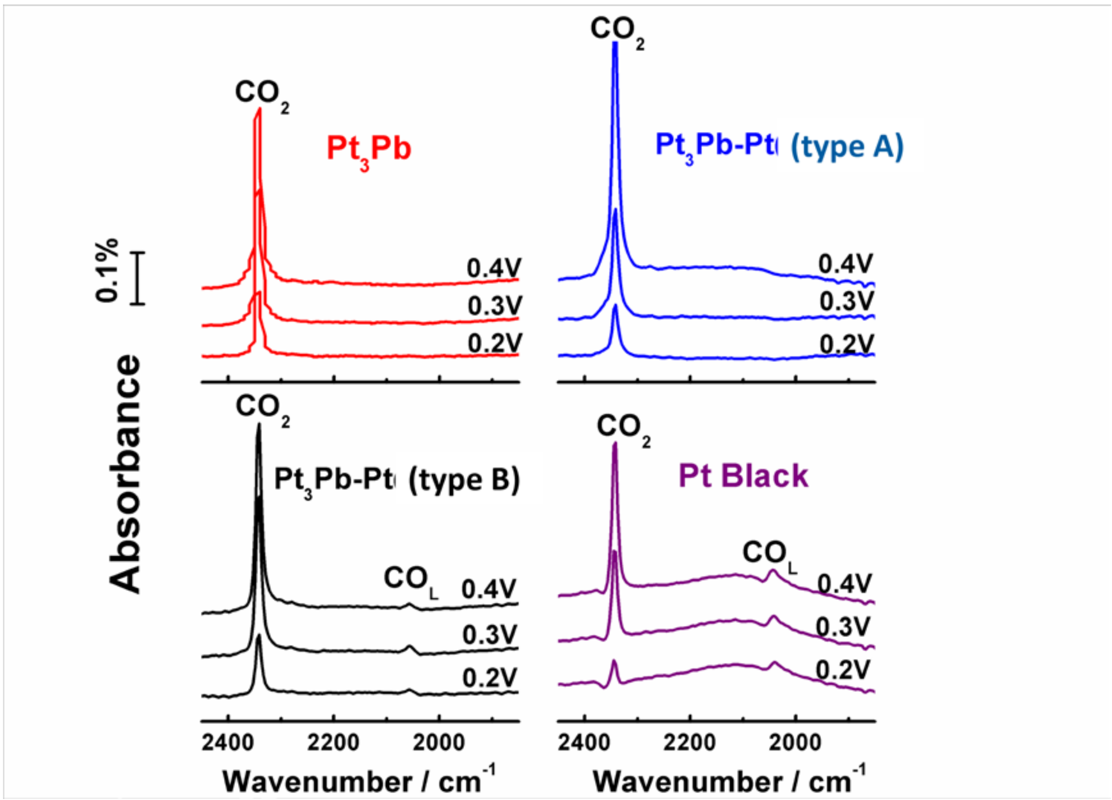

Figure 3.20. *in-situ* IRRAS spectra for formic acid oxidation on Pt-Pb nanostructures and Pt black.

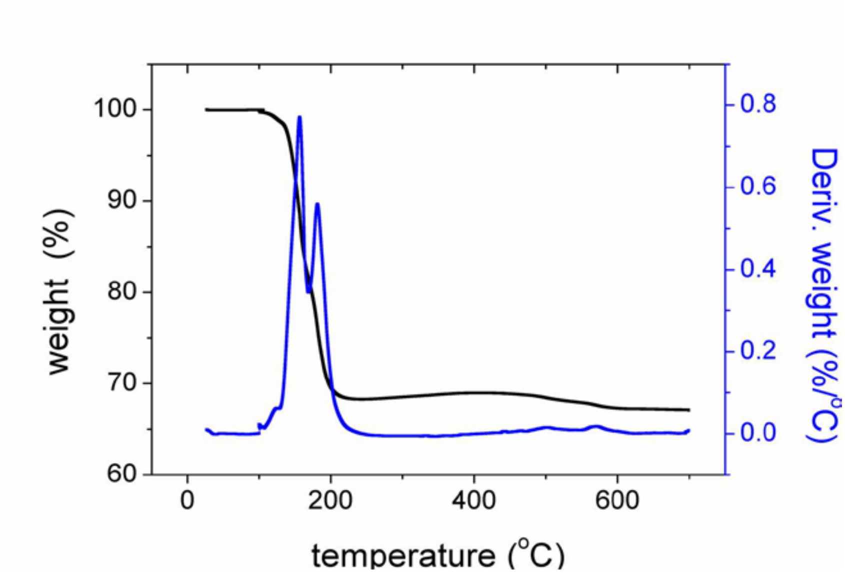

Figure 3.21. TGA data suggests that the organic ligands can be removed by thermal treatment at as low as 210°C under air.

No peak for CO oxidation is observed in the polarization curves for both Pt_3Pb and Pt_3Pb –Pt (type **A**) NCs, because Pb alloying can relieve the CO-poisoning effect by weakening the adsorption strength of CO, as predicted in previous DFT calculations[143]. As a result, the FA oxidation activity increases at low potential due to the reduced CO poisoning. On the other hand, the low activity of Pt_3Pb-Pt (type **B**) NCs can be explained by the structural relaxation of the Pt atoms deposited on Pt_3Pb NCs. According to XRD results, the Pt_3Pb-Pt (type **B**) NCs have a lattice constant close to pure Pt, smaller than lattice constants for Pt_3Pb NCs and Pt_3Pb-Pt (type **A**) NCs. Excess Pt atoms form thick Pt-layers and Pt cluster islands on the Pt_3Pb NCs. These Pt thick layers and islands have similar electrocatalytic properties to pure Pt, which generates CO^* from FA dehydration and decreases the overall activity. However, this mechanism cannot explain the further increase of total activity for Pt_3Pb–Pt (type **A**) NCs relative to Pt_3Pb NCs, since both have almost no CO poisoning effect, thus there must be other factors for the increase of the activity beside the avoidance of CO poisoning originated from Pb alloying.

In order to understand physical mechanisms of activity enhancements on these Pt_3Pb NCs, we perform a series of DFT calculations to obtain the reaction energetics in different possible reaction paths on several model surfaces. As shown in Figure 3.22a, pure Pt NCs are simulated by a Pt (111) surface; Pt_3Pb NCs are simulated by a (111) surface of Pt_3Pb crystal; Pt_3Pb –Pt (type **A**) NCs are simulated by the Pt_3Pb (111) surface with the top layer as pure Pt, labeled as Pt_3PbPt (111). Lattice constants of Pt and Pt_3Pb obtained from DFT calculations are 3.98 Å and 4.13 Å, respectively. Both the direct path and formate path are explored on these surfaces as following: (i) direct pathway: $HCOOH \rightarrow HCOOH^* \rightarrow COOH^* + H^* \rightarrow CO_2 + 2H^*$; (ii) formate pathway: $HCOOH \rightarrow HCOOH^* \rightarrow HCOO^* + H^* \rightarrow CO_2 + 2H^*$. Here we use these surface reactions under ultra-high-vacuum (UHV) conditions to simulate the corresponding electrochemical reactions, which is a general procedure to qualitatively describe the activities of electrocatalysts.

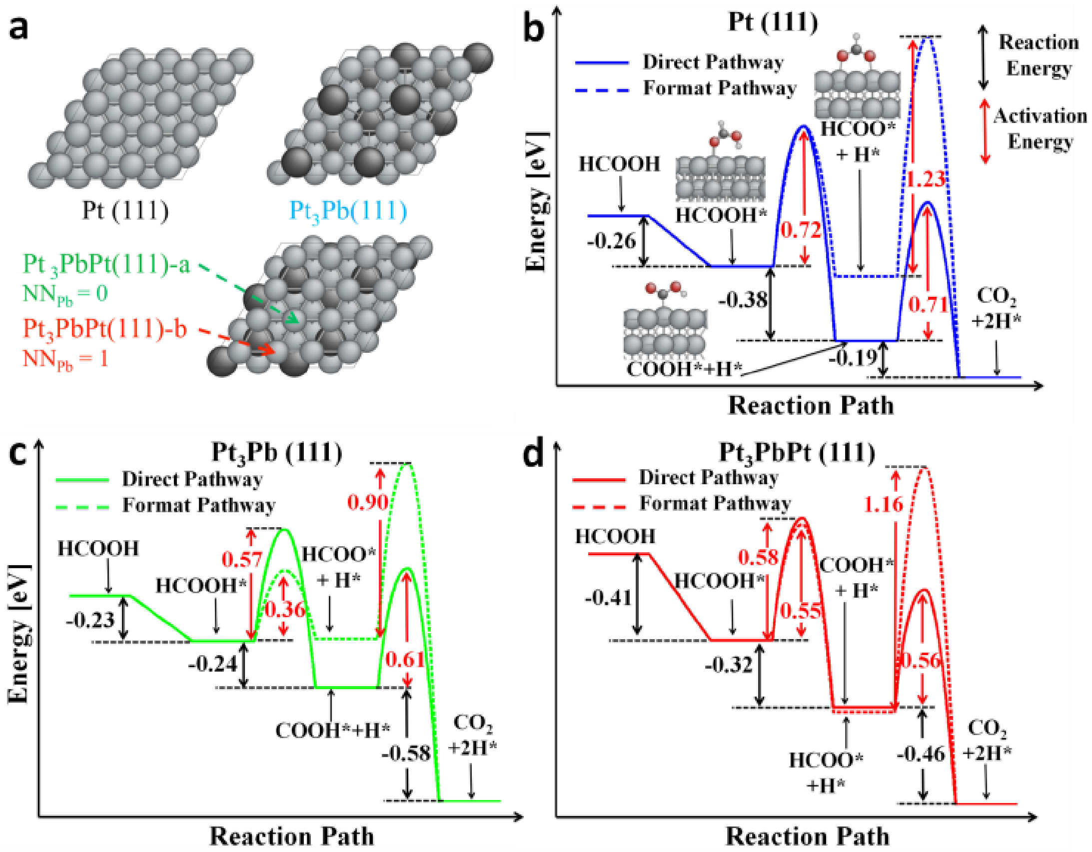

Figure 3.22. a) Surface models of Pt (111), Pt_3Pb (111) and Pt_3Pb-Pt (111) atoms. Grey (black) stands for Pt (Pb) atoms. b, c, d) Reaction pathways of HCOOH → $CO_2 + 2H^*$ with reaction/activation energies of elementary steps on different model surfaces. Here the final product H* is located at the most stable adsorption site on the corresponding surface, thus three surfaces have different total reaction energies because of different H adsorption strengths.

The reaction and activation energies for all elementary steps in both pathways on these three types of model surfaces are listed in Figure 3.22b, c, and d, respectively. On the Pt (111) surface, the first dehydrogenation step in the formate pathway has almost the same activation barrier as the direct pathway (0.71 eV), indicating a significant proportion of HCOOH* may first lose the hydrogen atom connected to the oxygen atom; however, the formate pathway has much higher activation barrier than the direct pathway for the second dehydrogenation step (1.23 eV vs. 0.71 eV). Thus, even without CO poisoning, the total reaction rate may be impeded by the stable formate intermediate occupying a large fraction of active sites on the surface. On the

Pt_3Pb (111) surface, all the activation barriers are decreased in comparison with Pt (111), indicating that the total activity of FA oxidation may increase. However, the activation barrier for the first dehydrogenation step in direct pathway is much higher than its counterpart in the formate pathway (0.57 eV vs. 0.36 eV), which means formate "poisoning" could become worse on the Pt_3Pb (111) surface. Finally, for the Pt_3PbPt (111) surface, there are two types of Pt atoms on the top Pt layer, type **a** [without Pb as nearest neighbor ($NN_{Pb} = 0$)] and type **b** [with one Pb as nearest neighbor ($NN_{Pb} = 1$)], and type **a** has a stronger adsorption strength for reaction intermediates than type **b**. The paths are found to have lowest activation barriers when carbon-related intermediates (HCOOH*, COOH*, HCOO*) are adsorbed on type **a** atom and H atoms are adsorbed on type **a** atoms. In these paths, the dehydrogenation steps for both direct and formate pathways have comparable activation barriers (0.58 eV vs. 0.55 eV), much smaller than those on Pt (111), which means that the formate "poisoning" effect on Pt_3PbPt (111) surface is much smaller than on Pt_3Pb (111) surface. For the second dehydrogenation step in the direct pathway, the dehydrogenation barrier is also smaller than that on Pt_3Pb (111) surface (0.56 eV), so this path has the smallest maximum barrier on these investigated surfaces. In addition, as shown in Figure 3.22b-d, the adsorption strengths of HCOOH on Pt_3PbPt (111) increase compared with Pt (111) and Pt_3Pb (111) surface. Because the adsorption energy of HCOOH is relatively weak compared with those of typical small molecules, such as H_2, O_2 and is even comparable with H_2O (~ -0.2 eV), a stronger adsorption strength may increase the coverage of HCOOH* on catalyst surfaces for the following reaction steps.

In summary, combined experimental and theoretical studies show that the increased activity for Pt_3Pb NCs and Pt_3Pb–Pt (type **A**) NCs relative to Pt NCs results from the elimination of CO poisoning and decreased barriers for dehydrogenation steps. The further increase of activity for Pt_3Pb–Pt (type **A**) NCs relative to Pt_3Pb NCs may result from continuous decreases of dehydrogenation barriers, strong adsorption of reactant molecules and, most importantly, the suppression of the formate path and avoidance of stable formate intermediates. However, the overall activity decreases with further increase of Pt ratio due to CO* poisoning caused by structural relaxation of the extra Pt atoms. Thus, both the existence and thickness of the Pt shell surrounding Pt_3Pb NCs are critical to achieve high reaction rate, reinforcing the notion that even materials with very similar chemical compositions can be manipulated by control of nano-scale structure to obtain high catalytic activities.

Metals other than Pt have also been extensively investigated. Nevertheless, noble metals are still the focus. Pd has comparable activity to Pt in nanocrystalline form. Additionally, a Pd thin film deposited on Au shows a high CO poisoning tolerance, and an improved activity in the low oxidation potential region. The FA electrooxidation on Au/Pd is structure sensitive, as Au(100)/Pd exhibits the highest activity among Au/Pd electrocatalysts. Besides the metal (or alloy) electrocatalysts themselves, the supporting materials and their interaction with an electrocatalyst are receiving more and more attention in recent years, especially since materials such as carbon nanotubes and graphene have emerged as potentially useful supporting materials. Nonetheless, there is still a long way to go before the discovery of either “super cheap” or “super active” electrocatalysts suitable for the large scale adoption of DFAFC.

Future Directions

Though many improved electrocatalysts have been reported, the development of practical electrocatalysts for FA oxidation remains challenging due to the following issues.

1. Insufficient activities: existing electrocatalysts for FA oxidation are still not active enough for the practical application of DFAFC at large scale.
2. Poor stabilities: Pt-Pb electrocatalysts have already achieved high activities, especially at low oxidation potentials; however, their stabilities are still less than projected. Pt-based alloys have a variety of advantages, but all such alloys face the problem of leaching, especially in acid-media. None of the existing electrocatalysts meets the standard of stability for industrial implementation (e.g. 5000 hours lifetime).
3. High cost: considering the cost for large scale applications (e.g., automobile), Pt-based materials and other noble metals are far too costly for wide adoption.

Therefore, the future research on FA electrooxidation should address the issues stated above. Possible future directions are:

1. Further understanding of the electrocatalytic processes on electrode surfaces. For this purpose, Pt and Pt-based alloys are still appropriate to be the research subject. The knowledge learned from noble metals and their alloys are to be generalized and then applied as guidelines for developing inexpensive electrocatalysts.
2. Improvement of stability. In the discussed Pt-Pb case, Pb leaches out from electrocatalysts in acid electrolyte. It is believed that a complete Pt shell can better protect the Pt_3Pb core. On the other hand, if the Pt shell is too thick, it lowers the overall performance. Such a dilemma exists in many cases of electrocatalyst development. Improving the stability, while maintaining the activity, will be a major challenge in the future research.

3. Development of inexpensive electrocatalysts: For instance, Pb nanoparticles covered with a monolayer of Pt could be an option of an “inexpensive” electrocatalyst, although it is very challenging to make such a structure (e.g. the large lattice mismatch between Pt and Pb prohibits the epitaxial growth of Pt on Pb). Ultimately, non-noble-metal electrocatalyst are expected to be the main research direction for DFAFC applications.

DFT Calculation Procedures (conducted by Liang Qi). All DFT calculations are performed by using the Vienna *ab initio* simulation package (VASP). We use projector augmented wave (PAW) potentials with Perdew-Burke-Ernzerhof (PBE) exchange-correlation functional in none-spin-polarized condition, because all the adsorbed intermediates are found to be at non-magnetic states. All (111) surfaces are modeled by (4 × 2) super cells with four-layer slabs (8 atoms per layer), where the top two layers are fully relaxed and the vacuum size is larger than 15 Å. Monkhorst-Pack k-point of 3 × 5 × 1 grids is applied for Brillouin-zone integration. Partial occupancies of eigenstates are determined by first-order Methfessel-Paxton smearing of $\sigma = 0.2$ eV. Cut-off energy for plane wave basis is 400 eV. Minimum energy path (MEP) of each dehydrogenation step is searched by climbing image nudged elastic band (CI-NEB) method integrated in VASP.

3.3.2 Methanol oxidation

Electrocatalytic properties of cubic and spherical Mn-Pt NCs for methanol oxidation are also tested (Figure 3.23). The polarization curves representing the oxidation activities are normalized to surface areas, which are calculated by measuring the charge of hydrogen adsorption-desorption. The activities of cubic and spherical Mn-Pt NCs for methanol oxidation are compared to those for the ETEK Pt catalyst. For methanol oxidation, the cubic Mn-Pt NCs show better activity than ETEK Pt, while spherical Mn-Pt NCs are comparable in activity to ETEK Pt for methanol oxidation. These results suggest that the (100) surface of Mn-Pt is more active for methanol oxidation than the (111) surface of Mn-Pt. The Mn-Pt also shows enhanced poisoning tolerance, as shown in Figure 3.24.

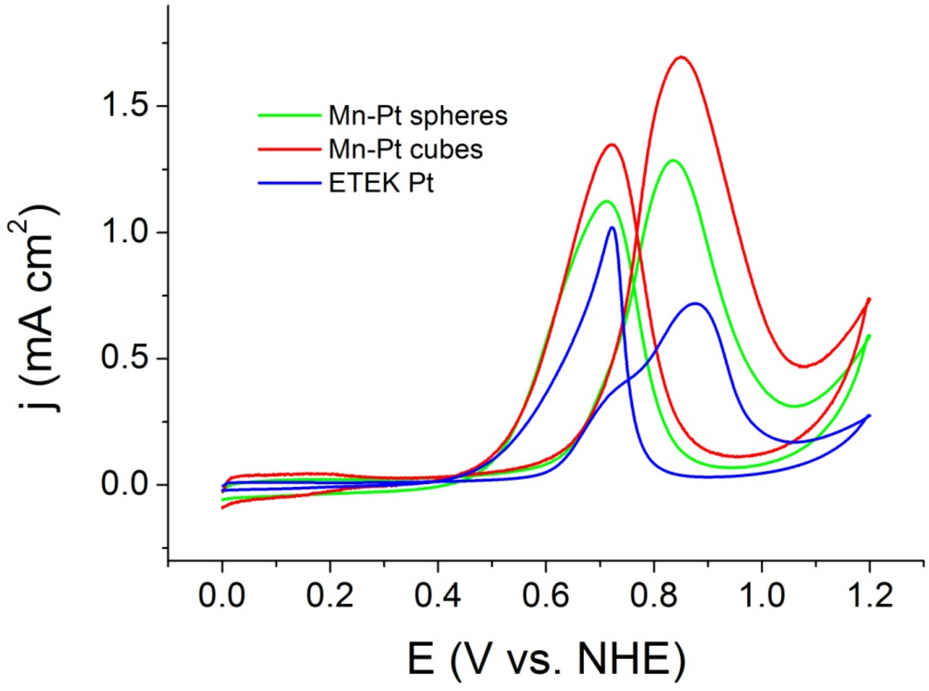

Figure 3.23 Polarization curves for methanol oxidation on Mn-Pt spheres, nanocubes, and ETEK Pt.

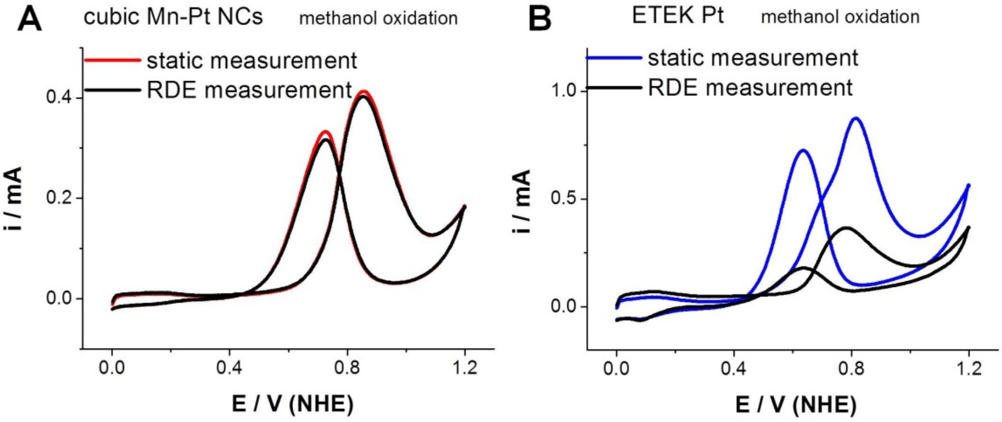

Figure 3.24. Methanol oxidation measurements performed on static electrodes and RDE (2500rpm). Each RDE measurement is carried out immediately after the static measurement on the same electrode. On Pt catalysts, the poisoning CO species are usually formed during the anodic sweep, and are partially removed at high potentials. The rotating disc brings fuels to electrode much faster than diffusion, poisoning the electrode even faster. Therefore, the RDE measurements show lower current than the static measurements. However, on cubic Mn-Pt nanocrystals, this accelerated poisoning effect is not as significant as in the case of on ETEK Pt catalysts, indicating that Mn-Pt may have better tolerance to poisoning.

The Pt_3Zn nanocrystals are also tested for methanol oxidation reaction. The methanol electrooxidation properties of the Pt_3Zn NCs are tested in 0.5M methanol + 0.1M H_2SO_4 solution. As shown in Figure 3.25a, the Pt_3Zn NCs have comparable maximum methanol electrooxidation activity (current density normalized to catalyst surface area) to commercial ETEK Pt catalyst. The typical methanol oxidation polarization curves for spherical Pt_3Zn NCs, cubic Pt_3Zn NCs and ETEK Pt are shown in Figure 3.25b. The current density peak in the forward sweep is ascribed to the methanol oxidation on the catalyst, which forms CO, CO_2, and other carbonaceous intermediates that adsorb onto the catalyst surface. During the backward sweep, the adsorbed carbonaceous species are further oxidized to CO_2, which contributes to the current density peak around 0.65 V. Therefore, the ratio of forward sweep current density peak to backward sweep peak, J_f / J_b, can be used to describe the tolerance of catalyst to the carbonaceous species accumulation. In Figure 3b, the ratio of J_f/J_b is 1.46 and 1.80 for spherical and cubic Pt_3Zn NC respectively, much higher than 0.99 for ETEK Pt. In contrast to previous studies of Pt and Pt-alloys in which cubic NCs (or {100} facets) show higher activity than spheres (or mixture of {100} and {111} facets) in H_2SO_4, here spherical Pt_3Zn NCs are shown to exhibit better methanol oxidation activity than cubic NCs in both H_2SO_4 and $HClO_4$ (Figure 3.26), suggesting that the sulfate anion adsorption effect may be very weak on the Pt-Zn surface. The chronoamperometric measurements further confirm that the methanol oxidation activity on spherical Pt_3Zn NCs is higher than that on cubic Pt_3Zn NCs (Figure 3.25c).

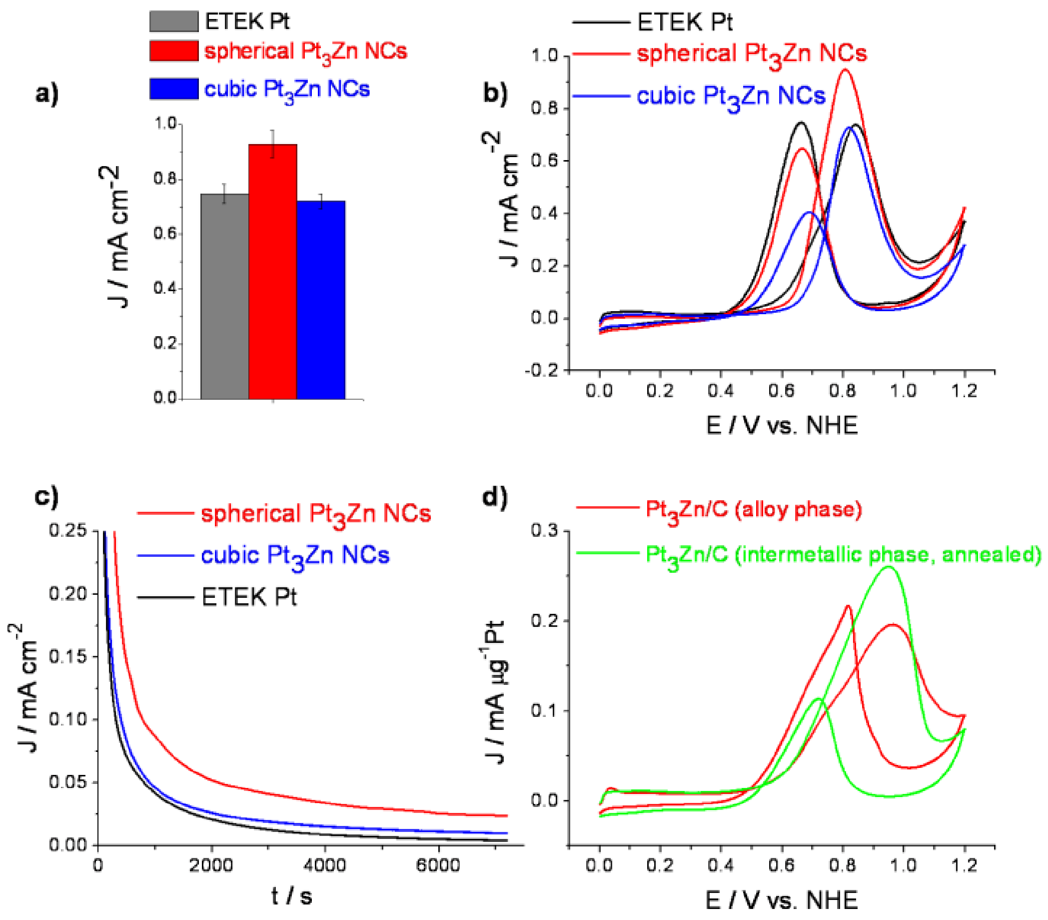

Figure 3.25. a) Surface area normalized activities, and b) representative polarization curves of methanol oxidation on spherical Pt_3Zn NCs, cubic Pt_3Zn NCs, and ETEK Pt; c) the chronoamperometric curves of methanol oxidation on spherical Pt_3Zn NCs, cubic Pt_3Zn NCs, and ETEK Pt at 0.8V; d) polarization curves of methanol oxidation on alloy phase Pt_3Zn/C

and intermetallic phase Pt_3Zn/C catalysts. All measurements were carried out in 0.5M methanol + 0.1M H_2SO_4.

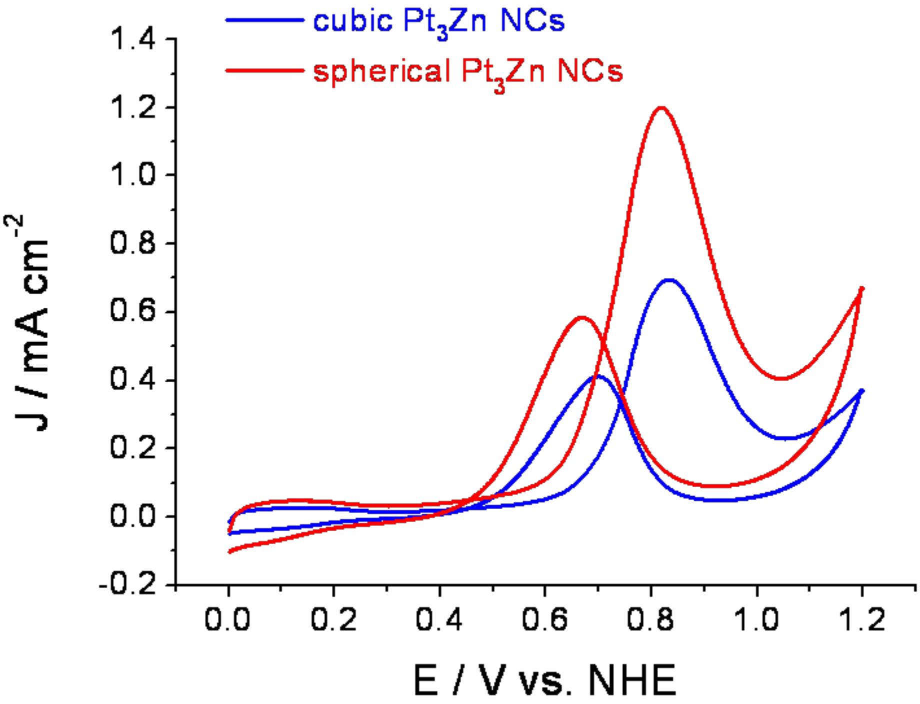

Figure 3.26. Polarization curves of methanol oxidation on ETEK Pt, spherical Pt_3Zn NCs, and cubic Pt_3Zn NCs. All measurements are performed in 0.1M $HClO_4$ + 0.5M methanol at a scan rate of 20mV/s.

The methanol oxidation activities for the alloy phase Pt_3Zn and intermetallic phase Pt_3Zn are also compared. High temperature annealing (600°C, 30 min) is necessary to obtain intermetallic Pt_3Zn phase. Considering that the morphology of cubic NCs changes under such high temperature, the spherical Pt_3Zn NCs are used to make this comparison. The alloy phase Pt_3Zn/C catalysts are made by loading as-synthesized spherical Pt_3Zn NCs onto Vulcan XC72R (Cabot), followed by a thermal treatment under air at 210°C to remove the organic ligands. The intermetallic Pt_3Zn catalysts are prepared by annealing the alloy phase Pt_3Zn catalysts at 600°C for 30min. As shown on Figure 3.25d, the activities on two catalysts are similar, while the intermetallic phase Pt_3Zn has a higher J_f / J_b ratio than the alloy phase Pt_3Zn, implying that the intermetallic phase has greater tolerance to carbonaceous poisoning than the alloy phase of Pt_3Zn. Considering the surface area loss of the NCs as a result of sintering and coalescence at high temperature, the intermetallic Pt_3Zn could potentially have even higher activity, if optimized.

In the methanol oxidation reactions performed on a RDE, a current density drop from three successive measurements after the current density reached the maximum on ETEK Pt catalysts, is observed (Figure 3.27a). This current density drop is ascribed to the poisoning of the catalyst at an accelerated rate due to the fact that the RDE brings the reactant to the electrode much faster than the pure diffusion. However, this accelerated poisoning effect is not observed on spherical Pt_3Zn NCs supported on carbon, on which the polarization curves of three successive measurements are nearly identical (Figure 3.27b). The current drop is neither found on cubic Pt_3Zn NCs nor on spherical Pt_3Zn NCs (Figure 3.28), implying that Pt-Zn has higher poisoning tolerance than pure Pt.

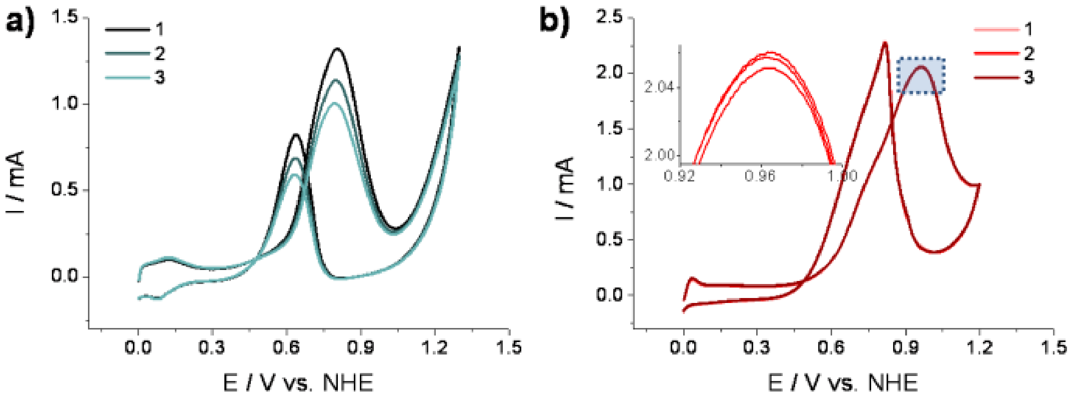

Figure 3.27. Polarization curves of three successive RDE measurements taken on a) ETEK Pt and b) Pt_3Zn/C, after the maximum methanol oxidation current densities are reached. Inset of b) magnified view of selected area in b. All measurements are carried out in 0.5M methanol + 0.1M H_2SO_4 at a rotating rate of 2500 rpm.

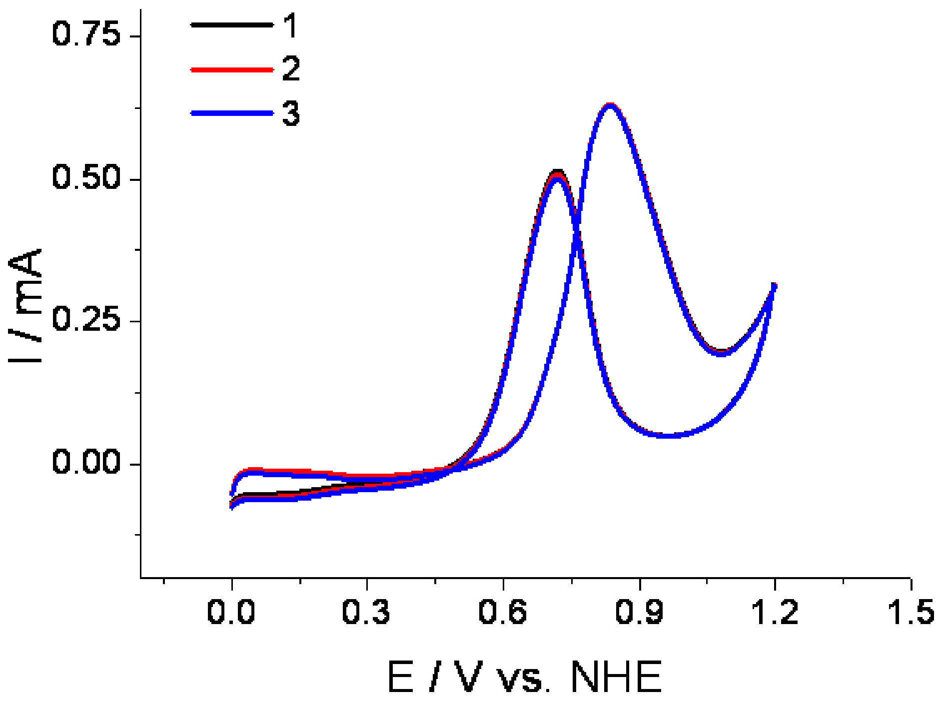

Figure 3.28. Polarization curves of three successive measurements for methanol oxidation on cubic Pt_3Zn NCs. All measurements are performed in 0.1M H_2SO_4 + 0.5M methanol at a scan rate of 20mV/s.

4. Catalysis (others)

In this chapter, the application of nanocrystals in catalysis other than electrocatalysis is reported. The content of this chapter covers the oxygen storage properties of ceria nanomaterials and the significantly enhanced activity toward CO oxidation on the interface of Au-FeOx. In the end, a guideline to improve the stabilities of catalysts raised from the research based on the artificial crystals is also introduced.

4.1 Oxygen storage

The ability of ceria for oxygen storage originates from the easy conversion between CeO_2 and CeO_{2-x}. Ceria has found its primary utilization in catalysis as an oxygen carrier, due to its high OSC. Ceria nanomaterials with various morphologies including square ceria nanoplates (S-nanoplates), elongated ceria nanoplates (L-nanoplates), hydrothermal treatment prepared nanospheres, and combustion prepared ceria nanopowders, have been described in chapter 2.5. The OSC of prepared ceria nanomaterials has been tested with a newly designed testing system based on a TGA.

The typical OSC measurements involve gas phase reactions in pulse mode (flow titration), and gas chromotography for detection[19,99]. These OSC measurements usually require relative complicated experimental setups. Here, we introduce a simple OSC measurement technique using cyclic thermal gravimetric analysis. In brief, oxygen gas and reductive hydrogen gas are alternately introduced in to a commerical TGA system (e.g. TA Instruments, SDT Q600 TGA/DSC), the mass changes of the ceria samples are then measured and converted to OSC. The very similar method for OSC measurement has also been reported by Zhang et al recently[144].

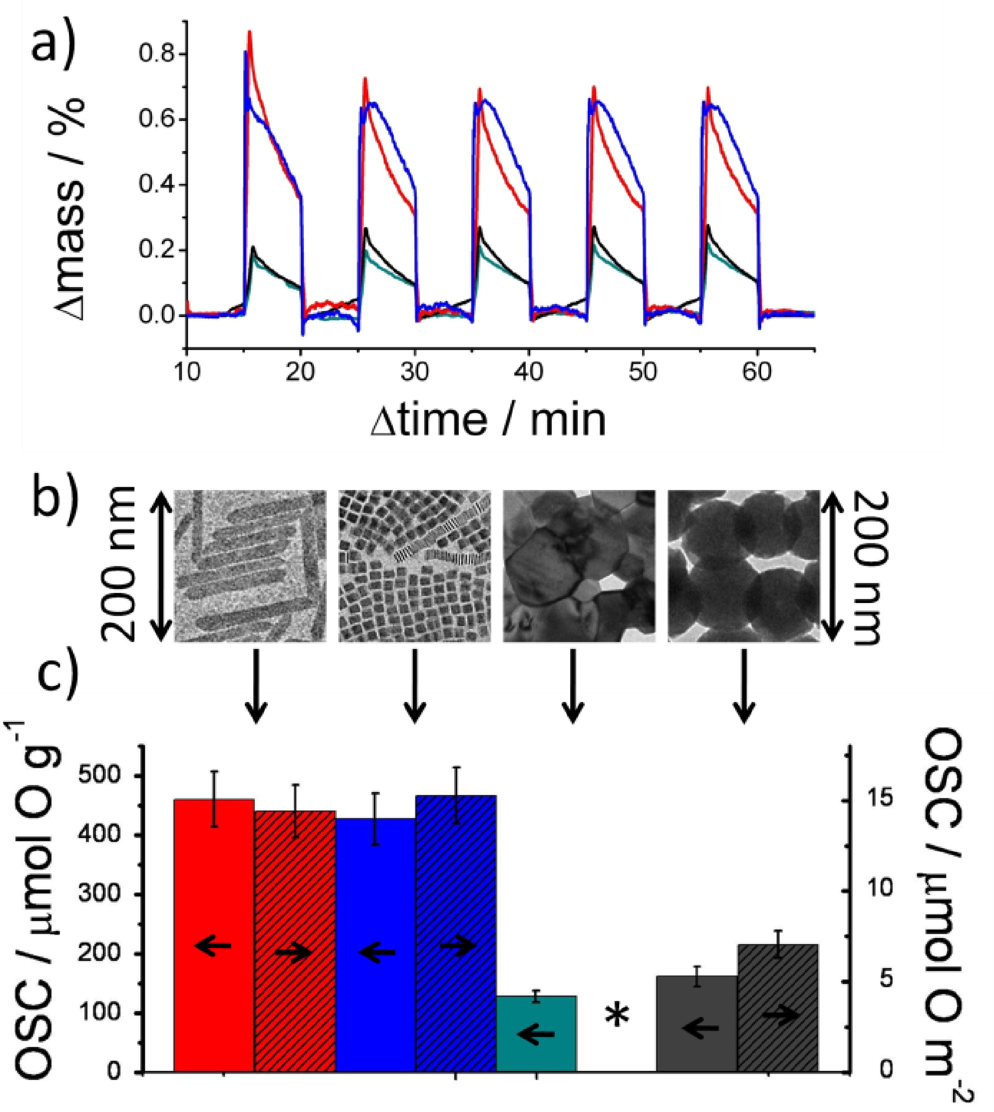

Figure 4.1. a) TGA data show the periodical mass change of ceria nanomaterials when O_2 and H_2 are alternately introduced. b) TEM images and c) OSC of ceria nanomaterials. Color code: red) elongated ceria nanoplates, blue) square ceria nanoplates, green) combustion prepared ceria nanomaterials, black) hydrothermal synthesized ceria spheres. *surface area of combustion prepared ceria is too small to make this comparison.

The OSC measurements are carried out at 300ºC. For pre-treatment, each ceria sample is heated in an oxygen-rich environment to remove the organic stablizers and subsequently heated in 5% hydrogen (Ar balance) to reduce the surface. The mass change in response to alternating oxidative and reducing environments, indicates the cycles of oxygen uptake and release (Figure 4.1a). The TGA data are averaged and then are converted to OSC, as shown in Figure 4.1c. The L-nanoplates exihibit the highest OSC of 461 μmol O g^{-1}, almost triple that of the ceria nanospheres synthesized through hydrothermal method (162 μmol O g^{-1}) and approximately 4 times that of combustion-prepared ceria nanomaterials (128 μmol O g^{-1}). For the S-nanoplates, the reduced OSC of 427 μmol O g^{-1} is ascribed to the stacking of nanoplates, which leads to a reduction in the accessible surface area of ceria nanoplates. Previous studies have reported that the surface reactivity is higher on the (100) surface of ceria than on either (110) or (111)[105], and the energy required to form oxygen vacancies is less on (100) and (110) than that on (111)[145]. Therefore, these earlier research results predict that exposure of more {100} planes should facilitate the formation of oxygen vacancies, thus, enhancing the OSC of ceria materials. Our ceria nanoplates are enclosed by (100) facets, allowing us to test this prediction.

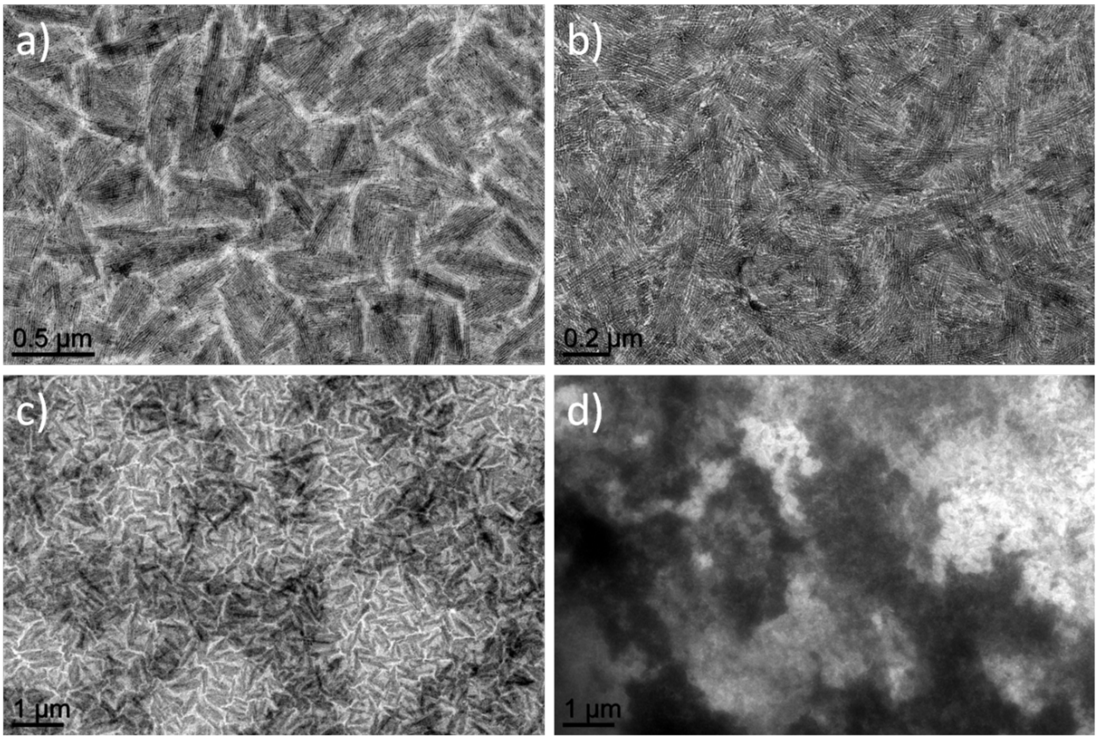

Figure 4.2. TEM images of the aggregated ceria nanoplates in the form of powder.

The measured surface area of ceria nanoplates is 28 m^2 g^{-1} for S-nanoplates and 32 m^2 g^{-1} for L-nanoplates. These surface areas are lower than reported ceria nanomaterials, and maybe the result of significant aggregation (Figure 4.2) due to the plate-morphology. The S-nanoplates should have higher surface area; however, they actually show a lower surface area than L-nanoplates. This confirms that the aggregation causes the reduction in surface area, due to the S-nanoplates being able to more easily stack than L-nanoplates as described earlier in chapter 2.5. The surface area normalized OSC for ceria spheres is 7.0 μmol O m^{-2}, which is close to the theoretical OSC of ceria surfaces [5.7 μmol O m^{-2} for (100) and 6.6 μmol O m^{-2} for (111)][19], indicating that the oxygen storage at 300ºC is restricted to surface for the hydrothermal treatment prepared ceria spheres. In contrast, the surface area normalized OSC for ceria nanoplates (15.3 μmol O m^{-2} for S-nanoplates and 14.4 μmol O m^{-2} for L-nanoplates) implies that the oxygen storage is not limited to the surface of the 2-D ceria nanocrystals, even at temperature as low as 300ºC. Because the oxygen adsorption first occurs on the surface, the surface-area-to-volume (SA/V) ratio is an important parameter to an oxygen storage material. Regardless of the roughness of surface, the SA/V ratio of the S-nanoplates, L-nanoplates and nanospheres are calculated to be 1.33, 1.16, and 0.066 nm^{-1} respectively. The combustion-prepared ceria materials have an even lower SA/V ratio due to their large grain size. Therefore, with the high theoretical value of SA/V ratio, the OSC and related catalytic performance of ceria nanoplates have much room to be optimized.

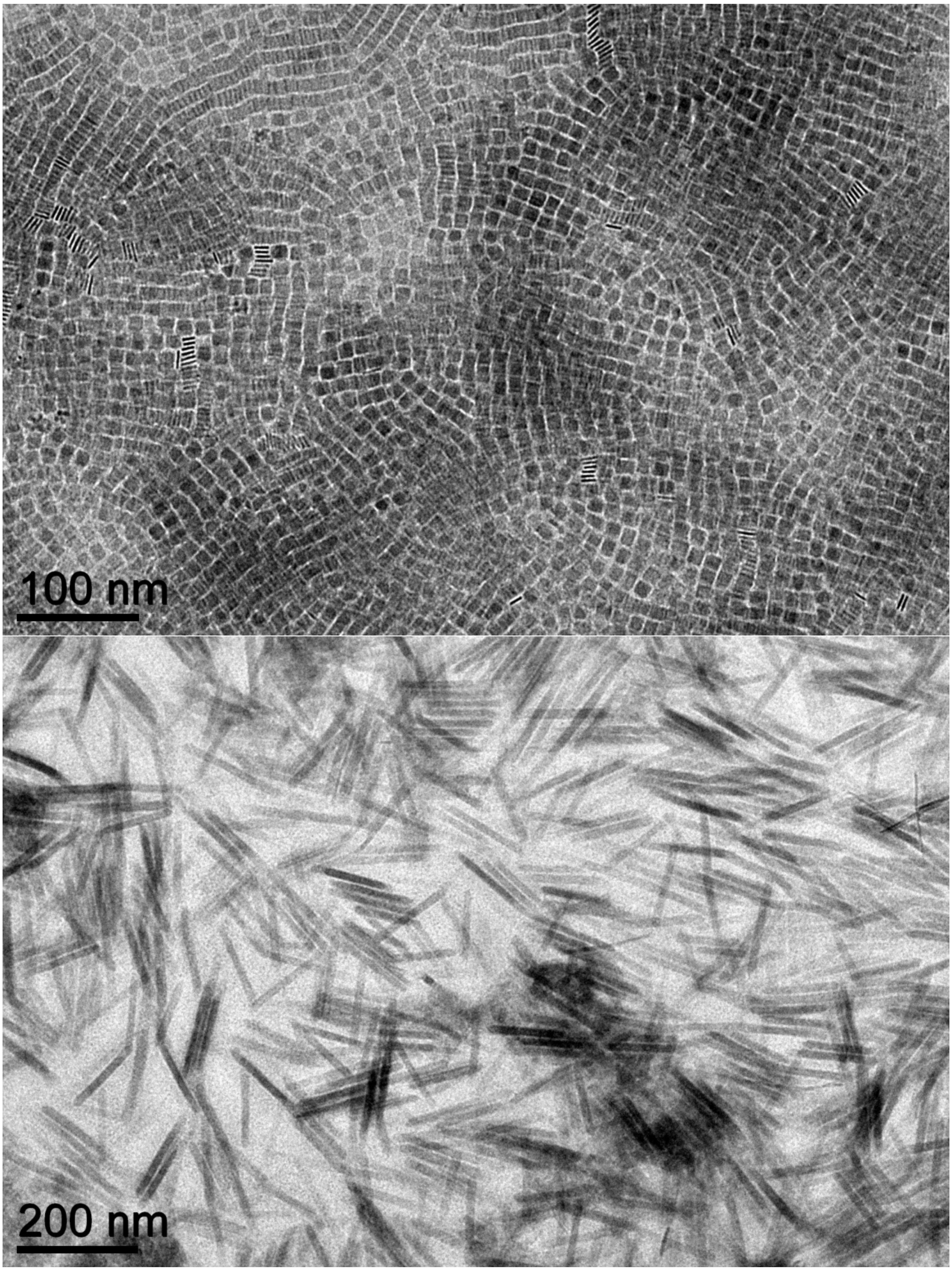

Figure 4.3. TEM image of the ceria nanoplates heated at 300 ºC.

4.2 CO oxidation

The catalyzed CO oxidation is of great interest in industry. For instance, in a three-way catalytic converter used in automobile, CO is oxidized to CO_2 and then removed from the exhaust by reacting with O_2 or NO on Pt, Pd and Rd catalysts. In addition, that the CO oxidation is one simple reaction makes it an ideal model reaction to study catalysis.

The reaction is thermodynamically favorable with a free energy of -122 kcal mol^{-1} for the formation of CO_2. A gas phase CO oxidation is limited by the adsorption and dissociation of O_2. The role of a catalyst is to reduce such activation energy to as low as zero. There are many proposed reaction mechanism for the CO oxidation, and the real mechanism has not been nailed yet. The generally accepted mechanism of CO oxidation on transition metal (especially precious metal) surface is a Langmuir-Hinshelwood mechanism involving adsorbed CO and O atoms, as described below

$$CO_{(g)} \leftrightarrow CO_{(ads)}$$

$$O_{2\ (g)} \leftrightarrow 2\ O_{(ads)}$$

$$CO_{(ads)} + O_{(ads)} \leftrightarrow CO_{2\ (ads)} \leftrightarrow CO_{2\ (g)}$$

Another proposed mechanism called Eley-Rideal mechanism, where CO gas molecule directly reacts with adsorbed O atom to form CO2, is described below

$$O_{2\ (g)} \leftrightarrow 2\ O_{(ads)}$$

$$CO_{(g)} + O_{(ads)} \leftrightarrow CO_{2\ (g)}$$

CO oxidation on Au-FeOx

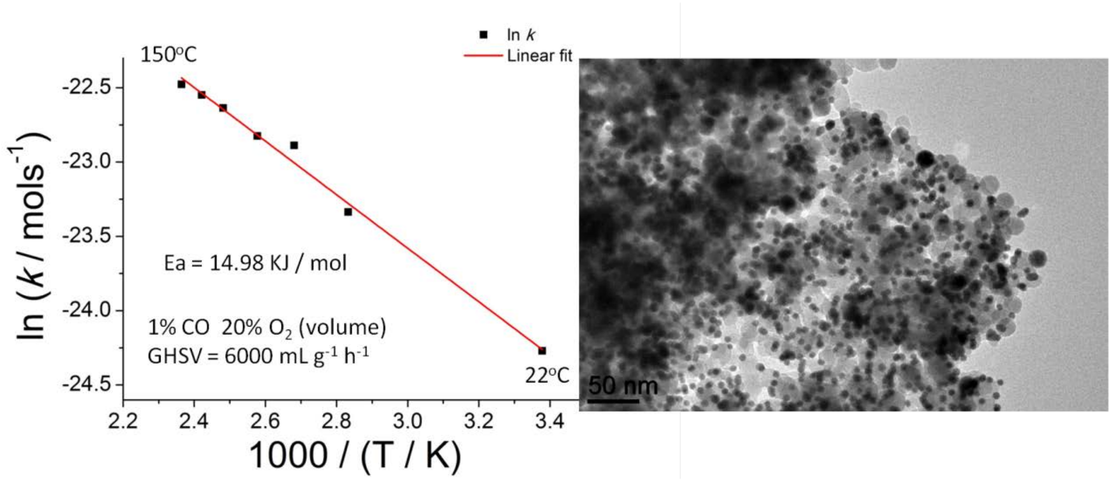

Figure 4.4. A mixture of 6 nm Au and 12 nm Fe_3O_4 is catalytic active toward CO oxidation.

For long time, Au has been considered to be catalytic inactive toward CO oxidation. However, some Au catalysts supported on oxides, especially on iron oxides, have been identified to be extremely active for CO oxidation, even at ambient temperature. The origin of such high activity is currently under debate. One popular argument is that only small Au particles under a critical size are active[15,146-150]. The critical size is reported in the range of 0.5-5 nm[15,146-150]. Based on such theory, one can conclude that the Au particles larger than 5 nm should not be particularly active for CO oxidation. However, we notice that Sun et al. report a synthesis of Au-Fe_3O_4 dumbbell nanoparticles with a 5 nm Au attached on 12 nm Fe_3O_4. Such dumbbell nanoparticles are active toward CO oxidation, even below 0°C. We have also observed active CO oxidation on a mechanical mixture of 6 nm Au and 16 nm Fe_3O_4, while 16 nm Fe_3O_4 solely exhibits little activity and 6 nm Au is inactive for CO oxidation at the same reaction condition (Figure 4.4). The evidence indicates that the Au may not need to be smaller than 5 nm to be active, and the interaction between Au and FeOx seems to be the origin for the exceptional activity. Noting some proposals emphasize the interface of Au-FeOx, and postulate that the activity may be proportional to the perimeter of the interface though it is challenging to prove in experimental, we take advantage of these artificial crystals with high degree of control to carry out the experiments to identify the active sites. The significant advantages of artificial crystals include:

1) The size of building blocks can be precisely controlled, eliminating the interference from polydispersity of materials. In this demonstration, the size of Au NCs is strictly kept above 6 nm (larger than any reported critical size), so that Au itself will not contribute to the overall activity.

2) The structure of artificial crystals is tunable in certain extent, giving the freedom to choose desired stoichiometry of Au:Fe. The available structure of Au-FeOx artificial includes AB, AB_2, AB_6, and AB_{13}–type structures (here, FeOx is A, Au is B), analogous to CuAu, AlB_2, CaB_6, and $NaZn_{13}$, as well as a structure of A_2B_3, which does not exist in known compounds[151,152]. Among them, AB, AB_2, and AB_{13} of Au-FeOx are chosen due to their optimized high phase-purity (~100%) and continuous coverage (up to cm^2). In AB-type structure, an Au NC directly contacts to 4 neighboring FeOx NCs, and there are 4 contacting sites (we call it "interface" for simple) per FeOx NCs. The numbers are 12 (6 for monolayer)/FeOx and 6 (3 for monolayer)/Au for AB_2–type, 24/FeOx and 2(counts for 12 Au out of 13 in a unit cell) for AB_{13}–type structure.

The artificial crystals are made by the self-assembly at liquid-air interface, then transferred onto Si wafers and loaded into a batch reactor. That the overall reaction rate is proportional to the loading of catalysts indicates that the diffusion of gas molecules is not the limiting step in such batch reactor. In addition, we have mathematically deduced a data processing method (see supporting information) which theoretically enables the assessment of reaction rate with a single data point, and most importantly, it minimizes the common source of error rooted in the inconsistent sample sizes for the injection-mode GC measurements. A temperature of 150^{o}C is selected for the reaction temperature, because higher reaction rates obtained at higher reaction temperatures compensate for the low loadings of catalyst. This makes the concentration of CO_2 high enough to be detected by GC, while at 150^{o}C the activities of Au and FeOx alone are as low as negligible. Most importantly, the artificial crystal catalysts do not change in morphology at 150^{o}C.

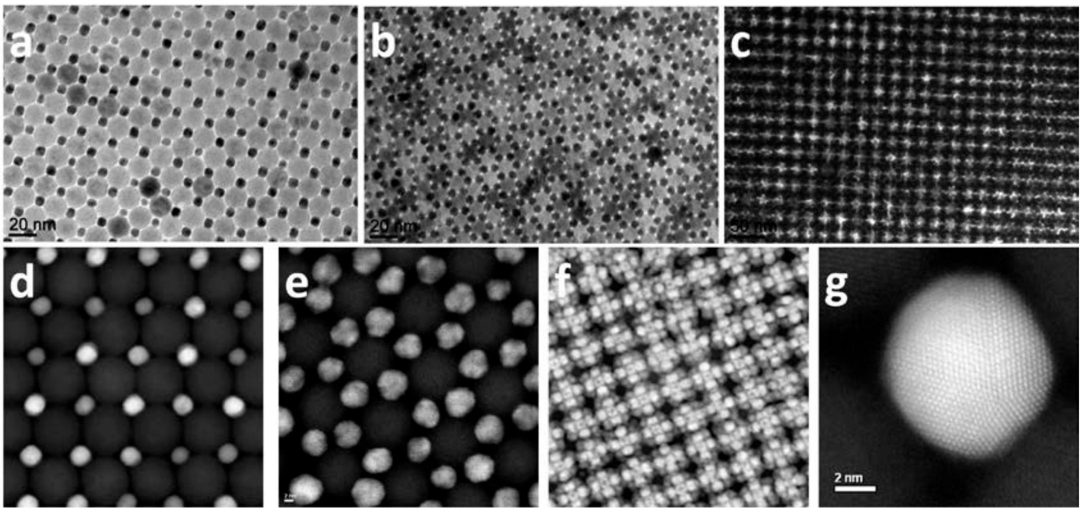

Figure 4.5. TEM images of a) AB, b) AB_2, and c) AB_{13}-type of Au-FeOx artificial crystals; STEM-HAADF images of d) AB, e) AB_2, and f) AB_{13}-type of Au-FeOx artificial crystals; g) high-resolution HAADF image of Au-FeOx showing that one Au NC contacts with four FeOx NCs.

As the sizes of building blocks are fixed, we assume the size of interface of Au-FeOx is also fixed. Therefore, according to the theory that the active site is the interface, the overall activity should be proportional to the population of the interface. Indeed, our measurements on Au-FeOx artificial crystals support this hypothesis, as shown in Figure 4.6. The overall specific rates are normalized to the mass of Au and Fe respectively, and then plotted versus the number of Au-FeOx interface. Because the

AB_2–type artificial crystal has the best quality in terms of phase-purity and domain size, the rates obtained on AB_2–type Au-FeOx are averaged, divided by its number of interface, and then extrapolated to AB and AB_{13} as the calculated values. The experimental measured rates for AB and AB_{13} are consistent with the linear correlation derived from the calculated values. Given that the Au and FeOx show negligible activity at same reaction conditions, such linear correlation between overall activities and overall Au-FeOx interface numbers is a strong evidence that the active sites for CO oxidation is the Au-FeOx interface. On another hand, the disordered mixtures of Au and FeOx nanocrystals show significantly lower activities compared to the ordered artificial crystals, and the overall reaction rates obtained from these random mixtures do not show apparent linear correlation to the mass of Au or Fe in the mixtures. This observation also supports that the Au-FeOx interface is the actual active site.

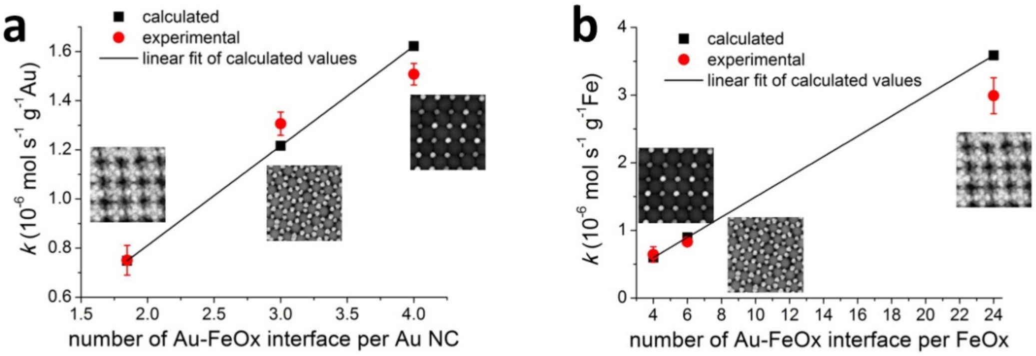

Figure 4.6. Plots of reaction rate for CO oxidation on Au-FeOx artificial crystals

The activities obtained on artificial crystals are about 2 orders of magnitude lower than the reported highly active catalysts[15,146-150]. However, the TOF normalized to number of interface is close to 1 s^{-1}, which is on the same order of magnitude as the reported high TOFs. This can be explained by the actual number of active center. Assuming the NCs are near spherical and they contact with each other via the way hard particles do, the atoms involved in the contact are described in Figure 4.7. For 6 nm Au NC, the individual atoms at the Au-FeOx interface represent only 0.48% of the total Au loading. However, the number for 0.5 nm Au cluster is 50%, which means giving the same Au loading the 0.5 nm Au NCs possess ~100 times "effective" Au atoms than 6 nm Au NCs. This suggests that the number of active center at the Au-FeOx interface can be increased by decreasing the Au NC size. Therefore, though the small size of Au particle is not necessary for Au to be active, it is desirable for maximizing the number of active sites.

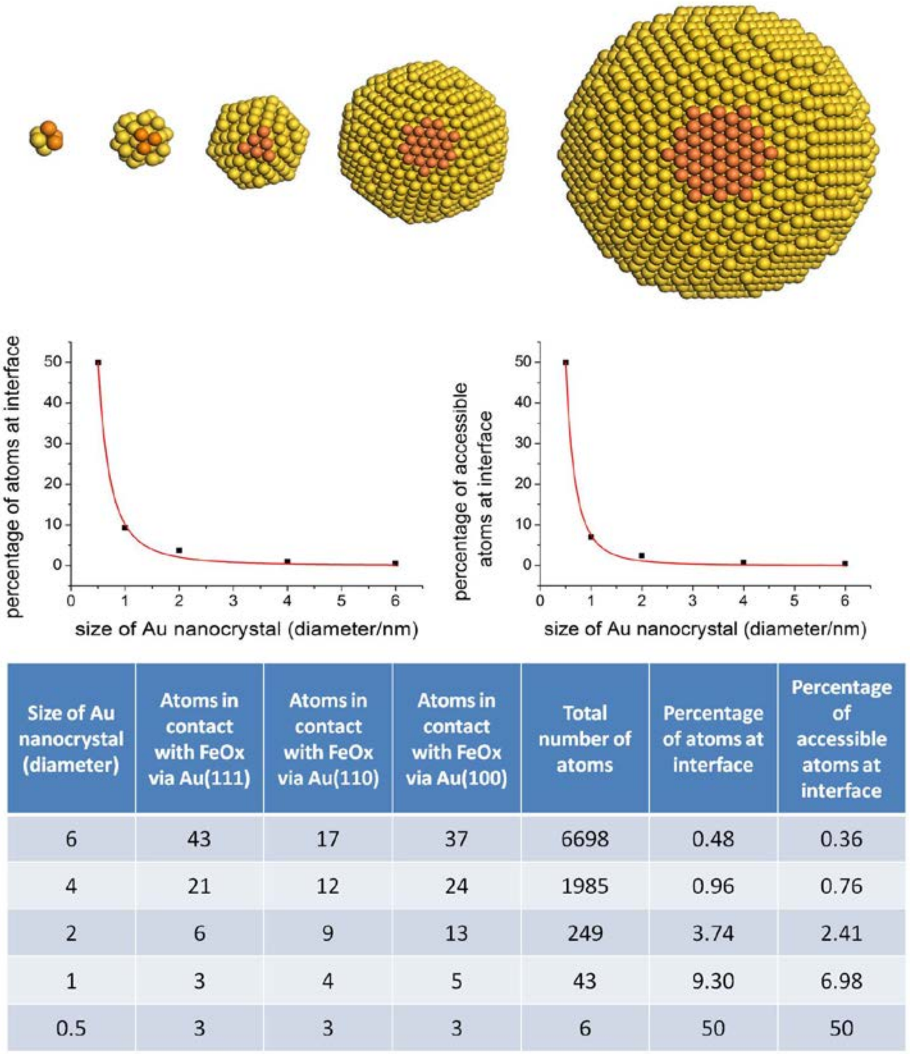

Size of Au nanocrystal (diameter)	Atoms in contact with FeOx via Au(111)	Atoms in contact with FeOx via Au(110)	Atoms in contact with FeOx via Au(100)	Total number of atoms	Percentage of atoms at interface	Percentage of accessible atoms at interface
6	43	17	37	6698	0.48	0.36
4	21	12	24	1985	0.96	0.76
2	6	9	13	249	3.74	2.41
1	3	4	5	43	9.30	6.98
0.5	3	3	3	6	50	50

Figure 4.7. The correlation between the size of Au NCs and the numbers of Au atoms involved in the Au-FeOx interface.

To rationalize our observations, we employ a DFT study to further investigate this case. According to Langmuir-Hinshelwood mechanism, both CO and O_2 need to adsorb on catalyst surface for the reaction of CO oxidation. However, the O_2 molecules do not or only very weakly adsorb on Au surface at the conditions which the activity test is usually carried out. The low activity on pure Au may be ascribed to this weak adsorption of O_2. We have investigated the adsorption on the interface of Au-FeOx. As shown in Figure 4.8, the adsorption of O_2 is strongest on the interface, where the E_{ads} is -0.73 eV. The adsorption strength drops quickly whereas the investigated site moves away from the Au-FeOx interface. Since the real origin for the high activity on the interface could be much more pronounced and the real mechanism of CO oxidation has not been pin down yet, the investigation of O_2 adsorption merely provides a plausible angle to understand the CO oxidation on Au-FeOx.

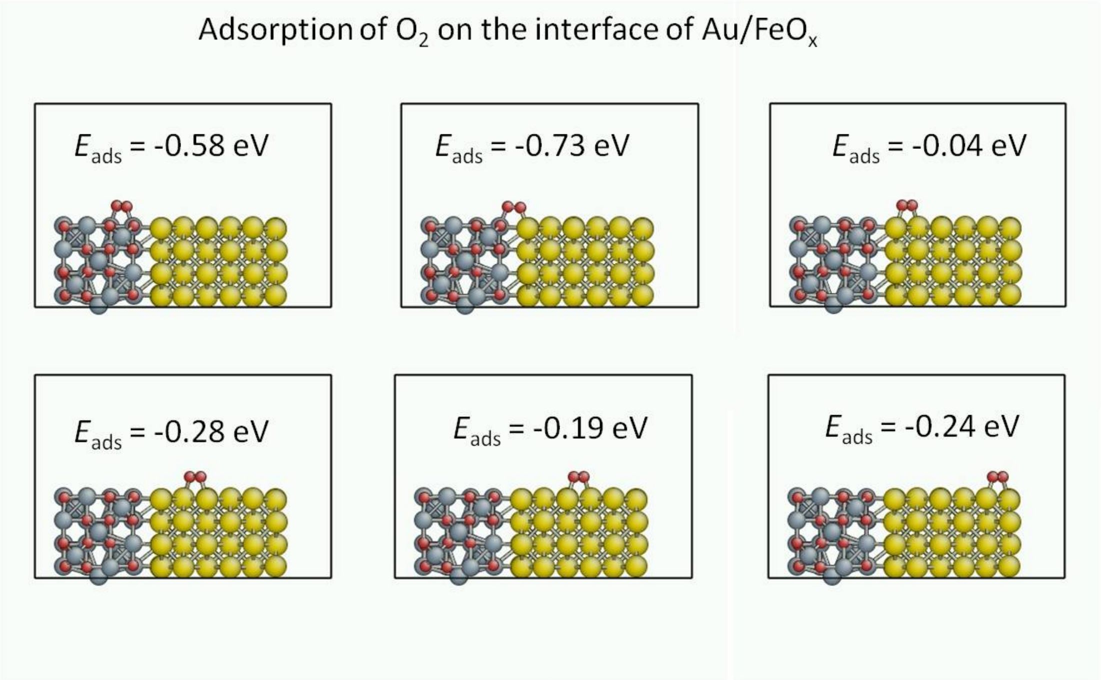

Figure 4.8. The results of DFT studies for adsorption of O_2 on the interface of Au/FeOx. The results show that the adsorption of O_2 at Au/FeOx interface is strongest.

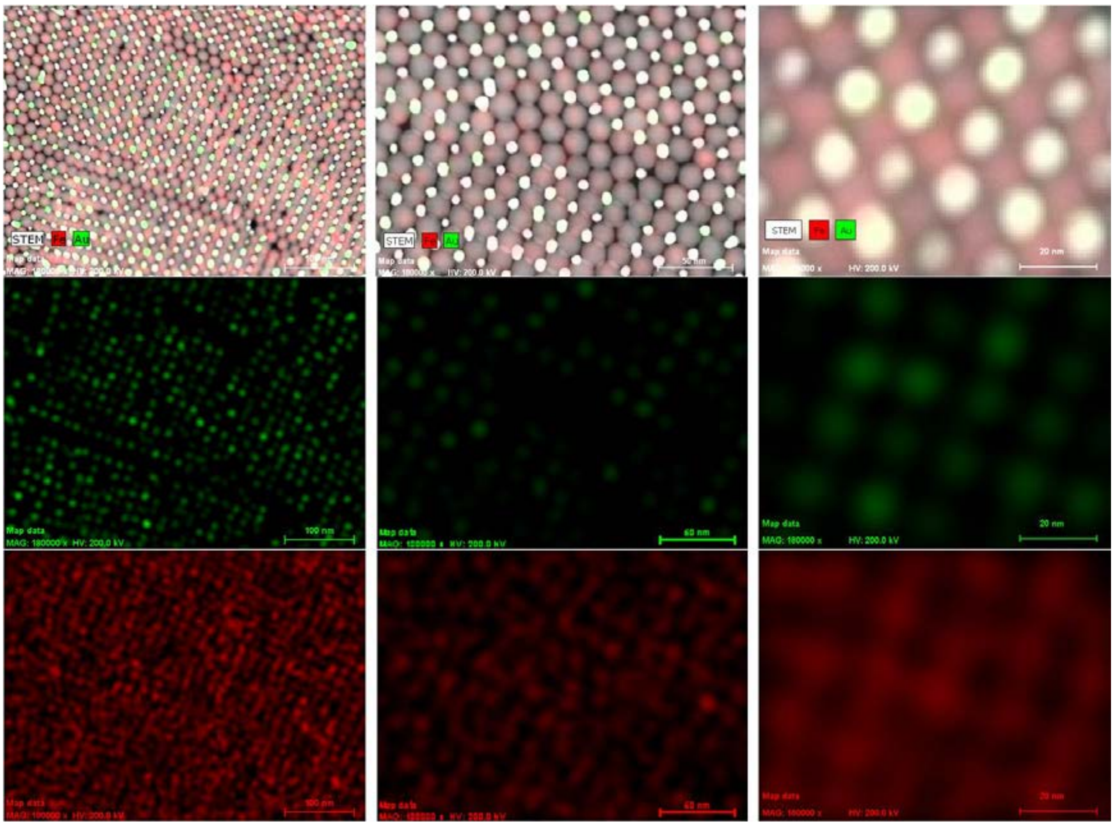

Figure 4.9. EDX mapping of AB-type Au-FeOx artificial crystals. Au: green, Fe: red

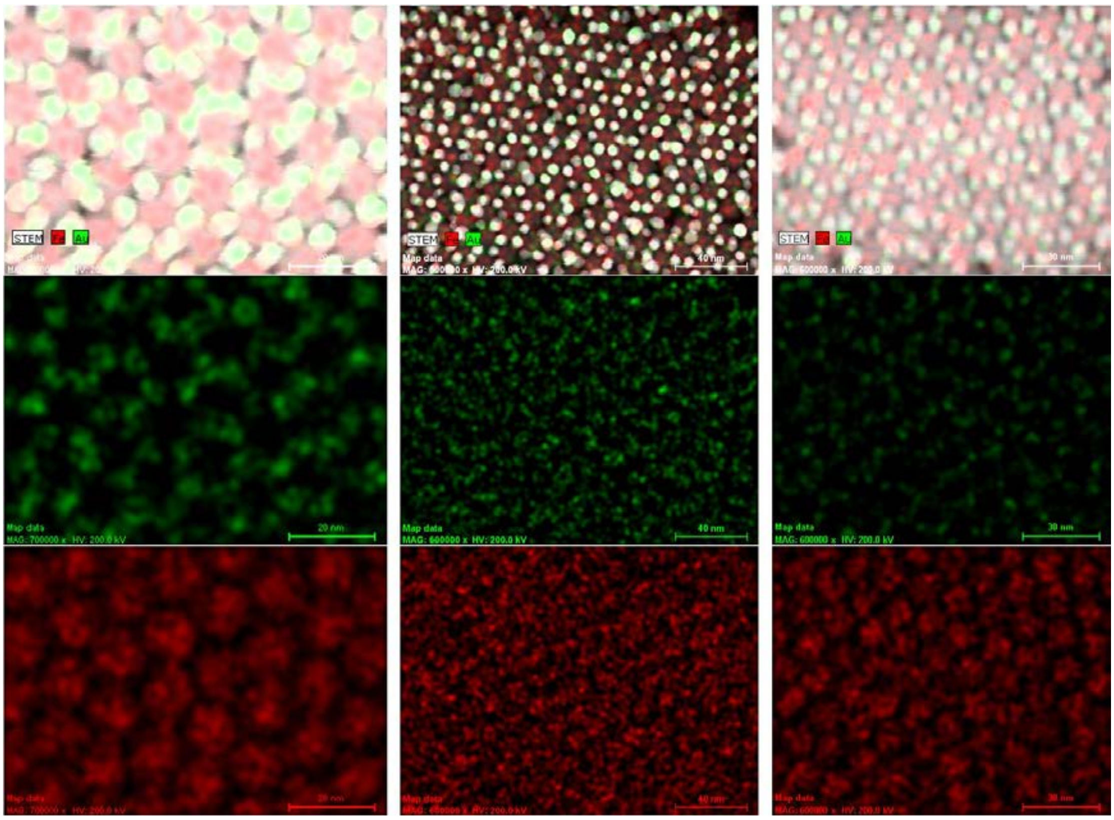

Figure 4.10. EDX mapping of AB_2-type Au-FeOx artificial crystals. Au: green, Fe: red

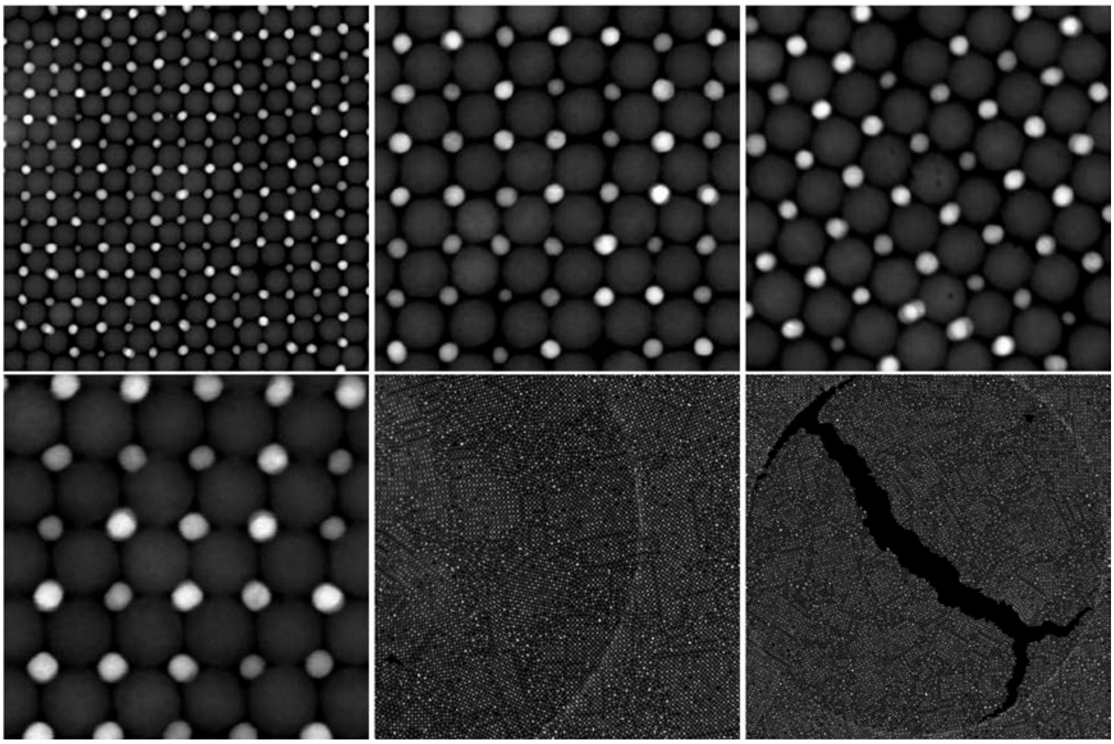

Figure 4.11. STEM-HAADF images of AB-type Au-FeOx artificial crystals.

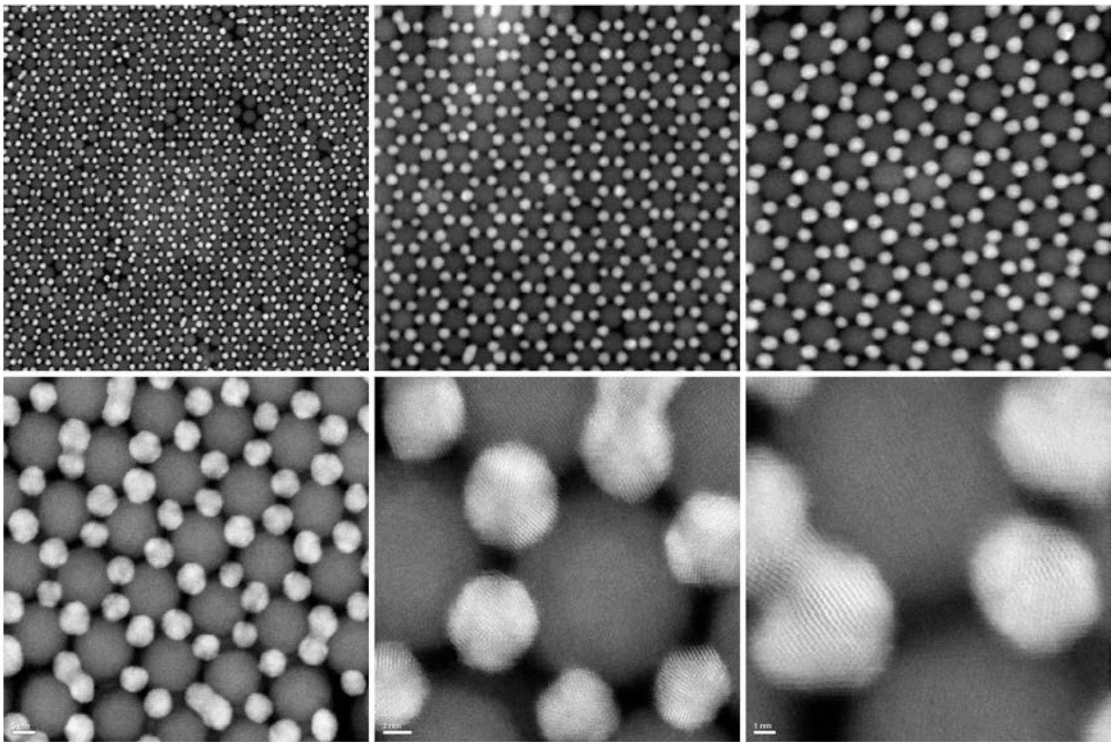

Figure 4.12. STEM-HAADF images of AB_2-type Au-FeOx artificial crystals.

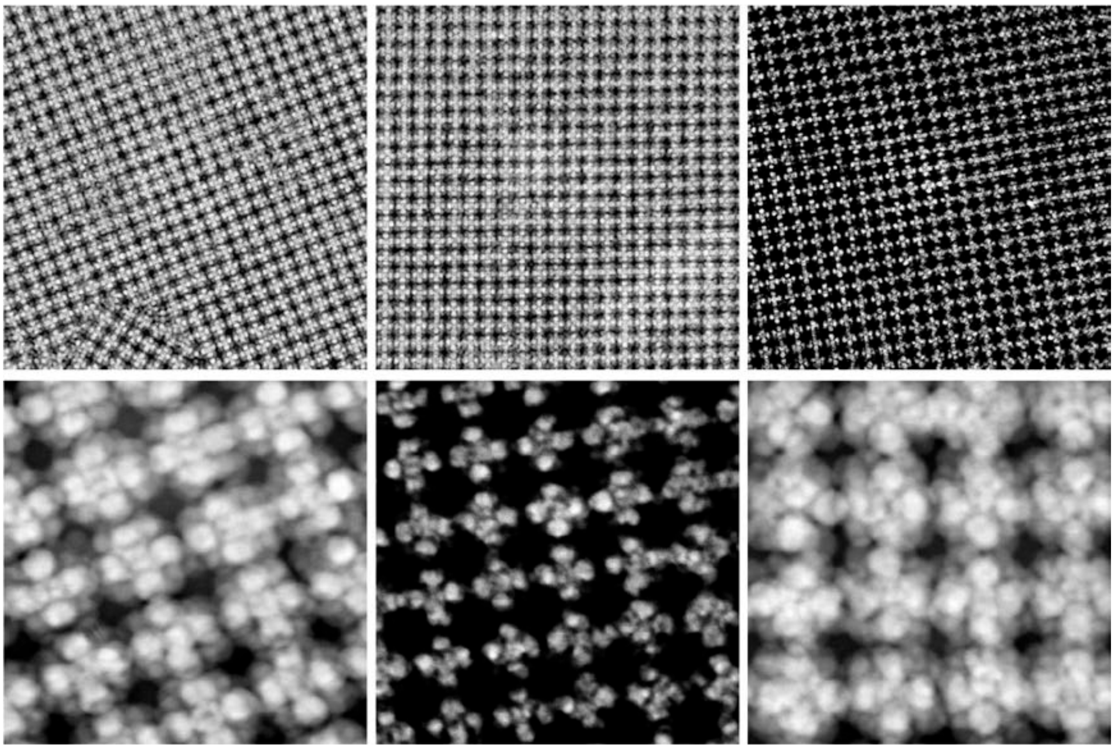

Figure 4.13. STEM-HAADF images of AB_{13}-type Au-FeOx artificial crystals.

4.3 A guideline to improve the stability of catalysts

Besides the activities, the artificial crystals also provide valuable information to improve stability of catalyst. Metals usually exhibit significantly reduced melting point when their size drop into the nanometer regime, as known as melting-point-depression phenomenon. 2.5nm Au has been found to have an m.p. reduced to ~300°C[1], and we have observed that 6nm Au and 12 nm Cu NCs are sintered under a thermal treatment as low as 200°C. This behavior of metal sintering at reduced temperature causes the problem of losing effective surface area of metal catalysts in the catalytic reactions, thus losing their overall activities. However, in the studies of catalysis with artificial crystals, we notice that oxides supported metals, particularly the metal-oxide artificial crystals with some ordered structures, exhibit significantly enhanced stability at high temperature. Our observations are presented in Figure 4.14.

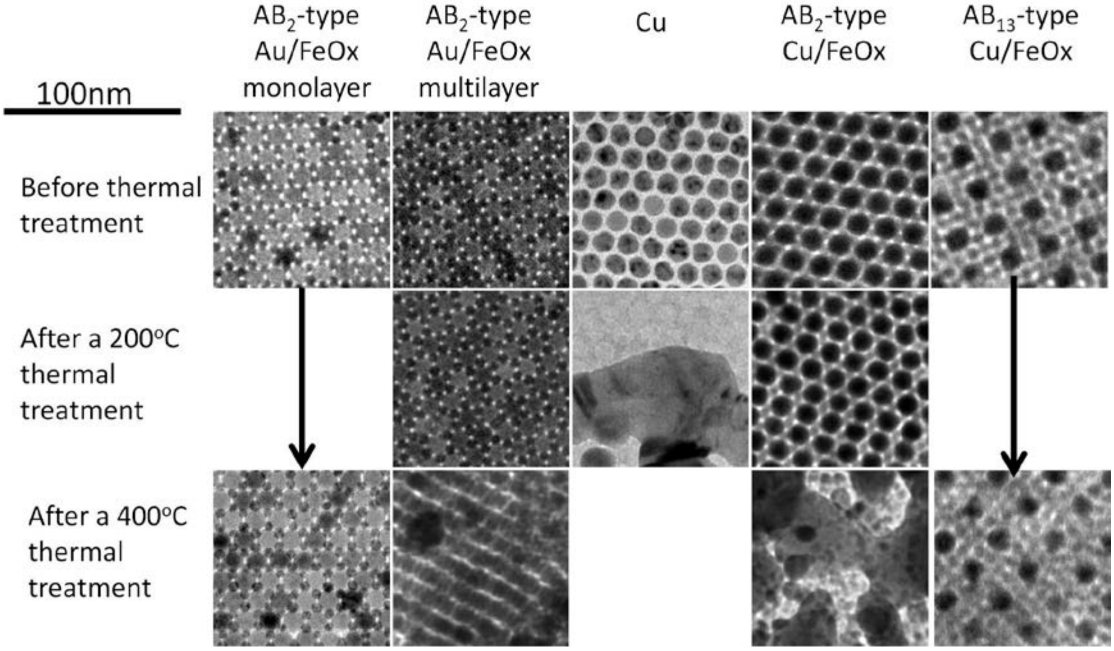

Figure 4.14. The observed correlation between structures and thermal stabilities of materials. The TEM images are 100 nm by 100 nm.

Au-FeOx AB_2-type artificial crystals retain their long range ordered structures under a thermal treatment at 200°C, while the single component thin film of Au NCs as well as the disordered Au-FeOx mixtures is severely sintered. As a demonstration, a thin film shown in Figure 4.16, in which the ordered and disordered domains co-exist, has been prepared in a control experiment by increasing the evaporation rate of solvent. After a 200°C thermal treatment, the disordered domains are sintered while the ordered domains are well-preserved. When the temperature of thermal treatment further increases to 400°C, in an AB_2-type Au-FeOx artificial crystal with multi-layers Au "leaks" from the vacancies of FeOx, but the FeOx skeleton is preserved; in contrast, the monolayer of AB or AB_2-type structure of Au-FeOx shows little morphology change. In Cu-FeOx, the AB_2 (here, Cu is A, FeOx is B) survives under 200°C, but not under 400°C. However, the AB_{13}-tpye Cu-FeOx is stable up to 400°C, the temperature which is high enough for most catalytic reactions. These results indicate that the stability of catalyst can be substantially improved in certain structures of artificial crystals. The common part of the stable phases is that the metal NCs are well isolated from each other in spatial, by the oxides. The 3D AB_2 structures of Au-FeOx and Cu-FeOx are destructed under high temperature, because in multi-layer of AB_2 Au-FeOx, 2 neighboring Au NCs located in 2 adjacent layers share a same vacancy of FeOx. This increases the probability of coalescence. In AB_2 Cu-FeOx, Cu is the larger building block in the two types of NCs, which does not give a Cu-Cu distance that far enough to prevent the coalescence. In monolayer structures and AB_{13} of Cu-FeOx, the metal NCs are spatially well-confined, thus are less likely to coalesce. Herein, by using artificial crystals as models, we can propose a general strategy of keeping metal spatially confined to enhance the stability of metal catalysts. Due to the desirable structure, the artificial crystal catalysts are stable under the temperature as high as 400°C, enough for most catalytic processes. Our recently result on FePt-MnO shows that the well-confined metals can even be stable under a thermal treatment up to 650°C[153].

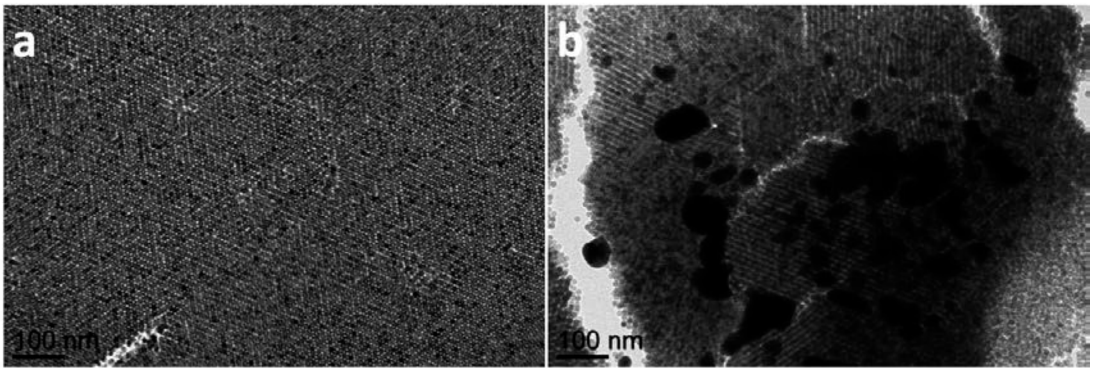

Figure 4.15. TEM images show AB_2-type Au-FeOx artificial crystals a) before and b) after a thermal treatment at 400°C.

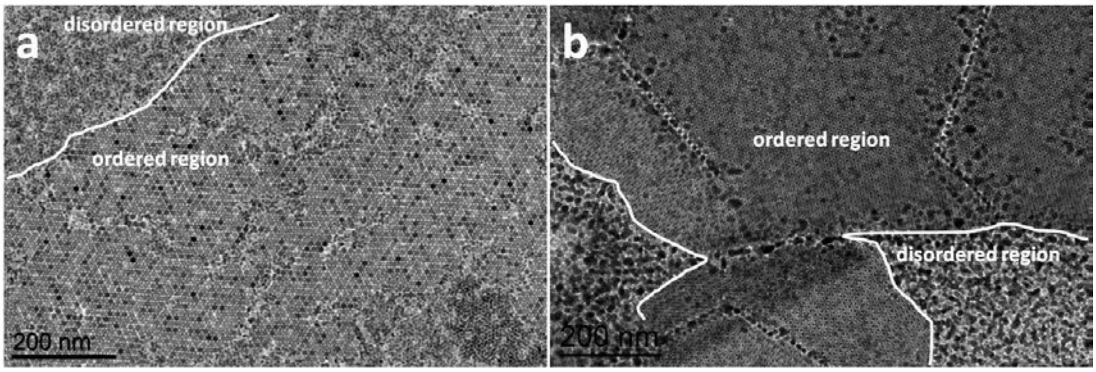

Figure 4.16. TEM images show co-existed ordered AB_2-type Au-FeOx artificial crystals and disordered Au-FeOx mixture a) before and b) after a thermal treatment at 200°C.

References:

(1) Buffat, P.; Borel, J. P. *Physical Review A* **1976**, *13*, 2287-2298.

(2) Murray, C. B.; Kagan, C. R.; Bawendi, M. G. *Annual Review of Materials Science* **2000**, *30*, 545-610.

(3) Sun, S. H.; Murray, C. B.; Weller, D.; Folks, L.; Moser, A. *Science* **2000**, *287*, 1989-1992.

(4) Spencer, N. D.; Schoonmaker, R. C.; Somorjai, G. A. *Journal of Catalysis* **1982**, *74*, 129-135.

(5) Zaera, F.; Somorjai, G. A. *Journal of Physical Chemistry* **1985**, *89*, 3211-3216.

(6) Solla-Gullon, J.; Vidal-Iglesias, F. J.; Lopez-Cudero, A.; Garnier, E.; Feliu, J. M.; Aldaza, A. *Physical Chemistry Chemical Physics* **2008**, *10*, 3689-3698.

(7) Lee, I.; Delbecq, F.; Morales, R.; Albiter, M. A.; Zaera, F. *Nature Materials* **2009**, *8*, 132-138.

(8) Bratlie, K. M.; Lee, H.; Komvopoulos, K.; Yang, P. D.; Somorjai, G. A. *Nano Letters* **2007**, *7*, 3097-3101.

(9) Stamenkovic, V. R.; Mun, B. S.; Arenz, M.; Mayrhofer, K. J. J.; Lucas, C. A.; Wang, G. F.; Ross, P. N.; Markovic, N. M. *Nature Materials* **2007**, *6*, 241-247.

(10) Adzic, R. R.; Simic, D. N.; Despic, A. R.; Drazic, D. M. *Journal of Electroanalytical Chemistry* **1975**, *65*, 587-601.

(11) Adzic, R. R.; Simic, D. N.; Despic, A. R.; Drazic, D. M. *Journal of Electroanalytical Chemistry* **1977**, *80*, 81-99.

(12) Zhang, J. L.; Vukmirovic, M. B.; Xu, Y.; Mavrikakis, M.; Adzic, R. R. *Angewandte Chemie-International Edition* **2005**, *44*, 2132-2135.

(13) Zhang, J. L.; Vukmirovic, M. B.; Sasaki, K.; Nilekar, A. U.; Mavrikakis, M.; Adzic, R. R. *Journal of the American Chemical Society* **2005**, *127*, 12480-12481.

(14) Zhang, J.; Sasaki, K.; Sutter, E.; Adzic, R. R. *Science* **2007**, *315*, 220-222.

(15) Herzing, A. A.; Kiely, C. J.; Carley, A. F.; Landon, P.; Hutchings, G. J. *Science* **2008**, *321*, 1331-1335.

(16) Li, Y. M.; Somorjai, G. A. *Nano Letters* **2010**, *10*, 2289-2295.

(17) Cushing, B. L.; Kolesnichenko, V. L.; O'Connor, C. J. *Chemical Reviews* **2004**, *104*, 3893-3946.

(18) Hench, L. L.; West, J. K. *Chemical Reviews* **1990**, *90*, 33-72.

(19) Mai, H. X.; Sun, L. D.; Zhang, Y. W.; Si, R.; Feng, W.; Zhang, H. P.; Liu, H. C.; Yan, C. H. *Journal of Physical Chemistry B* **2005**, *109*, 24380-24385.

(20) Zhou, K. B.; Wang, X.; Sun, X. M.; Peng, Q.; Li, Y. D. *Journal of Catalysis* **2005**, *229*, 206-212.

(21) Wang, C. C.; Ying, J. Y. *Chemistry of Materials* **1999**, *11*, 3113-3120.

(22) Veith, G. M.; Lupini, A. R.; Pennycook, S. J.; Ownby, G. W.; Dudney, N. J. *Journal of Catalysis* **2005**, *231*, 151-158.

(23) Hanada, N.; Ichikawa, T.; Fujii, H. *Journal of Physical Chemistry B* **2005**, *109*, 7188-7194.

(24) Carp, O.; Huisman, C. L.; Reller, A. *Progress in Solid State Chemistry* **2004**, *32*, 33-177.

(25) Xia, Y. N.; Rogers, J. A.; Paul, K. E.; Whitesides, G. M. *Chemical Reviews* **1999**, *99*, 1823-1848.

(26) Dimitrakopoulos, C. D.; Malenfant, P. R. L. *Advanced Materials* **2002**, *14*, 99-+.

(27) Kang, Y. J.; Murray, C. B. *Journal of the American Chemical Society* **2010**, *132*, 7568-+.

(28) Wang, D. Y.; Kang, Y. J.; Doan-Nguyen, V.; Chen, J.; Kungas, R.; Wieder, N. L.; Bakhmutsky, K.; Gorte, R. J.; Murray, C. B. *Angewandte Chemie-International Edition* **2011**, *50*, 4378-4381.

(29) Kang, Y. J.; Ye, X. C.; Murray, C. B. *Angewandte Chemie-International Edition* **2010**, *49*, 6156-6159.

(30) Lamer, V. K.; Dinegar, R. H. *Journal of the American Chemical Society* **1950**, *72*, 4847-4854.

(31) Puntes, V. F.; Krishnan, K. M.; Alivisatos, A. P. *Science* **2001**, *291*, 2115-2117.

(32) Lacroix, L. M.; Huls, N. F.; Ho, D.; Sun, X. L.; Cheng, K.; Sun, S. H. *Nano Letters*, *11*, 1641-1645.

(33) Sun, S. H.; Murray, C. B. *Journal of Applied Physics* **1999**, *85*, 4325-4330.

(34) Murray, C. B.; Sun, S. H.; Doyle, H.; Betley, T. *Mrs Bulletin* **2001**, *26*, 985-991.

(35) Hung, L. I.; Tsung, C. K.; Huang, W. Y.; Yang, P. D. *Advanced Materials* **2010**, *22*, 1910-+.

(36) Wang, C.; Daimon, H.; Lee, Y.; Kim, J.; Sun, S. *Journal of the American Chemical Society* **2007**, *129*, 6974-+.

(37) Zhang, J.; Fang, J. Y. *Journal of the American Chemical Society* **2009**, *131*, 18543-18547.

(38) Lim, S. I.; Ojea-Jimenez, I.; Varon, M.; Casals, E.; Arbiol, J.; Puntes, V. *Nano Letters* **2010**, *10*, 964-973.

(39) Grass, M. E.; Yue, Y.; Habas, S. E.; Rioux, R. M.; Teall, C. I.; Yang, P.; Somorjai, G. A. *Journal of Physical Chemistry C* **2008**, *112*, 4797-4804.

(40) Amiens, C.; Decaro, D.; Chaudret, B.; Bradley, J. S.; Mazel, R.; Roucau, C. *Journal of the American Chemical Society* **1993**, *115*, 11638-11639.

(41) Rodriguez, A.; Amiens, C.; Chaudret, B.; Casanove, M. J.; Lecante, P.; Bradley, J. S. *Chemistry of Materials* **1996**, *8*, 1978-1986.

(42) Nishihata, Y.; Mizuki, J.; Akao, T.; Tanaka, H.; Uenishi, M.; Kimura, M.; Okamoto, T.; Hamada, N. *Nature* **2002**, *418*, 164-167.

(43) Kim, S. W.; Kim, M.; Lee, W. Y.; Hyeon, T. *Journal of the American Chemical Society* **2002**, *124*, 7642-7643.

(44) Zhao, M. Q.; Crooks, R. M. *Angewandte Chemie-International Edition* **1999**, *38*, 364-366.

(45) Lim, B.; Jiang, M. J.; Camargo, P. H. C.; Cho, E. C.; Tao, J.; Lu, X. M.; Zhu, Y. M.; Xia, Y. N. *Science* **2009**, *324*, 1302-1305.

(46) Habas, S. E.; Lee, H.; Radmilovic, V.; Somorjai, G. A.; Yang, P. *Nature Materials* **2007**, *6*, 692-697.

(47) Xiong, Y. J.; Xia, Y. N. *Advanced Materials* **2007**, *19*, 3385-3391.

(48) Kim, S. W.; Park, J.; Jang, Y.; Chung, Y.; Hwang, S.; Hyeon, T.; Kim, Y. W. *Nano Letters* **2003**, *3*, 1289-1291.

(49) Huo, Z. Y.; Tsung, C. K.; Huang, W. Y.; Zhang, X. F.; Yang, P. D. *Nano Letters* **2008**, *8*, 2041-2044.

(50) Wang, C.; Hu, Y. J.; Lieber, C. M.; Sun, S. H. *Journal of the American Chemical Society* **2008**, *130*, 8902-+.

(51) Lu, X. M.; Yavuz, M. S.; Tuan, H. Y.; Korgel, B. A.; Xia, Y. N. *Journal of the American Chemical Society* **2008**, *130*, 8900-+.

(52) Pazos-Perez, N.; Baranov, D.; Irsen, S.; Hilgendorff, M.; Liz-Marzan, L. M.; Giersig, M. *Langmuir* **2008**, *24*, 9855-9860.

(53) Feng, H. J.; Yang, Y. M.; You, Y. M.; Li, G. P.; Guo, J.; Yu, T.; Shen, Z. X.; Wu, T.; Xing, B. G. *Chemical Communications* **2009**, 1984-1986.

(54) Pyayt, A. L.; Wiley, B.; Xia, Y. N.; Chen, A.; Dalton, L. *Nature Nanotechnology* **2008**, *3*, 660-665.

(55) Lu, Y.; Huang, J. Y.; Wang, C.; Sun, S. H.; Lou, J. *Nature Nanotechnology* **2010**, *5*, 218-224.

(56) Ahmadi, T. S.; Wang, Z. L.; Green, T. C.; Henglein, A.; ElSayed, M. A. *Science* **1996**, *272*, 1924-1926.

(57) Sun, Y. G.; Xia, Y. N. *Science* **2002**, *298*, 2176-2179.

(58) Wiley, B.; Sun, Y. G.; Mayers, B.; Xia, Y. N. *Chemistry-a European Journal* **2005**, *11*, 454-463.

(59) Xia, Y. N.; Xiong, Y. J.; Lim, B.; Skrabalak, S. E. *Angewandte Chemie-International Edition* **2009**, *48*, 60-103.

(60) Narayanan, R.; El-Sayed, M. A. *Nano Letters* **2004**, *4*, 1343-1348.

(61) Song, H.; Kim, F.; Connor, S.; Somorjai, G. A.; Yang, P. D. *Journal of Physical Chemistry B* **2005**, *109*, 188-193.

(62) Yavuz, M. S.; Li, W. Y.; Xia, Y. N. *Chemistry-a European Journal* **2009**, *15*, 13181-13187.

(63) Xiong, Y. J.; McLellan, J. M.; Yin, Y. D.; Xia, Y. N. *Angewandte Chemie-International Edition* **2007**, *46*, 790-794.

(64) Lim, B.; Jiang, M. J.; Tao, J.; Camargo, P. H. C.; Zhu, Y. M.; Xia, Y. N. *Advanced Functional Materials* **2009**, *19*, 189-200.

(65) Kuai, L.; Geng, B. Y.; Wang, S. Z.; Zhao, Y. Y.; Luo, Y. C.; Jiang, H. *Chemistry-a European Journal* **2011**, *17*, 3482-3489.

(66) Li, C. C.; Sato, R.; Kanehara, M.; Zeng, H. B.; Bando, Y.; Teranishi, T. *Angewandte Chemie-International Edition* **2009**, *48*, 6883-6887.

(67) Ling, T.; Xie, L.; Zhu, J.; Yu, H. M.; Ye, H. Q.; Yu, R.; Cheng, Z.; Liu, L.; Yang, G. W.; Cheng, Z. D.; Wang, Y. J.; Ma, X. L. *Nano Letters* **2009**, *9*, 1572-1576.

(68) Xu, D.; Liu, Z. P.; Yang, H. Z.; Liu, Q. S.; Zhang, J.; Fang, J. Y.; Zou, S. Z.; Sun, K. *Angewandte Chemie-International Edition* **2009**, *48*, 4217-4221.

(69) Gasteiger, H. A.; Kocha, S. S.; Sompalli, B.; Wagner, F. T. *Applied Catalysis B-Environmental* **2005**, *56*, 9-35.

(70) Mukerjee, S.; Srinivasan, S.; Soriaga, M. P.; McBreen, J. *Journal of the Electrochemical Society* **1995**, *142*, 1409-1422.

(71) Tian, N.; Zhou, Z. Y.; Sun, S. G.; Ding, Y.; Wang, Z. L. *Science* **2007**, *316*, 732-735.

(72) Markovic, N. M.; Gasteiger, H. A.; Ross, P. N. *Journal of Physical Chemistry* **1995**, *99*, 3411-3415.

(73) Wang, C.; Daimon, H.; Onodera, T.; Koda, T.; Sun, S. H. *Angewandte Chemie-International Edition* **2008**, *47*, 3588-3591.

(74) Ono, K.; Okuda, R.; Ishii, Y.; Kamimura, S.; Oshima, M. *Journal of Physical Chemistry B* **2003**, *107*, 1941-1942.

(75) Lee, D. C.; Ghezelbash, A.; Stowell, C. A.; Korgel, B. A. *Journal of Physical Chemistry B* **2006**, *110*, 20906-20911.

(76) Shevchenko, E. V.; Talapin, D. V.; Rogach, A. L.; Kornowski, A.; Haase, M.; Weller, H. *Journal of the American Chemical Society* **2002**, *124*, 11480-11485.

(77) Ahrenstorf, K.; Albrecht, O.; Heller, H.; Kornowski, A.; Gorlitz, D.; Weller, H. *Small* **2007**, *3*, 271-274.

(78) Xu, D.; Bliznakov, S.; Liu, Z. P.; Fang, J. Y.; Dimitrov, N. *Angewandte Chemie-International Edition* **2010**, *49*, 1282-1285.

(79) Liu, Q. S.; Yan, Z.; Henderson, N. L.; Bauer, J. C.; Goodman, D. W.; Batteas, J. D.; Schaak, R. E. *Journal of the American Chemical Society* **2009**, *131*, 5720-5721.

(80) Miura, A.; Wang, H. S.; Leonard, B. M.; Abruna, H. D.; DiSalvo, F. J. *Chemistry of Materials* **2009**, *21*, 2661-2667.

(81) Casado-Rivera, E.; Volpe, D. J.; Alden, L.; Lind, C.; Downie, C.; Vazquez-Alvarez, T.; Angelo, A. C. D.; DiSalvo, F. J.; Abruna, H. D. *Journal of the American Chemical Society* **2004**, *126*, 4043-4049.

(82) Maksimuk, S.; Yang, S. C.; Peng, Z. M.; Yang, H. *Journal of the American Chemical Society* **2007**, *129*, 8684-+.

(83) Park, J.; An, K. J.; Hwang, Y. S.; Park, J. G.; Noh, H. J.; Kim, J. Y.; Park, J. H.; Hwang, N. M.; Hyeon, T. *Nature Materials* **2004**, *3*, 891-895.

(84) Gorte, R. J. *Aiche Journal* **2010**, *56*, 1126-1135.

(85) Patsalas, P.; Logothetidis, S.; Metaxa, C. *Applied Physics Letters* **2002**, *81*, 466-468.

(86) Jasinski, P.; Suzuki, T.; Anderson, H. U. *Sensors and Actuators B-Chemical* **2003**, *95*, 73-77.

(87) Park, S. D.; Vohs, J. M.; Gorte, R. J. *Nature* **2000**, *404*, 265-267.

(88) Yao, H. C.; Yao, Y. F. Y. *Journal of Catalysis* **1984**, *86*, 254-265.

(89) Trovarelli, A. *Catalysis Reviews-Science and Engineering* **1996**, *38*, 439-520.

(90) Bunluesin, T.; Gorte, R. J.; Graham, G. W. *Applied Catalysis B-Environmental* **1998**, *15*, 107-114.

(91) Putna, E. S.; Bunluesin, T.; Fan, X. L.; Gorte, R. J.; Vohs, J. M.; Lakis, R. E.; Egami, T. *Catalysis Today* **1999**, *50*, 343-352.

(92) Trovarelli, A.; de Leitenburg, C.; Boaro, M.; Dolcetti, G. *Catalysis Today* **1999**, *50*, 353-367.

(93) Fu, Q.; Weber, A.; Flytzani-Stephanopoulos, M. *Catalysis Letters* **2001**, *77*, 87-95.

(94) Yang, L.; Kresnawahjuesa, O.; Gorte, R. J. *Catalysis Letters* **2001**, *72*, 33-37.

(95) Fu, Q.; Saltsburg, H.; Flytzani-Stephanopoulos, M. *Science* **2003**, *301*, 935-938.

(96) Zhang, F.; Wang, P.; Koberstein, J.; Khalid, S.; Chan, S. W. *Surface Science* **2004**, *563*, 74-82.

(97) Gorte, R. J.; Zhao, S. *Catalysis Today* **2005**, *104*, 18-24.

(98) Si, R.; Flytzani-Stephanopoulos, M. *Angewandte Chemie-International Edition* **2008**, *47*, 2884-2887.

(99) Zhou, G.; Hanson, J.; Gorte, R. J. *Applied Catalysis a-General* **2008**, *335*, 153-158.

(100) Chueh, W. C.; Falter, C.; Abbott, M.; Scipio, D.; Furler, P.; Haile, S. M.; Steinfeld, A. *Science* **2010**, *330*, 1797-1801.

(101) Zhang, F.; Jin, Q.; Chan, S. W. *Journal of Applied Physics* **2004**, *95*, 4319-4326.

(102) Yu, T. Y.; Joo, J.; Park, Y. I.; Hyeon, T. *Angewandte Chemie-International Edition* **2005**, *44*, 7411-7414.

(103) Feng, X. D.; Sayle, D. C.; Wang, Z. L.; Paras, M. S.; Santora, B.; Sutorik, A. C.; Sayle, T. X. T.; Yang, Y.; Ding, Y.; Wang, X. D.; Her, Y. S. *Science* **2006**, *312*, 1504-1508.

(104) Yu, T.; Lim, B.; Xia, Y. N. *Angewandte Chemie-International Edition* **2010**, *49*, 4484-4487.

(105) Sayle, D. C.; Maicaneanu, S. A.; Watson, G. W. *Journal of the American Chemical Society* **2002**, *124*, 11429-11439.

(106) Cao, Y. C. *Journal of the American Chemical Society* **2004**, *126*, 7456-7457.

(107) Fu, Y. P.; Lin, C. H.; Hsu, C. S. *Journal of Alloys and Compounds* **2005**, *391*, 110-114.

(108) Liang, X.; Wang, X.; Zhuang, Y.; Xu, B.; Kuang, S. M.; Li, Y. D. *Journal of the American Chemical Society* **2008**, *130*, 2736-+.

(109) Wang, C.; Xu, C. J.; Zeng, H.; Sun, S. H. *Advanced Materials* **2009**, *21*, 3045-3052.

(110) Alayoglu, S.; Nilekar, A. U.; Mavrikakis, M.; Eichhorn, B. *Nature Materials* **2008**, *7*, 333-338.

(111) Wang, C.; Yin, H. F.; Dai, S.; Sun, S. H. *Chemistry of Materials* **2010**, *22*, 3277-3282.

(112) Wang, C.; van der Vliet, D.; More, K. L.; Zaluzec, N. J.; Peng, S.; Sun, S. H.; Daimon, H.; Wang, G. F.; Greeley, J.; Pearson, J.; Paulikas, A. P.; Karapetrov, G.; Strmcnik, D.; Markovic, N. M.; Stamenkovic, V. R. *Nano Letters* **2011**, *11*, 919-926.

(113) Figuerola, A.; Fiore, A.; Di Corato, R.; Falqui, A.; Giannini, C.; Micotti, E.; Lascialfari, A.; Corti, M.; Cingolani, R.; Pellegrino, T.; Cozzoli, P. D.; Manna, L. *Journal of the American Chemical Society* **2008**, *130*, 1477-1487.

(114) Dong, A. G.; Chen, J.; Vora, P. M.; Kikkawa, J. M.; Murray, C. B. *Nature* **2010**, *466*, 474-477.

(115) Shevchenko, E. V.; Talapin, D. V.; Kotov, N. A.; O'Brien, S.; Murray, C. B. *Nature* **2006**, *439*, 55-59.

(116) Yamada, Y.; Tsung, C. K.; Huang, W.; Huo, Z. Y.; Habas, S. E.; Soejima, T.; Aliaga, C. E.; Somorjai, G. A.; Yang, P. D. *Nature Chemistry* **2011**, *3*, 372-376.

(117) Markovic, N. M.; Schmidt, T. J.; Stamenkovic, V.; Ross, P. N. *Fuel Cells* **2001**, *1*, 105-116.

(118) Lee, H. J.; Habas, S. E.; Somorjai, G. A.; Yang, P. D. *Journal of the American Chemical Society* **2008**, *130*, 5406-+.

(119) Sasaki, K.; Naohara, H.; Cai, Y.; Choi, Y. M.; Liu, P.; Vukmirovic, M. B.; Wang, J. X.; Adzic, R. R. *Angewandte Chemie-International Edition* **2010**, *49*, 8602-8607.

(120) Wang, J. X.; Inada, H.; Wu, L. J.; Zhu, Y. M.; Choi, Y. M.; Liu, P.; Zhou, W. P.; Adzic, R. R. *Journal of the American Chemical Society* **2009**, *131*, 17298-17302.

(121) Markovic, N. M.; Adzic, R. R.; Cahan, B. D.; Yeager, E. B. *Journal of Electroanalytical Chemistry* **1994**, *377*, 249-259.

(122) Ross, P. N. *Journal of the Electrochemical Society* **1979**, *126*, 78-82.

(123) Chen, J.; Ye, X. C.; Murray, C. B. *Acs Nano* **2010**, *4*, 2374-2381.

(124) Zhu, Y. M.; Ha, S. Y.; Masel, R. I. *Journal of Power Sources* **2004**, *130*, 8-14.

(125) Rice, C.; Ha, R. I.; Masel, R. I.; Waszczuk, P.; Wieckowski, A.; Barnard, T. *Journal of Power Sources* **2002**, *111*, 83-89.

(126) Rice, C.; Ha, S.; Masel, R. I.; Wieckowski, A. *Journal of Power Sources* **2003**, *115*, 229-235.

(127) Capon, A.; Parsons, R. *Journal of Electroanalytical Chemistry* **1973**, *45*, 205-231.

(128) Capon, A.; Parsons, R. *Journal of Electroanalytical Chemistry* **1973**, *44*, 1-7.

(129) Samjeske, G.; Miki, A.; Ye, S.; Osawa, M. *Journal of Physical Chemistry B* **2006**, *110*, 16559-16566.

(130) Neurock, M.; Janik, M.; Wieckowski, A. *Faraday Discussions* **2008**, *140*, 363-378.

(131) Clavilier, J.; Parsons, R.; Durand, R.; Lamy, C.; Leger, J. M. *Journal of Electroanalytical Chemistry* **1981**, *124*, 321-326.

(132) Adzic, R. R.; Tripkovic, A. V.; Ogrady, W. E. *Nature* **1982**, *296*, 137-138.

(133) Markovic, N. M.; Gasteiger, H. A.; Ross, P. N.; Jiang, X. D.; Villegas, I.; Weaver, M. J. *Electrochimica Acta* **1995**, *40*, 91-98.

(134) Xia, X. H.; Iwasita, T. *Journal of the Electrochemical Society* **1993**, *140*, 2559-2565.

(135) Alden, L. R.; Han, D. K.; Matsumoto, F.; Abruna, H. D.; DiSalvo, F. J. *Chemistry of Materials* **2006**, *18*, 5591-5596.

(136) Roychowdhury, C.; Matsumoto, F.; Zeldovich, V. B.; Warren, S. C.; Mutolo, P. F.; Ballesteros, M.; Wiesner, U.; Abruna, H. D.; DiSalvo, F. J. *Chemistry of Materials* **2006**, *18*, 3365-3372.

(137) Zhang, L. J.; Wang, Z. Y.; Xia, D. G. *Journal of Alloys and Compounds* **2006**, *426*, 268-271.

(138) Liu, Z. L.; Guo, B.; Tay, S. W.; Hong, L.; Zhang, X. H. *Journal of Power Sources* **2008**, *184*, 16-22.

(139) Kowal, A.; Li, M.; Shao, M.; Sasaki, K.; Vukmirovic, M. B.; Zhang, J.; Marinkovic, N. S.; Liu, P.; Frenkel, A. I.; Adzic, R. R. *Nature Materials* **2009**, *8*, 325-330.

(140) Gong, K. P.; Vukmirovic, M. B.; Ma, C.; Zhu, Y. M.; Adzic, R. R. *Journal of Electroanalytical Chemistry* **2011**, *662*, 213-218.

(141) Nilekar, A. U.; Sasaki, K.; Farberow, C. A.; Adzic, R. R.; Mavrikakis, M. *Journal of the American Chemical Society* **2011**, *133*, 18574-18576.

(142) Wang, J. X.; Ma, C.; Choi, Y. M.; Su, D.; Zhu, Y. M.; Liu, P.; Si, R.; Vukmirovic, M. B.; Zhang, Y.; Adzic, R. R. *Journal of the American Chemical Society* **2011**, *133*, 13551-13557.

(143) Wang, L. L.; Johnson, D. D. *Journal of Physical Chemistry C* **2008**, *112*, 8266-8275.

(144) Zhang, J.; Kumagai, H.; Yamamura, K.; Ohara, S.; Takami, S.; Morikawa, A.; Shinjoh, H.; Kaneko, K.; Adschiri, T.; Suda, A. *Nano Letters* **2011**, *11*, 4.

(145) Conesa, J. C. *Surface Science* **1995**, *339*, 337-352.

(146) Haruta, M.; Tsubota, S.; Kobayashi, T.; Kageyama, H.; Genet, M. J.; Delmon, B. *Journal of Catalysis* **1993**, *144*, 175-192.

(147) Haruta, M. *Catalysis Today* **1997**, *36*, 153-166.

(148) Haruta, M.; Date, M. *Applied Catalysis a-General* **2001**, *222*, 427-437.

(149) Haruta, M. *Gold Bulletin* **2004**, *37*, 27-36.

(150) Liu, Y.; Jia, C. J.; Yamasaki, J.; Terasaki, O.; Schuth, F. *Angewandte Chemie-International Edition* **2010**, *49*, 5771-5775.

(151) Dong, A. G.; Ye, X. C.; Chen, J.; Murray, C. B. *Nano Letters* **2011**, *11*, 1804-1809.

(152) Ye, X. C.; Chen, J.; Murray, C. B. *Journal of the American Chemical Society* **2011**, *133*, 2613-2620.

(153) Dong, A. G.; Chen, J.; Ye, X. C.; Kikkawa, J. M.; Murray, C. B. *Journal of the American Chemical Society* **2011**, *133*, 13296-13299.